

**Structure-function relationship of the Patched family of
proteins**

Alex James Timmis

Submitted in accordance with the requirements for the degree of Doctor of
Philosophy

The University of Leeds

School of Molecular and Cellular Biology

Faculty of Biological Sciences

February 2021

The candidate confirms that the work submitted is his/her own and that appropriate credit has been given where reference has been made to the work of others.

This copy has been supplied on the understanding that it is copyright material and that no quotation from the thesis may be published without proper acknowledgement.

Acknowledgements

First, I must thank my PhD supervisor Professor Natalia Riobo-Del Galdo. It was a great opportunity and an honour to be her very first PhD student at the university of Leeds. It has been quite a journey from then to now. I appreciate the freedom and trust she gave me, to take the reins on my own work, in an environment that I could seek advice if required. Ultimately, I believe I am a better scientist because of this.

I must thank Professor Adrian Goldman for including me in his group for the structural biology work. He is a straight to the point, no nonsense expert of membrane biology. Without him I wouldn't have experienced this whole side of biology. I also thank Professor Colin Johnson for his guidance and encouragement, particularly during the first year, with the ciliary related work.

I thank my lab members, in particular; Dom, Cintli and Ioanna. I truly know we are all gluttons for scientific punishment. Having each other's support has really helped us get through this this long, but ultimately rewarding PhD endeavour.

I must thank Dr Maren Thomsen, for providing the opportunity for me to traverse into to the world of structural biology, within Professor Goldman's lab. She provided me with sound guidance and was like the post doc I had never had.

Finally, I am extremely grateful to my girlfriend Chelsea as well as my family, for all their support over the years. Whether she wanted to or not, Chelsea might well be the most knowledgeable layman of the hedgehog signalling pathway, through my constant bombardment of ideas, explanations of hypothesises and questions.

Abstract

The Patched protein family is characterised by a conserved sterol sensing domain (SSD). The receptor of Hedgehog, Patched-1, is believed to mobilise endogenous cholesterol to elicit a non-stoichiometric repression of the pathway activator Smoothed. How Patched-1 transports cholesterol, and whether this mechanism is shared by other Patched family proteins remains unclear. My doctoral dissertation work demonstrates an essential role of the SSD and several sites that interact with cholesterol in Patched-1, Patched-2, and a distant relative PTCHD1. I also present biochemical and functional evidence of Patched-1 and Patched-2 heterodimeric/oligomeric interactions, with synergistic activity.

In Chapter 3, I describe mutational experiments that support the requirement of a hydrophobic cavity within Patched-1, for repression of Smoothed and canonical Hh signalling. Further experiments suggested a structural dependency of the C-terminal domain (CTD) upon the middle cytoplasmic loop (ML). Removal of these domains did not prevent dimerization, but impaired canonical activity.

Chapter 4 describes experiments that revealed significant similarities between Patched-1 and Patched-2. Functionally, I identified the existence of Patched hetero-interactions, which exhibited direct competition with homo-interactions and displayed a synergistic effect on canonical activity. Further experiments using non-functional Patched mutants, revealed this synergistic activity is solely dependent on the activity-state of Patched-1 in the heterodimer. Moreover, I demonstrated that the CTDs of Patched-1 and Patched-2 regulate the inhibitory activity over Smoothed, possibly through interaction with the ML. Substitution of the CTD of Patched-1 with that of Patched-2 produced a non-functional protein.

In Chapter 5, I optimised purification conditions of PTCHD1, mutated in some individuals with autistic spectrum disorder, generating an initial low-resolution model by negative stain electron microscopy. I demonstrate that PTCHD1 binds cholesterol, but cannot inhibit Smoothed function, nor bind Sonic Hedgehog ligand. Finally, proteomic analysis of PTCHD1-interacting proteins suggest a role in ribonucleoprotein granule formation and a biological function in neurons.

Table of Contents

Contents

Table of Contents	vi
List of Tables	x
List of Figures	xi
Abbreviations	xvi
Chapter 1 Introduction	- 2 -
1.1 The Canonical Hedgehog Signalling Pathway	- 2 -
1.1.1 A simplified overview of Hedgehog signalling	- 2 -
1.1.2 A General Introduction to the Primary Cilium	- 4 -
1.1.3 The Architecture of the Primary Cilium	- 5 -
1.1.4 The Importance of the ciliary microenvironment to maintain correct canonical hedgehog signalling	- 8 -
1.1.5 Canonical Hedgehog signalling in the primary cilium	- 9 -
1.2 Molecular Components of Hh Signalling	- 13 -
1.2.1 Sonic Hedgehog Ligand.....	- 13 -
1.2.2 Smoothened Structure	- 16 -
1.2.3 Roles of co-receptors in ligand binding	- 20 -
1.3 The Patched family of Proteins	- 22 -
1.3.1 Common Structural Architecture of Patched Proteins.....	- 22 -
1.3.2 Oligomerisation of Patched.....	- 24 -
1.3.3 PTCH1 and its interaction with Shh	- 26 -
1.3.4 The Role, Relevance and Redundancy of PTCH2.....	- 35 -
Chapter 2 Material and Methods	- 40 -
2.1 Cell Lines & Culture Procedures	- 40 -
2.2 Freezing and Thawing Cells	- 41 -
2.3 Cell Counting	- 41 -
2.4 Gli-Luciferase Assay	- 42 -
2.5 Co-immunoprecipitation Assays.....	- 43 -
2.6 Co-IP Competition Assay	- 44 -
2.7 Western Blotting.....	- 45 -
2.8 Site Directed Mutagenesis	- 47 -
2.9 Transformation, Selection, DNA extraction and Sequencing	- 49 -
2.10 Ciliary pH Fluorescent Biosensor Imaging	- 50 -

2.11 FRET-Based imaging.....	- 51 -
2.12 FRET-Based Data Processing.....	- 52 -
2.13 FRET-Based Competition Assay	- 52 -
2.14 Immunofluorescence.....	- 53 -
2.15 Fluorescent LED Microscopy	- 54 -
2.16 PTCH2 CRISPR/Cas9 Stable Cell Knockout.....	- 54 -
2.17 Cloning of PTCH1, PTCH2 and PTCHD1 pFastBac Vectors.....	- 55 -
2.18 Generation of Baculovirus.....	- 56 -
2.19 Production of Baculovirus Infected Cells (BIICs).....	- 57 -
2.20 Large Scale Protein Expression.....	- 58 -
2.21 Membrane Preparation	- 58 -
2.22 Large Scale Protein Purification.....	- 59 -
2.23 Immunoprecipitation for Mass Spectrometry.....	- 60 -
2.24 Mass Spectrometry	- 61 -
2.25 PhotoClickable Cholesterol Assay	- 62 -
2.26 EM Grid Glow Discharge	- 62 -
2.27 Electron Microscopy Negative Staining.....	- 63 -
2.28 Vitrification of purified protein.....	- 64 -
2.29 Electron Microscope Negative Stain Image Analysis	- 65 -
Chapter 3 Specific mutation of the Ptc1 SSD residue P490, or removal of the cytoplasmic domains impairs activity, without disrupting oligomerisation.....	- 71 -
3.1 Introduction	- 71 -
3.2 Aims and Hypothesis	- 75 -
3.3 Results.....	- 76 -
3.3.1 Mutation of Ptc1 P490, corresponding to the NPC1 residue P691, implicated in cholesterol transfer, had significant impact on canonical function	- 76 -
3.3.2 Activation of canonical Hedgehog signalling does not induce significant changes in ciliary pH	- 90 -
3.3.3 Removal of the two cytoplasmic domains of Patched 1 reveals a mutual dependency for stable expression.....	- 94 -
3.3.4 The middle loop and CTD are not required for Patched 1 self-oligomerisation.....	- 100 -
3.3.5 Removal of the cytoplasmic domains impairs Patched 1 inhibition of canonical Hh signalling.	- 105 -
3.4 Discussion	- 108 -

Chapter 4 Patched homologs form homo- and heterodimer interactions of close resemblance, but differing canonical functionality, due to influences of the cytoplasmic domains.....	- 122 -
4.1 Introduction	- 122 -
4.2 Aims and Hypothesis	- 125 -
4.3 Results.....	- 126 -
4.3.1 Patched 1 and 2 are capable of forming homo- and hetero-interactions.....	- 126 -
4.3.2 The heterodimer interactions of Patched 1 and Patched 2 are competitive with their homodimer counterparts.	- 134 -
4.3.3 In the absence of Patched 1, Patched 2 displays low level activity, which is responsive to N-Shh.....	- 138 -
4.3.4 Replication of a PTCH1 inactivating mutation in PTCH2 failed to impair activity.	- 144 -
4.3.5 Replication of a PTCH1 Gorlin Syndrome related mutation in PTCH2 simulated a cancerous phenotype, only in the absence of Ptc1.....	- 154 -
4.3.6 Patched hetero-interactions confer synergistic canonical activity, in a Patched 1 activity-dependent manner.	- 161 -
4.3.7 The middle cytoplasmic loop and CTD are not essential for Patched heterodimer interactions.....	- 167 -
4.3.8 Effect of Patched cytoplasmic domain mutants on Patched 2 homodimer and Patched 1 and 2 heterodimer canonical activity.	- 174 -
4.3.9 Substitution of the CTD of PTCH1 with that of PTCH2 results in a non-functional chimeric protein.	- 180 -
4.4 Discussion	- 188 -
Chapter 5 Expression, purification and structural analysis of PTCHD1	- 198 -
5.1 Introduction	- 198 -
5.2 Aims and Hypothesis	- 207 -
5.3 Results.....	- 208 -
5.3.1 Cloning and Production of PTCHD1 Baculovirus Infected Cells	- 208 -
5.3.2 Expression and Membrane Preparations.....	- 209 -
5.3.3 Small Scale Detergent Screening	- 211 -
5.3.4 SEC-MALS and mass spectrometry analysis identified a monodispersed peak of PTCHD1 in GDN purification....	- 215 -
5.3.5 Optimisation for Large Scale Purification of PTCHD1 with GDN.....	- 221 -

5.3.6 Structural analysis of PTCHD1 by negative stain.....	- 229 -
5.3.7 Progress toward Cryo-EM investigation of PTCHD1.....	- 233 -
5.3.8 PTCHD1 binds cholesterol, but displays no function as a Hh pathway negative regulator.	- 235 -
5.3.9 Immunoprecipitation and mass spectrometry analysis revealed an interaction between PTCHD1 and neuronal ribonucleoprotein granule associated proteins.	- 239 -
5.4 Discussion	- 246 -
Chapter 6 General Discussion	- 251 -

List of Tables

Table 2.1 Antibody Table.....	- 46 -
Table 2.2 Thermocycler PCR set-ups for different polymerases.....	- 49 -
Table 2.3 Summary of FRET-Based data processing	- 52 -
Table 2.4 Summary of RELION 3.0 work flow for EM micrograph processing.....	- 66 -
Table 5.1 Key proteins identified in PTCHD1 Immunoprecipitates by mass spectrometry.....	- 244 -

List of Figures

Figure 1.1 Simplified switch-based model of Shh Signalling.....	- 3 -
Figure 1.2 Architecture of the Primary Cilium.....	- 7 -
Figure 1.3 Simplified schematic of Shh stimulation of the canonical Hedgehog signalling pathway.	- 12 -
Figure 1.4 Simplified depiction of the maturation of Shh ligand	- 14 -
Figure 1.5 The crystal structure of SMO- Δ C with cholesterol bound to the CRD.....	- 18 -
Figure 1.6 Computational inferred relatedness of Patched proteins and other Hh pathway SSD containing proteins.	- 23 -
Figure 1.7 The two distinct PTCH1 binding interfaces of N-Shh.	- 28 -
Figure 1.8 Monomeric and dimeric PTCH1 bound to different forms of Shh.....	- 31 -
Figure 1.9 Functional relevance of the 2:1 PTCH1:N-Shh complex..	- 32 -
Figure 1.10 Schematic of N-Shh binding of PTCH1 dimer.....	- 33 -
Figure 2.1 Hierarchical tree of PTCH2 plasmids generated.	- 67 -
Figure 2.2 Hierarchical tree of Ptc1 plasmids generated.....	- 68 -
Figure 2.3 Hierarchical tree of PTCH1 plasmids generated.	- 69 -
Figure 3.1 RND protein 'GxxxDD' consensus sequence is present in several Hh pathway components.	- 73 -
Figure 3.2 Identification of integral residues of Ptc1 through homology modelling to NPC1.....	- 81 -
Figure 3.3 Ptc1-F1109A displayed reduced protein expression compared to full length Ptc1.....	- 82 -
Figure 3.4 Immunocytochemistry revealed similar subcellular localisation and expression of Ptc1 mutants to wild type Ptc1.-	- 83 -
Figure 3.5 Co-IP confirmed full length and point mutants of Ptc1 interact with full length Ptc1-HA in HEK293 cells.....	- 84 -
Figure 3.6 Mechanistic depiction of the Patched FRET-Based Assay.....	- 85 -
Figure 3.7 C-terminally fluorescently labelled PTCH1 monomers express and co-localise in HEK293 cells.	- 86 -
Figure 3.8 PTCH1 homo-interactions were confirmed by live cell FRET confocal imaging in HEK293 and <i>Ptc1</i> ^{-/-} MEFs.....	- 87 -
Figure 3.9 Competition-Based FRET assay in HEK293 cells confirmed all Ptc1 point mutants can form homo-dimers with PTCH1.....	- 88 -
Figure 3.10 Ptc1-P490A displayed impaired inhibition of canonical signalling.....	- 89 -

Figure 3.11 Activation of Hh signalling does not significantly alter ciliary pH.....	- 93 -
Figure 3.12 Individual removal of either Ptc1 cytoplasmic domain impairs protein expression, whilst combined removal restores protein expression.....	- 97 -
Figure 3.13 Removal of a single intracellular domain leads to impaired Ptc1 protein maturity and expression.....	- 98 -
Figure 3.14 Large deletions of the cytoplasmic domains increase PTCH1 expression and membrane localisation.....	- 99 -
Figure 3.15 Removal of the middle and C-terminal cytoplasmic domains of Ptc1 does not disrupt direct interaction with full length PTCH1... ..	- 102 -
Figure 3.16 Removal of the middle cytoplasmic loop is not sufficient to disrupt PTCH1 homo-interactions.....	- 103 -
Figure 3.17 Combined removal of the middle cytoplasmic loop and CTD is not sufficient to disrupt PTCH1 homo-interactions.....	- 104 -
Figure 3.18 Removal of one or both cytoplasmic domains of Patched 1 results in impaired activity.....	- 107 -
Figure 3.19 Predicted structural impact of Ptc1 P490 mutation on predicted sterol cavity identified via NPC1 homology modelling.	- 109 -
Figure 3.20 Mapping of the predicted structural location and side chain alterations of the Ptc1 point mutants.....	- 112 -
Figure 3.21 Effect on FRET from the removal of the CTD of PTCH1.-	114
-	
Figure 3.22 Deletion of the CTD effects Patched 1 turnover but not dimerization.....	- 117 -
Figure 3.23 Hypothetical PTCH1 Na ⁺ and K ⁺ dependent modes of action.	- 120 -
Figure 4.1 PTCH2 directly associates with Ptc1 in HEK293 cells... -	129 -
Figure 4.2 PTCH2 forms homo-interactions in HEK293 cells.....	- 130 -
Figure 4.3 C-terminally fluorescently labelled PTCH2 plasmids show similar expression profiles and co-localisation in transfected HEK293 cells.	- 131 -
Figure 4.4 Live FRET-based assay confirmed PTCH1 and PTCH2 homo-interactions in HEK293 cells.....	- 132 -
Figure 4.5 Live FRET-based assay confirmed PTCH1:PTCH2 hetero-interactions in HEK293 cells.....	- 133 -
Figure 4.6 Excess over-expression of PTCH2 minimally impaired Patched 1 homo-interactions in HEK293 cells.....	- 136 -
Figure 4.7 Competition-Based FRET assay confirmed an excess of PTCH2-FLAG reduced the frequency of PTCH1 homodimers.-	137 -

Figure 4.8 Patched 2 displays low level inhibition of the canonical Hh pathway, independent of Patched 1.....	- 141 -
Figure 4.9 Treatment with KAAD-Cyclopamine confirmed maximal inhibition achieved by Patched 1, but not PTCH2 alone.	- 142 -
Figure 4.10 PTCH2 activity is responsive to N-Shh.	- 143 -
Figure 4.11 Structural alignment of Ptc1 (PDB ID:) and the secondary sequence of PTCH2, threaded to PTCH1 (PBD ID:) Indicating the predicted location and side chain alterations of residues identified to impair canonical function.	- 149 -
Figure 4.12 PTCH1-VLW forms homo-interactions with itself and with full length PTCH1 in HEK293 cells, despite a reported lack of activity.	- 150 -
Figure 4.13 PTCH2-LLW, forms homo-interactions with full length PTCH2 in HEK293 cells.	- 151 -
Figure 4.14 PTCH1-VLW has significantly reduced activity, whilst PTCH2-LLW shows no significant difference in activity.	- 152 -
Figure 4.15 <i>Ptc1</i> ^{-/-} MEFs Selected for Ptc2 CRISPR KO displayed higher sensitivity to transfected PTCH2.....	- 153 -
Figure 4.16 Structural comparison of Ptc1-D499 and PTCH2-D469 and their predicted interaction partners.	- 157 -
Figure 4.17 Immunofluorescence revealed altered localisation for PTCH2-D469A in HEK293 cells.	- 158 -
Figure 4.18 PTCH2-D469A showed significantly impaired activity. -	159 -
Figure 4.19 KAAD-cyclopamine treatment is less effective in cells transfected with PTCH2-D469A, compared to Ptc1 or PTCH2.-	160 -
Figure 4.20 Patched heterodimer interactions conferred additional Gli inhibition activity.	- 164 -
Figure 4.21 Patched heterodimer activity is dependent on the activity-state of the Patched 1 monomer involved.	- 165 -
Figure 4.22 Co-transfection of a functionally impaired PTCH2-D469A with Ptc1-HA still produces an additional inhibitory effect on Gli.. -	166 -
Figure 4.23 Immunofluorescence of PTCH2 and the cytoplasmic domain mutants, PTCH2-ΔC and PTCH2-ΔMLΔC.....	- 170 -
Figure 4.24 The hetero-interaction of Ptc1 and PTCH2 does not require the middle loop or CTD of Ptc1, despite the CTD being able to interact with PTCH2 independently.....	- 171 -
Figure 4.25 Deletion of cytoplasmic domains potentially impaired but did prevent Patched hetero-interactions in HEK293 cells.....	- 172 -
Figure 4.26 Removal of the CTD of PTCH2 does not prevent homodimer interactions with full length PTCH2.....	- 173 -
Figure 4.27 Removal of the CTD alone or in combination with the middle loop did not impair PTCH2 activity.....	- 176 -

Figure 4.28 Removal of the cytoplasmic domains of PTCH2 does not diminish increased heterodimer activity.	177 -
Figure 4.29 PTCH2-ΔC activity is impaired by co-transfection with inactive PTCH1-VLW.....	178 -
Figure 4.30 Hetero-interactions involving PTCH1-9:18ML display no increase in activity.....	179 -
Figure 4.31 PTCH1CTD2 displayed comparable expression and localisation to that of PTCH1 and PTCH2.....	183 -
Figure 4.32 PTCH1CTD2 co-localised with PTCH1 in HEK293 cells.-	184 -
Figure 4.33 PTCH1CTD2 directly interacts with Patched 1 and Patched 2 in HEK293 cells.	185 -
Figure 4.34 PTCH1CTD2 forms heterodimer interactions with both PTCH1 and PTCH2, displaying a CTD-length dependent effect on FRET.....	186 -
Figure 4.35 PTCH1CTD2 displayed no activity in <i>Ptc1</i> ^{-/-} MEFs.....	187 -
Figure 4.36 Hypothetical differences in protein stability and turnover of Patched homo and heterodimers	190 -
Figure 4.37 Hypothetical impact of the newly discovered Heterodimeric Patched.....	192 -
Figure 5.1 Alignment of PTCHD1 mutations to Patched 1 and 2 sequences.	201 -
Figure 5.2 Alignment of the C-terminal domain of PTCHD1 to PTCH1 and PTCH2.....	204 -
Figure 5.3 Expression and membrane fractionation of PTCHD1 from Sf9 BIIcs.....	210 -
Figure 5.4 Small scale membrane solubilisation detergent screen.-	214 -
Figure 5.5 SEC-MALS analysis of determined GDN superior to LMNG + CHS for purification of a protein corresponding to the mass of PTCHD1.	218 -
Figure 5.6 Mass Spectrometry confirmed the identity of the purified protein as PTCHD1.	220 -
Figure 5.7 A longer solubilisation time resulted in increased PTCHD1 in the soluble fraction.....	225 -
Figure 5.8 Increasing the concentration of GDN during solubilisation increased protein solubilisation.....	226 -
Figure 5.9 Increasing GDN concentration or HisPur™ Cobalt resin volume increased PTCHD1 concentration in elution fractions.-	227 -
Figure 5.10 Final optimised GDN purification of PTCHD1.....	228 -
Figure 5.11 Negative stain and 3D model of PTCHD1.....	231 -
Figure 5.12 Alignment of 2:1 PTCH1:Shh-N complex EM density map to 3D PTCHD1 model.	232 -

Figure 5.13 PTCHD1 was found to bind cholesterol through Click-reaction assay..... - 237 -

Figure 5.14 PTCHD1 displays no apparent function in canonical Hh signalling..... - 238 -

Figure 5.15 Immunofluorescence of PTCHD1 in SH-SY5Y and HEK293 cells..... - 243 -

Figure 5.16 STRING analysis of PTCHD1 and mass spectrometry interaction partners..... - 245 -

Figure 5.17 ShhN:PTCH1 ECD interface is not conserved in PTCHD1..... - 249 -

Abbreviations

ATP	Adenosine triphosphate
ASD	Autism spectrum disorder
Boc	Brother of CDO
BIICs	Baculovirus-infected insect cells
BSA	Bovine serum albumin
cAMP	Cyclic adenosine monophosphate
CDO	Cell adhesion molecule-related/down-regulated by oncogenes
CHS	Cholesterol hemisuccinate
CMC	Critical micelle concentration
CNV	Copy number variant
Co-IP	Co-immunoprecipitation
CRD	Cysteine rich domain
Cryo-EM	Cryo-electron microscopy
CTD	C-terminal domain
CTF	Contrast transfer function
DDM	N-Dodecyl-beta-Maltoside
Dhh	Desert hedgehog
DISP1	Dispatched
DMEM	Dulbecco's modified eagle medium
DMSO	dimethyl sulfoxide
DNA	Deoxyribose nucleic acid
eGFP	enhanced green fluorescent protein
EM	Electron microscopy
FBS	Foetal bovine serum
FRET	Fluorescence resonant energy transfer
GAPDH	Glyceraldehyde-3-phosphate dehydrogenase
GDN	Glyco-diosgenin
GO	Gene Ontology
Gli	Glioma-associated oncogene
GPCR	G-protein coupled receptor
GSK-3 β	glycogen synthase kinase 3 β

HECT E3	Homologous to E6AP C-terminus E3
Hh	Hedgehog
His	Histidine tag
HRV	Recombinant 3C protease
ID	Intellectual disability
Ihh	Indian hedgehog
IP	Immunoprecipitation
LMNG	Lauryl maltose neopentyl glycol
MCS	Multiple cloning site
MEFs	Mouse embryonic fibroblasts
ML	Middle loop
MS	Mass spectrometry
NPC1	Niemann-Pick C1
N-Shh	recombinant N-terminal fragment of Shh
PA	Proliferation arrest
PAPB	Polyadenylate-binding protein 1
PDK1	Phosphoinositide-dependent kinase-1
PKA	protein kinase A
PMF	Proton motive force
Ptc	Drosophila
Ptc1	Mouse Patched 1
PTCH1	human Patched 1
PTCH2	human Patched 2
PTCHD1	Patched domain-containing protein 1
(PtdIns(3,4,5)P3)	Phosphatidylinositol (3,4,5)-trisphosphate
PtdIns(4,5)P2	Phosphatidylinositol 4,5-bisphosphate
RLUs	Relative luciferase units
RNA	Ribonucleic Acid
RND	Resistance nodulation division
RNPs	Ribonuclease protein granules
ROI	Region of interest
RPM	Revolutions per minute
SAG	Smoothened Agonist
SDS	Sodium dodecyl sulphate

SDS-PAGE	Sodium dodecyl sulphate polyacrylamide gel electrophoresis
SEC-MALS	Size exclusion chromatography multi-angled light scattering
sgRNA	Single guide RNA
SGs	Stress granules
Shh	Sonic hedgehog
Smo	Smoothened
SSD	Sterol sensing domain
TEV	Tobacco etch virus protease
TM	Transmembrane domain
WCL	Whole cell lysate
YFP	Yellow fluorescent protein

Chapter 1

Introduction

Chapter 1

Introduction

1.1 The Canonical Hedgehog Signalling Pathway

1.1.1 A simplified overview of Hedgehog signalling

The Hedgehog (Hh) signalling pathway is fundamental to embryonic development, and regulates cell maintenance and differentiation in many adult tissues (Ihrie et al., 2011). Mutations within several of the key protein components of the pathway instigate aberrant Hh signalling, which has been associated with cancer formation and tumour survival (Dahmane et al., 1997; Taylor et al., 2002; Bakshi et al., 2017). The mammalian genome encodes three Hh proteins, which activate signalling: Sonic Hh (Shh), Indian Hh (Ihh) and Desert Hh (Dhh). Shh is the most widely expressed, whilst Ihh and Dhh are largely restricted to roles within bone and gonad differentiation respectively (Echelard et al., 1993; Pathi et al., 2001). Hh signal transduction ultimately functions through the proteolytic regulation of its downstream effectors, the Glioma-associated transcription factors (Gli) (Jacob and Briscoe, 2003; Humke et al., 2010).

As opposed to functioning as direct pathway activators, the Hh proteins actually bind to, and inhibit, the main negative regulator of Hh signalling, Patched 1 (Ptch1) (Denef et al., 2000). Vertebrates also possess another Patched homolog, Patched 2 (Ptch2), which is viewed as largely non-essential, performing redundant or supportive roles (Carpenter et al., 1998). In the absence of Hh ligands, Ptch1 indirectly represses a key activator of Hh signalling, Smoothened

(Smo). Upon Hh ligand binding to Ptch1, Smo is de-repressed and, in turn, prevents Suppressor of Fused (Sufu)-mediated retention and partial proteasomal degradation of constitutively expressed Glis. Full length Glis are then able to activate Hh target genes (**Figure 1.1**) (Humke et al., 2010; Tukachinsky et al., 2016).

There are three vertebrate Gli proteins, Gli1 Gli2 and Gli3. Whilst Gli1 functions only as a transcriptional activator and is induced by Hh signalling, both Gli2 and Gli3 can function as positive or negative regulators of Hh signal transduction. Full length Gli2/3 are activators of Hh signalling, whilst truncated forms (primarily Gli3R) are repressors (Hui et al., 1994; Niewiadomski et al., 2014).

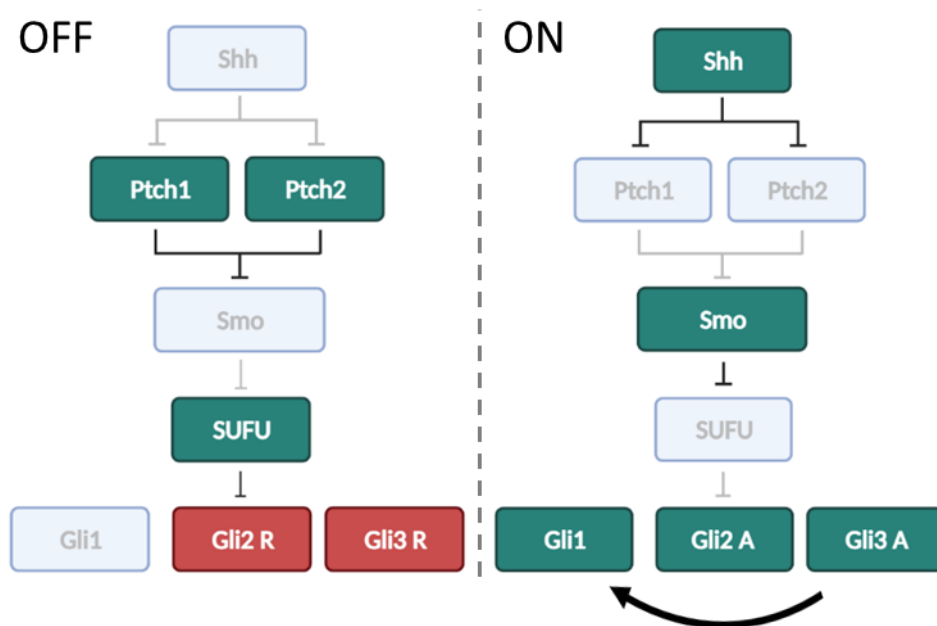


Figure 1.1 Simplified switch-based model of Shh Signalling

The switch-based model shows proteins that are active in green, inactive in grey and in the case of repressor forms of Gli2/3, red. Left: the pathway is off, right: the pathway is on by way of Shh ligand stimulation.

1.1.2 A General Introduction to the Primary Cilium

It was almost two decades after the initial identification of the Hh gene in *Drosophila*, that a connection with the primary cilium was discovered (Huangfu et al., 2003). Fundamental to the vertebrate Hh signalling pathway, the primary cilium provides a dynamic, regulatory micro-domain, highly enriched in intracellular and extracellular signalling molecules (Huangfu and Anderson, 2005; Ishikawa et al., 2012). This highly evolutionary-conserved structure functions as the central node for several signalling cascades (Rix et al., 2011; Ezratty et al., 2011; Lee et al., 2012). The primary cilium can simultaneously instigate, propagate, maintain, dampen and block intracellular signalling, to achieve appropriate cellular responses (Hilgendorf et al., 2016).

The primary cilium is a non-motile, flagella-like structure, protruding from the plasma membrane of the cell into the extracellular matrix (Sun et al., 2019). Much like an antenna, the primary cilium detects mechanical and chemical signals, resulting in responses in the cell, through the use of a specialised microtubule-based transport machinery (Battle et al., 2015). Typically, there is a single primary cilium per cell, originating from the basal body during interphase and reabsorbed as the cells progresses into mitosis (Spasic and Jacobs, 2017).

With an average diameter of 0.2 μM and length of 3 μM (length range: 1-10 μM), the primary cilium has a large surface area to volume ratio (~20-fold) (Delling et al., 2013). Due to this physical structure, very small concentrations of signalling ligands can be detected and direct rapid cellular responses. Such responses would not be feasible within the vast volume of the cytoplasm (Nachury and Mick, 2019). Unlike other specialist organelles, which are completely enclosed within a

membrane, separate from the cytoplasm, the primary cilium is continuous with the plasma membrane. This pseudo-organelle lacks any physical separation, but successfully maintains a distinct micro-environment to that of the cytoplasm. Through a series of co-ordinated features, both physical and chemical, the primary cilium operates a selective, flexible regulatory barrier to control entry and exit to its lumen (Nachury et al., 2010).

1.1.3 The Architecture of the Primary Cilium

From base to tip the primary cilium can be divided into four main zones; the basal body, the transition zone, the axoneme, and the tip (**Figure 1.2**). Originating from the mother centriole, the basal body harbours three key extensions, which anchor the primary cilium to the plasma membrane (Seeley and Nachury, 2010). Ciliary roots descend into the cell, providing physical support; basal feet aid in anchoring microtubules, and transition fibres connect the triplet microtubule barrel to the plasma membrane, obstructing periciliary entry. Acting in conjunction with the transition zone, these components form the 'ciliary gate' (Ramsbottom and Pownall, 2016).

Sitting atop the basal body is the transition zone (TZ), an important component and hotspot of ciliopathy related proteins (**Figure 1.2**) (Garcia-Gonzalo et al., 2011). Often compared to the nuclear pores, the TZ is a selective barrier that regulates entry and exit to the ciliary lumen (Inoue et al., 2013). Molecular studies show that the TZ exerts a size-dependent restriction on diffusion. Molecules below 30 kDa move freely, whilst molecules between 30-60 kDa experience increasing diffusion restriction, and molecules above 60 kDa are entirely restricted from diffusion-mediated entry (Nachury et al., 2010). Super resolution

imaging of the TZ has enhanced our understanding of how in part this is achieved. Nine alar sheets (propeller-like transition fibres) sit at the entrance of the lumen, arranged so that the space between each accommodates a maximal molecule size <60 nm diameter (Anderson, 1972).

Further to the physical pore-like barrier of the TZ, there is a body of evidence that ciliary membrane patterning is also fundamental to the maintenance of the ciliary microenvironment. The lipid composition of the majority of the primary cilia membrane is enriched for PI(4)P as opposed to PI(4,5)P₂, which is enriched in the extraciliary plasma membrane. Where the two membranes meet, at the proximal region of the cilia, there is a locally restricted membrane enrichment of PI(4,5)P₂ which appears integral for the localisation of many membrane proteins to the TZ (Jacoby et al., 2009; Garcia-Gonzalo et al., 2015).

The axoneme is characterised by a (9 + 0) microtubule doublet ultrastructure with 9-fold symmetry (**Figure 1.2**). These microtubules serve as 'railway lines' for the bidirectional transport of molecular cargoes along the axoneme (He et al., 2016). This active transport is facilitated by the intraflagella transport machinery (IFT). Two sub-complexes of IFT, IFT-A and IFT-B, carry cargo in opposing directions, along the opposing microtubules in each of the 9 doublets (Broekhuis et al., 2014). Each IFT complex forms a 'train' of proteins, which are mobilised by a coupled protein motor. IFT-B couples with Kinesin-2 to perform anterograde movement (towards the tip), whilst IFT-A couples with Cytoplasmic Dynein-2 for retrograde movement (towards the base). Both IFT complexes are essential for primary cilia assembly and maintenance (Mikami et al., 2002; Funabashi et al., 2018).

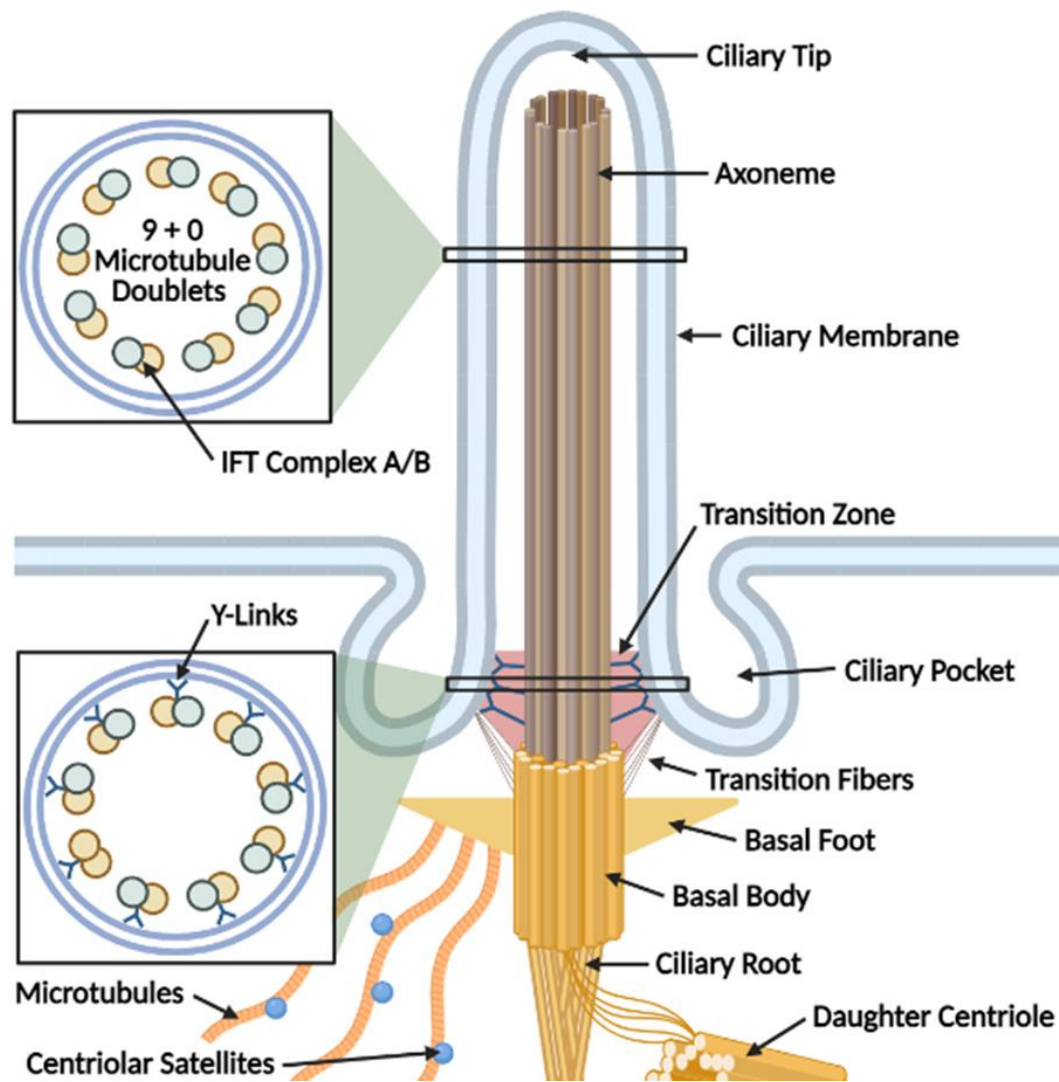


Figure 1.2 Architecture of the Primary Cilium.

Schematic of the main structural components of the primary cilium. The four main regions: the ciliary tip, the axoneme, the transition zone, and the basal body. The axoneme cross sections show the 9 + 0 microtubule doublet formation. Within the transition zone Y-links can be seen extending to the ciliary membrane. The basal feet, ciliary root and transition fibres help to stabilise basal body and axoneme.

1.1.4 The Importance of the ciliary microenvironment to maintain correct canonical hedgehog signalling

Canonical Hh signalling is entirely dependent upon the primary cilia, both for its structural components and chemical properties. Loss of the cilium, like in *Kif3a*^{-/-} mouse embryonic fibroblasts (MEFs), completely abrogates canonical Hh signalling (Huangfu et al., 2003). Even the dysfunction of components of the cilia that are unrelated to the Hh signalling machinery can impact Hh reception, transduction and signalling strengths. Mutations in ciliary structural regulatory proteins, that effect length or trafficking, but don't prevent ciliogenesis, perturb Hh signalling (Vorobyeva and Saunders, 2018). Ciliary length is both tissue and function specific, requiring tight regulation. *In vitro* overexpression of TGF- β or *Arl13b* has been shown to reduce and increase cilia length respectively, impacting Hh signalling (Larkins et al., 2011; Kawasaki et al., 2015).

Impairment of TZ or IFT components can cause aberrant Hh signalling, either directly or indirectly. Expression of GTP-locked Rab8 GTPase causes elongation of the cilium, through constitutive vesicle fusion and trafficking into the lumen (Nachury et al., 2007). IFT27 does not affect formation of the cilia, but is directly involved in the retrograde trafficking of Smo. Removal of IFT27 causes aberrant accumulation of Smo in the cilium, in a ligand-independent manner (Eguether et al., 2014; Desai et al., 2020).

1.1.5 Canonical Hedgehog signalling in the primary cilium

In a healthy cell in the absence of ligand, the Hh pathway remains inactive, through the action of its main inhibitory component, Ptch1. Ptch1 functions to inhibit the activation and accumulation of Smo to the primary cilium (Corbit et al., 2005; Rohatgi et al., 2007). Ptch1 inhibition of Smo is achieved in a non-stoichiometric manner, whereby no physical binding interaction occurs between the two proteins (Taipale et al., 2002). In this state, Ptch1 is localised in the cilium and indirectly inhibits ciliary accumulation of Smo and the subsequent activation of the Gli transcription factors, which drive Hh target gene expression (**Figure 1.3**) (Rohatgi et al., 2007; Rohatgi, Milenkovic, Ryan B Corcoran, et al., 2009).

Without ligand stimulation, full length, active Gli2/3 isoforms are bound and sequestered to the cytoplasm and the ciliary tip by another pathway inhibitor, SUFU (Ding et al., 1999). KIF7, a kinesin 4 family protein, is believed to maintain a 'tip compartment' for the regulation of Gli/SUFU activation (Pedersen and Akhmanova, 2014). KIF7 is also proposed to function at the base of the cilium alongside three protein kinases, PKA, GSK3 β and CK1, phosphorylating full length Gli2/3 isoforms, targeting them for partial proteasomal degradation into truncated transcriptional repressor forms (**Figure 1.3**) (Liem et al., 2009).

Interestingly, cilia of unstimulated cells do contain small concentrations of Smo as a consequence of low level lateral diffusion (Milenkovic et al., 2009). However, this population of Smo resides close to the cilia base, is inactive, and displays no significant directional movement or retention within the cilium. This suggests Ptch1 primarily inhibits the activation of Smo rather than sequestration or outrightly blocking ciliary entry. The ciliary localisation of Ptch1 and Smo are

inversely correlated and upon ligand stimulation, ciliary Ptch1 is diminished and ciliary Smo enriched (Denef et al., 2000). Nonetheless, work with Smo agonists, such as SAG and purmorphamine and constitutively active Smo mutants indicates that activated Smo enters the cilium in a ligand-independent manner, despite the presence of Ptch1 (Sinha and Chen, 2006; Mao et al., 2006; Rohatgi, Milenkovic, Ryan B Corcoran, et al., 2009).

Moreover, the Smo inhibitor cyclopamine, but not others, induces its ciliary accumulation (Wilson et al., 2009). Those results established that Smo is under a two-step process of regulation. Both the activation and the ciliary translocation of Smo can be decoupled mechanistically, but both are required for effective Hh signalling (Arensdorf et al., 2016). Use of the Smo antagonist cyclopamine demonstrated that ciliary localisation of Smo alone was not sufficient to drive downstream target gene transcription. Cyclopamine binds Smo, blocking its activation, but causing ciliary localisation independent of ligand. Addition of Shh to cyclopamine treated cells failed to stimulate Gli1 transcription, despite significant ciliary localised Smo and presumed inactivation of Ptch1 (Chen et al., 2002).

Interestingly, a mutant of Ptch1 lacking both PPXY motifs for HECT E3 ubiquitin ligase binding, Ptch1^{PY}, was observed to be retained within the cilium, even after Shh stimulation (Kim et al., 2015). Despite physical ciliary retention, the binding of Shh alone was sufficient to relieve Ptch1 inhibition of Smo, resulting in their co-localisation within the cilium and downstream transcription of Gli1.

In physiological conditions, direct binding of a Hh ligand to Ptch1 directs downstream protein ubiquitination, internalisation and lysosomal degradation of

the complex (Deneff et al., 2000). This relieves the inhibitory action of Ptch1 on Smo, which then enters the cilium through direct transport and diffusion, accumulating at the tip, within Kif7 mediated Gli/SUFU enriched compartments (**Figure 1.3**). Simultaneously, Hh stimulation drives a redistribution of Gli2-3/SUFU and KIF7 to the ciliary tip (Chen et al., 2009; Milenkovic et al., 2015). Ligand stimulation also reduces PKA activity through Smo-coupling to heterotrimeric Gi proteins and ciliary removal of the heterotrimeric Gs protein-coupled Gpr161 (Riobo et al., 2006). This in turn reduces PKA phosphorylation of full length Gli2/3 and the production of Gli2/3R.

Co-localisation of Smo and SUFU at the ciliary tip signals the dissociation of SUFU from Gli2/3FL. Released Gli2/3FL migrates to the nucleus and upregulates the transcription of Hh target genes, including, but not limited to *Gli1*, *Ptch1*, *Ptch2* and *HHIP* (**Figure 1.3**) (Tukachinsky et al., 2010). The upregulation of *Ptch1* and *HHIP* provides a negative feedback mechanism by sequestration of Hh ligands, whereby intracellular responses to stimulation can be limited or fine-tuned (Chuang and McMahon, 1999; Jeong and McMahon, 2005). In embryonic development, gradients of Shh ligand drive essential tissue patterning, and cell autonomous upregulation of Ptch1 helps to shape these gradients (Holtz et al., 2013). In tandem to the upregulation of negative feedback Hh target genes, several Hh promoting genes are down regulated. The Hh ligand co-receptors, GAS1, BOC and CDO all display a reduction in expression in cells receiving high levels of morphogen (Allen et al., 2007).

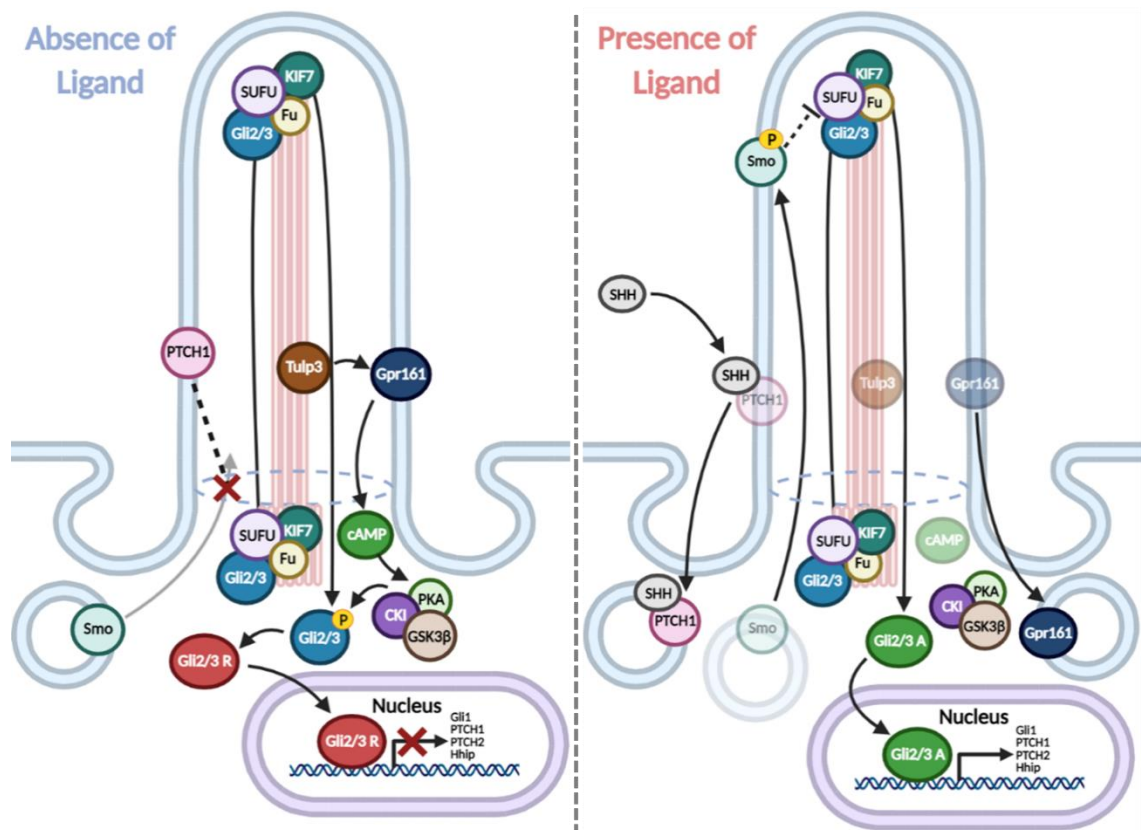


Figure 1.3 Simplified schematic of Shh stimulation of the canonical Hedgehog signalling pathway.

In the absence of ligand: PTCH1 is localised within the cilium and inhibits ciliary localisation and activation of Smo. Gli activation is inhibited by SUFU and is retained at the base and tip of the cilia, in coordination with KIF7. Gpr161 is ciliary localised via Tulp3 and activates cAMP, which in turn activates PKA along with GSK3 β and CKI to phosphorylate Gli2 and Gli3 for partial proteasomal degradation into repressor forms, which inhibit the transcription of Hh target genes. **In the presence of ligand:** Shh binds PTCH1 and the pair are internalised to late endosomes and degraded. Smo is localised to the cilium, activated, and travels to the tip, where it releases Gli from the repression by SUFU. Gli2 and Gli3. Gpr161 is expelled from the nucleus, reducing the levels of cAMP and thereby reducing the activity of PKA, GSK3 β and CKI. Full-length activator forms of Gli2 and Gli3 accumulate and promote the transcription of Hh target genes.

1.2 Molecular Components of Hh Signalling

1.2.1 Sonic Hedgehog Ligand

Of the three vertebrate Hh genes, Shh is most highly studied, owing to its essential requirement to embryogenesis and adult homeostasis. As a morphogen, Shh has been shown to be released from cells and to diffuse across both short and long distances (Gritli-Linde et al., 2001). There is evidence of contact-dependent Shh signalling *in vivo* and *in vitro*, as well as longer range tissue patterning roles in limb bud development (Tickle and Towers 2017). Production of an active, secreted Shh ligand requires extensive processing and lipid modifications. Lipid modification of Hh is essential for its activity, regulating release, distribution, and receptor binding (Grover et al., 2011). Within the ER, immature Shh precursor undergoes autocatalytic cleavage through a thioester intermediate during which cholesterol is attached to the newly C-terminal glycine, directed by its C-terminal domain. This yields an N-terminal cholesterolated fragment, whilst the C-terminal fragment is degraded. The N-terminal fragment subsequently undergoes acylation with palmitate to the N-terminal cysteine via amide-linkage (**Figure 1.4**) (Porter et al., 1995).

Skinny hedgehog (Ski) in *Drosophila*, or Hedgehog acyltransferase (HHAT) in vertebrates catalyses the palmitoylation of the N-terminus of Shh. HHAT has been shown to be essential for the amino-terminal palmitate modification of C24 in N-Shh (Buglino and Resh, 2008). In agreement, a knockout of Ski, or inhibition by siRNA produces a near Shh null phenotype, indicating that palmitoylation is essential for Hh activation (Chen et al., 2004). In fact, while preventing the palmitoylation of N-Shh does not completely abrogate N-Shh activity *in vitro*,

unpalmitoylated N-Shh is approximately 30 x less potent. This reduction in activity was found not to be consequence of reduced binding affinity for PTCH1 (Pepinsky et al., 1998). *In vivo* studies also discovered that the loss of palmitoylation disrupted cellular N-Shh distribution.

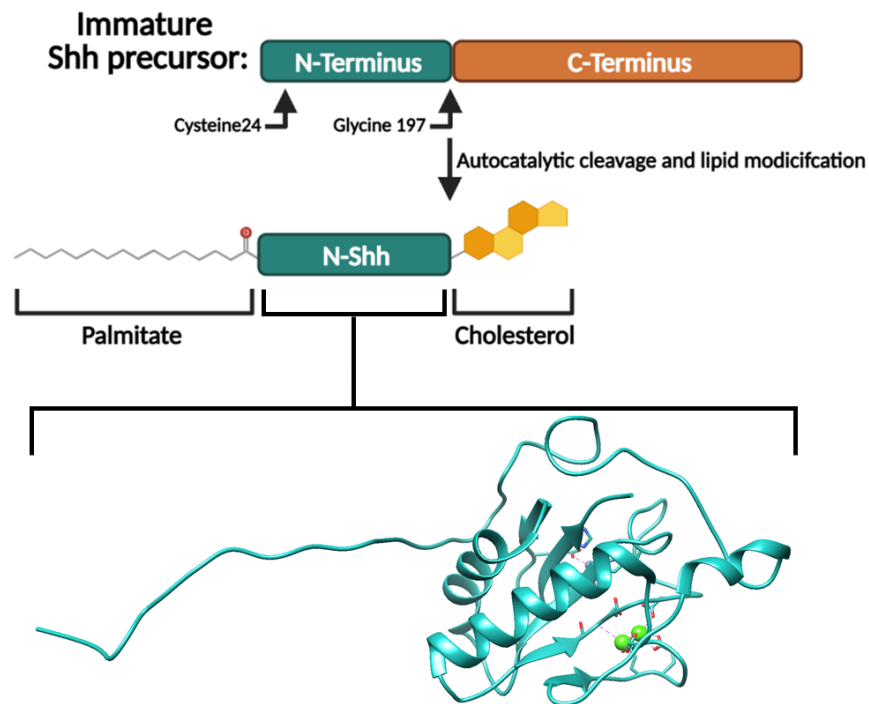


Figure 1.4 Simplified depiction of the maturation of Shh ligand

Immature Shh precursor undergoes autocatalytic cleavage and lipid modification in the ER to produce a mature N-terminal fragment N-Shh ligand modified with an N-terminal palmitate and a C-terminal cholesterol. The mature N-Shh ligand has an extended stretch of N-terminal residues as seen in the structure, adapted from PDB ID: 6E1H.

Subsequent crystal structures of N-Shh revealed that the first 15 N-terminal residues display an extended conformation (**Figure 1.4**) (Goetz et al., 2006). The importance of this extended region and its palmitoylation was recently validated after structural determination of dimeric PTCH1 bound to a single N-Shh (Qi, Schmiede, Coutavas and Li, 2018). Within the 2:1 PTCH1:N-Shh complex, N-

Shh engages both PTCH1 monomers asymmetrically: one via the previously identified pseudo active-site and the other through the palmitoyl moiety. Both unpalmitoylated N-Shh and a palmitoylated pseudo-active site mutant N-Shh have been shown to bind a PTCH1 monomer individually. This strongly indicates that these two interaction interfaces are distinct, and lack any mutual dependency for binding. It also nicely explains why unpalmitoylated N-Shh is less potent, despite still binding PTCH1.

The dual-lipidation of N-Shh during processing make it a very hydrophobic molecule, with a strong membrane association. This mechanism enhances the degree of control over the release of ligand, which is mediated cooperatively by Dispatched (DISP1) and SCUBE2 (Tukachinsky et al., 2012). Similar to Patched, DISP1 is a 12-transmembrane protein, with two extracellular loops, an SSD, and is a member of the RND family. Loss of DISP1 was shown to result in the accumulation of Cholesterol modified N-Shh in producing cells (Etheridge et al., 2010). Importantly, a loss of DISP1 does not impact the autocatalytic processing of Shh or the acceptance of N-Shh in responsive cells. DISP1 and SCUBE2 engage N-Shh in a cholesterol-dependent manner, but at different regions of the cholesterol molecule, resulting in a 'hand off' interaction (Tukachinsky et al., 2012). This hand off appears to be integral to correct N-Shh activity post secretion. Artificial induction of N-Shh release, through the use of heparin has been reported to produce an inactive form of secreted N-Shh (Tukachinsky et al., 2012). However, specific forms of purified heparan sulfate are believed to cause pancreatic cancer cells to release active N-Shh (Ortmann et al., 2015).

An apparent conundrum of the Hh signalling pathway relates to the ability of mature N-Shh to signal across large distances despite its hydrophobicity. There is evidence that through an association with lipid rafts, N-Shh can form a multimeric complex, whereby the hydrophobic lipid modifications are concealed from the extracellular matrix to facilitate increased diffusion. Moreover, both lipid modifications have since been shown to be essential for the multimerization of N-Shh (Zeng et al., 2001a; Chen et al., 2004).

1.2.2 Smoothened Structure

Smoothened is a 7-transmembrane (7TM) domain protein, classified as part of the Frizzled 'F' GPCR superfamily. Uniquely, Smo is not regulated by an extracellular-ligand directly, but instead through changes in cholesterol and oxysterol availability regulated by PTCH1 (Corcoran and Scott, 2006; Blassberg et al., 2016; Raleigh et al., 2018). Smo contains four key domains: a cysteine-rich N-terminal domain (CRD), a linker domain (LD), a 7TM α -helical bundle, and a long C-terminal domain (**Figure 1.5**) (Nachtergaele et al., 2013; Byrne et al., 2016). Smo contains at least two distinct sterol ligand binding sites, one within the cavity of the 7TM and one within a shallow groove on the CRD (Deshpande, Liang, Hedeem, Kelsey J. Roberts, et al., 2019). An array of synthetic and exogenously expressed compounds selectively engage these sites and have revealed an allosteric interaction between the 7TM and CRD. In particular, activation of Smo appears to confer a conformational change. Conversely, some Smo antagonists appear to lock Smo in an inactive conformation (Huang et al., 2018).

The allosteric interaction between the 7TM and the CRD affords a higher level of complexity to Smo activation than previously believed. Based on the presence of

the SSD in Patched 1, initial studies of Smo focused on the identification of a sterol derivative, small molecule Smo activator. The sterol based model is supported by evidence that depletion of cholesterol impaired the transcription of Gli1 in response to Hh ligand (Cooper et al., 2003; Blassberg et al., 2016). Furthermore, cholesterol has been reported to be sufficient to stimulate canonical Hh signalling independently of Hh ligand (Luchetti et al., 2016).

One limitation of this model is the natural abundance of cholesterol in the Plasma membrane. PTCH1 has been shown to reduce cholesterol levels on the inner leaflet of the lipid bilayer, but the exact mechanism remains unknown. Suggested methods include active transport, flipping and sequestration of cholesterol, however these processes are energetically unfavourable (Zhang et al., 2018). The fact that PTCH1 is capable of achieving ~80% inhibition of Smo at a 1:45 molar ratio also conflicts with the above models. Cholesterol has rapid equilibration rates within the PM and it would require high activity of many PTCH1 molecules to maintain its depletion alone. It has been more recently proposed that Ptch1 regulates accessible cholesterol rather than its concentration (Kinnebrew et al., 2019).

The CRD was originally highlighted as the probable target for the binding of the endogenous small molecule effector, inhibited by PTCH1. It was discovered that oxysterols and cholesterol are capable of binding the CRD, promoting Smo activation, ciliary accumulation and Gli1 transcription, albeit to differing extents (**Figure 1.5**) (Rana et al., 2013; Huang et al., 2016; Radhakrishnan et al., 2020). Interestingly, despite abrogating oxysterol binding, deletion of the CRD does not prevent activation by Shh ligand. In fact, Smo- Δ CRD displays mildly increased

basal activity than wild type Smo, but lower sensitivity to the presence of Shh, suggesting that another site on Smo plays a critical role in its activation (Taipale et al., 2002a; Aanstad et al., 2009). This is further supported by the fact that SAG, which binds in the 7TM cavity can activate Smo- Δ CRD (Nachtergaele et al., 2013).

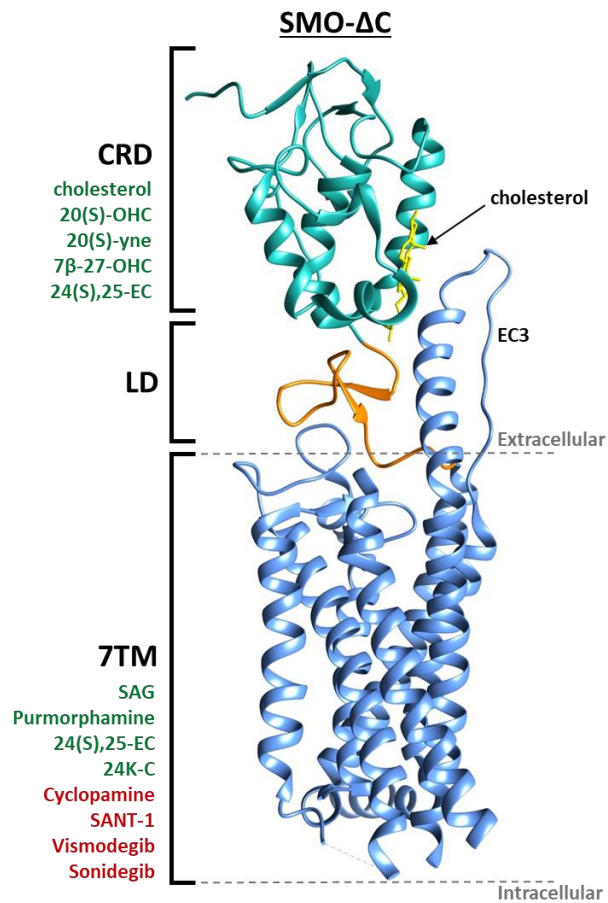


Figure 1.5 The crystal structure of SMO- Δ C with cholesterol bound to the CRD.

The structure of Smo- Δ C adapted from (PDB ID:5L7D), depicting the 7-transmembrane bundle (7TM) in blue, the linker domain (LD) in orange, the cysteine-rich domain (CRD) in green, and a CRD bound cholesterol density in yellow. Molecules known to bind to the CRD or 7TM of Smo are listed to the left. Antagonists in red and agonists in green.

Until recently, it was commonly accepted that, uncharacteristically for GPCRs, the 7TM domain of Smo showed little conformational change upon activation. Only synthetic compounds were known to bind the heptahelical bundle and no endogenous small molecule had been identified (**Figure 1.5**). Mutations within the 7TM cavity also displayed little effect on canonical Hh signalling, with exception of the oncogenic SmoM2 mutation. However, high-performance liquid chromatography mass spectrometry (HPLC-MS/MS) of isolated sea urchin cilia identified several ciliary-associated oxysterols. Analysis revealed that two oxysterols, 7 β -27-dihydroxycholesterol and 24(s),25-epoxycholesterol competed with 20(s)-OHC for CRD binding. Further deletion of the CRD showed that 24(s),25-epoxycholesterol and 24K-cholesterol retained binding ability lost by 20(s)-OHC and 7 β -27-dihydroxycholesterol, presumably within the 7TM bundle (Raleigh et al., 2018).

Recent structural studies of mouse Smo and *Xenopus* SmoCRD in complex with SAG21k and cholesterol respectively, has revealed several interactions that provide explanations for these functional observations (Huang et al., 2016; Deshpande, Liang, Hedeem, Kelsey J Roberts, et al., 2019). A key conformational change of the 7TM, previously missed due to the use of stabilising compounds, mutations and truncations, occurs through the outward movement of TM helix 6. This shift elongates the α -helices and opens a hydrophobic tunnel, in which a sterol density was observed. The extension of TM6 and part of the 3rd extracellular loop allows contact with the CRD, suggesting that specific ligand binding of either 7TM or CRD might propagate signal transmission to the other, by means of allosteric conformational reorientation and increased/decreased ligand accessibility (Deshpande, Liang, Hedeem, Kelsey J Roberts, et al., 2019).

There are copious examples of such allosteric interactions, particularly with GPCRs and this dynamic relationship might explain why several oxysterol species have been proposed as cargos of PTCH1, enriched within the primary cilium (Raleigh et al., 2018). Combinations of these oxysterols might facilitate tight regulation of Smo for optimal signalling.

1.2.3 Roles of co-receptors in ligand binding

Besides its interaction with Ptch1, N-Shh has several other membrane localised receptors. The involvement of three co-receptor, cell surface proteins, Gas1, Cdo and Boc have been identified in vertebrate Hh signalling (Allen et al., 2007; Allen et al., 2011). These proteins are now known to be semi-redundant and essential in many Hh responsive tissues. Gas1 is a vertebrate-specific protein, whilst Cdo and Boc appear to be structurally related to *Drosophila* equivalents, Ihog and Boi (Tenzen et al., 2006a; Martinelli and Fan, 2007). Inhibition of Hh signalling in mutants results in increased Cdo and Boc protein expression, establishing them as downregulated transcriptional targets (Tenzen et al., 2006).

All three co-receptors have been demonstrated to directly bind N-Shh in a competitive manner to Ptch1. Cdo and Boc are single transmembrane proteins with an extracellular domain consisting of a group of immunoglobulin and fibronectin-like repeats. The first of these FNIII domains is sufficient to interact with Shh in Co-IP assays, whilst the second is required for enhanced binding in Ptch1 co-expressing cells (Tenzen et al., 2006; McLellan et al., 2008). The interaction with N-Shh is calcium-dependent and all three forms of Hh ligand have been shown to bind the co-receptors in this manner. More recent structural studies indicate that this calcium-dependent binding is also present in both Shh-

PTCH1 and Shh-Hhip interactions (Bosanac et al., 2009; Gong et al., 2018a; Qi et al., 2019).

Intriguingly, a mutant Shh able to bind Ptch1 but unable to bind the three co-receptors, could not activate Hh signalling (Izzi et al., 2011). This mutation 'E90A' effects one of the glutamic acid residues that coordinate the calcium binding site. The retained ability of N-Shh-(E90A) to bind Ptch1 was later explained through the existence of another interaction interface which involved the palmitoylated moiety (Qi, Schmiede, Coutavas and Li, 2018).

Distinct to their interaction with Shh, Boc and Gas1 physically interact with Ptch1 by way of co-immunoprecipitation (Izzi et al., 2011). Importantly, these co-receptor interactions appear to be inversely correlated, suggesting the existence of distinct populations of Ptch1 and different co-receptors, with potentially differing functions. Despite their commonality, the Hh co-receptors do appear to have some distinct functions. While Gas1 is negatively regulated by Hh, it has been evidenced to act as an enhancer of long distance and low level Shh signalling (Martinelli and Fan, 2007).

1.3 The Patched family of Proteins

1.3.1 Common Structural Architecture of Patched Proteins

In the context of this thesis, the 'patched family of proteins' relates to PTCH1, its close homolog, PTCH2, and the more distally related, patched domain-containing protein, PTCHD1 (**Figure 1.6**). All three proteins display striking structural similarities and experimental evidence suggests they might share a common receptor function to the ligand Shh. Patched 1 and 2 are integral membrane proteins with 12-transmembrane domains. Similarly, PTCHD1 is predicted to be an integral membrane protein with 12 transmembrane domains and an overall topology alike to that of Patched 1 and 2 (Carpenter et al., 1998; Noor et al., 2010).

There are three other Patched domain-containing proteins expressed in humans (PTCHD2, 3 and 4), all characterised by the presence of an SSD. PTCHD2 and 3 appear to be distally related to PTCHD1, displaying almost negligible sequence conservation, bar for the SSD. PTCHD4 (also called PTCH53) on the other hand, shows greater similarity and sequence alignment to PTCHD1, with an identity of ~45.3% (**Figure 1.6**). PTCHD4 has been described as a Hh pathway regulator previously, so it bodes well that due to their similarity, PTCHD1 might also have a role in Hh signalling (Chung et al., 2014).

In terms of the functional domains, again there are strong similarities. All three proteins contain two large extracellular loops, the first between TM1-2 and the second between TM7-8. These extracellular loops effectively sandwich an SSD and the core of the first 6 transmembrane domains. Finally, there are two

intrinsically disordered cytoplasmic domains; a middle cytoplasmic loop, located between TM6-7; and a cytoplasmic C-terminal tail. The cytoplasmic domains harbour the greatest divergence between the three proteins. The middle loop of PTCHD1 is roughly half the length of Patched 1 and 2; while the CTD of both Patched 2 and PTCHD1 are significantly shorter than Patched 1.

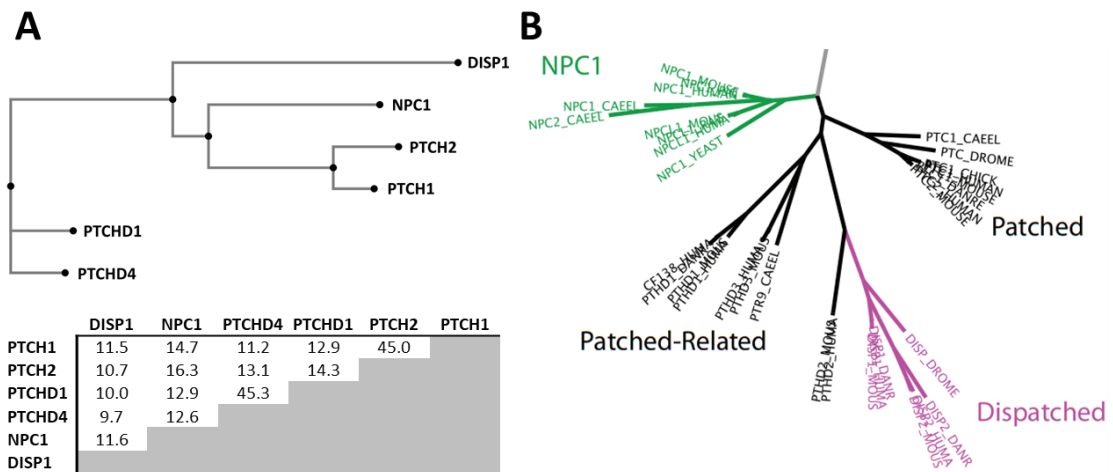


Figure 1.6 Computational inferred relatedness of Patched proteins and other Hh pathway SSD containing proteins.

The relatedness of PTCH1, PTCH2 and PTCHD1 was compared to each other and a selection of other SSD containing proteins either with known roles in Hh signalling (DISP1, PTCHD4) or known similar functional mechanics (NPC1). **(A)** Sequence alignment of human proteins, top image: a maximum-likelihood phylogenetic inference tree, generated using RAxML (Kozlov et al., 2019). Bottom table: Percentage identity of individual protein alignments, performed with UniProt protein alignment tool. **(B)** A maximum-likelihood phylogenetic tree of 59 SSD regions, adapted from (Strope, 2015), showing the branches of NPC1, Patched, Dispatched and Patched-related groups.

The CTD of PTCH2 appears to be a shorter form of the PTCH1 CTD, with low sequence identity resulting from the absence of large conserved regions. Whereas in PTCHD1, not only is the CTD shorter in comparison to PTCH1, but lacks any significant sequence homology. Two features, a lysine-rich region and

a PDZ-binding motif are exclusively present in the CTD of PTCHD1 (Ung et al., 2018). Conversely, the HECT E3 ubiquitin protein ligase PPXY motif in the CTD of PTCH1 is absent in PTCH2 and PTCHD1 (Yue et al., 2014). This suggests potentially divergent activities by the three proteins, through their cytoplasmic tails. Despite this, the impact of the CTD upon canonical Hh signalling for PTCH1 and PTCH2 is believed to be negligible but is largely experimentally unknown (Lu et al., 2006).

1.3.2 Oligomerisation of Patched

Another intriguing aspect of Patched is its capability and propensity to form oligomers. Co-IP experiments have shown that full length *Drosophila* Ptc and its isolated CTD can self-interact (Lu et al., 2006). Observations of the sequence similarity of Ptch1 and the bacterial Resistance Nodulation Domain (RND) protein family provided a potential explanation for oligomerisation, as well as a mechanism by which Ptch1 could regulate Smo (Taipale et al., 2002). RND proteins function as homo- and heterotrimeric complexes, actively facilitating the extrusion, or transport of small molecules and heavy metals from the cell (Murakami et al., 2002; Pos, 2009). RND permeases utilise proton motive force (PMF) to transport these small molecules against their concentration gradients (Kim et al., 2011). Interestingly, several residues fundamental for proton translocation and stability of RND trimers are present in the Ptch1 amino acid sequence. A highly conserved RND GxxxD motif discovered within TM4 of Ptch1, was found to be mutated in some cases of Gorlin syndrome (Taipale et al., 2002). Experimental mutation of this aspartic acid to alanine, asparagine or lysine in the RND permease MexB completely abrogates antibiotic resistance. A lack of MexB-dependent antiporter activity was identified by quantitative analysis of dye

accumulation in cells carrying mutant MexB (Guan and Nakae, 2001). The GxxxD motif is also present in Ptch2 and DISP1, further aligning the Hh pathway with that of the RND family (Ma et al., 2002).

Interestingly, the structural determination of tetrameric PTCH1 in complex with two N-Shh molecules indicates that the dimer might be the optimal oligomeric state of PTCH1 (Qian et al., 2019). The tetramer is a loose form of two PTCH1 dimers, each bound asymmetrically to one molecule of N-Shh. This complex effectively utilises all the known binding interfaces of N-Shh and there is almost certainly no physical room to accommodate any additional PTCH1 molecules. While Ptch1 is therefore unlikely to mimic the trimeric complex of RND proteins, at least in the N-Shh-bound state, its GxxxD remains functionally important, sitting within the SSD as a potential link to a PMF-mediated small molecule transport.

In NIH3T3 cells, internalisation of Ptch1 upon binding of N-Shh, increased intracellular cholesterol concentrations and reduced cholesterol efflux (Bidet et al., 2011). Furthermore, through the use of a fluorescent sensor of intracellular cholesterol, Zhang et al., (2018) found that expression of Ptch1 reduced the concentration of cholesterol in the inner membrane leaflet of the plasma membrane. A fundamental limitation of these experiments is that they were conducted in HEK293 cells and not a Hh responsive, cilium producing cell line. However, the findings that Ptch1 SSD mutants, unable to inhibit Smo in canonical Hh signalling, could not alter inner membrane cholesterol concentration strongly supports the function of the SSD in the inhibition of Smo and cholesterol mobilisation. Within an isolated micro domain such as the cilium, such a function of Ptch1 is a feasible mechanism of Smo inhibition.

1.3.3 PTCH1 and its interaction with Shh

In its role as a morphogen, extracellular Shh ligand mediates pathway activation in cells that recognise its presence at the plasma membrane and internalise the ligand. Ptch1 is the endogenous Shh receptor and it has been long established that the extracellular loops, ECD1 and ECD2 of Ptch1, are essential for ligand interaction. This has been demonstrated by the diminished binding affinity of N-Shh and mutant PTCH- Δ loop1/2 (Zheng et al., 2010; Tukachinsky et al., 2016). Thanks to a recent flurry of publications, five different PTCH1 structures, produced by three independent groups, have now confirmed that monomeric PTCH1 displays a two-fold pseudosymmetry reminiscent of the RND family architecture. As expected, the protein lies perpendicular to the plasma membrane. The presence of two distinct binding interfaces between N-Shh and PTCH1 have been well resolved and each evidenced separately for monomeric PTCH1 and together for dimeric and tetrameric PTCH1. Finally, multiple sterol densities have been reported to occupy sites in the SSD as well as in surface pockets on PTCH1, at the inner and outer lipid bilayer, suggesting the existence of a tunnel that transports sterols (Qi, Schmiede, Coutavas, Wang, et al., 2018; Gong et al., 2018a; Qi, Schmiede, Coutavas and Li, 2018a; Qi et al., 2019; Qian et al., 2019).

N-Shh is known to contain a palmitoylated N-terminal extension, a Z^{2+} metalloprotease pseudo-active site binding groove, an adjacent Ca^{2+} binding site, and a C-terminal cholesterol (**Figure 1.7**) (Buglino and Resh, 2008; McLellan et al., 2008; Bosanac et al., 2009). The C-terminal cholesterol modification of N-Shh is important for multimerisation and long distance signalling (Zeng et al., 2001; Gallet et al., 2006). However, investigations using monomeric N-Shh show that it

retains some activity, despite the absence of this cholesterol modification. The structures of PTCH1 bound to N-Shh strongly suggest that the cholesterol modification is not involved in the interaction. The extreme C-terminal region (~20 residues) and cholesterol are unresolved in these structures, but appear to be emerging from the opposite side of the globular region to the Z^{2+} and Ca^{2+} sites **(Figure 1.7)**.

The Z^{2+} metalloprotease pseudo active site binding groove has been described as the primary binding site to Hhip, although other findings indicate a reliance upon calcium for maximal binding (Bosanac et al., 2009). As previously discussed, the Hh co-receptors engage Shh through their third Fibronectin repeat in a calcium-dependent manner. Although the ECD2 of Ptch1 appears to compete with the ECD2 of Hhip for binding at or near the Z^{2+} site, it also displays a calcium-dependent interaction with N-Shh. Chelation of the adjacent Ca^{2+} and mutations to residues that constitute the Ca^{2+} binding site reduce the binding to Ptch1 as well Hhip and the co-receptors (McLellan et al., 2008; Bosanac et al., 2009). Due to the proximity of the Z^{2+} and adjacent Ca^{2+} sites, it is likely competition between N-Shh binding partners is a result of steric hindrance and not necessarily an indication of direct binding competition.

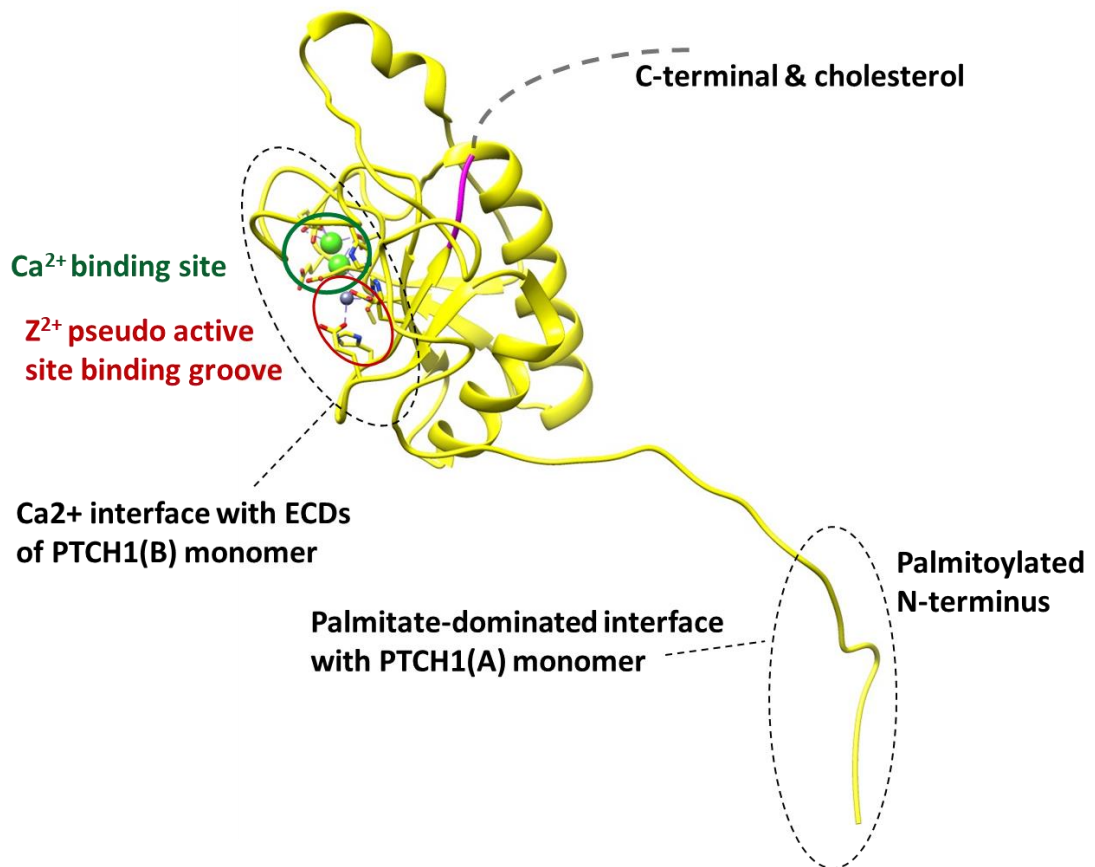


Figure 1.7 The two distinct PTCH1 binding interfaces of N-Shh.

The structure of N-Shh shown in yellow was taken from the 2:1 PTCH1:N-Shh complex (PDB ID: 6E1H) and adapted in Chimera (Pettersen et al., 2004). The Ca²⁺ binding site and Z²⁺ pseudo-active site binding groove are indicated by the green and red ovals, respectively. The Ca²⁺ ions and Z²⁺ ion are shown as green and grey spheres, respectively. The last C-terminally resolved region of N-Shh is highlighted in magenta, with the hypothetical unresolved region, depicted by the dashed grey line, extending away. The two distinct binding interfaces, the Ca²⁺ binding site and the palmitate-dominated binding site of N-Shh are indicated by the dashed lined ovals.

In terms of its interaction with N-Shh, the structural determination of monomeric PTCH1 (1-1305) with unpalmitoylated N-Shh demonstrated a binding-dependent movement of the ECDs of PTCH1 (Gong et al., 2018). In particular, the upper helical regions of the ECDs contributed to a binding interface with the Lys/Arg-rich pseudo-active site groove of N-Shh, whilst the transmembrane core

remained largely unaffected. The binding interface is mediated by polar and charged residues that when mutated diminished complex formation. Of particular note is an extended loop (residues 206-213) which was found to cover a pocket on the interface of the ECDs upon Shh binding. A density similar to the cholesterol hemisuccinate (CHS), which was included in the purification buffer, was seen within this E loop extracellular steroid-binding site. Another similar density was found in a surface cavity on the membrane facing side of the SSD, the same cavity seen within NPC1 (Li et al., 2016). Fundamentally, a synergistic effect was indicated by the presence of these steroid binding sites and the interaction with N-Shh at the Ca²⁺ binding site. Mutations to L282Q, T500F/P504L separately and in combination resulted in reduced Shh affinity respectively. This might suggest that sterol binding influences the flexibility of the E loop, facilitating the Ca²⁺-dependent binding.

The two ECDs have differing spatial arrangements despite their similar core helical regions and number of glycosylation sites (4 ECD1 vs 2 ECD2). In fact, the total estimated residue contribution of each ECD to the Ca²⁺ site in this structure, as well as the palmitoylated site not shown, is ~80% ECD1 vs ~20% ECD2 (Qian et al., 2019). This fits with previous findings that Ptch1 Δ loop1 and Ptch1 Δ loop2 mutants produced significantly divergent impairment. Whilst Ptch1 Δ loop1 is inactive and not localised to the cilia, Ptch1 Δ loop2 displays ciliary localisation and constitutive inhibition of Smo (Tukachinsky et al., 2016).

Two other structures of monomeric forms of PTCH1 bound to different forms of N-Shh have been determined by independent groups. The first is consistent with Gong, and describes PTCH1 engagement of the same Ca²⁺ binding site on a

palmitate mimicking N-Shh_{C24II} molecule (**Figure 1.8A**) (Qi et al., 2019). Additional sterol densities were observed in 10 locations around PTCH1. However, the relevance of several of these sites to the function of PTCH1 inhibition of Smo is debateable. Mutations of residues in three of these sites to bulky tryptophan residues did not result in reduced activity of full length PTCH1 in Gli-luciferase assays. In contrast, the second structural determination of monomeric PTCH1, with native palmitoylated N-Shh, provided evidence of a palmitoyl binding interface with monomeric PTCH1, with no involvement of the Ca²⁺ binding site (**Figure 1.8C**) (Qi, Schmiede, Coutavas, Wang, et al., 2018). This discrepancy with Qi et al., (2019) might be explained by two key differences in their purification processes. Whilst Qi et al., (2019) purified PTCH1 with DDM and CHS, Qi, Schmiede, Coutavas, Wang, et al., (2018) omitted CHS. As shown by Gong et al., (2018), the two cavities in which CHS like densities were bound, appeared synergistic to the binding of the Ca²⁺ site. Therefore, the use of CHS might have resulted in the occupation of these sites, creating a conformational bias of ECDs of PTCH1 for Ca²⁺-dependent binding over palmitate binding. Meanwhile, Qi, Schmiede, Coutavas, Wang, et al., (2018) used a buffer devoid of calcium, potentially inducing a bias for palmitate binding.

The oligomerisation of PTCH1 is well documented as a conserved characteristic of the bacterial RND proteins and *Drosophila* Ptc and its CTD are known to form trimers (Lu et al., 2006). As such it is likely that higher oligomeric complexes of PTCH1, dominate the endogenous population. In fact, Gong et al., (2018) reported that the monomeric PTCH1 peak selected for structural determination was secondary to a larger very heterogeneous peak of suspected oligomeric PTCH1. In fact, both the Ca²⁺ and the palmitate sites were validated by the

structural determination of a 2:1 PTCH1:N-Shh complex, which, importantly, used palmitoylated ligand and buffer at physiological calcium concentration (Qi, Schmiede, Coutavas and Li, 2018) (**Figure 1.8B**). An asymmetrical engagement between palmitoylated N-Shh and the PTCH1 dimer was observed. The two reported binding interfaces matched those seen separately with monomeric PTCH1. In the palmitate-dominated interface, N-Shh-P26 facilitates the insertion of the palmitate into the hydrophobic cavity of PTCH1(A) (**Figure 1.8A**). In the PTCH1(B) monomer, a gated tunnel of ~150 Å was calculated to project through the SSD to the neck region. The importance of the palmitate insertion in disrupting this tunnel was shown by the generation of a non-functional PTCH1 with a salt bridge that obscured this tunnel.

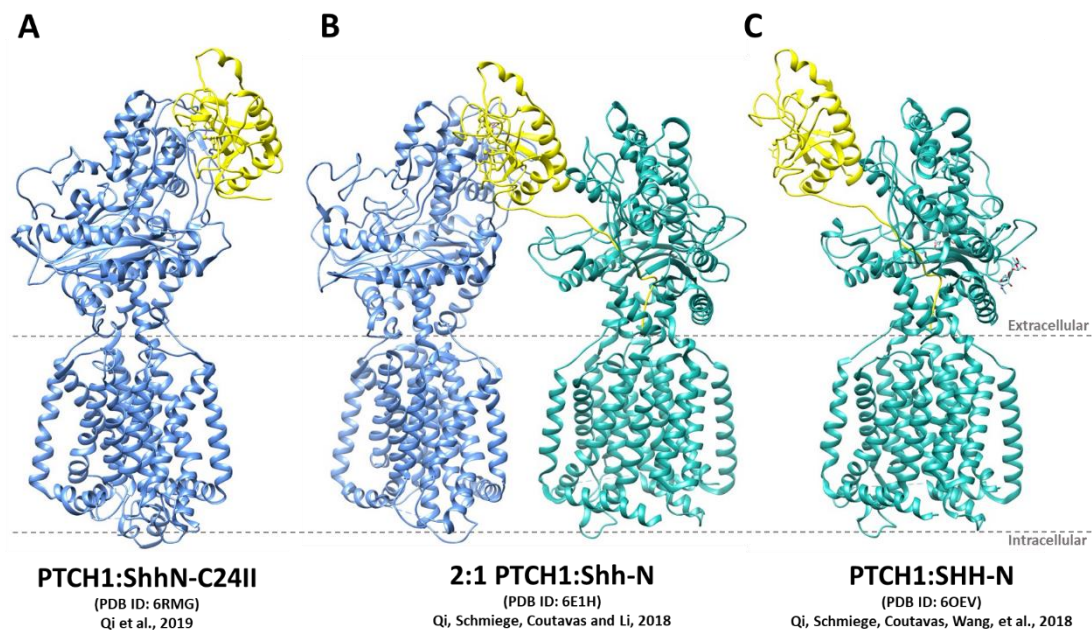


Figure 1.8 Monomeric and dimeric PTCH1 bound to different forms of Shh.

The structures of three human PTCH1:Shh complexes are displayed and were adapted from published PDB deposited structures. All forms of Shh are depicted in yellow, the PTCH1 which is bound through the ECDs is shown in blue, while the PTCH1 bound through its sterol cavity is shown in turquoise.

As previously discussed, the 2:1 PTCH1:N-Shh complex effectively resolves the apparent discrepancy of how unpalmitoylated N-Shh and mutants of the Ca^{2+} binding site can still bind PTCH1 with similar affinities, but have reduced inhibitory activity (**Figure 1.9**). It is apparent, that in the absence of palmitoylation, although N-Shh can bind PTCH1 via the Ca^{2+} binding site, it is likely to only engage a single monomer of the dimer, leaving the other monomer active. Steric hindrance of the bound N-Shh will prevent a second N-Shh, either palmitoylated or not, to bind as there is no room to accommodate another molecule.

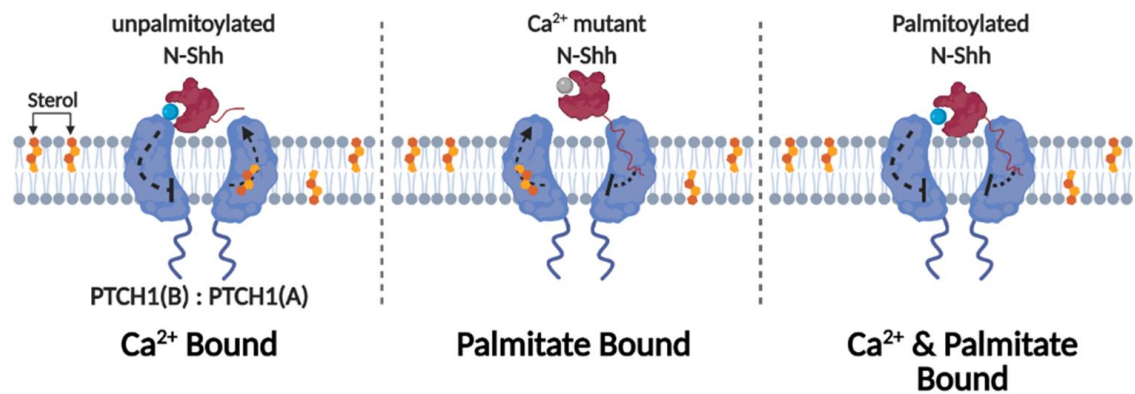


Figure 1.9 Functional relevance of the 2:1 PTCH1:N-Shh complex.

Cartoon schematic of the possible 2:1 PTCH1:N-Shh dimer interactions, dependent upon the activity state of the N-Shh molecule. Left: Unpalmitoylated N-Shh only binds to the PTCH1(B) monomer via the Ca^{2+} site, leaving PTCH1(A) active. Middle: A palmitoylated Ca^{2+} functional mutant of N-Shh only binds to the PTCH1(A) monomer, leaving PTCH1(B) active. Right: Palmitoylated N-Shh engages both PTCH1(A) and (B), rendering the dimer inactive.

An interesting question is whether N-Shh displays a favourable interaction interface with PTCH1, by means of differential affinity? This preference in regards to monomeric and dimeric forms of PTCH1 would surely be functionally relevant, when one considers the involvement and binding of the Hhip, PTCH2 and co-receptors, GAS1, BOC and CDO. The co-receptors of Shh bind exclusively

through the Ca^{2+} site and they have been described in complex with PTCH1 previously (Izzi et al., 2011). If monomeric PTCH1 is a functionally relevant molecule, it would be logical that Shh could engage a co-receptor via the Ca^{2+} site, whilst simultaneously binding PTCH1 through the palmitoylated extension. Dimeric forms of PTCH1 would also be seemingly unsuitable for these 'tripartite' interactions. There is some evidence that interaction with the palmitate binding site precedes interaction with the Ca^{2+} binding interface (**Figure 1.10**). The binding of palmitate has a greater surface contact and measurement of the solvation free energy gain upon interface formation Δ^iG predicts higher stability (Qi, Schmiede, Coutavas and Li, 2018). Moreover, mutations of the N-Shh globular domain display greater activity than unpalmitoylated N-Shh.

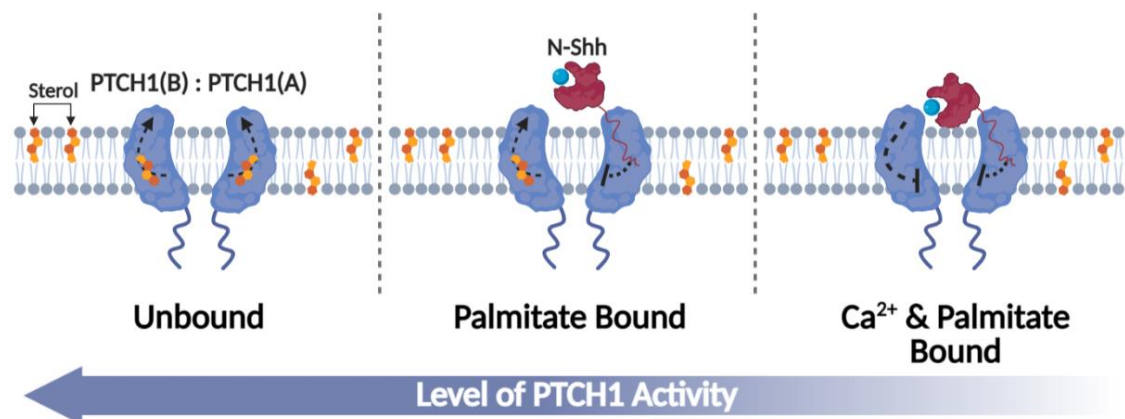


Figure 1.10 Schematic of N-Shh binding of PTCH1 dimer.

Left: PTCH1 dimer is unbound by N-Shh and displays maximal activity in the transport of sterol. Middle: N-Shh engages and nullifies the activity of PTCH1(A) of the dimer, through the palmitate binding site. Meanwhile PTCH1(B) remains active. Right: N-Shh bound to PTCH1(A) subsequently engages the other PTCH1(B) monomer, inhibiting its activity via the Ca^{2+} binding site.

A limitation of all the published PTCH1 structures is that the majority of the CTD has been removed, in addition to either removal of the middle cytoplasmic loop

or deletion of its PPXY motif. Whilst this is a practical approach, which improves both expression and stability, it has two clear drawbacks. Firstly, although the reported activity-state of these mutant PTCH1 is similar to wild-type PTCH1, many of the studies either overlook the additive effect an increased stability might have on a less active PTCH1. Gli-luciferase reporter activity can appear comparably inhibited when a saturating concentration of PTCH1 is transfected. Transfection of lower quantities or the stimulation with N-Shh can help to achieve sub-maximal concentrations of these PTCH1 constructs to better determine differences in activity.

Secondly, any influence these cytoplasmic domains might be exerting upon the protein is lost through their exclusion. It is interesting that the core structures of two SSD containing proteins involved in cholesterol transport, PTCH1 and NPC1 appear so similar and yet are not functionally equivalent. Both the elucidated structures harbour cytoplasmic deletions, suggesting that their absence might result in a structural 'reversion' where subtle features of functional importance are lost (Li et al., 2016; Gong et al., 2018; Fleet and Hamel, 2019).

At the present time, there are no structures of PTCH2 or PTCHD1 determined. However, PTCH2 was found to have comparable affinity to PTCH1 for N-Shh and the two other Hh ligands, IHH and DHH, through biochemical analysis. Despite this, cell membrane binding assays with N-Shh revealed less binding by PTCH2-expressing cells compared to PTCH1-expressing cells (Carpenter et al., 1998). If true, this might suggest a lower membrane-localised association of PTCH2 and N-Shh. It is unclear whether PTCHD1 binds N-Shh directly and its function within the Hh pathway is debated. PTCHD1 has been reported as active and inactive

from Gli-luciferase assays by separate groups (Noor et al., 2010; Chung et al., 2014; Ung et al., 2018).

1.3.4 The Role, Relevance and Redundancy of PTCH2

Although there is only a single *Ptc* gene in *Drosophila*, vertebrates contain 2 closely related, but non-equivalent homologs. Sharing ~45% overall homology, PTCH1 and PTCH2 display strong similarity in the transmembrane domains, but significant disparity within the cytoplasmic domains (Motoyama, Takabatake, et al., 1998; Carpenter et al., 1998). PTCH1 is widely considered the main Hh ligands receptor, with PTCH2 being largely disposable, performing negligible functions (Nieuwenhuis et al., 2006). Despite this common view, PTCH2 is localised to chromosome 1p33-34, which is often lost in a variety of tumours. In-situ hybridisation showed high expression of PTCH2 transcripts in both familial and sporadic BCC patients with known PTCH1 mutations (Zaphiropoulos et al., 1999). Furthermore, PTCH1-driven medulloblastoma often shows a concomitant upregulation of PTCH2, indicative of a tumour suppressor function (Lee et al., 2006).

During embryonic development, PTCH1 is expressed more ubiquitously than PTCH2. Furthermore, in tissues with co-expression of both proteins, such as the skin, developing limb and the neural tube, detection of *Ptc1* commonly precedes that of *Ptc2*. Early embryonic studies showed *Ptc1* knockouts to be lethal, whilst mice carrying a potential hypomorphic allele, *Ptc2^{tm1/tm1}*, developed grossly normal (Nieuwenhuis et al., 2006). Therefore, it can be inferred that *Ptc2* is not sufficient to compensate a *Ptc1* knockout, despite displaying similar binding affinity for Shh ligand *in vitro*. In fact, both Patched 1 and 2 have been found to

bind not only Shh, but also Dhh and Ihh with similar affinities, but with potentially differing cellular accessibilities. Cell surface binding assays in HEK293 and Cos7 cells transiently transfected with either Patched 1 or 2, indicated a weaker Shh-IgG binding in PTCH2 cells (Carpenter et al., 1998).

The presence of Patched 1 is a major obstacle to studying Patched 2 function *in vivo*. As such, much of the existing literature concerning the role Ptch2, comes from *in vitro* studies in Ptch1 heterozygous or null cell lines. This approach is justifiable, due to the predominant role of PTCH1 masking potential overlapping functional influences by PTCH2, in wild type cell lines. Use of Ptch1^{-/-} MEFs has revealed that despite the absence of Ptch1, maximal pathway activation is not observed without stimulation. Stimulation with the Smo agonist, SAG, further enhances signalling activity, measured by Gli-luciferase assay. This strongly suggested that Ptch2 is capable of at least a minor redundant function, to that of Ptch1 *in vitro* (Alfaro et al., 2014).

Within many tissues, but particularly during epidermal differentiation of the skin, there is a potential for cooperative or overlapping roles of the Patched proteins. While Ptc2-deficient mice, generated by Cre-Lox recombination are largely unaffected, both the frequency and range of tumours increase when combined with Ptc1 haploinsufficiency (Lee et al., 2006). Similarly, neoplastic transformation of skin treated with a tamoxifen-inducible Keratin-14 CreER harbouring Ptch1^{lox/lox};Ptch2^{tm1/tm1} developed features of BCC significantly sooner than Ptch1^{lox/lox} counterparts (Adolphe et al., 2016).

Investigations of limb development revealed stimulation of primary limb fibroblasts with 0.1 µg/mL N-Shh produced an increase, in Ptc1 and Ptc2 mRNA

transcripts of 40-fold and 300-fold respectively. Generation of an ectoderm-specific KO of *Ptc1* in the apical ectodermal ridge (AER) of the limb, revealed elevated activation of *Ptc1* and *Ptc2* promoters, suggestive of a co-operative role (Zhulyn et al., 2015). Furthermore, quantification of ciliary-localised Smo in fibroblasts found ~48% increase in *Ptc1* null cells, which further increased by ~20% in *Ptc1/2* null cells, whereas *Ptc2* null cells were undiscernible from wild-type fibroblasts, owing to the retained activity of *Ptc1* (Zhulyn et al., 2015).

There are two explanations for the striking difference in requirement of the two patched isoforms: differential expression patterns, and differential function, directed by the intrinsically disordered cytoplasmic domains. Recent work by Fleet et al., (2016) strongly supports that the distal cytoplasmic domains and flanking extracellular domains somehow dictate the functional output of the SSD. Expression of a hybrid PTCH1 with its SSD substituted for that of PTCH2 showed good canonical signalling activity. Therefore, the SSD of PTCH2, is functionally equivalent to the SSD of PTCH1, when placed within the physical context of the extracellular and cytoplasmic domains of PTCH1. Somewhat expectedly, this redundancy was not shared by the SSD of NPC1, most likely due the increased evolutionary divergence between the proteins. Whilst the SSD of PTCH2 shares ~73.3% identity with the SSD of PTCH1, NPC1 only displays ~32.5% identity. It remains unclear how the cytoplasmic domains influence the SSD, but it seems likely that they confer subtle conformational alterations, perhaps impeding the recently identified sterol binding cavities.

Unlike the 272 residue C-terminal tail of PTCH1, PTCH2 has a short cytoplasmic tail of only 89 residues. As an extensively profiled domain of PTCH1, the CTD is

known to be involved in a multitude of cellular processes, including driving apoptosis (Chen et al., 2018). The inherent difference in the CTD of PTCH2 suggests it cannot perform many of the roles afforded to PTCH1 by its CTD. In fact, the CTD of PTCH2 lacks a key PPXY motif identified as a binding target of the NEDD4 E3 ligase family. In particular, the binding by two members, ITCH and Smurf2 promote the degradation of PTCH1, through targeted ubiquitination (Chen et al., 2014). Interestingly, mutation of the PPXY motif in the CTD, but not the middle cytoplasmic loop, significantly impairs E3 ligase binding, resulting in higher stability of PTCH1 and increased basal levels. However, performing the mutation in the PPXY motif of the middle cytoplasmic loop in addition to that of the CTD, completely abolishes the interaction (Yue et al., 2014). The lack of this CTD PPXY motif is likely the explanation of the increased stability of PTCH2 compared to PTCH1.

Chapter 2

Material and Methods

Chapter 2

Material and Methods

2.1 Cell Lines & Culture Procedures

HEK293 human embryonic kidney epithelial cells and NIH3T3 murine embryonic fibroblast cells were obtained from American Type Culture Collection (ATCC). *Ptc1^{-/-}* MEFs, murine embryonic fibroblasts were a gift from Dr. Matthew Scott (Stanford University). Cells were maintained in Dulbecco's Modified Eagle's Medium (DMEM) (Gibco), supplemented with 10% Foetal Bovine Serum (FBS) and 1% Glutamax (Gibco). All cell lines were grown at 37°C in 5% CO₂ and passaged prior to reaching confluence. Typical sub-culturing ratios of 1/20, 1/10 and 2/10 were used. Briefly, cell media was aspirated, cells washed with 2 mL sterile PBS, aspirated and incubated with 2 mL 25% trypsin-EDTA for approximately 3 minutes. After successful detachment, cells were diluted with 8 mL of fresh media and seeded at the desired density in the required culture dish.

IMCD-3 mouse kidney collecting duct cells were a gift from co-supervisor Professor Colin Johnson (University of Leeds). IMCD-3 cells were maintained in DMEM: Nutrient Mixture F-12 (Gibco), supplemented with 10% FBS. IMCD-3 cells were grown at 37°C, 5% CO₂ and sub-cultured at a ratio of 1/20 or 1/10 every 2-3 days.

SF9 suspension cells, a clonal isolate from *S. frugiperda* *Sf21* cells, were kindly provided by Professor Adrian Goldman (University of Leeds). *SF9* cells were grown at 28°C, 5% CO₂, 220 RMP, in aerated glass culture flasks. *SF9* cells were

maintained in Insect-XPRESS™ Protein-free Insect Cell Medium with L-Glutamine (Lonza). Upon reaching a density of approximately 2×10^6 cells/mL, *SF9* cells were passaged via dilution to a density of $0.5-1 \times 10^6$ cells/mL in fresh media.

2.2 Freezing and Thawing Cells

For long-term storage, cells were cryopreserved in liquid nitrogen (LN2). Briefly, cells were grown to high density in 10 cm culture dishes, washed with 2 mL PBS and detached by incubation with 2 mL 25% trypsin-EDTA. Detached cells were diluted with 8 mL fresh media and pelleted by centrifugation at $3,000 \times g$, 4°C for 3 minutes. Cell pellets were re-suspended to approximately 1×10^7 cells/mL in FBS, supplemented with 10% Dimethyl sulfoxide (DMSO). Cryovials containing 1 mL of cell mixture were stably frozen at -80°C overnight, within a Mr. Frosty freezing container (ThermoFisherScientific). The cryovials were then transferred and stored in a LN2 dewar. For cell thawing, cryovials were rapidly thawed in either a water or gel bead bath at 37°C . Cells were quickly re-suspended directly in culture flasks, containing fresh, pre-warmed media.

2.3 Cell Counting

When required, adherent cell lines were counted manually with a haemocytometer. Briefly, after trypsinization and resuspension in fresh media, 10 μL of cells were pipetted onto a haemocytometer and imaged by a bright-field light microscope. Cells sat within the 4 quadrants, as well as cells in contact with the border lines on two edges of each quadrant, were counted. The total count of cells was multiplied by 10,000 then divided by 4, to obtain a value of cells per mL. The desired concentration of cells was then obtained by dilution in media.

For *SF9* suspension cell lines, a Countess II Automated Cell Counter (ThermoFisherScientific) was utilised. Briefly, 1 mL of cell culture was transferred to a 1.5 mL Eppendorf tube and inverted to mix. In a fresh 1.5 mL Eppendorf tube, 10 μ L of this culture was mixed with 10 μ L Trypan Blue (Brand) and half was pipetted into a Countess™ Cell Counting Chamber Slide (ThermoFisherScientific). Details of concentration (cells/mL) and percentage viability (live/dead) were generated automatically. The in-system dilution calculator was then used to obtain the desired cell concentrations and volumes for seeding.

2.4 Gli-Luciferase Assay

Ptc1^{-/-} MEFs or *Ptc2*-CRISPR-KO-Clone1-*Ptc1*^{-/-} MEFs were grown to ~90% confluence in a 10 cm culture dish. Cells were washed, detached and diluted 1/5 in DMEM, 10% FBS, 1% Glutamax for seeding in 24-well culture plates (0.5 mL/well). Cells were left for 24 h, then transfected using TransIT-X2® (Mirus) and opti-MEM reduced serum media (ThermoFisherScientific). Briefly, a master mix, containing opti-MEM and the two reporter plasmid constructs; p8xGBS-Luc (250 ng/ μ L) and pRL-SV40 (10 ng/ μ L) were made in 1.5 mL Eppendorf tubes. The master mix was vortexed briefly, then pipetted into individual Eppendorf tubes (50 μ L/well). To these tubes, individual and various combinations of plasmid DNA constructs were pipetted from 250 ng/ μ L stocks. A total of 375 ng of plasmid DNA was added per individual 50 μ L of master mix. In the cases where DNA concentrations did not total 375 ng, empty pcDNA 3.1+ plasmid DNA was added to make up the remaining quantity. Transfected cells were incubated for 24 h at 37°C, 5% CO₂, before being carefully washed with 0.5mL PBS per well. Media was then replaced with DMEM, 0.5% FBS. 1% Glutamax for 48 h serum

starvation. Cells were then carefully washed with 0.5 mL PBS and lysed with 100 μ L of 1 x passive lysis buffer per well. Plates were left to lyse at room temperature, shaking, for 15 m. *Firefly*-Luciferase and *Renilla*-luciferase activities were determined with the dual-luciferase reporter assay system (Promega) in a Promega Glomax 20/20 luminometer. Measurements were obtained in relative luciferase units (RLU's) and expressed as a ratio of *Firefly*-Luciferase/*Renilla*-luciferase.

2.5 Co-immunoprecipitation Assays

HEK293 cells were seeded at a density of 2×10^5 cells/mL in 10 cm culture dishes. Approximately 24 h later, at >90% confluence, transient co-transfection with Lipofectamine 2000 (ThermoFisherScientific) was performed. Briefly, the two DNA plasmids constructs (4 μ g each) were added to an Eppendorf tube containing 500 μ L opti-MEM, vortexed and left for 5 m. Conversely, 20 μ L Lipofectamine 2000 was added to an Eppendorf tube containing 500 μ L opti-MEM, vortexed and left for 5 m. The two mixtures were subsequently combined, vortexed and incubated at room temperature for 20 m. Next, the transfection mixture was added dropwise to the cells. After 24-36 h incubation at 37°C, 5% CO₂ the transfected cells were aspirated and washed with 2mL ice cold PBS. Cells were harvested in 700 μ L Co-IP lysis buffer (50 mM Tris-HCL pH 7.5, 150 mM NaCl, 1% Nonidet P-40, 0.5% Sodium deoxycholate, 1 mM EDTA, 2.5 mM MgCl₂ supplemented with 1x Proteoloc protease inhibitor, 0.4 mM PMSF, 1 mM DTT). Cell lysates were incubated at 4°C, rotating end over end for 30 m, before centrifugation at 13k RPM, 4°C for 15 m. The supernatant was transferred to a fresh 1.5 mL Eppendorf tube and 200 μ L was saved as a whole cell lysate sample. To the remaining supernatant, a primary epitope tag antibody was added

and incubated at 4°C, rotating end over end, for 1.5 h. After, 30 µL Dynabeads (ThermoFisherScientific) was added and returned to incubate for 2 h. The beads were collected using a magnetic rack and 3 washes of 1 mL Co-IP lysis buffer was performed. The Dynabeads were treated with 18 µL 2x Laemmli buffer (Pierce™) and heated to 45°C for 25 m. Lysates were stored at -80°C and run by SDS-PAGE as soon as possible.

2.6 Co-IP Competition Assay

Co-IP competition assays were carried out in the same manner as standard Co-IP experiments, with several alterations. Cells were transiently co-transfected with either, three DNA plasmids containing different epitope tags or, two DNA plasmids baring different epitope tags and one untagged. The additional DNA plasmid was transfected in excess of the other two plasmids (10x, 30x and 35x). Immunoprecipitation was performed with specific primary antibody for the bait protein and blotted for the target protein. Visual inspection and densitometry measurements (performed in FIJI) were used to confirm reductions in target protein precipitation in competitor protein conditions, compared to control conditions. Protein samples from 'unbound' supernatants were also blotted to ascertain saturation levels of both protein-protein interactions and Dynabeads binding. WCLs were blotted for all three protein species to confirm relative expression levels against loading controls of Beta-Actin monoclonal antibody (Invitrogen), or HRP-conjugated GAPDH monoclonal antibody (Proteintech HRP-60004).

Cells seeded in 6-well culture plates were washed with 2mL 1x PBS and lysed in 200µL 1x Laemmli buffer on ice. Samples were subsequently sonicated on ice (20s Amplitude 20%) and heated at 45°C for 25m. Processed lysates were stored at -80°C until required.

2.7 Western Blotting

Cell lysates were subjected to SDS-PAGE on either self-cast 6, 8, or 13% polyacrylamide gels or pre-cast 4-20% Mini-PROTEAN® TGX™ Precast Protein Gels (BIO-RAD 4561096). Gels were run in Running buffer (1x) (ThermoFisherScientific). Self-cast gels were run at 80 v for 30 m, then 120 v for ~1 h or until the proteins reached the end of the gel. Pre-cast 4-20% gels were pre-run at 120 v for 10 m before sample loading. After sample loading gels were run at 140 v for ~1 h or until the proteins reached the end of the gel. Precision Plus Protein™ Dual Colour Standard marker (Bio-Rad 1610374) was loaded to determine the relative mass of the protein bands detected.

Proteins were transferred to PDVF membrane via wet transfer at 50 v for 2 h. Transfer buffer (1x + 20% Methanol) (ThermoFisherScientific) was cooled during transfer and re-used for a maximum of 3 times. After transfer, membranes were washed for 5 m in 10 mL tris-buffered saline, 1% Tween-20 (TBST), before blocking at room temperature for 1 h in 10 mL TBST, 5% Milk (ThermoFisherScientific). Next, the membranes were washed 3 times with TBST for 5 m per wash, then incubated with appropriate primary antibodies overnight at 4°C, gently rocking. For antibody details, please see **(Table 2.1)**. The membranes were washed three times with TBST for 5 m per wash, then incubated with the appropriate secondary HRP-conjugated antibody for 1 h at

room temperature in TBST, 5% milk. Membranes were washed 3 times with TBST for 5 m per wash and developed using Clarity Western ECL Substrate (BIO-RAD). Membranes were visualised on a ChemiDoc imaging system (BIO-RAD) using the Image Lab software (BIO-RAD) according to the manufacturer's instructions.

Antibody Name	Species	Dilution	Company	Product Code
Acetylated Tubulin (Monoclonal)	Mouse	1:1000	Sigma	T7451
β -Actin (Monoclonal)	Mouse	1:1000	Sigma	A5316
DYKDDDDK Tag (D6W5B)	Rabbit	1:1000	CST	14793
DYKDDDDK tag (Monoclonal)	Mouse	1:2000	Proteintech	66008-3-Ig
GFP (4B10)	Mouse	1:1000	CST	2955
GFP tag (Monoclonal)	Mouse	1:4000	Proteintech	66002-1-Ig
HA-Tag (C29F4)	Rabbit	1:1000	CST	3724
HA tag (Polyclonal)	Rabbit	1:5000	Proteintech	51064-2-AP
HA tag (Monoclonal)	Mouse	1:5000	Proteintech	66006-2-Ig
His-Tag (27E8)	Mouse	1:1000	CST	2366
6*His, His-Tag (Monoclonal)	Mouse	1:2000	Proteintech	66005-1-Ig
HRP-conjugated GAPDH (Monoclonal)	Mouse	1:4000	Proteintech	HRP-60004
Myc-Tag	Mouse	1:1000	CST	2276
MYC tag (Monoclonal)	Mouse	1:2000	Proteintech	60003-2-Ig
PTCH1 (C53A3)	Rabbit	1:1000	CST	2468
PTCH2	Rabbit	1:1000	CST	2464
Goat anti-Mouse IgG (H+L) Highly Cross-Adsorbed Alexa Fluor Plus 594	Mouse	1:500	Invitrogen	A32742
Goat anti-Rabbit IgG (H+L) Cross-Adsorbed Alexa Fluor 488	Rabbit	1:500	Invitrogen	A-11008
Rabbit anti-Mouse IgG (H+L), Superclonal™ Recombinant Alexa Fluor 594	Mouse	1:500	Invitrogen	A27027
Goat anti-Mouse IgG (H+L) Highly Cross-Adsorbed Alexa Fluor Plus 488	Mouse	1:500	Invitrogen	A32723

Table 2.1 Antibody Table.

Details of the antibodies used for immunoblotting in this work. Abbreviations: CTS, Cell Signalling Technology; HRP, horse radish peroxidase.

2.8 Site Directed Mutagenesis

The following cloning kits were purchased and used according to the manufacturer's protocols; Q5 Site-Directed Mutagenesis Kit (NEB); QuikChange II XL Site-Directed Mutagenesis Kit (Agilent Technologies); In-Fusion HD Cloning Kit (TaKaRa); TOPO TA cloning kit (ThermoFisherScientific). Polymerase chain reaction (PCR) and restriction digest based sub-cloning was also performed. With the exception of QuikChange II XL, all primers were purchased from either Sigma Aldrich or Integrated DNA Technologies as unmodified desalted oligos. HPLC-purified primers were brought from Integrated DNA Technologies for QuikChange II XL cloning.

For Q5 Site-Directed mutagenesis, the following reagents were assembled in a thin-walled PCR tube: 1x Q5 Hot Start High Fidelity 2x Master Mix 0.5 μ M forward primer, 0.5 μ M reverse primer, 1-2 ng template DNA and nuclease-free water. Exponential amplification of the template DNA was performed in a PCR thermocycler (BIO-RAD). For details of thermocycler setup see **(Table 2.2)**. After amplification 1 μ L of the PCR product was transferred to a 0.5 mL Eppendorf tube containing 1x KLD reaction buffer, 1x KLD enzyme mix and nuclease-free water. This Kinase, Ligase and DpnI treatment was incubated at room temperature for 5 m. Next, 5 μ L of the KLD reaction was added to 50 μ L of NEB 5-alpha Competent *E.coli*, previously thawed in a Falcon™ Round-Bottom Polypropylene Tube (ThermoFisherScientific) for 10 m on ice. The *E. coli* was incubated for 30 m on ice, then heat shocked at 42°C for 30 s, before being returned to incubate on ice for a further 5 m. Super Optimal Broth (SOC) was added to the *E. coli* to bring the volume up to 1 mL and this was incubated at 37°C, 225 RPM for 1 h.

For QuikChange II XL, the following reagents were combined in a thin-walled PCR tube: 1x reaction buffer (10x), 10 ng template DNA, 125 ng forward primer, 125 ng reverse primer, 1 μ L dNTP mix, 3 μ L QuikSolution, 1 μ L PfuUltra High Fidelity DNA polymerase and nuclease-free water. Exponential amplification of the template DNA was performed in a PCR thermocycler (BIO-RAD). For details of thermocycler setup see **(Table 2.2)**. Following DNA amplification, 10 units of DpnI was added directly to the thin-walled PCR tube, mixed and incubated at 37°C for 1 h. Transformation was performed using XL10-Gold ultra-competent cells, thawed in Falcon™ Round-Bottom Polypropylene Tubes on ice. To a volume of 45 μ L of cells, 2 μ L β -mercaptoethanol was added and incubated on ice for 10 m. After, 2 μ L of the DpnI treated PCR product was added to the cells and the mixture was incubated on ice for 30 m. Heat shock was performed at 42°C, 30 s, returning the tube to incubate on ice for 2 m immediately after. Pre-warmed SOC (0.5 mL) was added to the cells and the mixture incubated at 37°C 225 RPM for 1 h.

Polymerase Used	PCR Cycling Steps						
	Initial Denaturation	No. Cycles	Repeated as per No. Cycles			Final Extension	Hold
			Denaturation	Annealing	Extension		
Phusion® High-Fidelity DNA Polymerase (NEB)	98°C, 30 s	30	98°C, 10 s	60-72°C, 25 s	72°C, 30 s per kb	72°C, 7 m	4°C
Q5® High-Fidelity DNA Polymerase (NEB)	98°C, 30 s	30	98°C, 10 s	60-72°C, 25 s	72°C, 30 s per kb	72°C, 7 m	4°C
QuikChange XL Site-Directed Mutagenesis PfuTurbo DNA polymerase	95°C, 1 m	18	95°C, 50 s	60°C, 50 s	68°C, 1 m per kb	68°C, 7 m	4°C

Table 2.2 Thermocycler PCR set-ups for different polymerases.

Details of the temperatures, times and cycles used for the different polymerase and cloning kits used. Annealing temperatures were dictated by the T_a^* of the primer pair used. Settings were altered after experimental practice, if optimisation to times and/or temperatures was required.

2.9 Transformation, Selection, DNA extraction and Sequencing

The basic protocol of transformation is briefly described below. An appropriate volume of competent *E. coli* was thawed on ice in Falcon™ Round-Bottom Polypropylene Tubes. To this, either treated PCR product, or purified miniprep DNA was added. The mixture was incubated on ice for 30 m then heat shocked at 42°C for 30 s. The mixture was returned to incubate on ice for 5 m, before SOC media was added and the tube incubated at 37°C, 225 RPM for 1 h. The mixture was spread on selective plates of Luria Broth (LB) agar (Invitrogen) and appropriate antibiotic. Plates were incubated at 37°C overnight before growth and colony number assessment. At least 6 colonies were selected per sample and incubated at 37°C, 225 RPM for 8 h in 3 mL LB broth with appropriate antibiotic. Plasmid DNA was purified using EZ-10 Spin Column Plasmid DNA Miniprep Kit, Low Copy Plasmid (Bio Basic) according to the manufacturer's protocol. DNA

concentration was quantified using Nanodrop 8000 spectrophotometer (ThermoFisherScientific). The highest yield samples (max 3 per construct) were sent for Sanger sequencing to confirm successful mutagenesis (SourceBioscience & GENEWIZ).

2.10 Ciliary pH Fluorescent Biosensor Imaging

IMCD-3 cells were seeded in pre-coated, glass bottom, 35 mm, low, μ -Dish (IBIDI) and incubated at 37°C, 5% CO₂ until >90% confluent. Transient transfection of the pH reporter, 5HT₆-CFP-Venus(H148G) or pcDNA 3.1⁺ control was performed using Lipofectamine 2000. After ~24 h, cells were serum starved with 0.5% FBS to induce ciliation. Live IMCD-3 cells were imaged for a maximum of 1 h and buffered with HEPES (25 mM), to ensure cell viability and to minimise the impact of temperature and CO₂ fluctuations, and fluorophore photobleaching. A Nikon A1R confocal microscope was used with sequential channel acquisition (CFP Ex/Em 404.5/488 nm, Venus(H148G) Ex/Em 488/525 nm). Images were obtained at 0.2 μ M increments through the Z-plane. Post-acquisition analysis was performed in FIJI and Microsoft Excel. Individual cilia were manually selected in FIJI, with maximal projection intensity values exported to Excel, where Venus(H148G) values were divided by CFP values to generate a ratio value per individual cilia in a given condition.

To assign a pH value to the ratio values, a calibration curve was generated using a series of buffered DMEM F12 media at different pH (5.0, 6.0, 7.0, 7.4 and 8.0). The pH of each medium was checked before and after each calibration experiment via pH meter. Cells were equilibrated in the desired media, supplemented with cell permeabilizing agents, monensin (5 μ M) and nigericin (5

μM) (Sigma-Aldrich) for 5 m prior to imaging. For N-Shh stimulation experiments, IMCD-3 cells were incubated with N-Shh (2.5 ng) or vehicle control for 30 m prior to imaging. Ratios generated during post-acquisition analysis were normalised against calibration measurements obtained at pH 7.4.

2.11 FRET-Based imaging

HEK293 cells and *Ptc1*^{-/-} MEFs were seeded in pre-coated, glass bottom, 35 mm, low, μ -Dish (IBIDI) and incubated at 37°C, 5% CO₂ until >90% confluent. Transient transfection of two different fluorescent tagged PTCH1 and/or PTCH2 plasmid constructs was performed. Approximately 24 h post-transfection, the cells were imaged using a Zeiss LSM 880 inverted confocal microscope. Cells were imaged using a pinhole of 1 airy unit (AU) and Plan-Apochromat 40x/1.4 Oil DIC. Throughout imaging a temperature of 37°C was maintained. The occurrence of FRET/FRAP was determined through the excitation of the donor protein at 488 nm, recording emission intensity before and after photo-bleaching the acceptor protein at 514 and 610 nm. Donor emission and acceptor excitation were measured throughout to determine any increase in donor emission intensity post acceptor bleaching. Regions of interest (ROIs) were created to sample multiple bleaching and control events in individual image series acquisitions. Within each image series, a corresponding control ROI was obtained for each sample ROI captured. Data was obtained over a series of 20 images, 4 pre-bleach and 16 post-bleach, to account for stage drift and observation of potential protein migration or recovery.

2.12 FRET-Based Data Processing

All image series collected were saved as .czi files for subsequent processing across Zen Black (Zeiss), Excel 2016 (Microsoft) and Prism 8 (GraphPad). See Table 2.1 for details.

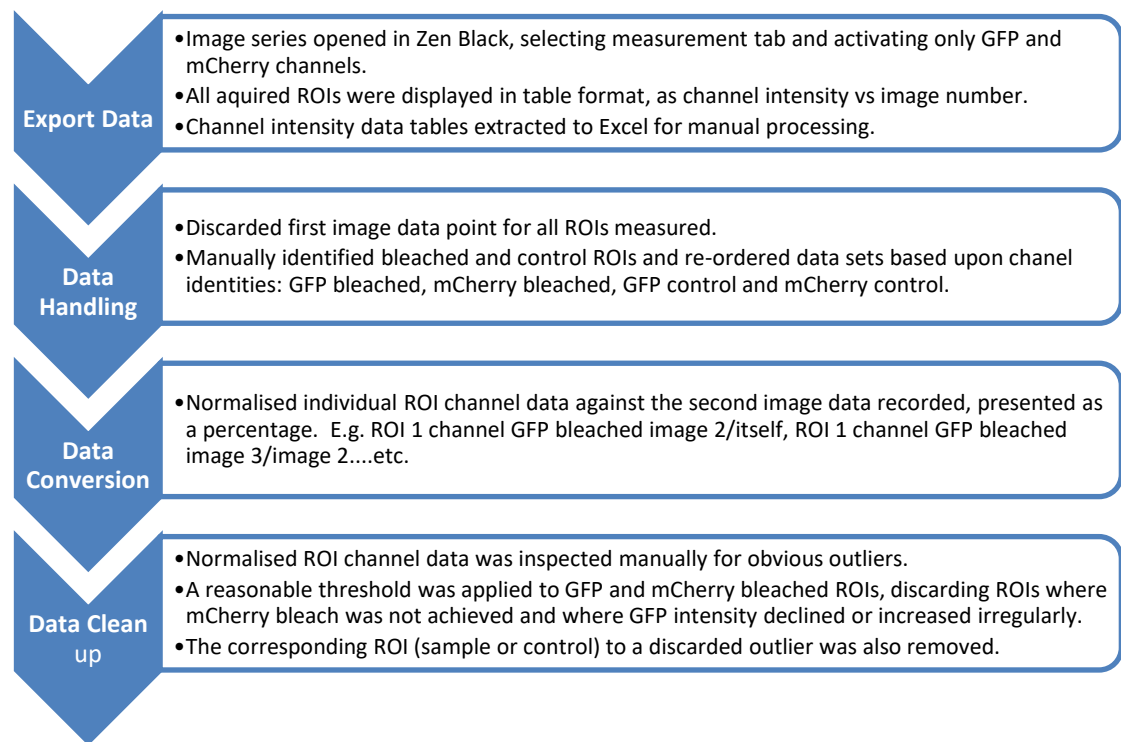


Table 2.3 Summary of FRET-Based data processing

Details of the data handling of FRET-based assay results, from acquisition to normalisation.

2.13 FRET-Based Competition Assay

Adapted from (2.11 FRET-Based imaging). For FRET-based competition assays a third DNA plasmid was co-transfected in an excess to the two fluorescently labelled DNA plasmids transfected for the detection of FRET. All microscope imaging and post-acquisition processes remained unaltered.

2.14 Immunofluorescence

HEK293, IMCD-3, and *Ptc1*^{-/-} MEFs were seeded in 4-well or 8-well glass bottom removable chamber slides (IBIDI) or in culture plates with glass slides inserted. Cells were incubated at 37°C, 5% CO₂ until appropriately confluent for transfection. Cells were transiently transfected with various plasmid DNA constructs under investigation. For observation of the cilia, IMCD-3, or *Ptc1*^{-/-} MEFs were serum starved with DMEM, 0.5% FBS, 1% Glutamax ~24 h after transfection. After 24-48 h post transfection (HEK293) or 24-48 h post serum starvation (cilia imaging), cells were washed with PBS and fixed using 4% paraformaldehyde (ThermoFisherScientific) for 15 m. Chambers or slides were washed 3 times for 5 m with PBST and then cells were permeabilised with PBST, 0.2% Triton-X100 for 15 m. Chambers or slides were washed 3 times for 5 m with PBST and then blocked with PBST, 3% Bovine Serum Albumin (BSA) for 1 h. Cells were incubated with primary antibody overnight at 4°C in PBST, 3% BSA. After, cells were washed 3 times for 5 m with PBST and incubated in PBST, 3% BSA with appropriate secondary AlexaFluor antibody (ThermoFisherScientific) for 2 h at room temperature in the dark. Cells were washed 3 times for 5 m with PBST and carefully aspirated completely. For mounting, the silicone chamber dividers were removed using the tool provided. Slides were transferred to microscope slides. ProLong™ Gold Antifade Mountant with DAPI (ThermoFisherScientific) was applied and coverslips sealed using clear nail varnish. Slides were kept in a light proof box until confocal imaging.

2.15 Fluorescent LED Microscopy

An EVOS FL Colour microscope (ThermoFisherScientific) was used to rapidly determine the expression of fluorescently tagged PTCH1, PTCH2 and PTCHD1 plasmid constructs in various cell lines. Briefly, cells were typically seeded in 12-well cell culture plates and incubated overnight at 37°C. 5% CO₂. Transient transfections were performed using plasmid DNA purified by either miniprep (Bio Basic) or maxiprep (Quiagen). After 24-48 h, cells were imaged directly, within the culture plate. Cell monolayers were located and focused through Trans or phase filters at 4x or 10x magnification. GFP (488 nm) and Texas Red (594 nm) channels were utilised, dependent on the application required. Images were taken at 4x, 10x, 20x, 40x and 60x magnification, dependent upon cell line and experimental objective. Post data acquisition analysis was performed on the free software package FIJI.

2.16 PTCH2 CRISPR/Cas9 Stable Cell Knockout

Small guide RNAs (sgRNAs) were generated to specifically introduce an indel within the mouse Patched 2 coding sequence of *Ptc1*^{-/-} MEFs. Using the free online software, Benchling, sgRNAs (20 nucleotides in length) were selected to target upstream of a 5'-NGG PAM site in exon 2 of the Patched 2 sequence. The sgRNAs were sub-cloned into the vector, lentiCRISPR Lko, via BsmB I restriction digest. Successful incorporation of the sgRNAs was confirmed by Sanger sequencing.

Ptc1^{-/-} MEFs were transfected with the sgRNA containing vector and left for 24 h. After, the media was re-refreshed and puromycin selection started. After 3 days of selection, the remaining cells were re-seeded in 24-well plates at a density of

~1 cell/well. Cells were grown in the presence of puromycin for 2 weeks, expanding to larger culture vessels when required. For validation of a successful knockout (in progress), DNA was isolated from cells and a region of ~1,000 nucleotides spanning the sgRNA target site was amplified by PCR, using specific primers. The amplified DNA was spin column purified, quantified by nanodrop 8000 and sent for Sanger sequencing using specific forward and reverse primers, flanking the target site for indel introduction.

2.17 Cloning of PTCH1, PTCH2 and PTCHD1 pFastBac Vectors

The cloning of pFastBac-CVGH-PTCHD1 was previously performed by Dr Maren Thomsen. The protein coding regions of human PTCH1 and PTCH2 were cloned into pFastBac-CVGH, kindly provided by the Goldman Group (University of Leeds). The In-Fusion cloning kit was used as per the manufacturer's instructions to amplify the coding regions of; PTCH1 from our myc-PTCH1 plasmid and; PTCH2 from our PTCH2-FLAG pcDNA 3.1+ plasmid. Forward and reverse primers were generated in the TaKaRA primer design tool and designed to incorporate an N-terminal AvrII and C-terminal SbfI restriction sites during PCR amplification. For restriction digest of pFastBac-CVGH, the following reagents were assembled in a 0.5 µL Eppendorf tube: 1 µL CutSmart 10x buffer, 1 µL AvrII, 1 µL SbfI, 1 µg pFastBac-CVGH and nuclease-free water. The mixture was incubated at 37°C for 1 h, then heat inactivated at 80°C for 20 m.

PCR products were spin-column purified, whilst restriction digested pFstBac-CVGH was gel purified. For the In-Fusion cloning reaction the following reagents were combined in a 0.5 mL Eppendorf tube: 2 µL 5x In-Fusion Enzyme Premix, (x) µL purified linearized vector, (x) µL PCR product and nuclease-free water. The

volume of vector and PCR product was determined by pmol of ends calculations, performed on an online calculator (Promega). A standard ratio of 3:1 insert to vector was used. The In-Fusion cloning product was then transformed into Stellar competent cells, and plated on selective LB agar plates overnight. For details of transformation, plating, selection and screening see **(2.9 Transformation, Selection, DNA extraction and Sequencing)**.

2.18 Generation of Baculovirus

The pFastBac-CVGH constructs were transformed into two *E. coli* strains: DH10Bac (Invitrogen) and Multibac EmBacY (Geneva Biotech). Briefly, 2 μ L of PTCH1-, PTCH2- or PTCHD1-pFastBac-CVGH was added to 50 μ L competent cells and incubated on ice for 20 m. Heat shock was performed at 42°C for 30 s, followed immediately by 2 m incubation on ice. LB broth (400 μ L) was added and the cell mixture transferred to a round bottom 15 mL falcon tube for incubation at 37°C, 225 RPM overnight. Cells were spread on selective LB agar containing: 50 μ g/mL Kanamycin, 10 μ g/mL Tetracycline, 7 μ g/mL Gentamycin, 0.16 mM IPTG and 100 μ g/mL X-Gal at 1/1, 1/10, 1/100 and 1/1000 dilutions. Plates were incubated at 37°C for 24 h. Plates were inspected and 4 white colonies and one blue colony were selected and streaked onto fresh LB agar antibiotic plates, incubated at 37°C overnight. The pipette tips used for streaking were ejected into 2 mL LB broth with antibiotics in a 15 mL round bottom falcon tube and incubated at 37°C 225 RPM overnight. Positive colonies were identified via the LB plate and the corresponding 2 mL culture was pelleted, via centrifugation at 4,000 RPM for 10 m.

Bacmid DNA was purified using the miniprep kit (Bio Basic) following the manufacturer's instructions and re-suspending in 30 μL nuclease-free water. Transfection was performed in duplicate, in 6-well culture plates, at a cell density of 0.33×10^6 cells/mL. In separate 1.5 mL Eppendorf tubes the following reagents were assembled: 10 μL of X-TremeGENE HP DNA transfection reagent (Roche) with 100 μL media and; 20 μL bacmid DNA diluted in 200 μL media. Both solutions were then combined, mixed and incubated for 30 m. The combined solution was added dropwise, 150 μL per well. The plate was incubated at 27°C, 5% CO_2 for ~60 h. The cells were subsequently inspected and the supernatant (V0) collected into light-safe 15 mL falcon tubes, stored at 4°C. Media was replaced on the 6-well plate and incubated for a further ~60 h, before harvesting the cells.

2.19 Production of Baculovirus Infected Cells (BIICs)

After baculovirus amplification was confirmed by western blot and wide-field fluorescent microscopy BIICs were generated. Briefly, an adapted 25mL culture of Sf9 cells at 1×10^6 /mL were infected with 3 mL of V0 baculovirus. Cells were monitored daily for proliferation arrest (PA) and diluted to 1×10^6 cells/mL. Upon PA, a volume containing 1×10^6 cells was removed, pelleted by centrifugation at 700 x g and stored at -20°C. Approximately 24 h after proliferation arrest (PA) supernatant (V1) was removed and stored at 4°C in a light-safe 50 mL falcon tube. Titer testing was performed by infecting three cultures of 100 mL 1×10^6 cells/mL with serial dilutions of V1. The culture which doubled once and reached PA was selected. At 24 h post PA, 50 mL of the culture was pelleted by centrifugation at 200 x g. The pellet was re-suspended to 1×10^7 cells/mL in an appropriate volume of filtered InsectXpress media, 10 g/L BSA, 10% DMSO and

aliquotted into 1 mL cryovials for LN₂ storage. The remaining 50 mL culture was maintained until PA + 72h, retrieving samples for protein expression assessment via western blot.

2.20 Large Scale Protein Expression

A BIIcS cyrovial was thawed and diluted in 49 mL media. To cells pre-adapted in 1 L culture flasks (400 mL 1 x 10⁶ cells/mL), 10 mL of re-suspended BIIcS was added. At 48 h post PA cells were pelleted via centrifugation at 800 x g for 25 m. Expression of protein was quickly checked by placing 1 mL of culture on a UV illuminator to observe YFP fluorescence compared to uninfected cells. Cell pellets were re-suspended in 10 mL of buffer (10 mM HEPES, 200 mM NaCl, 5% glycerol and nuclease-free water). The re-suspended cells were transferred to 50 mL falcon tubes and pelleted by centrifugation at 900 x g, 15 m. After removal of the supernatant, the pellets were flash frozen in LN₂ and stored at -80°C.

2.21 Membrane Preparation

Cell pellets were thawed and re-suspended in membrane preparation buffer (10 mM HEPES, 200 mM NaCl, 2.5 mM MgCl₂, 0.5 mM CaCl and nuclease-free water), supplemented with 1x Proteolock and 10 mM PMSF protease inhibitors. Lysis was performed on ice, via sonication at 40% amplitude for 2 m (10 s, on, 5 s off). Lysates were treated with DNase I (66 µg/mL) for 2 h, rotating at 4°C. Lysates were then centrifuged in a Ti-45 rotor (Beckmann Coulter) at 42,000 RPM, 4°C for 2 h. The membrane pellets were re-suspended in buffer (10 mM HEPES, 200 mM NaCl, 5% glycerol and nuclease-free water) at a ratio of 6.25 mL buffer per 300 mL culture. Membranes were homogenised on ice and flash frozen in LN₂ as droplets, stored at -80°C. An SDS-PAGE gel was run to evaluate

samples taken throughout the membrane preparation, imaging directly on a G-Box (SynGene) for GFP expression and then by Coomassie stain.

2.22 Large Scale Protein Purification

Sf9 cell membranes (15 g) were thawed on ice and diluted with purification buffer (10 mM HEPES, 200 mM NaCl and nuclease-free water). Membranes were solubilised through the addition of 0.8% glyco-diosgenin (GDN), incubating at 4°C overnight. Insoluble fractions were pelleted and removed by centrifugation at 42,000 RPM, 4°C, 1 h. The solubilised protein supernatant was incubated with 1,250 µL sedimented HisPur™ Cobalt Resin (ThermoFisherScientific), end over end, at 4°C for 1.5 h. The resin protein mix was centrifuged at 1,000 x g for 3 m at 4°C and the 'unbound' supernatant removed. The remaining resin was re-suspended in 30 column volumes (CVs) of equilibration buffer (10 mM HEPES, 200 mM NaCl, 0.004% GDN and nuclease-free water) and transferred to an Econo-Pac® Chromatography Column (BIO-RAD) at 4°C. The complete volume within the column was passed through by gravity flow and collected in a falcon tube labelled wash 1. Next, 20 CVs of wash buffer (10 mM HEPES, 200 mM NaCl, 20 mM Imidazole, 0.004% GDN and nuclease-free water) was added and allowed to flow through the chromatography column into a falcon tube labelled wash 2. A final wash with 20 CVs of equilibration buffer was applied to remove any residual imidazole in the resin. The resin was re-suspended in 1 CV of equilibration buffer and transferred to a 1.5 mL Eppendorf tube on ice. HRV protease, produced by the Goldman laboratory (University of Leeds) was added to the resin and incubated at 4°C, 1 h, rotating end over end. The tube was then centrifuged at 1,000 x g for 3 m at 4°C to sediment the resin. The supernatant containing cleaved protein was transferred to a fresh 1.5 mL Eppendorf on ice.

The resin was re-suspended with 0.5 CVs of equilibration buffer and centrifuged once more. The resultant supernatant was transferred and pooled with the first. A measurement of protein concentration was taken on a nanodrop 8000. The elution fraction was then concentrated in a Vivaspin 500, 30kDa molecular weight cut off (MWCO) Polyethersulfone membrane centrifuge concentrator (Sartorius). Samples were centrifuged at 4°C, 4,000 RPM for 3 m intervals with frequent pipetting to prevent aggregation. Concentrations of 5-8 fold were achieved, based on volume reduction. Concentrated samples were measured for protein concentration via nanodrop. Samples were used for a variety of applications, including mass spectrometry, fluorescence-detection size-exclusion chromatography (F-SEC), negative staining, cryo-EM, SDS-PAGE and photo-clickable cholesterol assays. If samples were not used immediately, they were stored at 4°C or -80°C, dependent on glycerol content.

2.23 Immunoprecipitation for Mass Spectrometry

HEK293 cells were seeded at a density of 2×10^5 cells/mL in 10 cm culture dishes. Approximately 24 h later, at >90% confluence, transient transfection with Lipofectamine 2000 was performed. Briefly, 8 µg of PTCH2-FLAG or 8 µg PTCHD1-CVGH plasmid DNA was added to 500 µL opti-MEM, vortexed and left for 5 m. Conversely, 20 µL Lipofectamine 2000 was added to 500 µL opti-MEM, vortexed and left for 5 m. The two mixtures were subsequently combined, vortexed and incubated at room temperature for 20 m. Finally, the transfection mixture was added dropwise to cells. After 48 h incubation at 37°C, 5% CO₂ cells were aspirated and washed with 2 mL ice cold PBS. Cells were harvested in 700 µL Co-IP lysis buffer (50 mM Tris-HCL pH 7.5, 150 mM NaCl, 1% Nonidet P-40, 0.5% Sodium deoxycholate, 1 mM EDTA, 2.5 mM MgCl₂ supplemented with 1x

Proteolock protease inhibitor, 0.4 mM PMSF, 1 mM DTT). Cell lysates were incubated for 30 m at 4°C, rotating end over end, before centrifugation at 13k RPM, 4°C for 15 m. The supernatant was transferred to a fresh 1.5 mL Eppendorf tube and 100 µL was saved as a WCL sample. To the remaining supernatant, 2 µL of mouse IgG control antibody (1 mg/mL) and 30 µL Dynabeads was added. The supernatant mix was incubated for 30 m at 4°C, rotating end over end, before being transferred to a fresh 1.5 mL Eppendorf, via magnetic sedimentation of the Dynabeads. Primary anti-FLAG and anti-His antibodies (Proteintech) were added and incubated at 4°C, rotating end over end, for 1.5 h. After, 30 µL Dynabeads was added and returned to incubate for 1 h. Dynabeads were collected using a magnetic rack and washed 3 times with 1 mL of Co-IP lysis buffer. The Dynabeads were treated with 18 µL 1x Laemmli buffer and heated at 45°C for 25 m. Samples were taken on ice, directly for mass spectrometry analysis.

2.24 Mass Spectrometry

Purified protein band identification, protein post-translation modification mapping and immunoprecipitation interaction protein identification, was performed in-house by the mass spectrometry facility (University of Leeds). Samples from protein purification experiments were submitted in SDS-PAGE gel, stained by InstantBlue Coomassie (Expedeon). A minimum of 5 µg protein was loaded per lane for analysis. Gel extraction and protein digestion was performed by the facility, using four reagents: trypsin, chymotrypsin, asp-N and trypsin with lys-c. Samples from immunoprecipitation interaction protein experiments were submitted in solution. All mass spectrometry data was provided electronically in both .csv and .html format and was processed through the software, Peaks.

2.25 PhotoClickable Cholesterol Assay

Purified PTCHD1 protein in different concentrations of GDN (0.004%, 0.006%, 0.008% and 0.01%) was incubated for 30 m on ice with 6 μ M inclusion bodies of β -Methyl-cyclodextrin and hex-5'-ynyl 3β -hydroxy-6-diaziriny-5 α -cholan-24-oate 'PhotoClick cholesterol' (Avanti Polar Lipids). Samples were irradiated with UV light at 365 nm using a CL-1000 Ultraviolet cross-linker UVP. A click-reaction was performed by adding 3 μ L the following reagents, premixed in the order listed at the following working concentrations: Azide reagent (100 μ M), CuSO₄ (1 mM), TCEP (1 mM) and TBTA (100 μ M). After 1 h incubation at room temperature, the reaction was stopped by the addition of EDTA (10 mM). Excess click reagents were precipitated by adding a 4 x volume of ice cold acetone, before centrifugation for 10 m at 13,000 RPM, 4 °C. The resulting pellet was washed 2 x with cold MeOH, re-centrifuged and air-dried. Pellets were then re-suspended in 2 x Laemmli buffer and run on SDS-PAGE gel with an all blue non-fluorescent marker. For visualisation of the bands on the SDS-PAGE a Cy3/TAMRA/Rhodamine filter set (Ex/Em ~540/568 nm) was used ~120 s. For visualisation of the marker a Cy5/Coomassie filter set was used.

2.26 EM Grid Glow Discharge

Grid glow discharge for both negative stain and cryo-EM was performed in a PELCO easiGlow discharge unit, using the pre-set standard parameters. Grids were carefully transferred onto a parafilm wrapped microscope slide, and placed in the glow discharge chamber. After securely seating the lid, the vacuum cycle was engaged by pressing 'auto run' on the display screen. Upon reaching the desired vacuum of 0.38 mBar, the system held steady for 10 s, before glow discharging for 30 s. Grids were removed once automatic venting had finished

and the display screen read 1 atmospheric pressure. Grids were processed immediately for downstream applications.

2.27 Electron Microscopy Negative Staining

For the purpose of negative staining, copper carbon coated grids were purchased from the electron microscopy facility (University of Leeds). Staining was performed via the single droplet method. Neat and serial dilutions of purified protein were applied to the discharged surface and incubated for 30 s. Filter paper was used to carefully remove all traces of liquid, and a 2% uranyl acetate solution was applied for 30 s. Excess stain was removed carefully using filter paper. The staining procedure was repeated once more and the grids dried under a lamp for 10 s. All grids were stored in a cassette, with their dilution, buffer and location recorded. Negative stain screening was performed using an FEI Technai G2-spirit, 120 KeV Lab6 electron source with Gatan US4000/SP 4k x 4k CCD camera. The accompanying software used was Digital Micrograph (DM) with a Cs of 6.3 mm. The screen down and screen up nominal magnifications used for imaging were 26.5 kx and 30 kx respectively, with a pixel size of 0.37 nm (EM facility). Additional data acquisition was performed on an FEI Tecnai F20, 200 KeV, FEG electron source with FEI CETA (CMOS CCD) camera. The accompanying software used was TEM Imaging & Analysis (TIA), SerialEM with a Cs of 2 mm. The screen down and screen up nominal magnifications used for imaging were 25.5 kx and 29 kx respectively, with a pixel size of 0.351 nm (EM facility).

2.28 Vitrification of purified protein

For the purpose of cryo-EM, Quantifoil 1.2 μM dia (1.3 μM) 400 Mesh Copper grids were purchased from the EM facility (University of Leeds). Grids were glow discharged, as described in 2.21 EM grid glow discharge, just before use. Grid protein samples were vitrified using a Vitrobot MK IV with foot peddle operation (ThermoFisherScientific). To provide sufficient humidity, the vitrobot reservoir was filled with 60 mL of milli-Q water. The chamber was set to 4°C, 0% humidity during initial set up. The copper ethane cup, metal puc holder legs and Styrofoam container were assembled and filled with LN₂. The level of LN₂ in the Styrofoam container was maintained throughout the process. Once the LN₂ in the copper ethane cup had evaporate completely, the cup was filled with liquid ethane. Once the liquid ethane turned milky in appearance, the puc holder legs were removed and the container placed in the loading position on the vitrobot. Fresh filter papers were punched and placed onto the pads with the vitrobot chamber and the humidity set to 100%. A glow discharged grid was fixed carefully between lockable vitrobot tweezers. Through use of the foot peddle, the pneumatic arm was released for manual tweezer attachment. The pneumatic arm was retracted and engaged for sample loading. The protein sample (3 μL) was pipetted onto the coated side of the grid through a window port on the side of the chamber. The grid was blotted and automatically plunged into the ethane cup. The tweezers were manually removed from the pneumatic arm, whilst ensuring the grid remained in the ethane. Quickly transferring to the LN₂ Styrofoam container, the grid was placed in a puc holder. Grids were loaded into the puc in a clockwise manner, slots numbered 1-4, and stored in a LN₂ dewar within a ventilated 50 mL falcon tube.

2.29 Electron Microscope Negative Stain Image Analysis

All processing of digital micrographs was performed in RELION 3.0 software, accessed through local GPU machines: fbsdpcu058, wkstn03 and workstn04. Electron micrographs were first converted from .dm3 file to .mrc format and imported into RELION 3.0 as input files. The standard work flow of the RELION 3.0 software was followed with instruction from the 'Single-particle processing in RELION-3.0' tutorial (Scheres, 2019). Details of the work flow are described in **(Table 2.4)**.

Chapter 2: Material and Methods

Data Conversion	Convert .dm3 files to .mrc files Command: 2proc2d.py * .dm3 @.mrc
Import	Module load relion On I/O tab: Input files: micrographs/*.mrc Node type: 2D micrographs/tomagrams (.mrc)
CTF Estimation	On I/O tab: Input micrograph STAR file: Job01/micrographs.star Use micrograph without dose-weighting: No Spherical aberration (mm): 2.7 Voltage (kV): 120 Amplitude contrast: 0.1 Magnified pixel size (A): No . Amount of astigmatism (A): 100 On Gtcf tab: Use Gtcf instead? Yes Gtcf executable: /wherever/it/is/Gtcf Ignore 'Searches' parameters? Yes Perform equi-phase averaging? Yes
Manual Picking	On I/O tab: Input file: micrographs_ctf.star On Display tab: Particle diameter (A): 200 Scale for micrographs: 0.25 Sigma contrast: 3 White value: 0 Black value: 0 Lowpass filter (A): 20 Highpass filter (A): 0 Pixel size: 0.885 Scale for CTF image: 1
Particle Extraction	On I/O tab: Input file: CtfFind/Job003/micrographs_ctf.star Coordinate-file suffix: job003/cords_suffix_manual_pick.star Or re-extract refined particles? No Manually set pixel size? No On Extract tab: Particle box size (pix): 220 Invert contrast? No Normalise particles? Yes Diameter background circle (pix): 220 stdev for white dust removal: -1 stdev for black dust removal: -1 Rescale particles? No
2D Classification	On I/O tab: Input file: extract/particles.star On CTF tab: Do CTF-correction? Yes have data been phase-flipped? No ignore CTFs until first peak? No On Optimisation tab: Number of classes: 30 regularisation parameter T: 2 number of iterations: 25 use fast subsets? Yes mask diameter (A): 200 mask individual particles with zeros? Yes Limit resolution E-Step to (A): -1 On Sampling tab: Perform image alignment? Yes in-plane angular sampling: 6 offset search RANGE (PIX): 5 offset search step (pix): 1 On Compute tab: Use parallel disc I/O: Yes number of pooled particles: 5,000 pre-read all particles into RAM? Yes combine iterations through disc? No use GPU acceleration? Yes
3D Initial Model	On I/O tab: Input file: 2D_class?particles.star On CTF tab: Do CTF-correction? Yes have data been phase-flipped? No ignore CTFs until first peak? No On Optimisation tab: Number of classes: 3 mask diameter (A): 200 Flatten and enforce non-negative solvent: Yes Symmetry: C1 initial angular sampling: 15 degrees offset search range (pix): 6 offset search step (pix): 2 On SGD tab: Number of initial iterations: 50 number in between iterations: 200 number of final iterations: 50 write-out frequency: 10 initial resolution (A) 35 final resolution (A): 20 initial mini-batch size: 100 final mini-batch size: 500 On Compute tab: Use parallel disc I/O: Yes number of pooled particles: 5,000 skip padding: No pre-read all particles into RAM? use GPU acceleration? Yes

Table 2.4 Summary of RELION 3.0 work flow for EM micrograph processing.

Work flow for EM micrograph processing in RELION 3.0 software, adapted from the tutorial 'Single-particle processing in RELION-3.0' (Scheres, 2019).

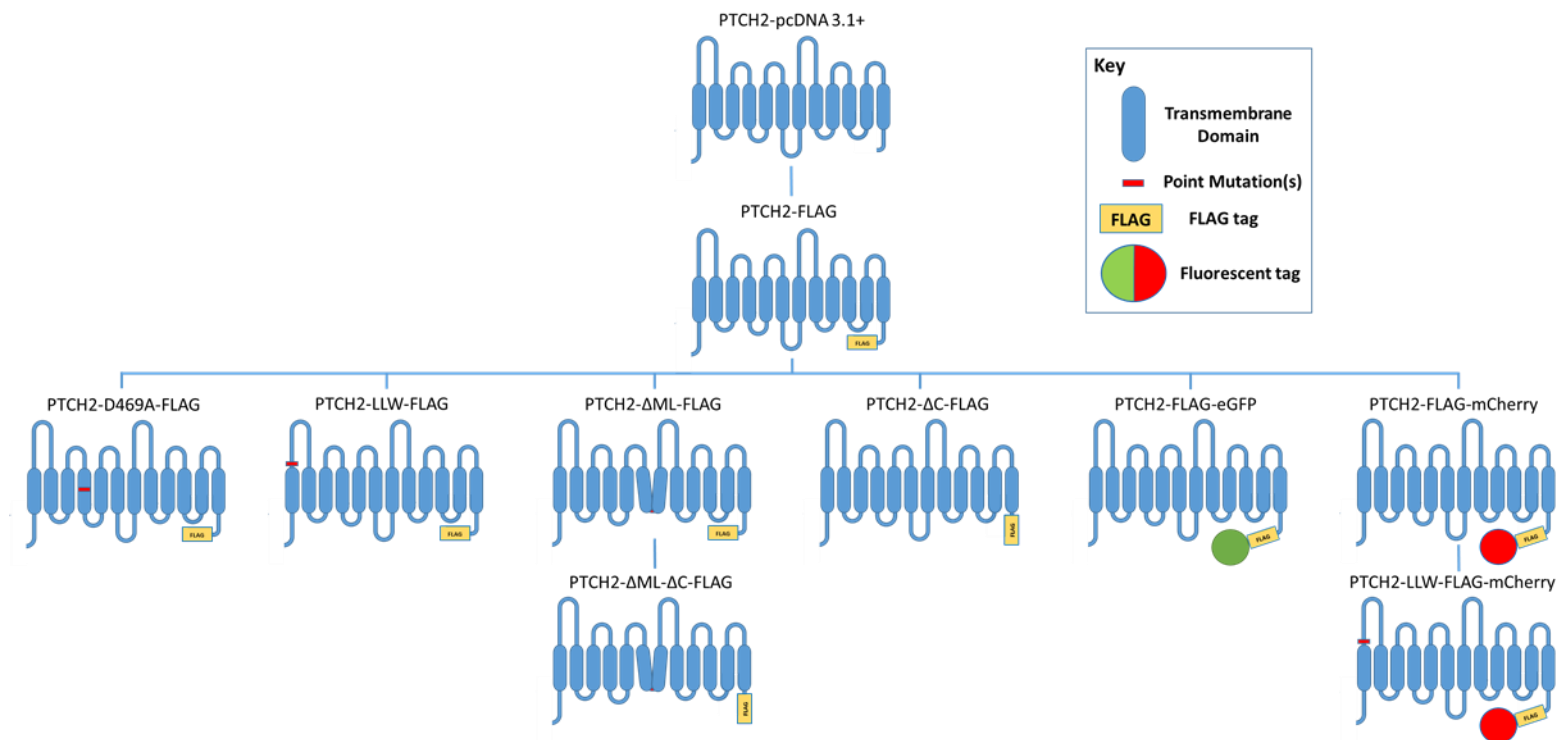


Figure 2.1 Hierarchical tree of PTCH2 plasmids generated.

Visual depiction of the various PTCH2 constructs generated during this doctoral work. Their specific alterations or mutations as well as their lineage is shown.

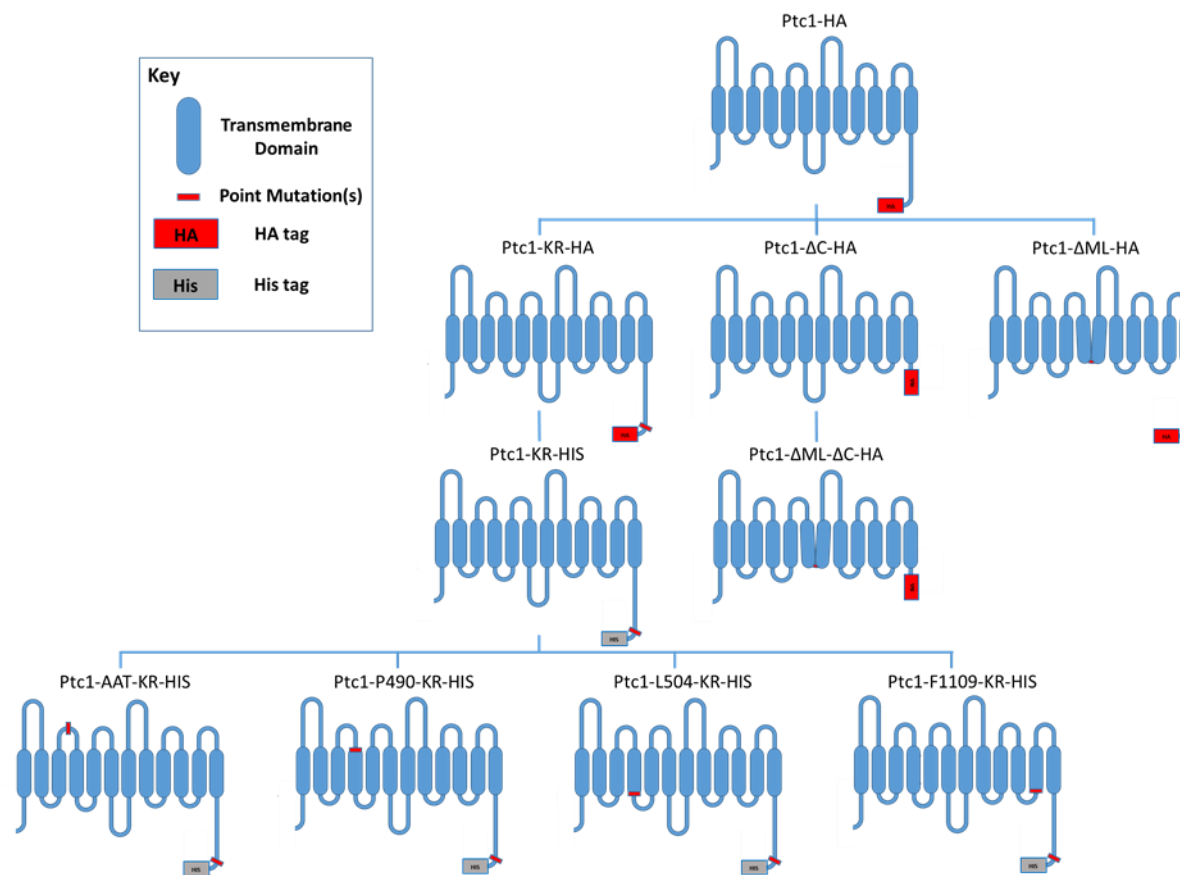


Figure 2.2 Hierarchical tree of Ptc1 plasmids generated.

Visual depiction of the various Ptc1 constructs generated during this doctoral work. Their specific alterations or mutations as well as their lineage is shown.

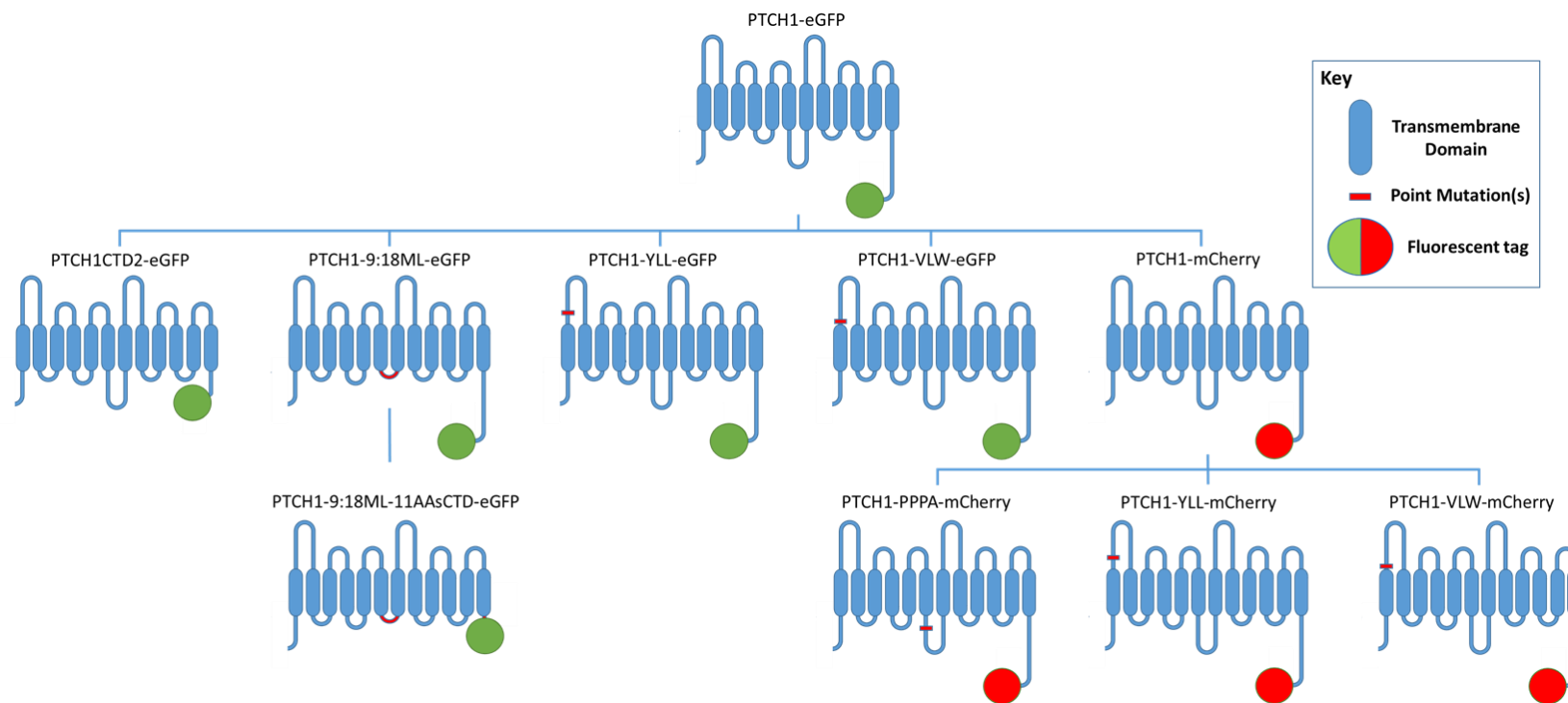


Figure 2.3 Hierarchical tree of PTCH1 plasmids generated.

Visual depiction of the various PTCH1 constructs generated during this doctoral work. Their specific alterations or mutations as well as their lineage is shown.

Chapter 3

Specific mutation of the Ptc1 SSD residue P490, or removal of the cytoplasmic domains impairs activity, without disrupting oligomerisation

Chapter 3

Specific mutation of the Ptc1 SSD residue P490, or removal of the cytoplasmic domains impairs activity, without disrupting oligomerisation

3.1 Introduction

The ability of Patched 1 to regulate Smo activation in a sub-stoichiometric manner is believed to revolve around its control over the availability of an endogenous small molecule agonist. The presence of an SSD within Patched, that is essential for canonical function, strongly suggests an endogenous sterol cargo (Strutt et al., 2001). Smo has been shown to be at least partially activated by exogenous cholesterol and other sterol derivatives (Corcoran and Scott, 2006; Xiao et al., 2017; Hu and Song, 2019). Therefore, it is logical that the endogenous Smo agonist is a sterol, but how Patched 1 mobilizes it remains unclear. Maintenance of a microenvironment devoid of this agonist, such as within the cilium, could have two-fold impact on Smo, reducing activation and preventing ciliary retention (Rohatgi, Milenkovic, Ryan B. Corcoran, et al., 2009). But to extrude a sterol molecule against its concentration gradient, Patched would require some form of energy source.

Patched 1 shares homology with the RND bacterial family of efflux pump proteins (Marigo et al., 1996; Deneff et al., 2000). From a mechanistic viewpoint, RND proteins are proton motive force (PMF) driven, utilising H⁺ ions to move small molecule substrates across membranes, against their concentration gradient (Amaral et al., 2014; Anes et al., 2015). A structural characteristic shared by Patched 1 and the RND proteins, is the ability to self-oligomerise. Homo and

Hetero-trimerisation has been found to be an essential requirement for RDN protein function (Murakami et al., 2002; Kim et al., 2010).

Interestingly, whilst Patched 1 CTD oligomerisation has been deemed nonessential for canonical activity, through CTD truncations, complete diminishment of oligomerisation has not been shown *in vitro* (Lu et al., 2006). Therefore, other intra-molecular contacts must be involved in the oligomerisation of Patched 1 and this process might still prove integral to activity.

Five highly conserved residues, essential for RND trimerisation, have been identified; D407 and D408 within TM4; Lys939 within TM10 and; T978 and R971 within TM11 (Guan and Nakae, 2001; Takatsuka and Nikaido, 2006). Of these five residues, the two Aspartic acids are also present within TM4 of Patched 1 and 2 (Tukachinsky et al., 2016). The consensus sequence 'GxxxDD' located in the 4th transmembrane, within the SSD, is also partially conserved in the 5th TM of NPC1 and appears twice in DISP1, proximal to the 4th and 10th TMs (**Figure 3.1**) (Scott and Ioannou, 2004; Chen et al., 2020). This consensus is not present in PTCHD1, although two neighbouring aspartic acids of unknown relevance, are located in the first extracellular loop.

Chapter 3: Specific mutation of the *Ptc1* SSD residue P490, or removal of the cytoplasmic domains impairs activity, without disrupting oligomerisation

PTCHD1	318	INLTGGKYNSTF-LGVPFVMI	GHG	LYGT	FEM	SSWRK	TRE
PTCH1	488	CSLIGISFNAAATQVLPFLAI	G	V	V	D	D
DISP1	546	RVVFHFEFFPFMNLTAIIILV	G	I	G	A	D
PTCH2	444	CALLGITFNAAATQVLPFLAI	G	V	V	D	D
NPC1	675	FSYICLPLTLIVIEVIPFLVLA	V	A	V	G	V
ACRB	383	LAAFGFSINTLTMFG-MVLAIG	L	L	V	D	D
MEXB	383	LAAFGFSINTLTMFG-MVLAIG	L	L	V	D	D

Figure 3.1 RND protein ‘GxxxDD’ consensus sequence is present in several Hh pathway components.

Alignment of human PTCHD1, PTCH1, DISP1 and PTCH2 and *E. coli* ACRB and *P. aeruginosa* MEXB protein sequences. Red box highlights the GxxxDD consensus sequence. Sequence alignments were performed using the complete protein sequences, with the alignment tool on UniProt.org.

In RND proteins, these aspartic acid residues are believed to be important for proton translocation (Guan and Nakae, 2001a; Takatsuka and Nikaido, 2006). Interestingly, at least one of these residues is present and essential to the function of PTCH1, NPC1 and DISP1. Mutation of PTCH1 ‘D513’ and NPC1 ‘D700’ have been reported in cases of Gorlin Syndrome and Neimann-Pick disease C1 respectively (Taipale et al., 2002a; Dardis et al., 2020). Meanwhile, combined mutation of the aspartic acids at both locations in DISP1 produced a dominant-negative protein (Etheridge et al., 2010). Another aspartic acid residue, preceding the ‘GxxxDD’ consensus sequence by two positions, is predominantly found in divalent cation transporters. This residue is absent in all the aligned sequences in **(Figure 3.1)**, as expected for monovalent cation transporters (Perrin et al., 2010).

Chapter 3: Specific mutation of the Ptc1 SSD residue P490, or removal of the cytoplasmic domains impairs activity, without disrupting oligomerisation

NPC1 is known to regulate cholesterol transfer from lysosomal compartments to the ER in neuronal cells (Scott and Ioannou, 2004). This transfer is essential, shown by the severe neurodegenerative disorder, Neimann-Pick disease, resulting from miss-folding mutations in NPC1 (Shioi et al., 2020). A hallmark of this fatal neurodegenerative disease is giant accumulation of intracellular cholesterol (Sturleya et al., 2009). X-ray crystallography studies have provided the structure for a large segment of NPC1, revealing an exposed cavity within the SSD, predicted to accommodate a single cholesterol molecule (Li et al., 2016). In agreement, mutations specific to the SSD of NPC1 have been found to prevent binding to a photoactivatable cholesterol analogue (Ohgami et al., 2004).

This provides evidence of a conserved region, essential to the activity of bacterial RND proteins, within the SSD of several vertebrate proteins that are associated with cholesterol transport.

3.2 Aims and Hypothesis

Upon commencement of this PhD, the structure of Patched 1; the identity of its endogenous cargo; and its mode of action remained unknown. However, a recent publication of a protein homolog, NPC1, provided both a structural model and evidence of the involvement of Cholesterol transportation. I therefore hypothesised that key functional residues within Patched 1 might be identifiable through homology modelling with NPC1. In brief, by threading the secondary structure of patched 1 to the model of NPC1 (PDB ID code 5I31) overlapping mutational hotspots were located and promising residues selected (**Figure 3.2**). Targeted mutation of said residues could reveal their essential requirement.

Additionally, I aimed to assess whether Patched 1 employed an RND PMF mode of action in its function. Finally, with growing evidence of the functional importance of the cytoplasmic domains within Patched 1, I further hypothesised that they might play a role in the architecture of the protein monomer and higher oligomer states. This chapter is presented in chronological order, introducing the published findings of others to highlight their impact, where applicable. The key aims discussed are:

- I. Mutation of Ptc1 residues corresponding to NPC1 residues implicated in cholesterol transfer, to identify their requirement for Ptc1 canonical function.
- II. Generation of an intra-ciliary pH calibration curve, to measure fluctuations in H⁺ ion concentration, as a potential PMF action of Patched 1.
- III. Mutation of Ptc1 intracellular domains to detect any impact on oligomerisation and canonical function.

3.3 Results

3.3.1 Mutation of Ptc1 P490, corresponding to the NPC1 residue

P691, implicated in cholesterol transfer, had significant impact on canonical function

To establish whether Patched was a transporter of cholesterol, mutagenic screening was performed, utilising the structure of a recently elucidated homolog, NPC1. One structure of NPC1 published (PDB ID code 5I31), displayed a hydrophobic cavity within the SSD able to accommodate a molecule of cholesterol. Due to the overall similarity to Patched 1 and the highly conserved nature of the SSD, it was logical to model the secondary structure of Patched 1 to NPC1.

The secondary structure of PTCH1 was obtained from the NCBI database, and threaded into the published model of NPC1 (PDB ID code 5I31), using the freely available online software I-TASSER. Known disease mutations in both NPC1 and PTCH1 were mapped onto the published structure and threaded model respectively. This revealed a strong correlation between a hotspot of PTCH1 mutations and mutations in NPC1, located within close proximity to the proposed SSD cavity. Proximity analysis was implemented to identify probable interacting PTCH1 residues within 5 Å of these mutations (**Figure 3.2A**). Analysis showed several Ptc1 residues that had reported mutations also aligned to NPC1 residues with known disease causing mutations (**Figure 3.2B**).

A conservative mutational strategy was implemented in the substitution of Ptc1 residues. This was done to ensure side chains properties such as charge and

hydrophobicity remained similar. Mutations were made in the construct Ptc1-KR-His, which was originally generated for expression, purification and structural work. Briefly, Ptc1-KR-His contains the substitution K1413R, within the CTD, which results in increased plasma membrane accumulation and protein half-life (Chen et al., 2014). This substitution prevents the interaction and ubiquitination of Ptc1 by an HECT E3 ubiquitin-protein ligase, Itch. In frame with the end of the CTD is a Serine/Glycine linker, TEV cleavage site and a 10 x His stretch. Unless stated otherwise, all Ptc1 constructs described within **(Results 3.3.1)** contain the KR substitution and C-terminal His tag.

In total, three point mutants, P490A, L504A and F1109A, and one triple point mutant, A483L,A484I,T485N were generated, using Q5 Site directed mutagenesis. Sanger sequencing and western blotting for the C-terminal His-tag, confirmed successful production and expression of the three point mutants as well as the triple point mutant **(Figure 3.3B)**.

Comparison of protein expression in HEK293, by western blot, showed a slight reduction in expression of Ptc1-F1109A, confirmed by densitometry analysis **(Figure 3.3C)**. Meanwhile, the other three mutants displayed a similar protein expression profile to that of each other, and to the parental Ptc1. QPCR analysis also revealed comparable mRNA levels between the majority of the constructs. Despite displaying the lowest mRNA level, Ptc1-F1109A, was not significantly different to Ptc1 **(Figure 3.3 D)**. It was concluded that while all four mutants and the parental Ptc1 displayed similar mRNA levels, Ptc1-F1109A had slightly reduced protein expression, indicating reduced protein stability.

Chapter 3: Specific mutation of the Ptc1 SSD residue P490, or removal of the cytoplasmic domains impairs activity, without disrupting oligomerisation

To elucidate whether any of the mutations effected the subcellular localisation of Ptc1, transiently transfected HEK293 cells underwent immunocytochemistry and confocal imaging (**Figure 3.4**). No clear discrepancies in localisation or expression were observed between the four Ptc1 mutants and the parental Ptc1 construct.

The ability of Patched to form higher level oligomers has been well documented, but its relevancy to the functional output of the protein remains unclear. Through Co-immunoprecipitation experiments it was confirmed that this self-interaction was retained by all four of the mutant Ptc1 constructs (**Figure 3.5**). Each Ptc1 mutant was co-expressed with Ptc1-HA in HEK293 cells, which were subsequently subjected to immunoprecipitation with anti-His antibody. Due to the predicted location of the residues altered in these mutants, it was not expected that they would constitute part of the dimer interface(s).

However, owing to technical issues associated with the Co-IP and the limitations of Ptc1 construct epitope-tag combinations, a second experimental method was implemented to validate these findings. A FRET-based protein-protein interaction assay was designed (**Figure 3.6**) and subsequently validated in HEK293 cells and *Ptc1*^{-/-} MEFs, confirming PTCH1 homo-interactions (**Figure 3.8**). Briefly, an existing PTCH1-eGFP plasmid was used to generate PTCH1-mCherry, through a two-step cloning strategy. Protein expression and individual subcellular localisation of both PTCH1-eGFP and PTCH1-mCherry was determined to be comparable (**Figure 3.7A&B**). Co-localisation of the two constructs was confirmed by live cell imaging prior to FRET-based photo-bleaching analysis (**Figure 3.7C**).

Although *Ptc1*^{-/-} MEFs successfully displayed increases in GFP intensity after mCherry photo-bleaching, HEK293 cells produced a significantly greater change in GFP, despite the potential impediment of endogenous Patched 1 (**Figure 3.8C**). This increase was likely a result of greater expression and transfection in HEK293 cells. While *Ptc1*^{-/-} MEFs were the more suitable line for studying the Hh signalling pathway, these experiments were not intended to be performed within the cilia. Thus, HEK293 were favoured in the hopes that their larger fold-change in GFP intensity, could provide a greater dynamic range to distinguish differences in protein-protein affinities.

After initial validation that the FRET-based assay could successfully detect direct PTCH1-eGFP and PTCH1-mCherry interactions, it was modified for a competition-based assay. Co-transfection of both fluorescent PTCH1 plasmids and a 4-fold excess of non-fluorescent 'competitor' plasmid allowed semi-quantitation of changes in the abundance of fluorescently labelled dimers. To this end, full length *Ptc1* and the four mutant plasmids were found to significantly reduce the abundance of PTCH1eGFP-PTCH1mCherry dimers (**Figure 3.9**). When compared to a four-fold excess of pcDNA 3.1⁺, all *Ptc1* transfected cells showed reduced increases in GFP fluorescence intensity post mCherry bleaching (**Figure 3.9A**). Normalisation of mean post-bleach GFP intensity, to mean GFP pre-bleach intensity, confirmed a significant reduction in mean GFP for all four-fold *Ptc1* conditions to that of four-fold pcDNA 3.1⁺ (**Figure 3.9B**).

Due to the nature and predicted location of the altered residues, it was necessary to investigate the functionality of the *Ptc1* point mutants. Implementation of the Gli-luciferase assay tested the ability of the *Ptc1* mutants to; inhibit Gli

Chapter 3: Specific mutation of the Ptc1 SSD residue P490, or removal of the cytoplasmic domains impairs activity, without disrupting oligomerisation

transcription and; to bind and be sequestered by N-Shh. The assay was conducted in *Ptc1*^{-/-} MEFs, which lack active endogenous Ptc1, and display near maximal canonical hedgehog signalling at baseline. This afforded the ability to assess each mutant in a 'Ptc1 free' background, where homodimer interactions with a native Ptc1 would not be present.

All four Ptc1 mutants were found to significantly reduce the transcription of the Gli, compared to empty vector, pcDNA 3.1+ (**Figure 3.10A**). Notwithstanding this finding, the construct Ptc1-P490A displayed significant functional impairment, compared to full length Ptc1. Unlike P490, residues A483, A484, T485 and L504 appeared not to be required for the proposed small molecule trafficking function of Ptc1, despite their close proximity to the predicted 'cholesterol pocket'.

This finding was further supported by a Gli-luciferase assay with conditions co-transfected with N-Shh and each Ptc1 mutant (**Figure 3.10B**). Co-transfection of N-Shh significantly reduced Ptc1-driven inhibition of Gli, in all conditions except Ptc1-P490A. Gli levels from the co-transfection of N-Shh and Ptc1-P490A were in line with that of the other constructs, suggesting the lack of canonical inhibition had not impaired ligand binding.

Chapter 3: Specific mutation of the Ptc1 SSD residue P490, or removal of the cytoplasmic domains impairs activity, without disrupting oligomerisation

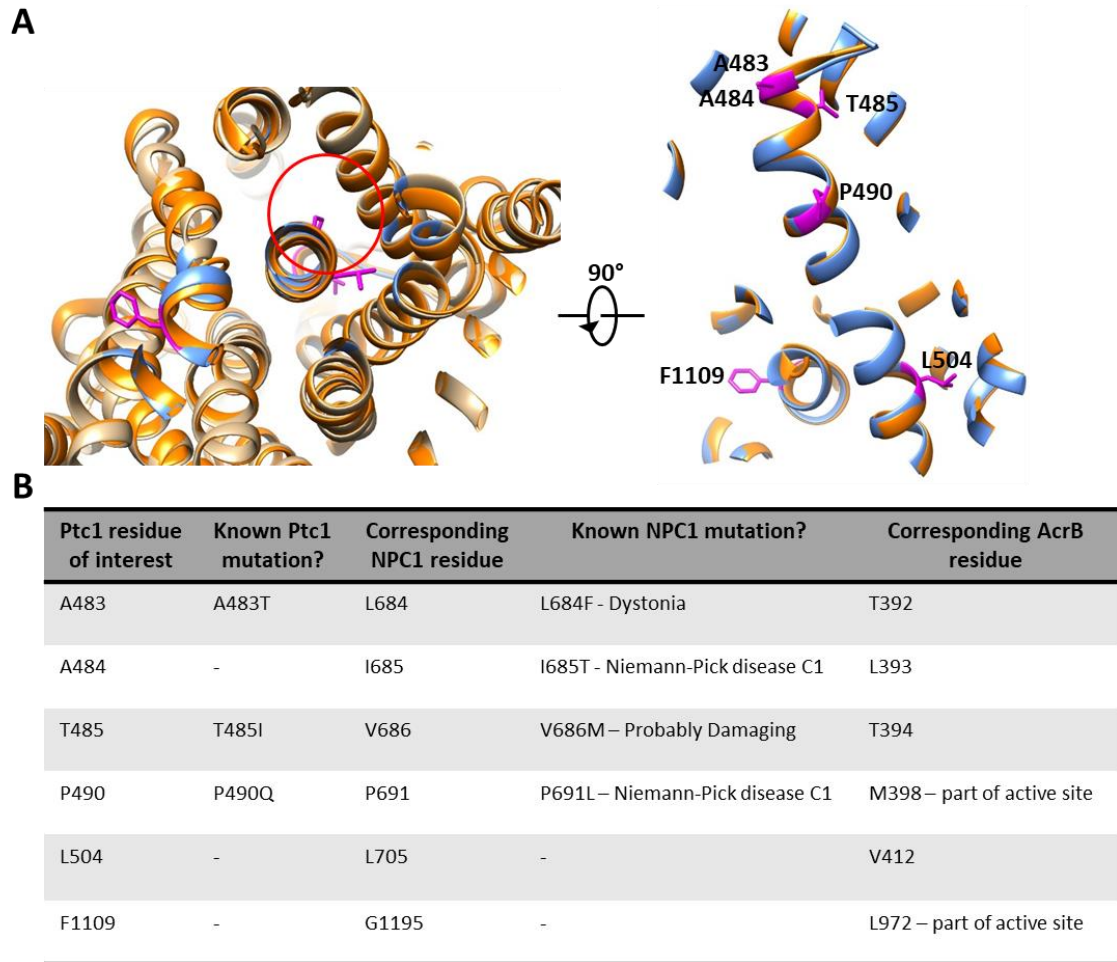


Figure 3.2 Identification of integral residues of Ptc1 through homology modelling to NPC1.

(A) Alignment of NPC1 (PDB ID: 5U73) shown in orange, against the secondary sequence of Ptc1, threaded through NPC1 (PDB ID: 5U73) shown in blue. Residues selected for mutational investigation are shown with side chains in magenta. Protein threading was performed in the online and template depository, Swiss-Model. Left: bottom up view of protein alignments, with the hydrophobic pocket of NPC1 indicated by a red circle. Right: restricted side view, depicting residues selected for mutational investigation. **(B)** Table detailing Ptc1 residues selected for mutational investigation with their corresponding residues in NPC1 and AcrB, identified by structural alignment.

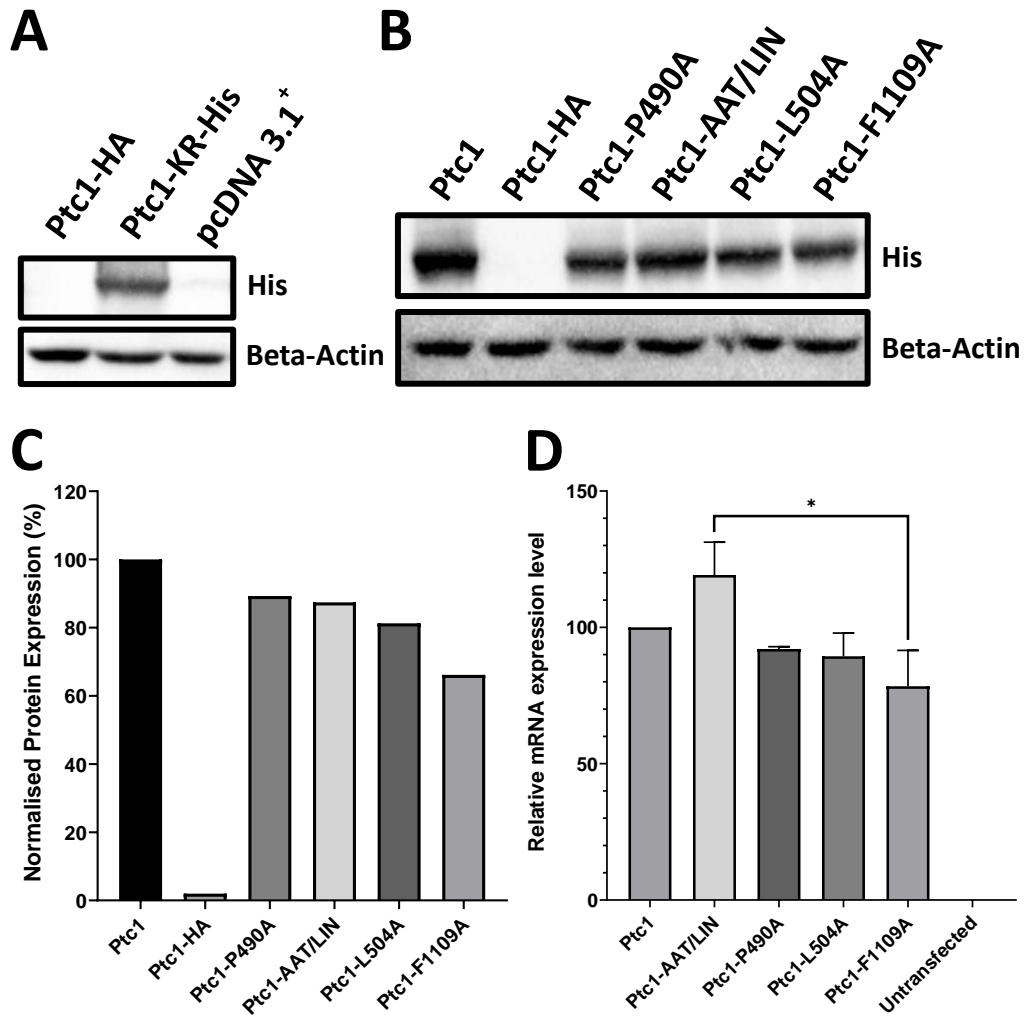


Figure 3.3 Ptc1-F1109A displayed reduced protein expression compared to full length Ptc1.

(A) Western blot confirming expression of Ptc1-KR-His in HEK293 cells, using anti-His antibody. Protein loading control anti-beta-actin confirmed total protein per lane. **(B)** Western blot confirming expression of Ptc1-KR-His point mutants; P490A, AAT/LIN, L504A, F1109A compared to full length Ptc1-KR-10xHis in HEK293 cells, using anti-His antibody. Protein loading control anti-beta-actin confirmed similar total protein per lane. **(C)** Densitometry of western blot of Ptc1 point mutations shown in (B), normalised to beta-actin. **(D)** qPCR showing relative mRNA expression of point mutant Ptc1-KR-10xHis constructs, normalised to full length Ptc1-KR-10xHis (n.3). GAPDH used as an internal control for total cDNA per well. Samples run in duplicate.

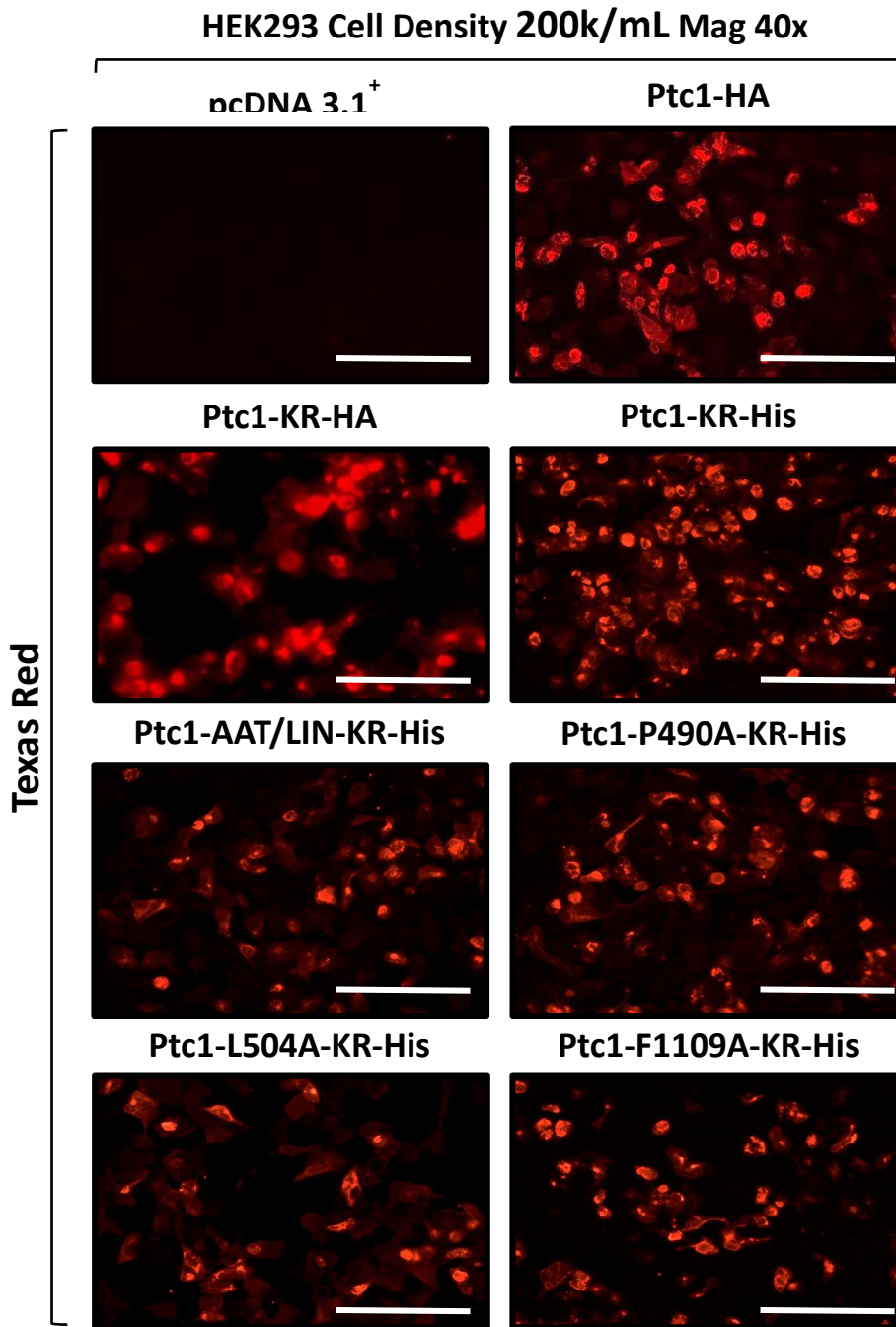


Figure 3.4 Immunocytochemistry revealed similar subcellular localisation and expression of Ptc1 mutants to wild type Ptc1.

Transiently transfected HEK293 cells were subjected to immunocytochemistry and imaged by EVOS fluorescent microscope. No obvious changes in subcellular localisation or protein expression level were seen either between the Ptc1 mutants or to that of the parental Ptc1 construct. Scale bar, 100 μ M.

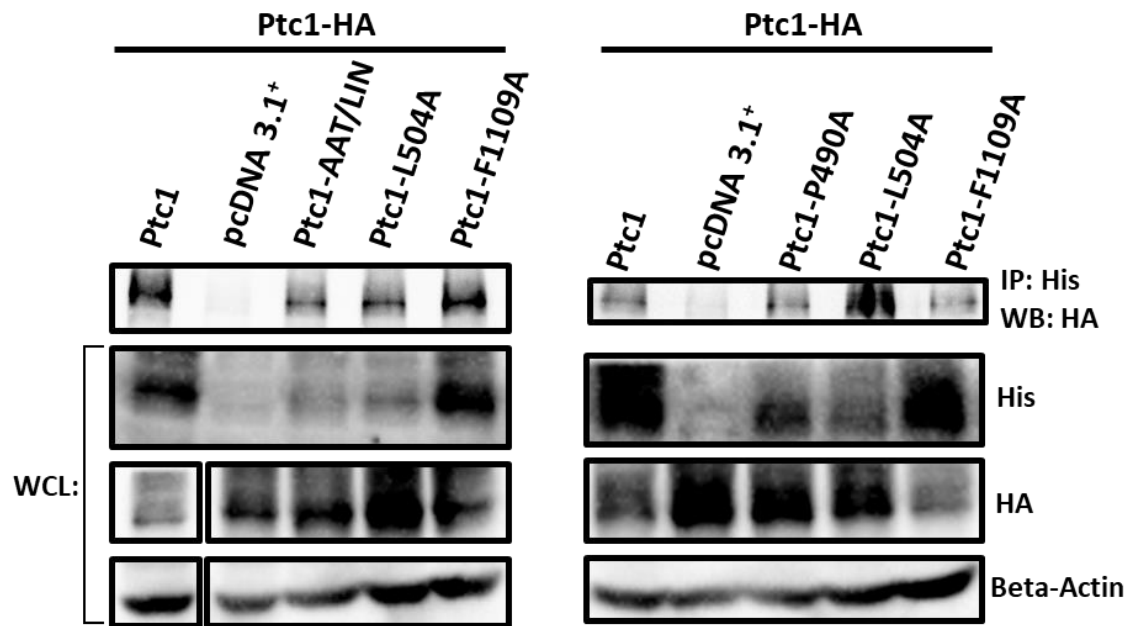


Figure 3.5 Co-IP confirmed full length and point mutants of *Ptc1* interact with full length *Ptc1*-HA in HEK293 cells.

HEK293 cells were co-transfected with *Ptc1*-HA and each of the *Ptc1* point mutants or pcDNA 3.1+. Cell lysates were subject to Co-IP with His antibody, to detect direct protein interactions with *Ptc1*-HA. IP lysates were probed with anti-HA antibody during western blotting. WCL's were run to determine relative input expression levels of each co-transfected plasmid. Total relative protein concentration was determined with anti-beta-actin loading control.

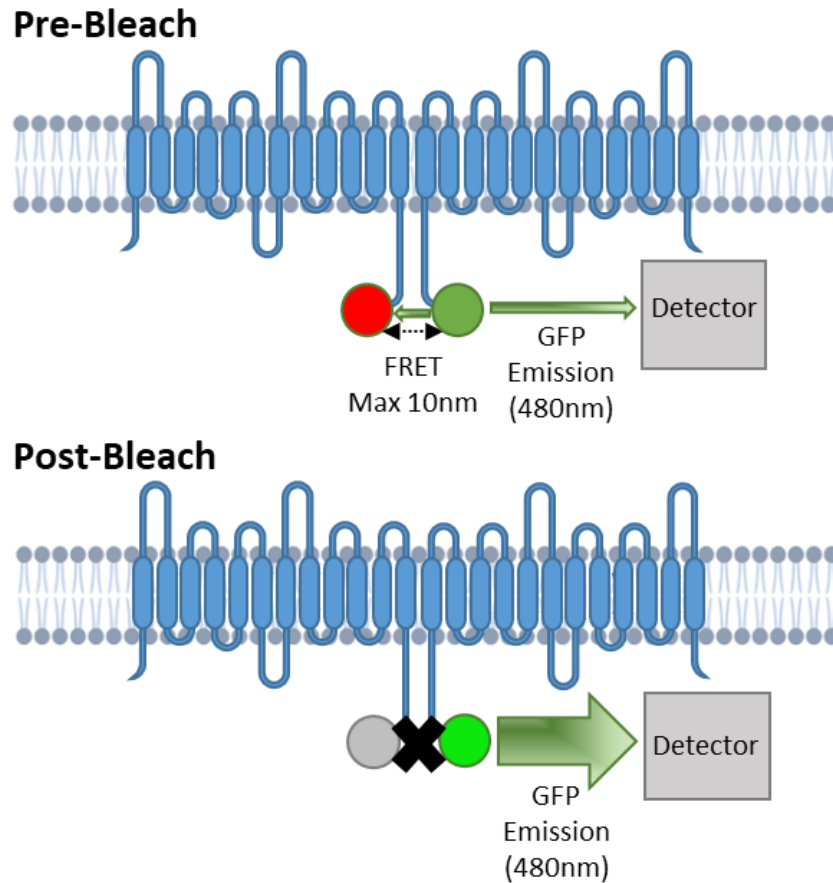


Figure 3.6 Mechanistic depiction of the Patched FRET-Based Assay.

Schematic depicting the FRET based assay, designed to detect direct patched protein interactions within live cells. Two Patched proteins, one containing a C-terminal mCherry and the other a C-terminal eGFP are co-expressed. If the two proteins directly interact, some emission energy from the eGFP is absorbed, through the excitation of mCherry. Photo-bleaching of mCherry prevents this excitation and the GFP emission energy previously absorbed by mCherry can be detected as additional post-bleach emission energy.

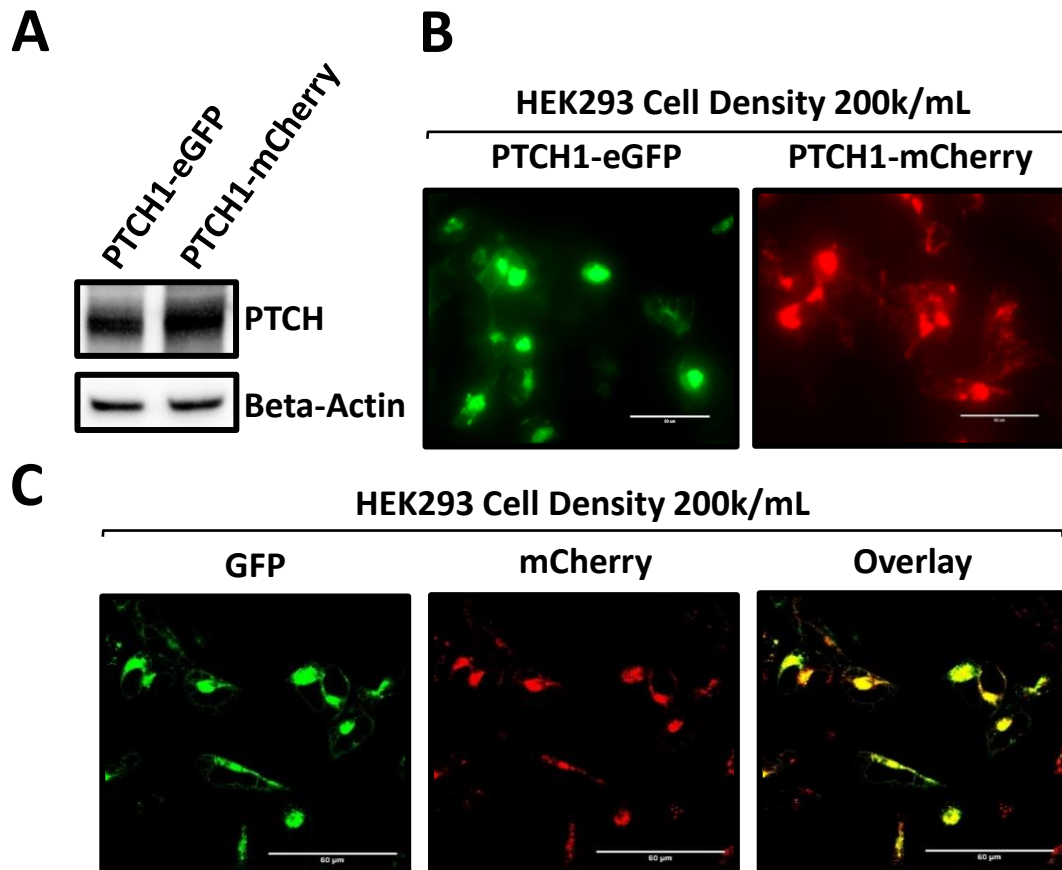


Figure 3.7 C-terminally fluorescently labelled PTCH1 monomers express and co-localise in HEK293 cells.

(A) Western blot confirming the expression of both PTCH1-eGFP and PTCH1-mCherry in HEK293 cells. **(B)** Live cell imaging (EVOS) of transiently transfected HEK293 cells, demonstrated a similar expression level and localisation of PTCH1-eGFP and PTCH1-mCherry. Scale bar, 50 μ M. **(C)** Live cell imaging (EVOS) of transiently co-transfected HEK293 cells, confirmed co-localisation of PTCH1-eGFP and PTCH1-mCherry. Scale bar, 60 μ M.

Chapter 3: Specific mutation of the *Ptc1* SSD residue P490, or removal of the cytoplasmic domains impairs activity, without disrupting oligomerisation

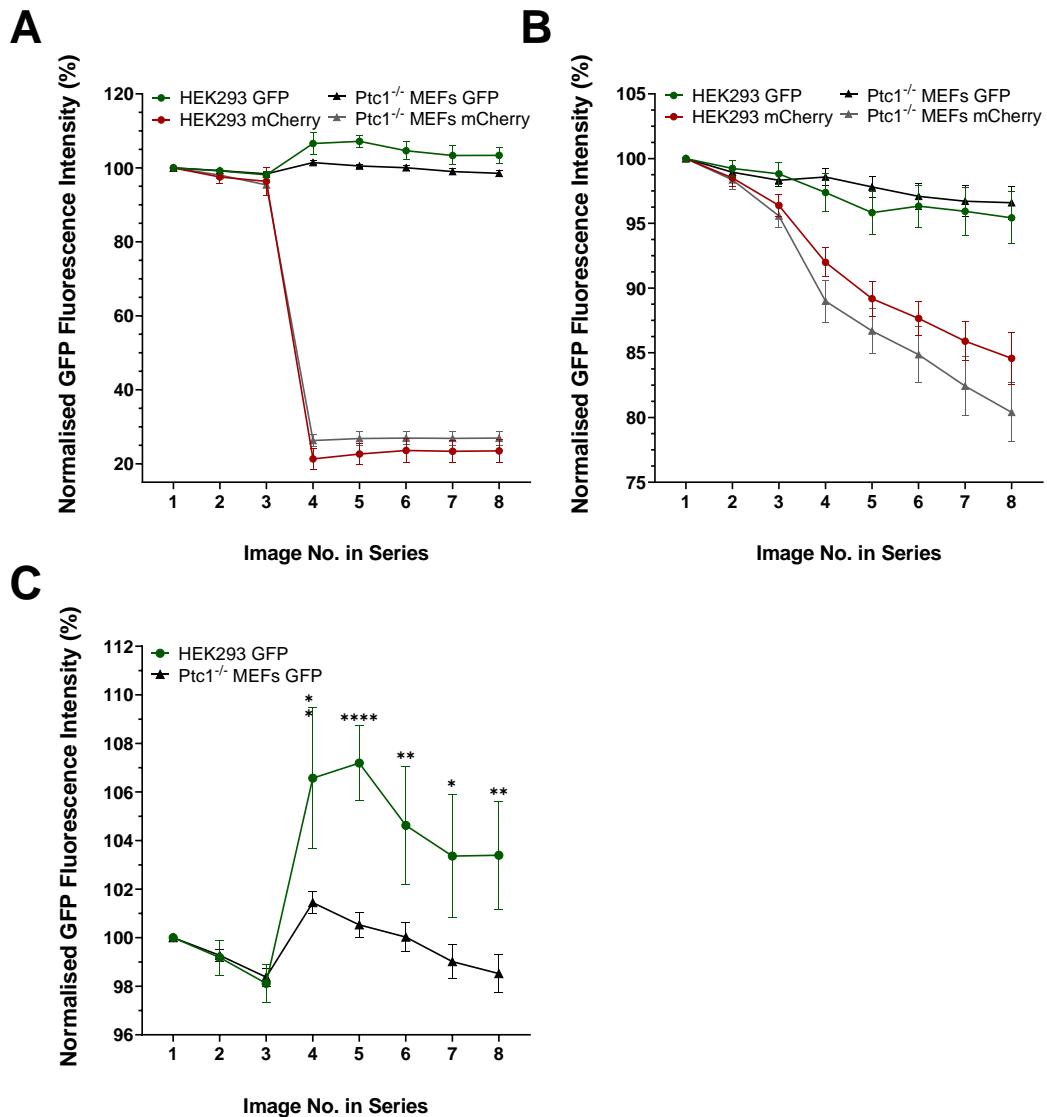


Figure 3.8 PTCH1 homo-interactions were confirmed by live cell FRET confocal imaging in HEK293 and *Ptc1*^{-/-} MEFs.

(A) HEK293 and *Ptc1*^{-/-} MEFs, transiently co-transfected with PTCH1-eGFP and PTCH1-mCherry, were subjected to confocal imaging with the FRET-based interaction assay. Emission of eGFP and mCherry was measured across 8 acquisitions, with ROIs photo-bleached with 100% 594 nm and 566 nm channels after the third image in the series. An increase in normalised GFP emission was detected in both cell lines after bleach, confirming protein interactions. **(B)** Control fluorescence, obtained from ROIs not subjected to photo-bleaching displayed no increase in GFP emission intensity across the image series. **(C)** Extract of normalised GFP fluorescence intensity data from (A). GFP intensity increase post bleach was significantly greater in HEK293 compared to *Ptc1*^{-/-} MEFs.

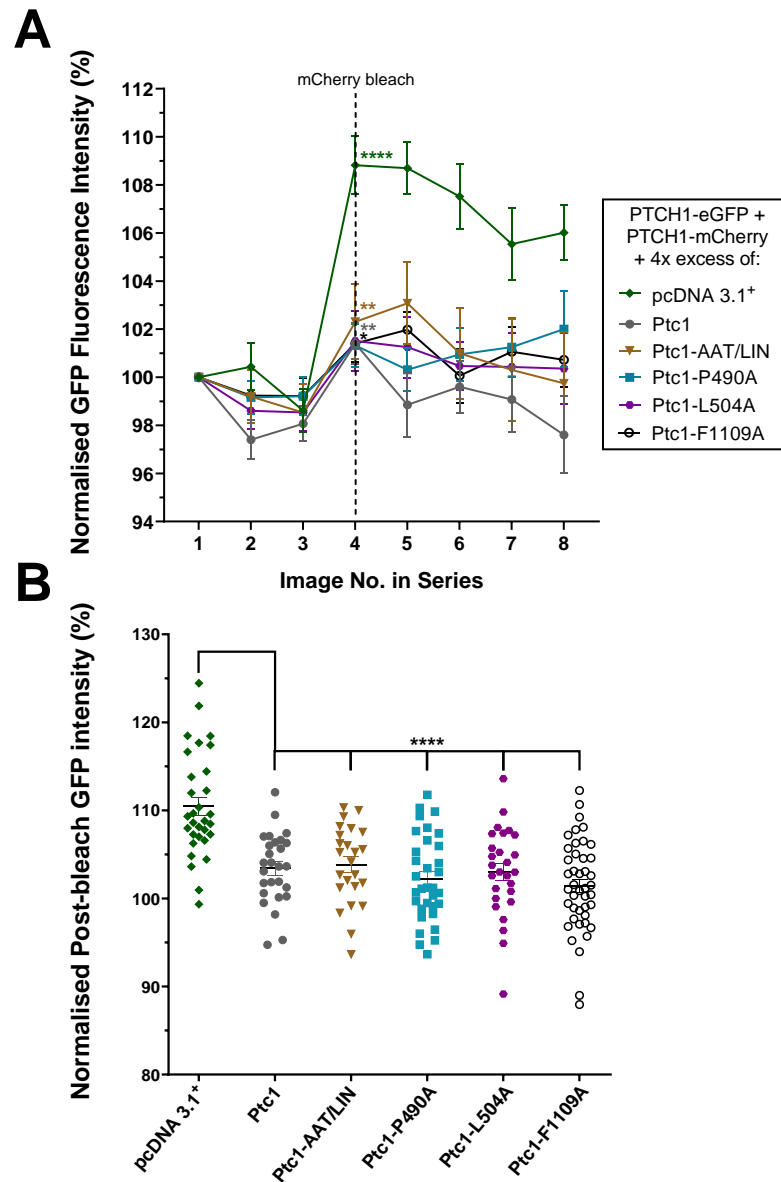


Figure 3.9 Competition-Based FRET assay in HEK293 cells confirmed all *Ptc1* point mutants can form homo-dimers with PTCH1.

(A) Normalised GFP fluorescence emission intensity of PTCH1-eGFP revealed significantly diminished FRET after the photo-bleaching of PTCH1-mCherry, when co-transfected in the 4 x excess of any *Ptc1*-KR-His plasmid but not pcDNA 3.1⁺. **(B)** Separated Scatter graph of post photo-bleach GFP emission intensity, normalised to pre photo-bleach emission intensity. A 4x excess of pcDNA 3.1⁺ showed significantly higher post bleach GFP fluorescence intensity compared to all *Ptc1*-KR-His constructs, strongly indicating their ability to outcompete PTCH1-eGFP and PTCH1-mCherry interactions.

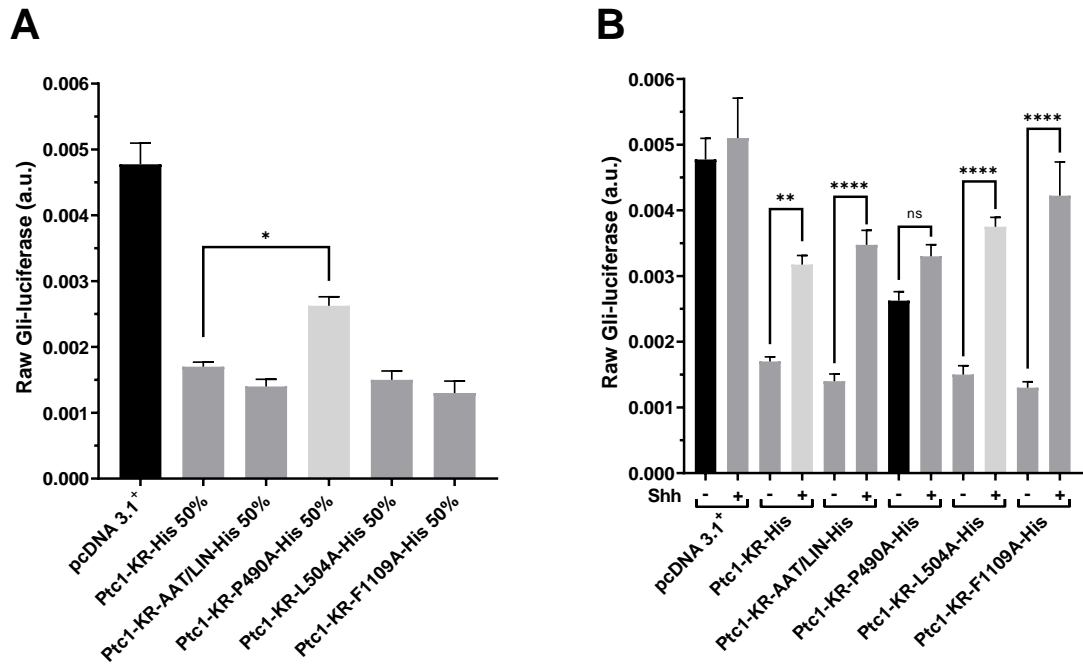


Figure 3.10 Ptc1-P490A displayed impaired inhibition of canonical signalling.

Ptc1^{-/-} MEFs, co-transfected with luciferase reporter constructs and either full length or point mutants of Ptc1-KR-His, were subjected to Gli-luciferase assay. Graphs displayed are a single representative experiment, performed with quadruplicate technical repeats. **(A)** Luciferase-renilla ratios indicated that whilst all Ptc1 constructs displayed significant inhibition of Gli, compared to pcDNA 3.1⁺, Ptc1-P490A showed significantly reduced activity compared to full length Ptc1-KR-His. **(B)** Additional co-transfection of N-Shh significantly reduced Ptc1 inhibition of Gli in all conditions except Ptc1-P490A.

3.3.2 Activation of canonical Hedgehog signalling does not induce significant changes in ciliary pH

The active expulsion or mobilisation of small molecule cargoes, requires either energy or a molecular exchange, down opposing concentration gradients. If Patched 1 inhibits Smo, by expelling or mobilising an endogenous small molecule agonist, it is likely to utilise an ion in the process. The RND protein family rely on H⁺ ions to extrude molecular cargoes from the cytoplasm and periplasm, into the extracellular space. Due to the similarities between Patched and this protein family, a possible mode of action could involve H⁺ ions.

To determine whether Patched 1 employed H⁺ ions in its inhibitory regulation of Smo, a ratio-metric fluorescent pH probe, 5HT₆-CFP-Venus(H148G) was utilised (**Figure 3.11A**). In brief, the probe is transfected and localises to the primary cilium, through the N-terminal 5HT₆ serotonin receptor sequence. A C-terminal pH sensitive Venus(H148G) fluorophore becomes increasingly quenched as ciliary H⁺ ion concentration increases. Meanwhile, a pH insensitive CFP fluorophore is used to generate a ratio of Venus(H148G)/CFP intensity.

A pH calibration curve was generated by obtaining fluorophore intensity ratios, across a range of artificially induced intra-ciliary pH (5.0-8.0) (**Figure 3.11C**). To achieve this, IMCD-3 cells were transiently transfected with the pH probe and serum starved, to induce ciliation. Prior to confocal imaging, cells were incubated in cell media at adjusted pH and buffered with 25 mM HEPES. The addition of two ionophores, monensin (5 µM) and nigericin (5 µM) effectively permeabilised cellular membranes, equilibrating intra-ciliary pH to that of the external media. All

Venus(H148G)/CFP ratios acquired at the different standard pH were normalised against ratio values obtained at pH 7.4.

Next, to quantitatively measure whether Hh pathway activation altered ciliary pH, IMCD-3 cells were stimulated with N-Shh (2.5 ng) or vehicle control for 30 m prior to imaging. During N-Shh experiments, cells were maintained un-permeabilised, in 0.5% FBS starvation media. Normalisation of ratios obtained for N-Shh (2.5 ng) and control, against the standard pH 7.4, revealed stimulation produced a small shift in intra-ciliary pH, towards a more alkaline environment (pH 7.04 to 7.23). However, the mean change in normalised ratio value between the two groups was not significant.

This finding was inconclusive, but might indicate a subtle change in ciliary pH via pathway activation. Moreover, the direction of the shift in pH agreed with the notion that Patched 1 is expelling a cargo, whilst internalising H⁺ ions. Another possibility is that Patched 1 does not utilise H⁺ ions, but perhaps Na⁺ or K⁺ ions. The movement of these ions has been implicated in small changes of cellular pH. Cells expressing a non-functional Na⁺,K⁺-ATPase (S23A) displayed increased intracellular pH (Belusa et al., 1997). Moreover, the reported change in pH was of a similar magnitude to that described here.

A caveat of this experimental approach arises from the highly dynamic nature of the cilium. Resting ciliary pH between ciliated cells in the same conditions was variable, and ratio measurements even fluctuated along the shaft of individual cilia. Distinct zones of protein localisation are often seen in the primary cilia, so this might explain this observation. The highly concentrated, dense protein

Chapter 3: Specific mutation of the Ptc1 SSD residue P490, or removal of the cytoplasmic domains impairs activity, without disrupting oligomerisation

environment of the cilia undoubtedly results in cross-talk between signalling pathways and somewhat compounded the experimental limitations.

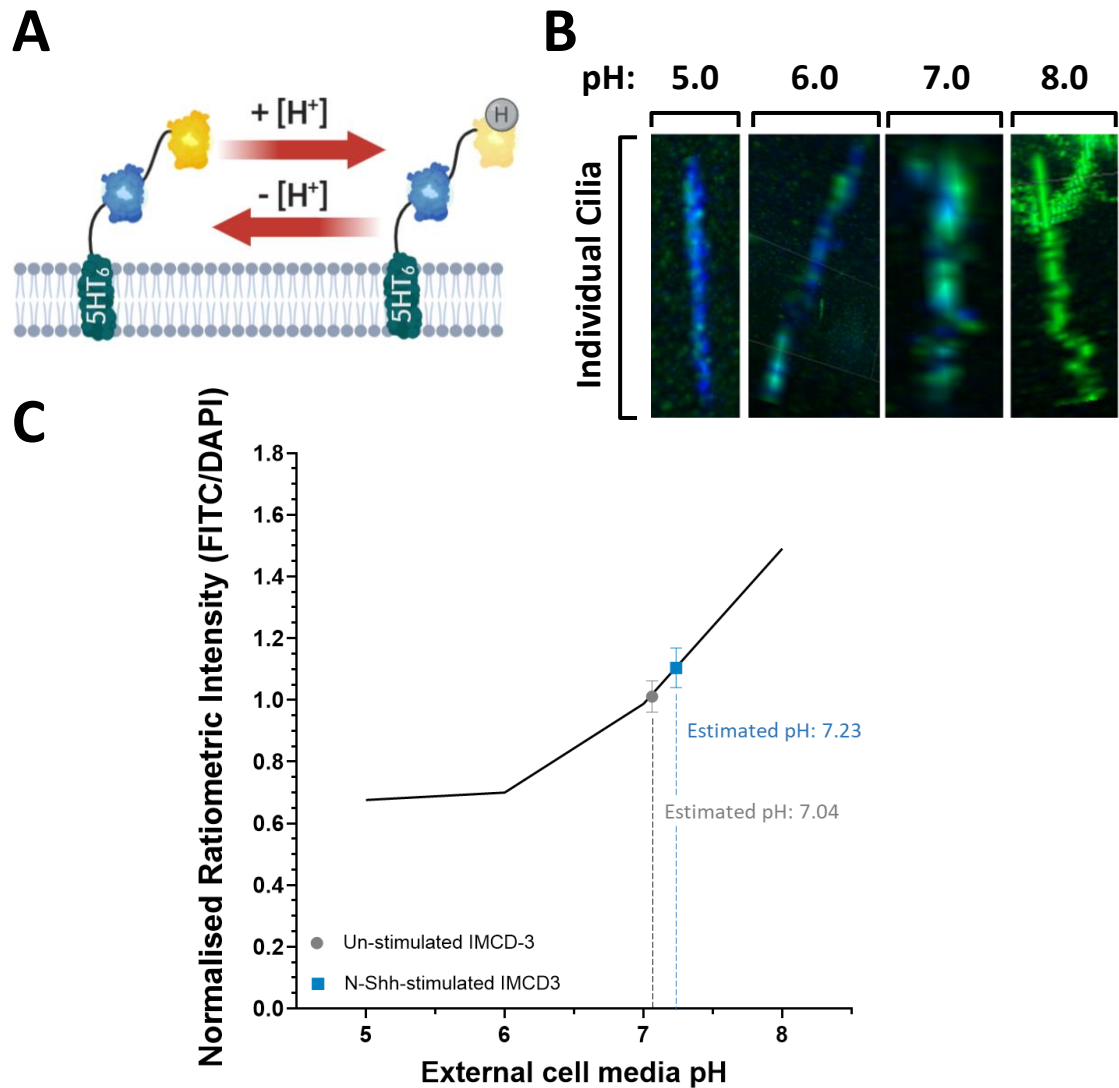


Figure 3.11 Activation of Hh signalling does not significantly alter ciliary pH

(A) Schematic of the ratio-metric pH sensor probe. The probe is localised to the plasma membrane of the primary cilia through the 5HT₆ serotonin receptor. Fluorescence from a pH insensitive tethered CFP and pH sensitive Venus(H148G) probe are measured to generate a ratio of YFP/CFP. An intracellular increase in H⁺ quenches Venus(H148G), producing a smaller ratio value. **(B)** Volume view of representative individual cilia of IMCD-3 cells, transfected with 5HT₆-CFP-Venus, permeabilised with monosin and nigericin (5 μ M) and incubated in media of differing pH. **(C)** pH calibration curve generated by ratio-metric measurements of permeabilised IMCD-3 at pH 5, 6, 7 and 8 and normalised to values at pH 7.4. Stimulation of non-permeabilised IMCD-3 with N-Shh (2.5 ng) did not show a significant increase in ciliary pH.

3.3.3 Removal of the two cytoplasmic domains of Patched 1 reveals a mutual dependency for stable expression.

Although expected, the lack of impairment to oligomerisation by the Ptc1-KR-His mutations, indicated a broader mutational strategy was required to investigate oligomerisation further. Targeting of the two most intrinsically disordered and evolutionary flexible regions of Ptc1, the large cytoplasmic loop and the C-terminal domain, could provide greater functional insight.

To this end, three Ptc1 domain deletion mutants, Ptc1- Δ ML-HA, Ptc1- Δ ML- Δ C-HA and Ptc1- Δ C-HA were utilised. Both Ptc1- Δ ML-HA and Ptc1- Δ ML- Δ C-HA were generated by Q5 SDM of Ptc1-HA and Ptc1- Δ C respectively. Successful removal of the middle loop was confirmed by Sanger sequencing. The generated constructs lacked the entirety of the middle cytoplasmic loop, with TM6-7 essentially directly fused. Both Ptc1- Δ ML- Δ C-HA and Ptc1- Δ C-HA had a truncated CTD, terminating after the third residue, F1164. Please refer to the Ptc1 hierarchical tree, for a visualisation of the plasmid mutations and their lineage (**Figure 2.2**).

Initial expression tests in HEK293, via western blot, revealed substantial differences between the domain mutants (**Figure 3.12**). Whilst Ptc1-HA and Ptc1- Δ ML- Δ C-HA displayed comparable expression levels, both the single domain mutants, Ptc1- Δ C-HA and Ptc1- Δ ML-HA, showed near undetectable expression levels (**Figure 3.12A**). The apparent discrepancy between protein expression is most likely due to increased protein miss-folding, or reduced protein stability of the single domain mutants.

Chapter 3: Specific mutation of the Ptc1 SSD residue P490, or removal of the cytoplasmic domains impairs activity, without disrupting oligomerisation

The fact that the combined removal of both domains restored protein expression to that of full length Ptc1, suggests a co-dependency of the cytoplasmic domains. Whether this relationship extends beyond protein processing, to the mature protein, remains unclear. However, despite a reduced overall expression, the level of Ptc1- Δ C-HA was found to remain relatively stable between 24-48 h post transfection (**Figure 3.12B**). Sub-cellular localisation immunocytochemistry experiments agreed with the western blot findings (**Figure 3.13**). Both Ptc1-HA and Ptc1- Δ ML- Δ C-HA showed the highest expression level, with similar localisation patterning. The two single domain mutants showed greatly reduced expression.

Several structural publications of Patched 1 have subsequently supported this evidence of increased protein stability, when the majority of the cytoplasmic domains were removed (Zhang et al., 2018; Gong et al., 2018). As a result, two additional Patched 1 domain mutants were generated in the PTCH1-eGFP plasmid, specifically for use in FRET-based dimerization assays. The middle loop deletion, PTCH1-9:18ML-eGFP removed all but the first 9 and last 18 amino acids of the middle loop. Whilst the double mutant, PTCH1-9:18ML-11CTD-eGFP had a further deletion encompassing of all but the first 11 amino acids in the CTD.

In contrast to Ptc1- Δ ML-HA, PTCH1-9:18ML-eGFP displayed strong expression via western blot and immunofluorescence (**Figure 3.14**). Furthermore, both PTCH1-9:18ML-eGFP and PTCH1-9:18ML-11CTD-eGFP showed greater expression and increased membrane localisation than full length PTCH1-eGFP (**Figure 3.14**). Both the middle loop and CTD harbour an HECT E3 ubiquitin-protein ligase binding motif 'PPXY' which is directly related to Patched 1 turnover

Chapter 3: Specific mutation of the Ptc1 SSD residue P490, or removal of the cytoplasmic domains impairs activity, without disrupting oligomerisation

in the presence and absence of ligand. It is likely that the observed increased in protein stability and expression for the domain deletions is a result of the absence of these motifs (Yue et al., 2014; Chen et al., 2014).

The contrasting expression levels of Ptc1- Δ ML vs PTCH1-9:18ML appear to be directly linked to the differing severity of the deletions. Ptc1- Δ ML was the most severe deletion and displays undetectable expression. The fusion of TM6-7 is likely to have produced dramatic alteration in protein topology, however this was essentially rescued by Ptc1- Δ ML Δ C. PTCH1-9:18ML retained a linking region between TM6-7, but removed the region harbouring the 'PPXY' motif and has increased expression as expected. The corresponding mutant to Ptc1- Δ C, PTCH1-11CTD-eGFP, was not generated during this work, but its future inclusion would aid in understanding how and why the 4th to 11th residues of the CTD are important to protein expression.

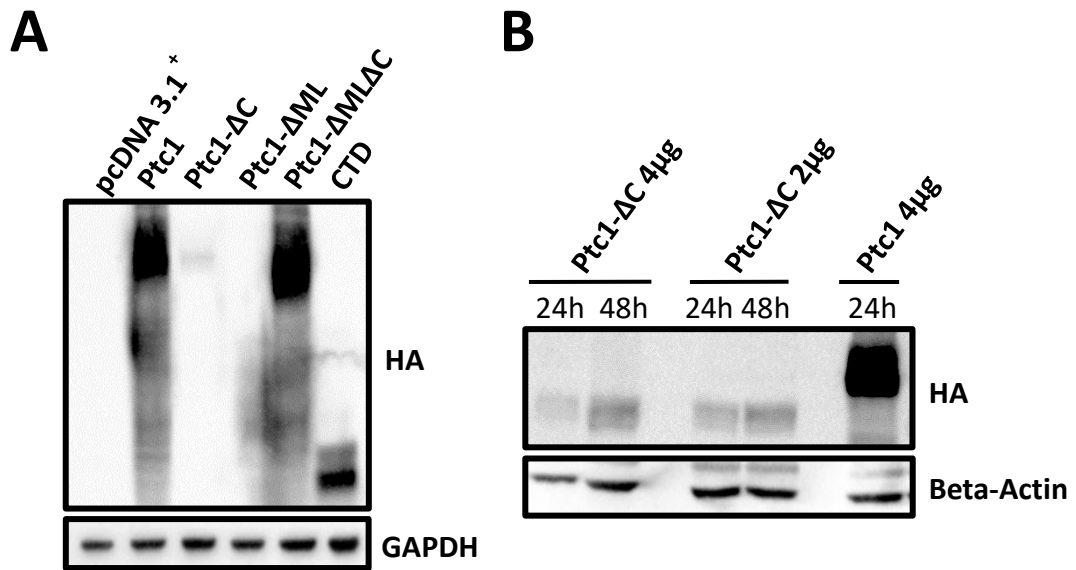


Figure 3.12 Individual removal of either Ptc1 cytoplasmic domain impairs protein expression, whilst combined removal restores protein expression.

(A) Single intracellular domain Ptc1 mutants display severely reduced protein expression via western blot of transiently transfected HEK293 cells. Full length Ptc1 and the double domain mutant, Ptc1-ΔMLΔC, exhibited similar expression.

(B) Time course of Ptc1-ΔC expression in transiently transfected HEK293 cells. Western blot with anti-HA antibody demonstrated a considerably lower level of expression compared to full length Ptc1.

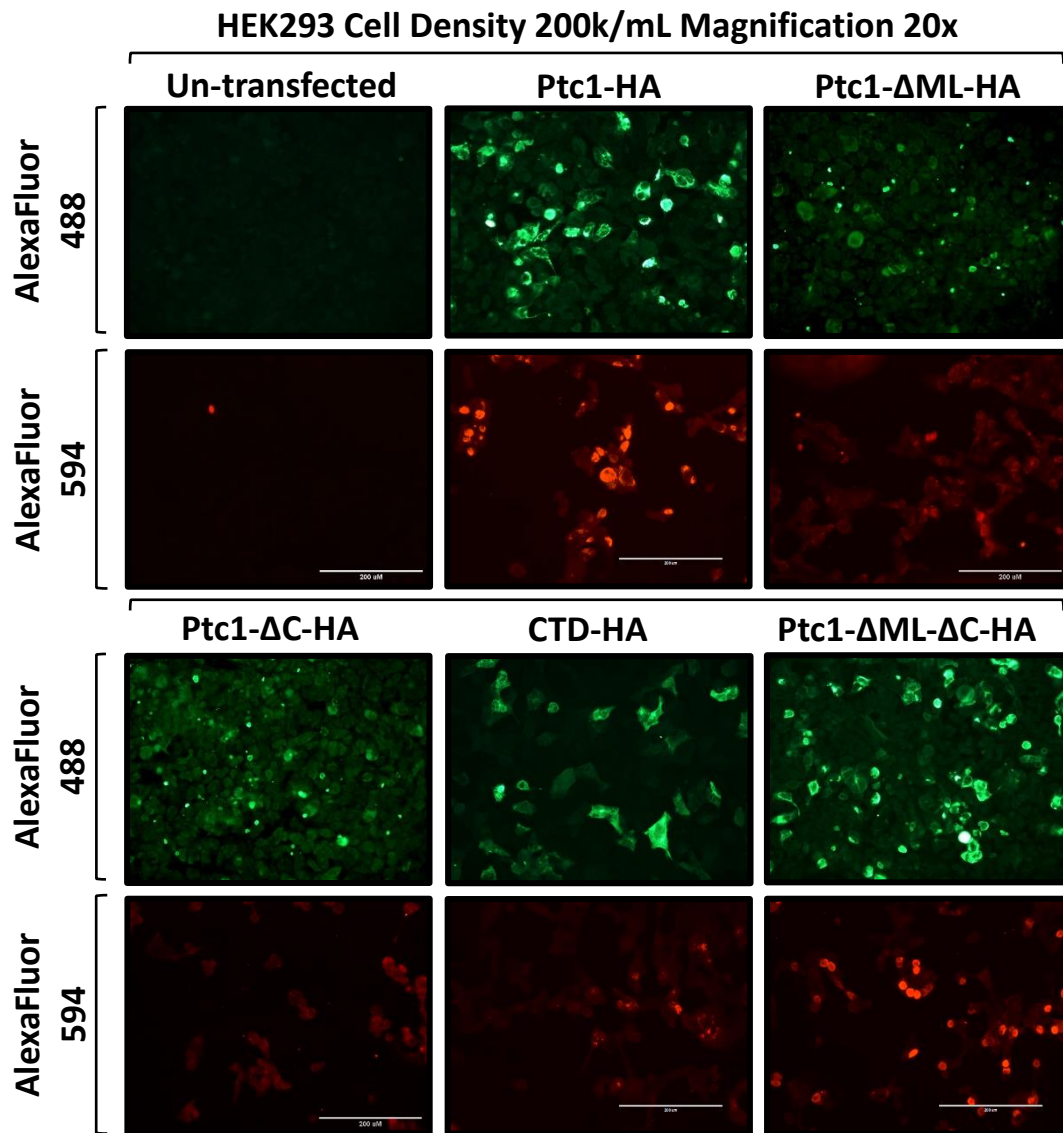


Figure 3.13 Removal of a single intracellular domain leads to impaired Ptc1 protein maturity and expression.

Immunofluorescence of fixed HEK293 cells, transiently transfected with full length and domain mutant Ptc1-HA constructs. Imaging was conducted on an EVOS fluorescent light microscope, magnification 40x, using Texas red (AlexaFluor 594) and FITC (AlexaFluor 488) filters. Imaging revealed a similar expression level for Ptc1-HA and Ptc1-ΔMLΔC-HA, but reduced expression for Ptc1-ΔML-HA and Ptc1-ΔC-HA. Antibody combinations: FITC: rabbit anti-HA (Proteintech) and Goat anti-rabbit AlexaFluor 488 (Invitrogen), Texas red: mouse anti-HA (Proteintech) and Rabbit anti-mouse AlexaFluor 594 (Invitrogen).

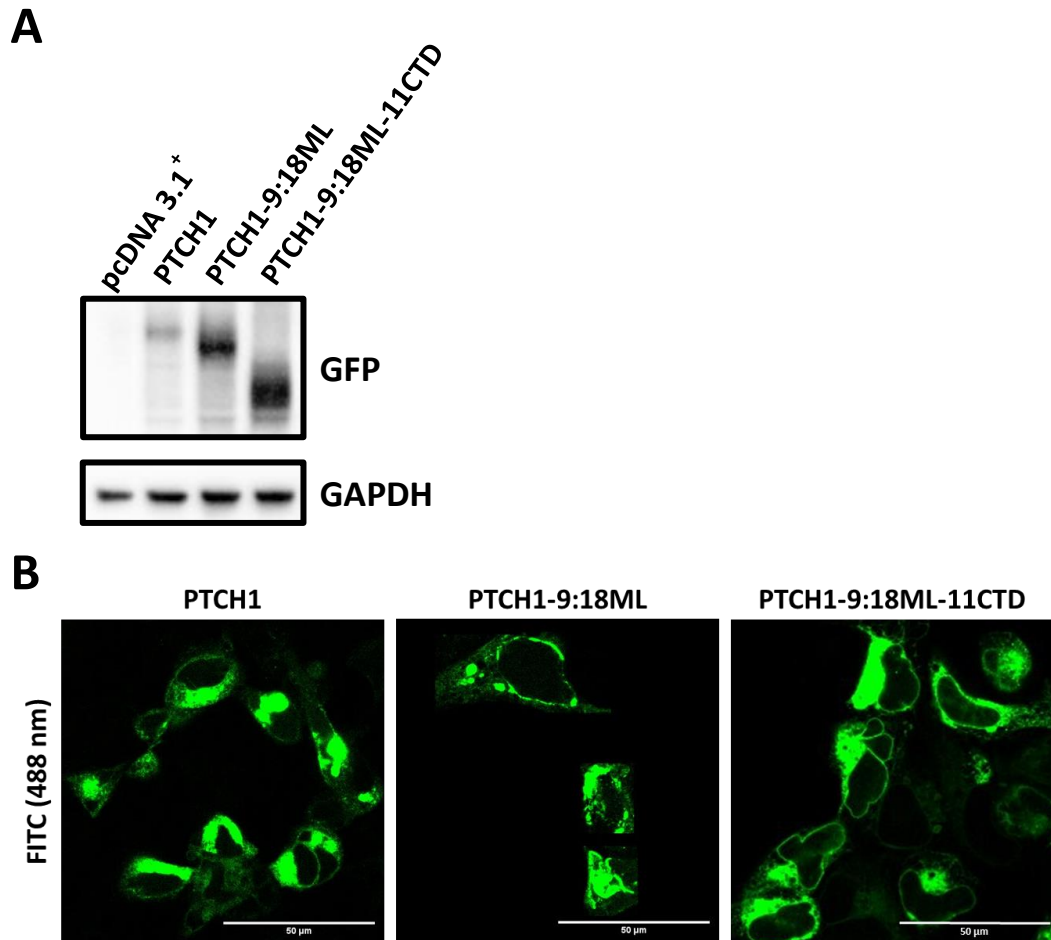


Figure 3.14 Large deletions of the cytoplasmic domains increase PTCH1 expression and membrane localisation.

(A) Removal of the majority of the middle loop alone or in combination with the CTD increased protein abundance via western blot. **(B)** Live cell fluorescence showed PTCH1 membrane localisation increased with the removal of the middle loop and CTD.

3.3.4 The middle loop and CTD are not required for Patched 1 self-oligomerisation.

Co-IP experiments were implemented to assess the ability of the more stably expressed domain mutants to interact with myc-PTCH1. The results confirmed that removal of either the middle loop alone, or in combination with the CTD, did not impede association with myc-PTCH1 (**Figure 3.15**). Myc-PTCH1 successfully co-precipitated PTCH1-9:18ML, PTCH1-9:18ML-11CTD and Ptc1- Δ ML Δ C, along with their corresponding full length proteins. There was an evident reduction of both myc-PTCH1 and Ptc1- Δ ML Δ C when co-expressed, which was not seen with the other plasmids. This most likely pertains to protein folding and maturation issues experienced by Ptc1- Δ ML Δ C, which is in turn, exerted onto myc-PTCH1 through their interaction.

To support this Co-IP data and to gain additional insight into structural influences of the cytoplasmic domains, both PTCH1-eGFP domain mutants were analysed by the same FRET-based assay previously described in Chapter 3 (**Results 3.3.1**). In agreement with Co-IP results, PTCH1-9:18ML was found to directly interact with co-transfected PTCH1-mCherry in HEK293 cells (**Figure 3.16**). A direct interaction was also observed between PTCH1-mCherry and PTCH1-9:18ML-11CTD (**Figure 3.17**). Both PTCH1-eGFP cytoplasmic domain mutants displayed a significant increase in normalised GFP fluorescence intensity, post photo-bleaching of PTCH1-mCherry, indicative of a FRET interaction between fluorophores <10 nm apart. However, PTCH1-9:18ML showed a significantly larger increase in GFP intensity post-bleach compared to PTCH1-9:18ML-11CTD (**Figure 3.16**) vs (**Figure 3.17**).

Chapter 3: Specific mutation of the Ptc1 SSD residue P490, or removal of the cytoplasmic domains impairs activity, without disrupting oligomerisation

There are several explanations for a difference in GFP intensity; the GFP fluorophore at the end of a truncated CTD might be better shielded by the core of the protein; the truncation of the CTD might increase the physical distance between the interacting CTDs and/or; the removal of the CTD might alter co-localisation rates with PTCH1-mCherry. Interestingly, the extent of PTCH1-mCherry photo-bleaching in conditions co-transfected with PTCH1-9:18ML-11CTD, was less than in co-transfections with PTCH1-9:18ML (data not shown). This reduction in PTCH1-mCherry bleaching is probably the cause of the reduced increase in GFP fluorescence intensity of PTCH1-9:18ML-11CTD. This finding is most suggestive of a shielding effect occurring in this condition. Increased shielding could be a result of the truncated CTD physically altering the location of the CTDs interaction between the PTCH1 monomers. An interaction closer to the protein transmembrane core could somewhat obscure the fluorophores from photo-bleaching.

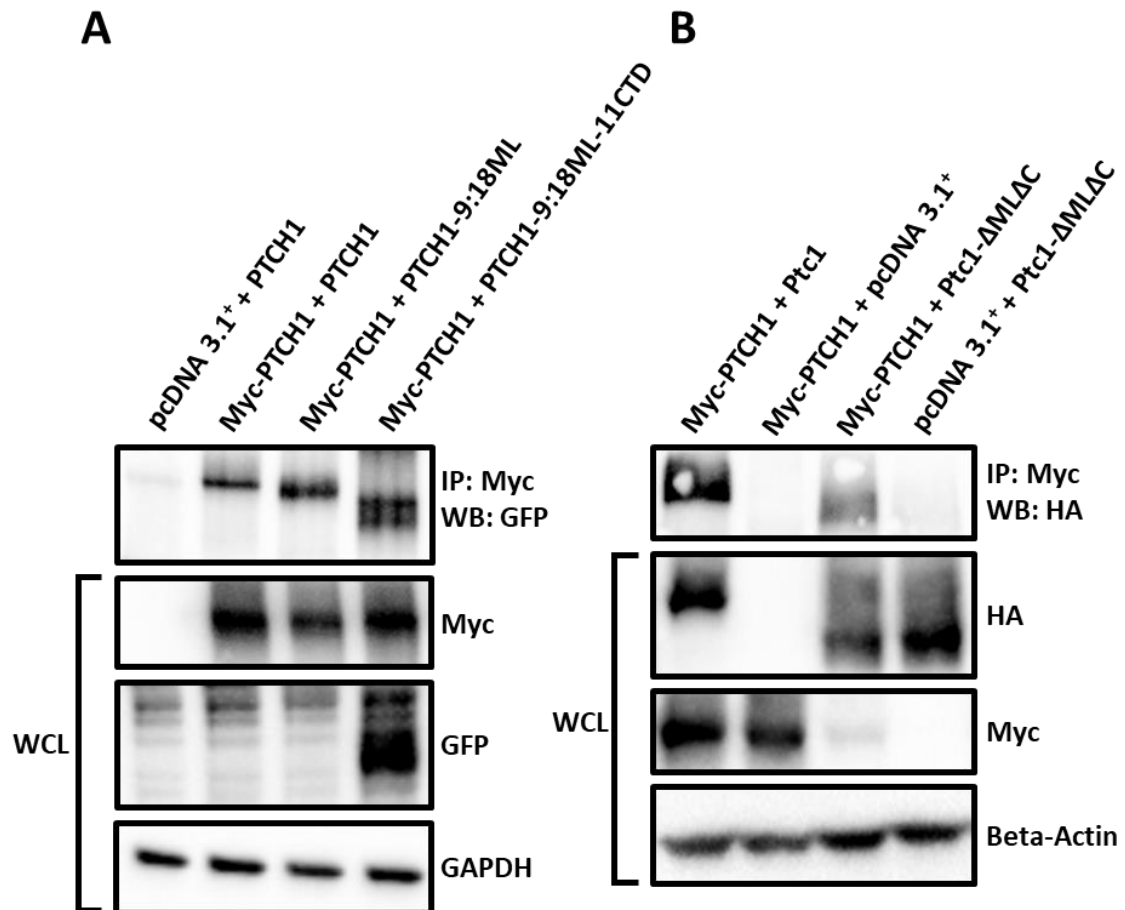


Figure 3.15 Removal of the middle and C-terminal cytoplasmic domains of Ptc1 does not disrupt direct interaction with full length PTCH1.

(A) Co-IP of full length or cytoplasmic domain mutants of PTCH1-eGFP via co-transfection with myc-PTCH1 or pcDNA 3.1⁺. Cell lysates were probed with anti-Myc (proteintech) and immobilised on dynabeads. Subsequent western blot of eluted fractions were probed with proteintech anti-GFP. WCLs were blotted to determine expression levels of each transfected construct. Proteintech anti-GAPDH was used as a total protein loading control. **(B)** Co-IP of full length or double cytoplasmic domain mutant of Ptc1-HA via co-transfection with myc-PTCH1 or pcDNA 3.1⁺. Cell lysates were probed with anti-Myc (proteintech) and immobilised on dynabeads. Subsequent western blot of eluted fractions were probed with proteintech anti-HA. WCLs were blotted to determine expression levels of each transfected construct. Cell Signalling technologies anti-Beta-Actin was used as a total protein loading control.

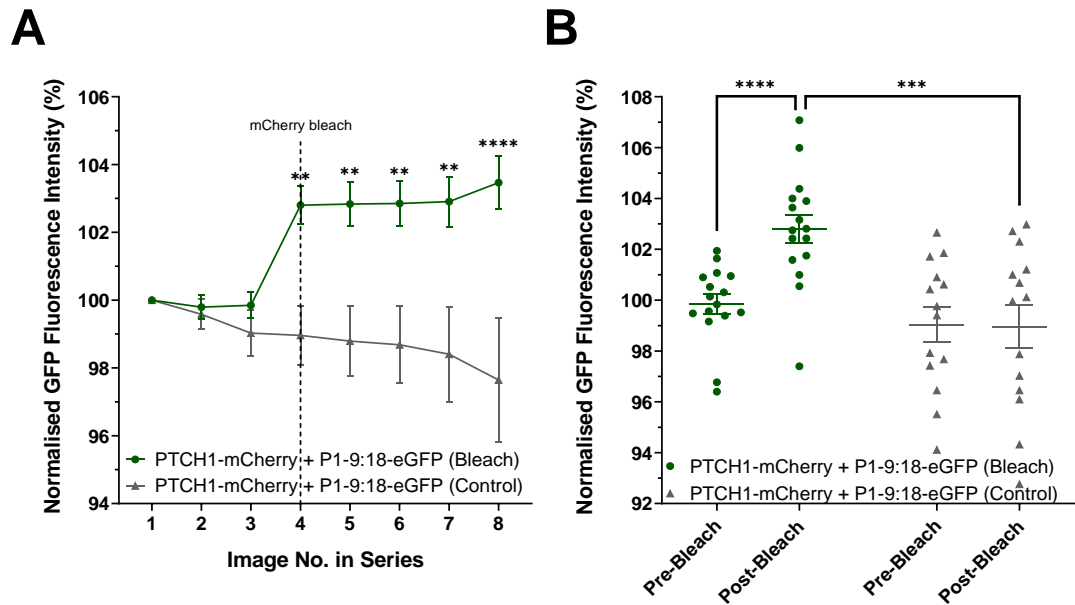


Figure 3.16 Removal of the middle cytoplasmic loop is not sufficient to disrupt PTCH1 homo-interactions.

(A) FRET analysis of HEK293 cells, transiently transfected with PTCH1-mCherry and PTCH1-9:18ML-eGFP (Each data point represents the average +/- SEM of 16 GFP and 14 control individual ROIs). Upon PTCH1-mCherry photo-bleaching after acquisition of image 3 (100% 564 nm and 594 nm) PTCH1-9:18ML-eGFP fluorescence intensity significantly increased, confirming direct protein-protein interaction. **(B)** Separated scatter graph of Pre and Post photo-bleach images, N.16 GFP, N.14 control. Average +/- SEM plotted and used to calculate significance via 2-way ANOVA with multiple t-tests. GFP post bleach fluorescence intensity was significantly higher than that of GFP pre-bleach and control pre and post bleach, confirming direct protein-protein interaction.

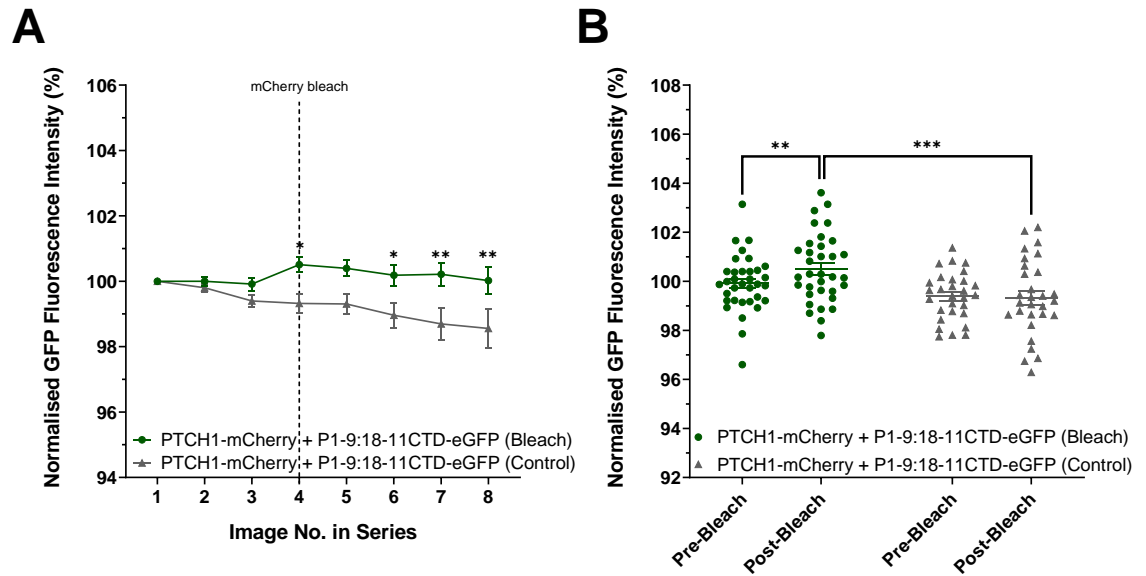


Figure 3.17 Combined removal of the middle cytoplasmic loop and CTD is not sufficient to disrupt PTCH1 homo-interactions.

(A) FRET analysis of HEK293 cells transiently transfected with PTCH1-mCherry and PTCH1-9:18ML-11CTD-eGFP (Each data point represents the average \pm SEM for 19 GFP and 22 control individual ROIs). Upon PTCH1-mCherry photo-bleaching a significant increase in PTCH1-9:18ML-11CTD-eGFP fluorescence intensity was observed. **(B)** Separated scatter graph of Pre and Post photo-bleach images, N.19 GFP, N.22 control. Average \pm SEM plotted and used to calculate significance via 2-way ANOVA with multiple t-tests. GFP post bleach fluorescence intensity was significantly higher than that of GFP pre-bleach and control pre and post bleach, confirming direct protein-protein interaction.

3.3.5 Removal of the cytoplasmic domains impairs Patched 1 inhibition of canonical Hh signalling.

A major caveat of the existing structures for Patched 1 is that large regions of both the middle loop and CTD are absent. From a membrane protein expression and purification perspective this is a logical method to optimise yield and improve particle quality. As my data show, PTCH1-9:18ML-11CTD-eGFP displays increased expression and greater membrane localisation, making it ideal for such work. However, the functionality of this and other truncated forms of Patched 1 should be scrutinised carefully. Any influence these domains might exert on their surrounding residue environment, is unknown due to their absence.

Therefore, I proceeded to investigate the impact of the middle loop and double cytoplasmic domain mutants on canonical Hh signalling. Utilising the Gli-luciferase assay, *Ptc1*^{-/-} MEFs were co-transfected with 8xGBS-luc, SV40 *Renilla* and either pcDNA 3.1⁺, the Patched 1 domain mutants, or their respective full length proteins. This uncovered that despite their increased expression and membrane localisation, PTCH1-9:8ML and PTCH1-9:8ML-11CTD had reduced activity, compared to PTCH1 (**Figure 3.18A**). This finding was recapitulated in the *Ptc1* constructs, where *Ptc1*- Δ ML Δ C showed significantly less activity in its inhibition of Gli (**Figure 3.18B**).

The responsiveness of the *Ptc1*-HA constructs to N-Shh was investigated and this too revealed discrepancies between the domain mutants (**Figure 3.18C**). For N-Shh experiments, *Ptc1*^{-/-} MEFs were co-transfected with *Ptc1*, *Ptc1*- Δ C or *Ptc1*- Δ ML Δ C and N-Shh or pcDNA 3.1⁺ (50:50). Whilst this maintained a consistent total DNA concentration to the previous Gli-luciferase assays, cells received 50%

less Ptc1, Ptc1- Δ C or Ptc1- Δ ML Δ C. This adjustment revealed greater differences in activity of the mutants, in the absence of N-Shh, compared to full length Ptc1 (**Figure 3.18C**). Co-transfection of N-Shh effectively inhibited the action of Ptc1- Δ C more significantly than full length Ptc1. Meanwhile, there was no observable effect of N-Shh on Ptc1- Δ ML Δ C, which showed no significant activity with or without N-Shh (**Figure 3.18C**).

This result suggests that whilst Ptc1- Δ C has lower expression than full length Ptc1, it achieves a similar level of overall activity, in the absence of N-Shh. This could be due to an increased ciliary stability and retention, afforded by the removal of the 'PPXY' motif within the CTD. In the presence of N-Shh a more dramatic increase in Gli is observed for Ptc1- Δ C, presumably due to its reduced expression, compared to full length Ptc1. Here a lower quantity of N-Shh is required to bind and inhibit the activity of Ptc1- Δ C.

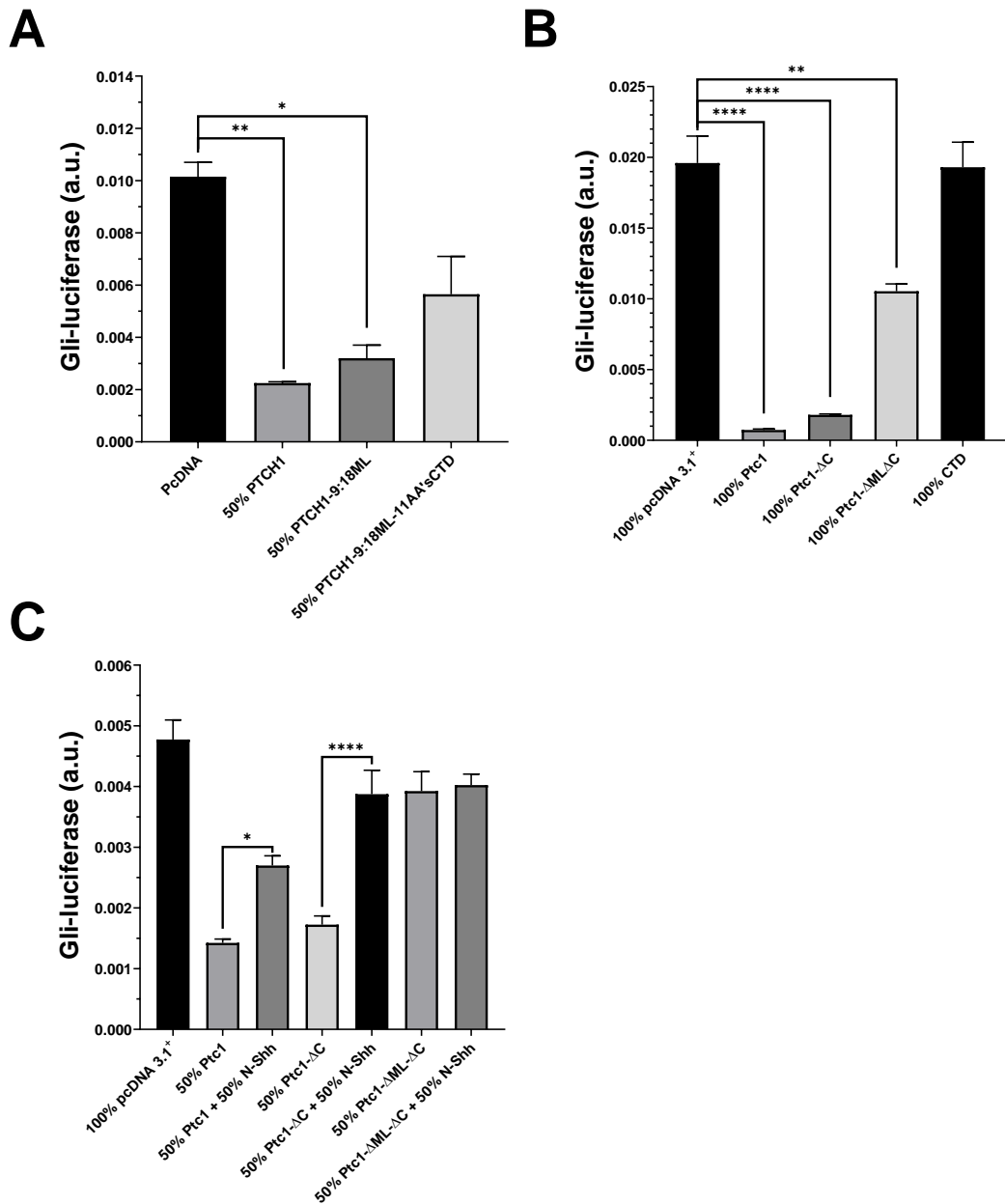


Figure 3.18 Removal of one or both cytoplasmic domains of Patched 1 results in impaired activity.

Gli-luciferase assays performed in *Ptc1*^{-/-} MEFs, transiently co-transfected with reporter constructs and specific plasmid combinations. Graphs are representative single experiments. **(A)** At 50% DNA concentration, Gli transcription was significantly inhibited by PTCH1-eGFP and PTCH1-9:18ML-eGFP but not PTCH1-9:18ML-11CTD-eGFP. **(B)** At 100% DNA concentration, Gli transcription was significantly reduced by Ptc1-HA and Ptc1-ΔC-HA, and to a lesser extent, Ptc1-ΔMLΔC-HA. **(C)** Cells received 50% Ptc1, Ptc1-ΔC or Ptc1-ΔMLΔC DNA concentration, co-transfected with 50% N-Shh or 50% pcDNA 3.1⁺.

3.4 Discussion

Multiple studies have now identified the capability of Patched 1 to form higher oligomer structures, which are directly involved in the transportation of a sterol-derivative (Bidet et al., 2011; Fleet et al., 2016; Zhang et al., 2018). In this chapter I endeavoured, through homology-based point mutations and intra-ciliary pH measurements, to gain further evidence of a sterol-dependent transport mechanism for canonical Patched 1 activity. Furthermore, via intracellular domain targeted mutations, I provided a greater understanding of the structural interactions and molecular influence the cytoplasmic domains exert on the PTCH1 dimer.

The finding that Ptc1-KR-P490A-His impedes Ptc1 function substantiates existing evidence of a cholesterol cavity in PTCH1, that is essential for canonical function. Despite this mutation being designed based on homology modelling to NPC1, subsequently published Patched 1 structures validate its predicted location, and its vicinity to a cholesterol-like density (**Figure 3.19**) (Zhang et al., 2018; Qi, Schmiede, Coutavas and Li, 2018a; Qi et al., 2019; Qian et al., 2019). This data also provides new insight into the mechanism by which the Gorlin Syndrome mutation P490Q retards the function of PTCH1 (**Figure 3.19**).

Structural modelling predicted that the Gorlin syndrome related mutation of proline to glutamine would obscure the hypothetical NPC1 cavity and come into close contact with the cholesterol density seen in the Patched 1 structure (**Figure 3.19**). The fact that a proline to alanine mutation resulted in reduced Ptc1 activity, despite having no physical side chain impediment to the cavity, suggests a strong requirement for proline. It seems logical to infer that, just like the NPC1 residue

Chapter 3: Specific mutation of the Ptc1 SSD residue P490, or removal of the cytoplasmic domains impairs activity, without disrupting oligomerisation

P691, from which Ptc1 P490 was selected, these proline residues provide the necessary structural rigidity to maintain the cholesterol cavity.

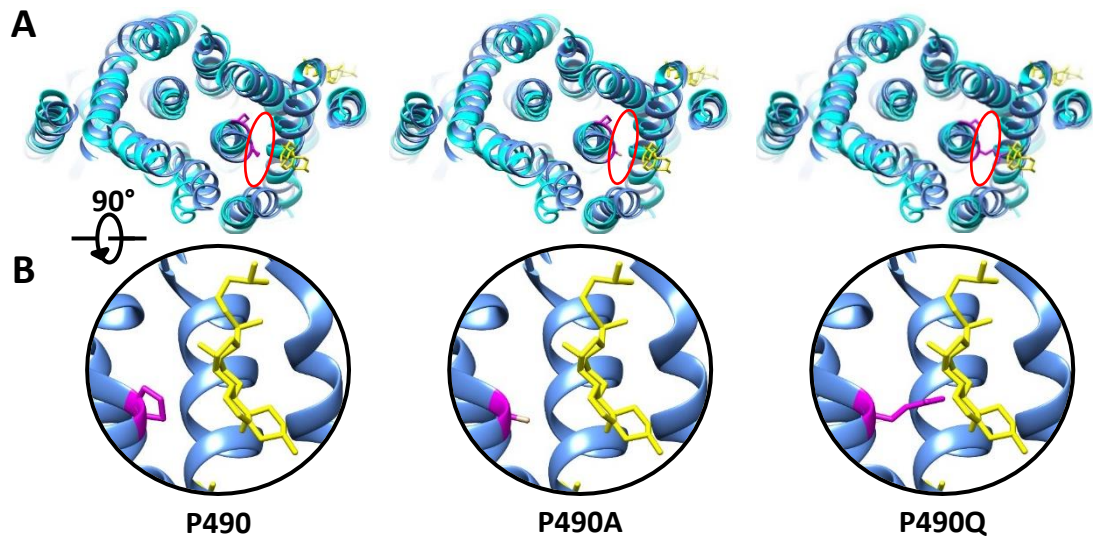


Figure 3.19 Predicted structural impact of Ptc1 P490 mutation on predicted sterol cavity identified via NPC1 homology modelling.

Structural alignment of Ptc1 (PDB ID: 6MG8) and NPC1 (PDB ID: 5U73) displayed in blue and cyan respectively. Proline residues Ptc1 P490 and NPC1 P691 depicted in magenta. Densities identified as cholesterol are shown in yellow. **(A)** top-down view of protein structures, the NPC1 SSD cavity is indicated by a red oval. Left image: native residues, Ptc1 P490 and NPC1 P691. Middle image: Ptc1 P490A mutation. Right image: NPC1 P691S and Ptc1 P490Q (Gorlin syndrome PTCH1 P504Q) mutation. **(B)** Expanded views of Ptc1 cavity, cholesterol molecule and P490 residue. From left to right: P490, P490A, P490Q.

However, this then raises the question of why the other SSD point mutations modelled off NPC1, failed to impact Ptc1 function. Here, the published structures of Ptc1 assist in providing an explanation for the contrasting findings for A483L/A484I/T485N, and L504A. Although A483L/A484I/T485N are shown to be located between two cholesterol-like densities in the core of the transmembrane

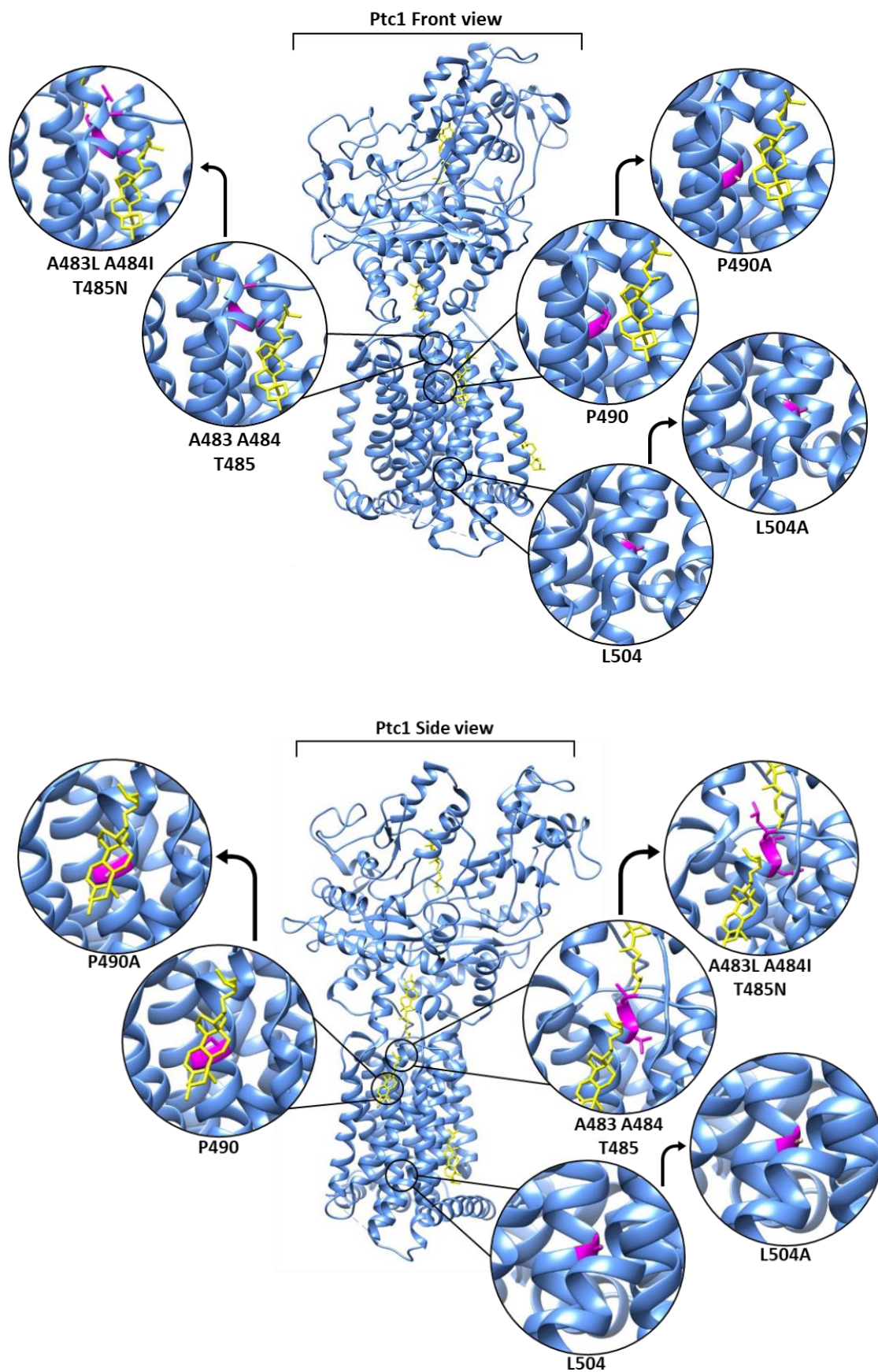
bundle, the substituted residues infer no decisive structural alterations (**Figure 3.20**).

This indicates that perhaps a less conservative residue substitution strategy could have produced greater disruption to proximal structures. The selection of A483L/A484I/T485N stemmed from a sound rationale that; these residues aligned closely to the NPC1 residues L684 and I685, which each had known disease causing variants; Ptc1 residue A483 itself had a known disease causing variant A483T and; these residues sat in close proximity to the NPC1 residue P691, which appeared essential for the proposed sterol cavity.

It is also important to consider the architecture of the SSD in the context of a recent study by Fleet and Hamel (2019). Despite the highly conserved nature of the SSD, it was found that direct substitution of the SSD of Patched 1 for that of NPC1 does not maintain a functional output in the resultant mutant. In contrast, the SSD of the Patched 1 homolog Patched 2, which displays little to no function in its native structure, was able to be successfully substituted into Patched 1. The regions of greatest variability between these three proteins are the cytoplasmic domains. This highlights their potential implication in dictating conformation and thus the functionality of the neighbouring SSD.

Unfortunately the published structures of Patched 1 and NPC1 lack segments of these two intrinsically disordered domains and as such their conformational influence is unknown. The loss of subtle structural alterations, normally induced by these domains, might explain why the SSD structures of Patched 1 and NPC1 are so strikingly similar, yet are not interchangeable.

Chapter 3: Specific mutation of the Ptc1 SSD residue P490, or removal of the cytoplasmic domains impairs activity, without disrupting oligomerisation



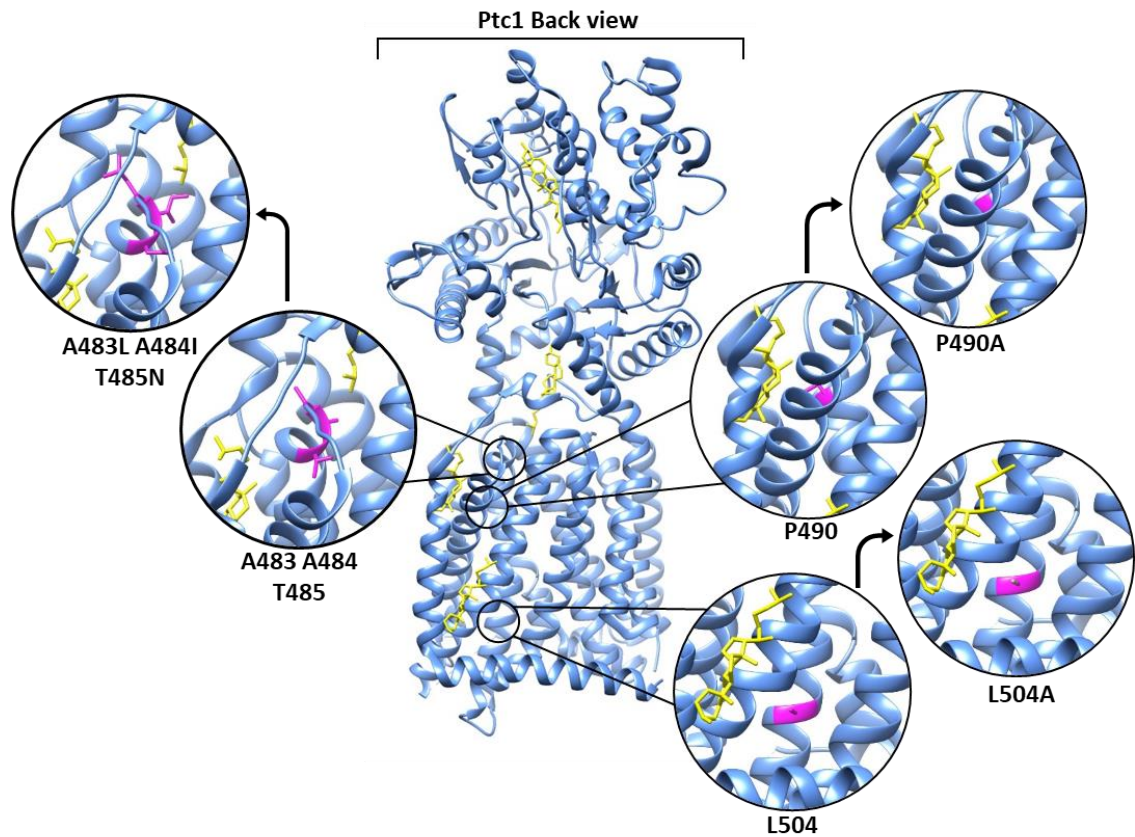


Figure 3.20 Mapping of the predicted structural location and side chain alterations of the Ptc1 point mutants.

Front **(A)**, Side **(B)** and Back **(C)** view of a 3D structure of Ptc1 (PDB ID: 6MG8) showing the location of residues targeted by site-directed mutagenesis in pink. Cholesterol-like densities are displayed in yellow. Expansion windows display predicted mutational alterations to side-chains and their proximal structural environment. Structural analysis and alterations were performed in Chimera (Pettersen et al., 2004).

Chapter 3: Specific mutation of the Ptc1 SSD residue P490, or removal of the cytoplasmic domains impairs activity, without disrupting oligomerisation

The work performed here also provides additional molecular insight on the Patched 1 cytoplasmic domains that is unavailable or neglected by the published structures. It has been known for some time that when expressed as a single domain, the CTD of Ptc is capable of self-interaction (Lu et al., 2006). It is also established that no negative impact on Patched 1 canonical activity ensues through the removal of the majority of CTD (Fleet et al., 2016).

The FRET-based experiments presented here advance our understanding further, confirming that the two CTD's, of interacting PTCH1 monomers directly interact. Computational distance measurements, performed on a dimeric PTCH1 structural model (PDB ID: 6E1H), predicts a void of ~74 Å between the terminal residues of each PTCH1 monomer. The PTCH1 monomers within this model are truncated, lacking 264 amino acids from their CTDs. Assuming an average size of 3.5Å/residue, this 264 amino acid truncation translates to ~924 Å for each monomer. This paints a picture of a highly convoluted, densely packed CTD, dominating the environment within the cytoplasm, just beneath the transmembrane domains.

Removal of the majority of the middle cytoplasmic loop (PTCH1-9:18ML) had no obvious impact upon the CTD interaction, between mature PTCH1 proteins in FRET-based assays. This might suggest that the apparent mutual dependency observed between the middle cytoplasmic loop and the CTD, does not extend beyond protein synthesis steps. Moreover, reduced expression is only seen in the Ptc1 constructs with a more severe domain deletion; Pct1-ΔML lacking the entire middle cytoplasmic loop; and Ptc1-ΔC lacking all but the first 3 residues of the CTD. Generation of a double mutant, harbouring both deletions, restored

protein expression, indicating the presence of a mutual requirement or dependency during early folding stages.

Less severe deletions, PTCH1-9:18ML and PTCH1-9:18ML-11CTD did not suffer expression issues and in fact produced greater expression and membrane location than wild-type. The Co-IP data clearly indicates that all the domain mutants could achieve direct interaction with full length Patched 1. This is corroborated by the finding that removal of the majority of the middle loop and CTD (PTCH1-9:18ML-11CTD) reduces, but does not prevent FRET, with full length PTCH1-mCherry. The smaller increase in GFP intensity, post mCherry photo-bleaching observed for interactions with PTCH1-9:18ML-11CTD compared to full length PTCH1, is most likely related to increase photo-shielding and/or an increase in the physical distance between fluorophores (**Figure 3.21**).

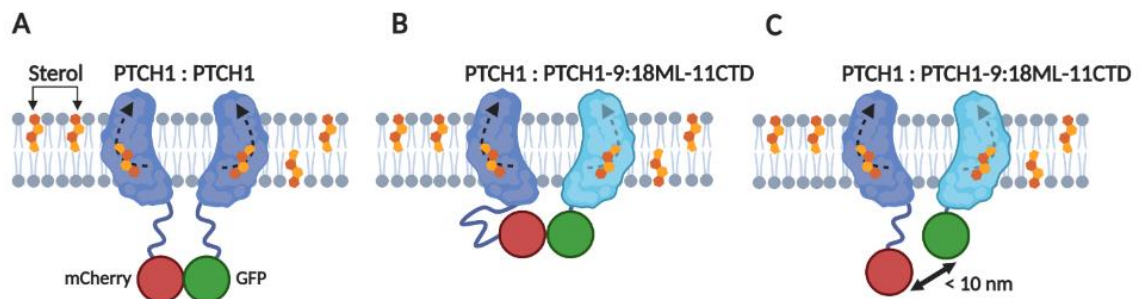


Figure 3.21 Effect on FRET from the removal of the CTD of PTCH1.

(A) FRET between C-terminal GFP and mCherry fluorophores confirmed direct PTCH1 homo-interaction. **(B & C)** Deletion of the majority of the middle loop and CTD of PTCH1, PTCH1-9:18ML-11CTD-eGFP reduced, but did not prevent FRET with full length PTCH1-mCherry. This reduction might be a result of: **(B)** photo-shielding because the interaction occurs closer to membrane and transmembrane domains. This is supported by the lower degree of mCherry photo-bleaching that was achieved, or: **(C)** The physical distance between the fluorophores is increased due to a loss of interaction, but they remain within 10 nm of each allowing some FRET to occur.

Chapter 3: Specific mutation of the Ptc1 SSD residue P490, or removal of the cytoplasmic domains impairs activity, without disrupting oligomerisation

The finding that both Ptc1- Δ ML Δ C and PTCH1-9:18ML-11CTD directly interact with full length PTCH1 via Co-IP and by FRET-based imaging contradicts the findings of Fleet et al., (2016). They proposed that combined removal of both cytoplasmic domains yields a protein that does not oligomerise, but retains both activity and responsiveness to N-Shh. Furthermore, they describe the removal of the middle loop alone to produce a protein with constitutive activity, unresponsiveness to N-Shh.

Therefore, of particular note are the functional Gli-luciferase assays of this chapter, which further dispute the published findings of 'similar' domain deletion mutants. Here, Patched 1 activity was impaired by the removal of the middle loop, which was further exacerbated by the combined removal of both cytoplasmic domains. This was shown in both mouse and human Patched 1, with different domain mutations. These results actually fit a model proposed by the Fleet group in a subsequent publication, whereby the cytoplasmic domains exert a conformational and in turn a functional influence on the SSD of Patched 1 (Fleet et al., 2018).

Interestingly, Ptc1- Δ C displayed reduced protein expression, but retained comparable overall activity to full length Ptc1. This was highly suggestive of increased activity and/or increase ciliary retention and protein half-life. An increase in protein half-life is likely due to the loss of the 'PPXY' motif in the CTD, which is directly associated with protein turnover by ubiquitination of K1413 (**Figure 3.22**) (Chen et al., 2014). Increased activity could result from a reduced

Chapter 3: Specific mutation of the Ptc1 SSD residue P490, or removal of the cytoplasmic domains impairs activity, without disrupting oligomerisation

physical impediment usually imposed by the CTD, on the accessibility of the sterol cavities seen in structures of Patched 1.

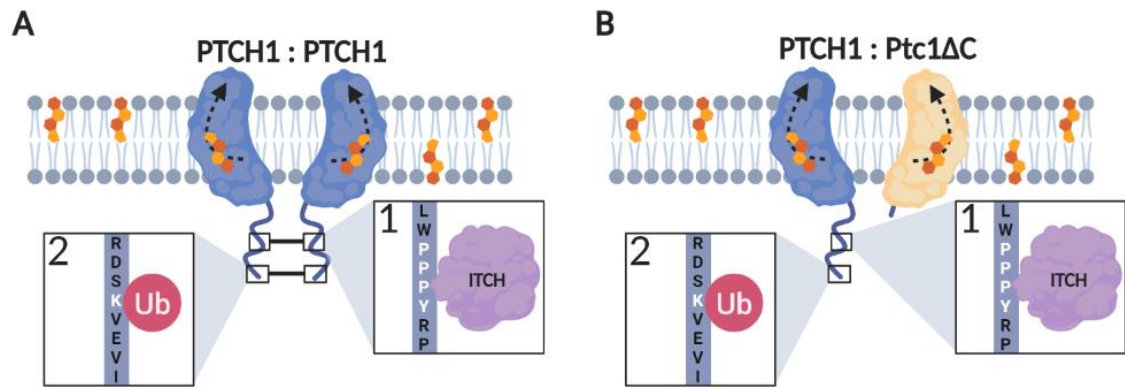


Figure 3.22 Deletion of the CTD effects Patched 1 turnover but not dimerization.

(A) Full length PTCH1 monomers contain a 'PPXY' motif in their CTD, targeted for ubiquitination in the absence of ligand, by ITCH. Ubiquitination at K1413 increases protein turnover. **(B)** Ptc1-ΔC has lost the CTD and so has reduced turnover.

Finally, the mechanism by which Patched 1 inhibits Smo was investigated, by way of a ciliary-based ratio-metric pH probe. The assay was experimentally validated and used to generate a calibration curve, to which intra-ciliary pH could be quantified in an un-invasive manner. Stimulation of ciliated cells with N-Shh appeared to result in a slight, but not significant, alkalinisation of the cilia. Several inherent limitations of the experimental design and tools prevented further classification of this small mean change in ciliary pH. Available confocal filter sets were not directly compatible for effective imaging of CFP and Venus(H148G); transient transfection of IMCD-3 cells and subsequent serum starvation to induce ciliation produced a small percentage of probe positive, ciliated cells; and differing

relative fluorescent intensities of CFP and Venus(H148G) resulted in a skewed calibration graph, with greater dynamic range towards acidic conditions.

Furthermore, intensities of the probe fluorophores fluctuated, with apparent intra-ciliary sub-localisation, potentially indicative of distinct enrichments of signalling components that influenced local pH. Whether these were directly related to Hh signalling, other unrelated cellular mechanisms, or were artefacts directly related to the probe, was undetermined. Stable-expressing clones of the pH probe were generated in an attempt to mitigate these issues, but characterisation showed highly variable expression, loss of ciliary localisation and in several cases exclusive expression of a single fluorophore tag (data not shown).

There still remains the possibility that Patched 1 utilises another ion in its transport of the Smo agonist (**Figure 3.23**). Na^+/K^+ gradients are major constituent of metazoan membrane potentials and have emerged as a favourable mechanism for investigation. Typically, a gradient of high $\text{Na}^+/\text{low K}^+$ extracellular concentration and low $\text{Na}^+/\text{high K}^+$ intracellular concentration is seen. Patched 1 activity was found to be directly associated with Na^+ concentration in a rapid, direct Smo assay (Myers et al., 2017). Here, inverting the extracellular Na^+/K^+ concentrations, resulted in a rapidly induced and reversible inhibition of Patched 1 activity. However, this finding has one major limitation in that the assay was performed in HEK293 cells, devoid of cilia, after attempts with conventional cilia-based assays were deemed unsuitable. Moreover, the assay is a measurement

of direct Smo G-protein coupling, which is not necessarily reflective of canonical Hh signalling, although it does require activation of Smo.

In further support of a Na⁺ chemiosmotic gradient influencing the Hh pathway, a recent structure of DISP1 revealed several intramembrane densities that are potentially Na⁺ (Wang et al., 2020). Substitution of three proximal aspartic acids, D571, D572 and D1049, to Asparagine perturbed ShhNp release. Structural analysis of this mutant DISP1, showed a loss of the Na⁺-like densities seen in wild-type DISP1. Whilst a second, independent group have also shown DISP1 as a SHH/Na⁺ antiporter, they proposed PTCH1 is a K⁺ driven transporter of cholesterol (Petrov et al., 2020). Incubation of ciliated NIH3T3 cells in media with different extracellular concentrations of K⁺ but not Na⁺ resulted in ciliary accumulation of Smo.

A potential issue arises from the direction of cellular K⁺ gradients. K⁺ driven PTCH1, would move K⁺ towards the extracellular space and cholesterol towards the intracellular space, or the inner membrane leaflet (**Figure 3.23**). This is reminiscent of NPC1/2, but makes assumptions that the activation of Smo by cholesterol is mediated at the CRD. However, it has been demonstrated that Smo-ΔCRD mutants can be activated by cholesterol at another site, the 7TM-helical bundle. This suggests that preventing CRD cholesterol interactions might only be part of the overall mechanism of Smo inhibition. The opposing conclusions around Na⁺/K⁺ driven activity, likely stem from inherent differences in the experimental approaches. As of yet, no definitive experiment has truly

Chapter 3: Specific mutation of the Ptc1 SSD residue P490, or removal of the cytoplasmic domains impairs activity, without disrupting oligomerisation

identified, beyond doubt, the endogenous sterol Smo agonist or the mode/source of Patched 1 activity.

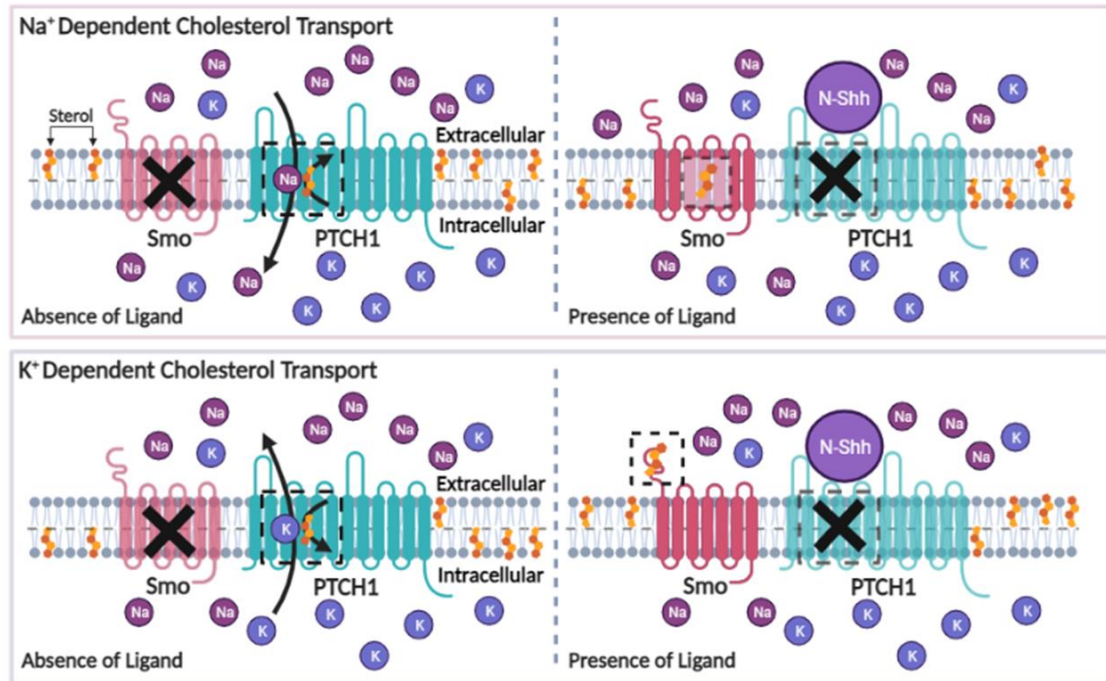


Figure 3.23 Hypothetical PTCH1 Na⁺ and K⁺ dependent modes of action.

Top Panel: Na⁺ dependent PTCH1 activity. In the absence of ligand, PTCH1 inhibits Smo through the redistribution of cholesterol from the inner membrane leaflet to the outer. This is achieved by moving a Na⁺ ion from the extracellular space to the intracellular space. In the presence of ligand, PTCH1 is inhibited and the redistribution of cholesterol ceases. Cholesterol equilibrates across the membrane leaflets and Smo is activated, primarily at its 7TM bundle. **Bottom Panel: K⁺ dependent PTCH1 activity.** In the absence of ligand, PTCH1 inhibits Smo through the redistribution of cholesterol from the outer membrane leaflet to the inner. This is achieved by moving a K⁺ ion from the intracellular space to the extracellular space. In the presence of ligand, PTCH1 is inhibited and the redistribution of cholesterol ceases. Cholesterol equilibrates across the membrane leaflets and Smo is activated, primarily at its extracellular CRD.

Chapter 4

Patched homologs form homo- and heterodimer interactions display close resemblance, but unequal canonical functionality, due to influences of the cytoplasmic domains

Chapter 4

Patched homologs form homo- and heterodimer interactions of close resemblance, but differing canonical functionality, due to influences of the cytoplasmic domains

4.1 Introduction

The human patched homolog, Patched 2, shares roughly 45% sequence identity with Patched 1, and like its relative, is strongly conserved across species. Both proteins possess a pair of 6 transmembrane domains, an SSD, two extracellular domains, and two cytoplasmic domains (Motoyama, Heng, et al., 1998; Pearce et al., 2001). Yet these two proteins have vastly contrasting reported functional activity (Zhulyn et al., 2015). It is well documented that the sequences of Patched 1 and 2 diverge most severely within the two intrinsically disordered cytoplasmic domains; the middle cytoplasmic loop (between TM6 and TM7); and at the cytoplasmic tail (CTD). The CTD of Patched 2 is shorter, in comparison to that of Patched 1 (Kawamura et al., 2008). It is of note that the cytoplasmic domains are the location of the proline rich motif, PPXY, exclusive to the Patched family (Yue et al., 2014; Chen et al., 2014).

Recent work by Fleet and Hamel (2019), shone some light onto the predominant question: why is Patched 2 not functionally equivalent to Patched 1? Through the generation of hybrid proteins they demonstrated that the SSD of Ptch2 is fully capable of potent Smo repression, when placed in the context of adjacent Ptch1 cytoplasmic domains. Therefore, the cytoplasmic domains, alongside the extracellular domains, appear to dictate the functionality of the transmembrane

Chapter 4: Patched homo- and heterodimer interactions display close resemblance, but differing canonical functionality, due to influences of the cytoplasmic domains

core. This could be achieved by inflicting conformational adjustments, essential or function; through direct intramolecular interactions; or by intermolecular associations between monomers of Patched. In fact, within *X. laevis* it is Patched 2, not Patched 1, that contains an extended CTD. Interestingly, in response to Hh activity, Patched 2 expression was greater than Patched 1 (Takabatake et al., 2000). Whether the respective changes in CTD length of the Patched proteins in *X. laevis* is functionally relevant to this apparent role reversal is unknown.

Whilst the functional relevance of PTCH2 remains debatable, there is growing evidence that PTCH2 mutations not only contribute, but in some cases drive NBCCS development (Fujii et al., 2013). Interestingly the patients suffering PTCH2 mutations fail to satisfy the standards required from a typical Gorlin syndrome diagnosis test. In fact, patients with a PTCH2 mutation present much milder associated disease phenotypes than that of PTCH1 or SUFU mutations. This is likely due to PTCH2 performing a less pivotal role, but none the less indicates some functionality.

Ptch2 is able to bind N-Shh to a similar affinity as Ptch1 and its overexpression is able to reduce smoothed ciliary localization when expressed in *Ptc1^{-/-}* MEFs (Carpenter et al., 1998a; Zhulyn et al., 2015). However, embryology studies have shown that Ptch1 is essential to development, whilst Ptch2 is dispensable. The loss of Ptch1 is embryonically lethal, whereas Ptch2 null embryos develop grossly normal (Nieuwenhuis et al., 2006). Intriguingly, although Ptch2 cannot compensate for a loss of Ptch1 during development, its effects can be observed in heterozygous *Ptch1^{+/-}* mice. A loss of Ptch2 in these mice exacerbates the disease phenotype compared to Ptch2 positive heterozygous *Ptch1^{+/-}* mice (Lee

Chapter 4: Patched homo- and heterodimer interactions display close resemblance, but differing canonical functionality, due to influences of the cytoplasmic domains et al., 2006). The recent Cryo-EM structure published of a 2:1 PTCH1-N:Shh complex (Qi, Schmiede, Coutavas and Li, 2018), has provided a rich source of data to extrapolate for the investigation of structure-function relationships within Patched 2. This paper and many other high impact publications have presented a form of Patched 1 lacking the majority of the CTD and often the middle loop, (or removal of the middle loop PPXY motif) (Qi, Schmiede, Coutavas, Wang, et al., 2018; Gong et al., 2018; Qi et al., 2019). One advantage of this is that the domains removed are the regions of lowest conservation in PTCH2. Conducting a sequence comparison of PTCH1 and PTCH2, excluding the two cytoplasmic domains improves 'identity' from ~45% to ~57%. Therefore, it seems likely that the core structural features of the Patched 1 dimer will be shared by Patched 2.

With this in mind, it is feasible that Patched 2 might share not only core structural elements with Patched 1, but also its ability to form homodimer and even higher order, tetramer complexes. If so, could Patched 2 engage N-Shh with a similar interaction interface as PTCH1, mobilise cholesterol in the same manner, and even form hetero-interactions with PTCH1, taking the place of one of the monomers within the dimer structure?

4.2 Aims and Hypothesis

There is conflicting evidence in regards to the function performed by PTCH2. Present in vertebrates, but not drosophila, PTCH2 is almost certainly an evolutionary paralogue of PTCH1, created by gene duplication. There is clear functional disparity, variability in localisation and differential expression profiles of both homologs, suggesting divergent roles. However, evidence of cooperation and overlapping functions still remain.

The overwhelming evidence that PTCH1 forms homodimer interactions and even possibly loose tetramer structures begs the question; is this ability shared by its closely related homolog, PTCH2? Furthermore, is the apparent role of PTCH1 in transporting cholesterol a shared capability of PTCH2? Finally, are heterodimer interactions between the two homologs possible and if so are they functionally relevant?

In this chapter I will discuss results associated with the following aims:

- I. Verify and semi-quantify the capability of Patched 1 and 2 to form both homo- and hetero-associations.
- II. Assess the functionality of such interactions and the effect of protein mutations, in relation to the canonical Hh signalling pathway.
- III. Utilise SDM and larger domain deletion cloning to identify essential/non-essential regions of Patched 1 and 2, for either homo- or hetero-interactions and canonical function.

4.3 Results

4.3.1 Patched 1 and 2 are capable of forming homo- and hetero-interactions.

To establish the groundwork to investigate Patched 1 and 2 co-functionality, I performed Co-IPs with transiently transfected HEK293 cells. For the purpose of this, C-terminal tagged plasmids Ptc1-HA and PTCH2-FLAG were used. Ptc1-HA was an existing construct, created and verified by the hedgehog lab (University of Leeds). PTCH2-FLAG was created by a two-step cloning process, from a parental plasmid, PTCH2-pcDNA-HisB (gift from Professor Peter Zaphiropoulos, Karolinska Institute). First, the coding region of PTCH2 was sub-cloned into the MCS of pcDNA 3.1⁺ via restriction digest with Not-I and XbaI. Next, a C-terminal FLAG tag 'DYKDDDDK' was introduced in frame, using In-Fusion cloning.

Co-IP results demonstrated a specific association between Ptc1-HA and PTCH2-FLAG, as validated by western blot. **(Figure 4.1)**. Negative controls confirmed antibody specificity and ruled out non-specific binding, between the target antibody and the Dynabeads resin. A slight reduction in PTCH2-FLAG expression was observed when co-transfected with Ptc1-HA, compared to co-transfection with pcDNA 3.1⁺.

The ability of PTCH2 to form homo-interactions was also confirmed by Co-IP with two PTCH2 constructs, PTCH2-FLAG and PTCH2-HA **(Figure 4.2)**. PTCH2-HA was generated from PTCH2-FLAG by Q5 SDM and confirmed by Sanger sequencing and western blot. As seen previously, when co-transfected with Ptc1-

Chapter 4: Patched homo- and heterodimer interactions display close resemblance, but differing canonical functionality, due to influences of the cytoplasmic domains

HA, a slight reduction in PTCH2-FLAG expression was observed when co-transfected with PTCH2-HA, compared to with pcDNA 3.1⁺.

To support the Co-IP findings and gain additional information about the nature of the homo and hetero-interactions of Patched 1 and 2, FRET-based assays were undertaken. For FRET-based investigation of PTCH1 homo and hetero-interactions, existing C-terminally tagged, PTCH1-eGFP and PTCH1-mCherry plasmids were utilised. For details of these constructs and the FRET experimental design, see **(Chapter 3, Results 3.3.1)**.

In order to conduct FRET-based assays with PTCH2, two C-terminally tagged constructs, PTCH2-eGFP and PTCH2-mCherry were generated through a two-step cloning strategy. In brief, eGFP or mCherry sequences from existing PTCH1 constructs were introduced C-terminally into PTCH2-FLAG via In-Fusion cloning, after which, the previous terminal stop codon was removed by QuikChange XL II, to produce in frame PTCH2-eGFP or PTCH2-mCherry. Plasmid colony mini-preps were screened by Sanger sequencing and expression confirmed by live cell fluorescence **(Figure 4.3)**.

Live FRET-based assays, performed in transiently transfected HEK293 cells, confirmed a direct homo-interaction for both PTCH1 and PTCH2 **(Figure 4.4)**. There was a significant increase in normalised GFP fluorescence intensity post mCherry photo-bleaching, in co-transfection conditions of PTCH1-eGFP and PTCH1-mCherry, as well as PTCH2-eGFP and PTCH2-mCherry **(Figure 4.4)**. No such increase was observed in control ROIs that did not undergo photo-bleaching of mCherry.

Chapter 4: Patched homo- and heterodimer interactions display close resemblance, but differing canonical functionality, due to influences of the cytoplasmic domains

The magnitude of the increase in normalised GFP intensity for PTCH1 homo-interactions was larger than that for PTCH2 homo-interactions (**Figure 4.4A**) vs (**Figure 4.4B**). The extent of mCherry bleaching achieved in both conditions was comparable, negating any possibility of 'photo-shielding' effects (data not shown). Therefore, this difference in GFP intensity likely signifies either; a greater frequency of CTD homo-association in PTCH1 compared to PTCH2 or; a greater physical distance between the fluorophores in PTCH2 homo-interactions.

PTCH1 and PTCH2 hetero-interactions were subsequently investigated using the FRET-based assay. To exclude any possible introduction of bias, through non-specific effects of differing protein expression and basal fluorescence intensity, both Patched 1 and 2 were tested in the role of donor (eGFP) and acceptor (mCherry). Photo-bleaching of mCherry resulted in a significant increase in normalised GFP fluorescence intensity in both co-transfected conditions; PTCH1-eGFP + PTCH2mCherry, and PTCH2-eGFP + PTCH1-mCherry (**Figure 4.5**).

The magnitude of the increase in normalised GFP intensity for both Patched hetero-interaction combinations was comparable to that of the previously reported Patched homo-interactions. In fact, both hetero-interaction combinations displayed increases in GFP (~3%) at a level between that seen for homo-interactions of PTCH2 (~2%) and PTCH1 (~4%). The simplest conclusion is that these differences are a result of different physical distances between the C-terminal fluorophores, due to different CTD lengths. These data firmly suggest that PTCH1 and PTCH2 form homo and hetero-interactions of strong similarity, in particular through associations in the CTD's, which were previously confirmed to be non-essential for Patched 1 oligomerisation (**Results 3.3.4**).

Chapter 4: Patched homo- and heterodimer interactions display close resemblance, but differing canonical functionality, due to influences of the cytoplasmic domains

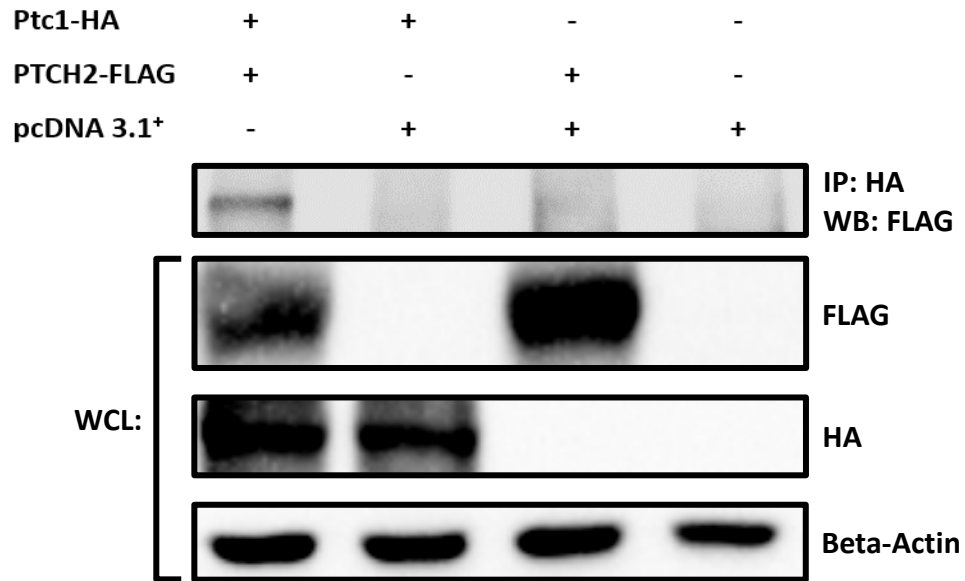


Figure 4.1 PTCH2 directly associates with Ptc1 in HEK293 cells.

HEK293 cells were co-transfected with Ptc1-HA, PTCH2-FLAG and pcDNA 3.1⁺ in the indicated combinations and immunoprecipitated with anti-HA antibody (4 µg Proteintech), and blotted against anti-FLAG and anti-HA. A clear band, corresponding to PTCH2-FLAG, showed at ~130kDa in the IP blot. Negative controls of; no PTCH2-FLAG, no Ptc1-HA and no Ptc1-HA or PTCH2-FLAG showed no obvious bands. WCL's showed similar levels of total protein expression (anti-Beta-Actin) but a small reduction in PTCH2-FLAG expression when co-transfected with Ptc1-HA. Results are representative of 3 independent experiments.

Chapter 4: Patched homo- and heterodimer interactions display close resemblance, but differing canonical functionality, due to influences of the cytoplasmic domains

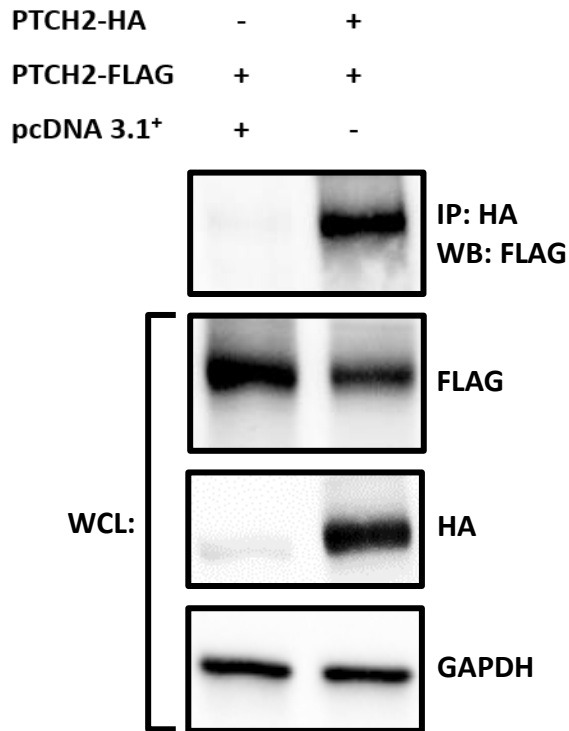
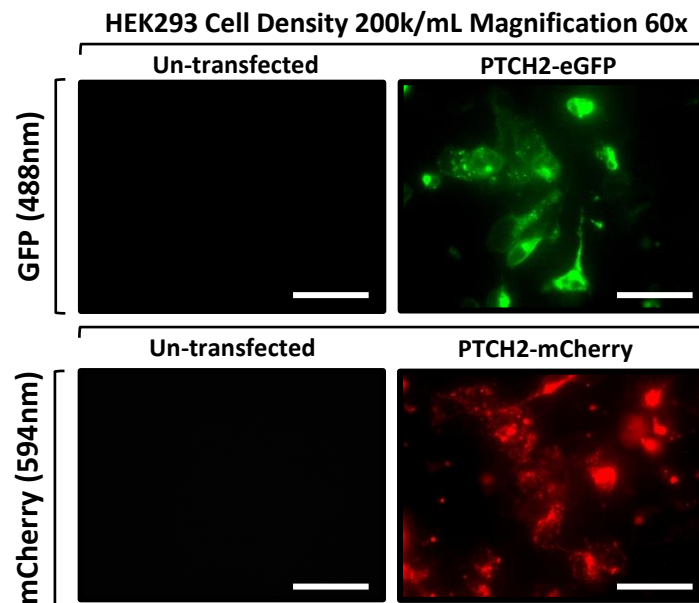


Figure 4.2 PTCH2 forms homo-interactions in HEK293 cells.

HEK293 cells were co-transfected with PTCH2-HA and PTCH2-FLAG or pcDNA 3.1⁺ and immunoprecipitated with anti-HA antibody (4 µg Proteintech), and blotted against anti-FLAG, anti-HA and anti-GAPDH. A clear band for PTCH2-FLAG was seen in the IP blot at ~130kDa for the combination PTCH2-HA + PTCH2-FLAG. Whereas the negative control of; no PTCH2-HA showed no obvious band. WCL's showed similar levels of total protein expression (GAPDH) but a small reduction in PTCH2-FLAG expression when co-transfected with PTCH2-HA.

A



B

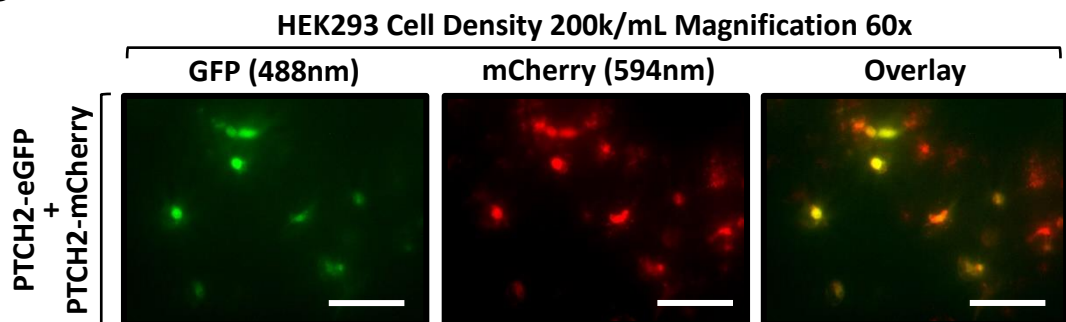


Figure 4.3 C-terminally fluorescently labelled PTCH2 plasmids show similar expression profiles and co-localisation in transfected HEK293 cells.

Live cell fluorescent microscopy of transiently transfected HEK293 cells captured via EVOS fluorescence light microscope, with excitation of PTCH2-eGFP or PTCH2-mCherry at 488nm or 594nm respectively. **(A)** Individually transfected PTCH2-eGFP and PTCH2-mCherry were visualised, confirming in frame expression of C-terminal fluorescent labels. **(B)** Co-transfection of PTCH2-eGFP and PTCH2-mCherry with GFP (488 nm) and mCherry (594 nm) channels shown separately and overlaid, confirming co-localisation. Scale bar, 50 μ M.

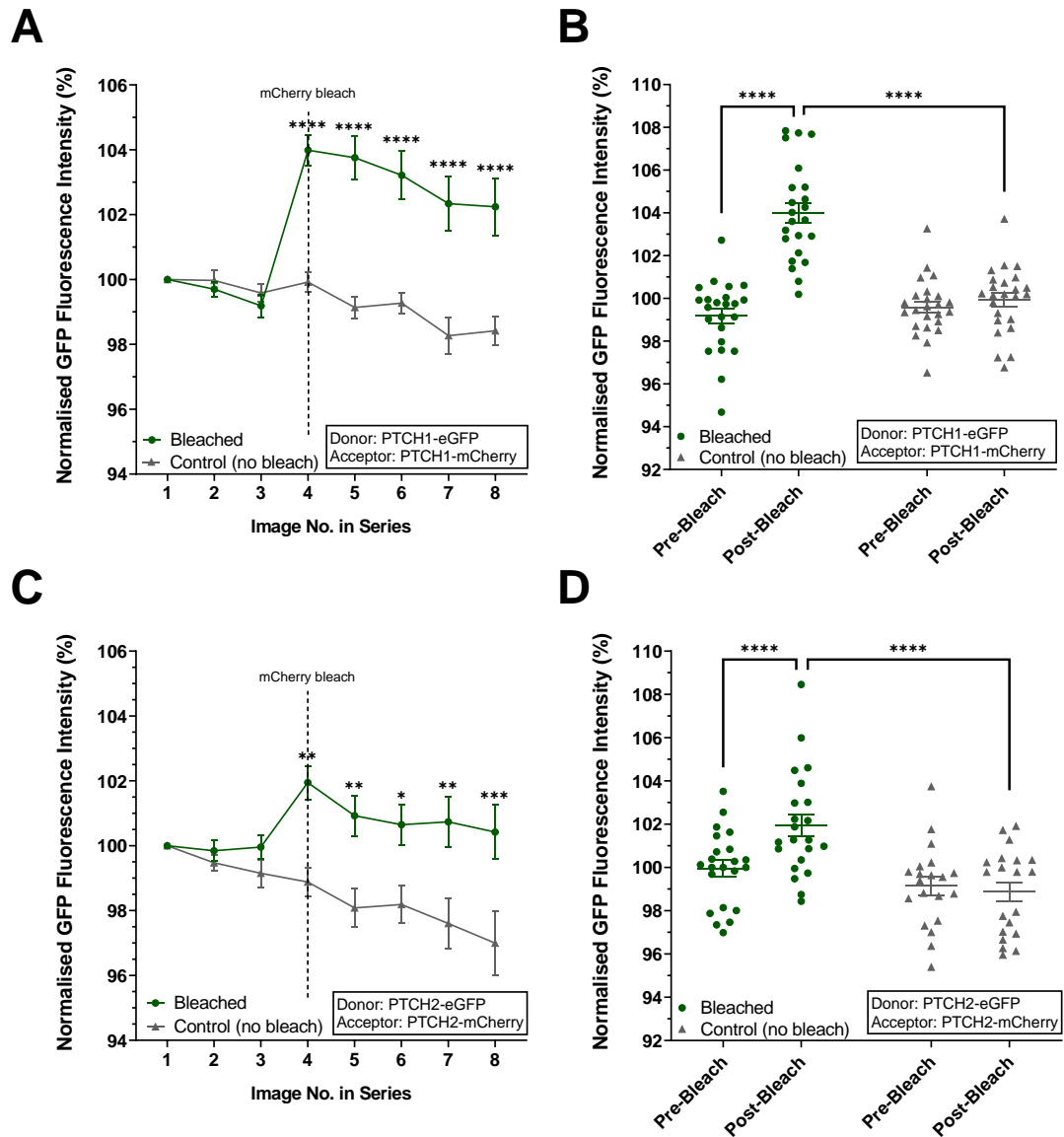


Figure 4.4 Live FRET-based assay confirmed PTCH1 and PTCH2 homo-interactions in HEK293 cells.

(A) FRET analysis of HEK293 cells transiently transfected with PTCH1-eGFP and PTCH1-mCherry confirmed direct interaction. Dashed line indicates start of PTCH1-mCherry photo-bleaching (100% 564 nm and 614 nm). Data points represent the average \pm SEM of 16 bleached and 14 control ROIs. **(B)** Separated scatter graph of individual ROIs for pre and post photo-bleach images (images 3 & 4). **(C)** Same as in (A), but co-transfection of PTCH2-eGFP and PTCH2-mCherry, confirmed direct interaction. (14 bleached and 14 control ROIs). **(D)** Same as in (C) but co-transfection of PTCH2-eGFP and PTCH2-mCherry.

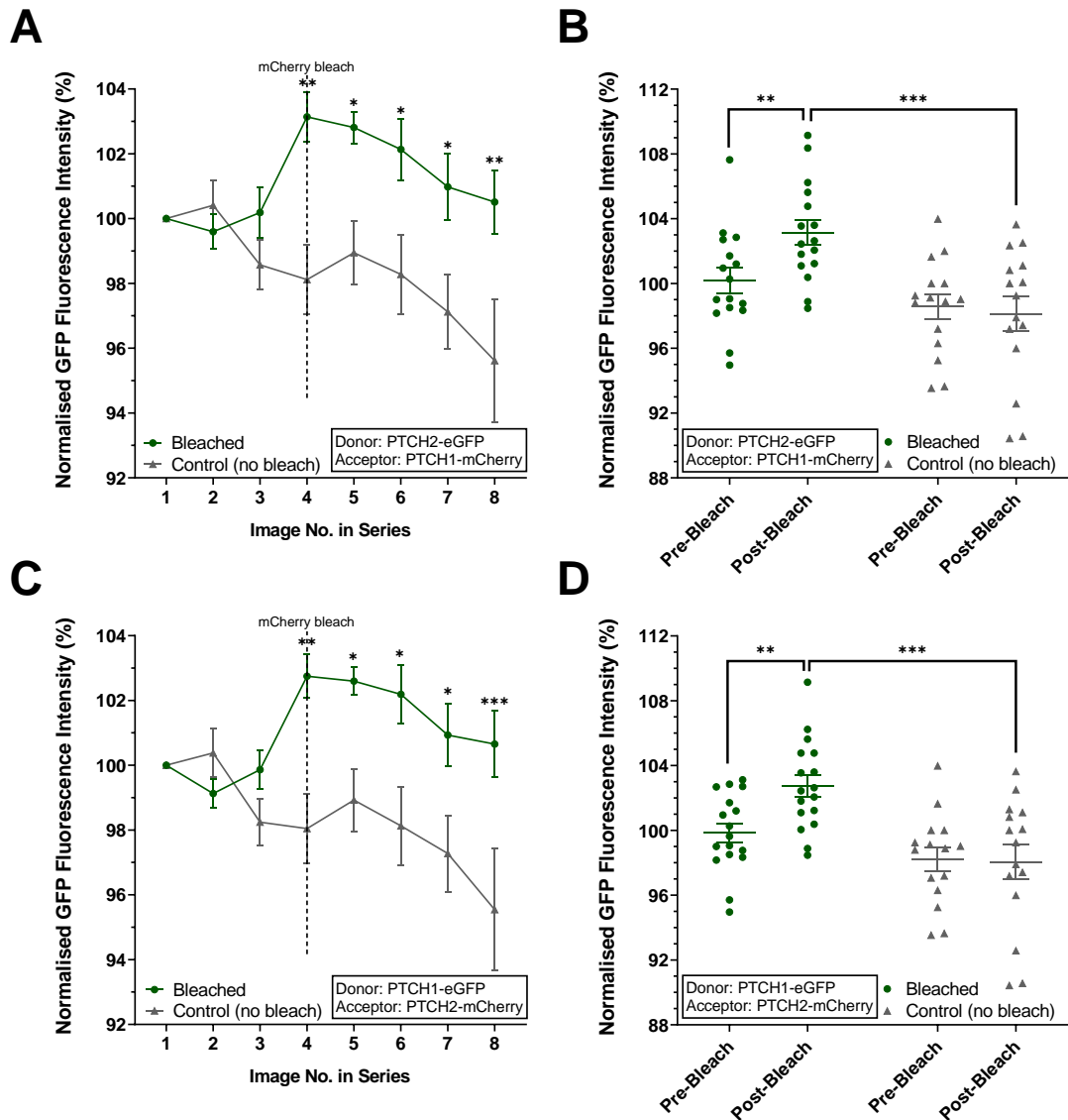


Figure 4.5 Live FRET-based assay confirmed PTCH1:PTCH2 hetero-interactions in HEK293 cells.

(A&C) FRET analysis of HEK293 cells transiently co-transfected with either PTCH2-eGFP and PTCH1-mCherry or PTCH1-eGFP and PTCH2-mCherry. Data points represent the average \pm SEM of 16 bleached and 14 control ROIs in each graph. Dashed line indicates start of mCherry photo-bleaching (100% 564 nm and 614 nm). **(B&D)** Separated scatter graph of individual ROIs shown in (A&C) for pre and post photo-bleach images (images 3 & 4).

4.3.2 The heterodimer interactions of Patched 1 and Patched 2 are competitive with their homodimer counterparts.

Due to the evolutionary relationship, and strong homology shared between Patched 1 and 2, it is rational to believe that homo-interactions and hetero-interactions would display a close resemblance. The Co-IP and FRET data thus far confirmed the existence of these interactions, and the presence a common structural feature of CTD association shared by all three. Therefore, it is highly probable that the interaction interface(s) of the proposed dimers would be extremely similar, for both homo and heterodimers. By this logic, Patched 1 and 2 should display some degree of competitive binding.

To this end, hetero- and homo-interaction affinities were compared, via competition based Co-IPs. Briefly, a reduced concentration of Ptc1-HA was co-transfected with 'target' myc-PTCH1, in the presence of excess 'competitor' PTCH2-FLAG. A Co-IP was then performed using anti-HA antibody, as described previously, with the exception that IP lysates were probed for the target and 'competitor' epitope tags.

Competition Co-IPs with reduced exogenous expression of Ptc1-HA (200 ng or 400 ng), and an excess of PTCH2-FLAG (30-fold) revealed an inverse relationship between the quantity of myc-PTCH1 and PTCH2-FLAG in IP lysates (**Figure 4.6**). Densitometry analysis of western blots showed that reducing the quantity of co-transfected myc-PTCH1 DNA from 2 μ g to 1 μ g (lanes 2 vs 3) resulted in ~60% less myc-PTCH1 and ~70% more PTCH2-FLAG in IP lysates (**Figure 4.6B**). The densitometry analysis also suggests that the system was

Chapter 4: Patched homo- and heterodimer interactions display close resemblance, but differing canonical functionality, due to influences of the cytoplasmic domains

successfully limited by the availability of Ptc1-HA. Increasing Ptc1-HA from 200 ng to 400 ng (lanes 1 vs 2) resulted in a greater quantity of myc-PTCH1 and PTCH2-FLAG in IP lysates (**Figure 4.6B**).

To elucidate these findings further, a similar competition approach to FRET-based microscopy assays, previously described in Chapter 3 (**Results 3.3.1**) was applied. HEK293 cells were co-transfected with PTCH1-GFP, PTCH1-mCherry and either 4-fold PTCH2-FLAG or 4-fold negative control, pcDNA 3.1+. PTCH1-GFP emission intensity was measured before and after photo-bleaching of PTCH1-mCherry, with unbleached ROIs serving as a negative control.

A significant and sustained increase in normalised GFP fluorescence intensity, was seen post mCherry photo-bleaching in samples with 4-fold pcDNA 3.1+, but not with 4-fold PTCH2-FLAG (**Figure 4.7A**). There was no significant change in GFP in either control (no bleach) group (**Figure 4.7C**). Scatter graphs of individual ROIs of 4-fold PTCH2-FLAG, pre and post photo-bleaching, showed a smaller, yet significant increase in normalised GFP post bleach, compared to 4-fold pcDNA 3.1+ (**Figure 4.7B**). This suggests that PTCH2-FLAG disrupted some of the PTCH1 homodimer interactions, but did not fully impede all associations.

In agreement, the co-transfection of 2-fold PTCH2-FLAG vs 2-fold pcDNA 3.1+ was not sufficient an excess of PTCH2 to impair PTCH1 homodimer interactions (data not shown). Together, the competition Co-IP and FRET data suggest a competitive binding relationship of Patched 1 and 2 for Patched 1, albeit with differing affinities. PTCH1 homodimers appear to be the favourable combination, but the interacting interface between the homo and heterodimers is likely to be highly conserved.

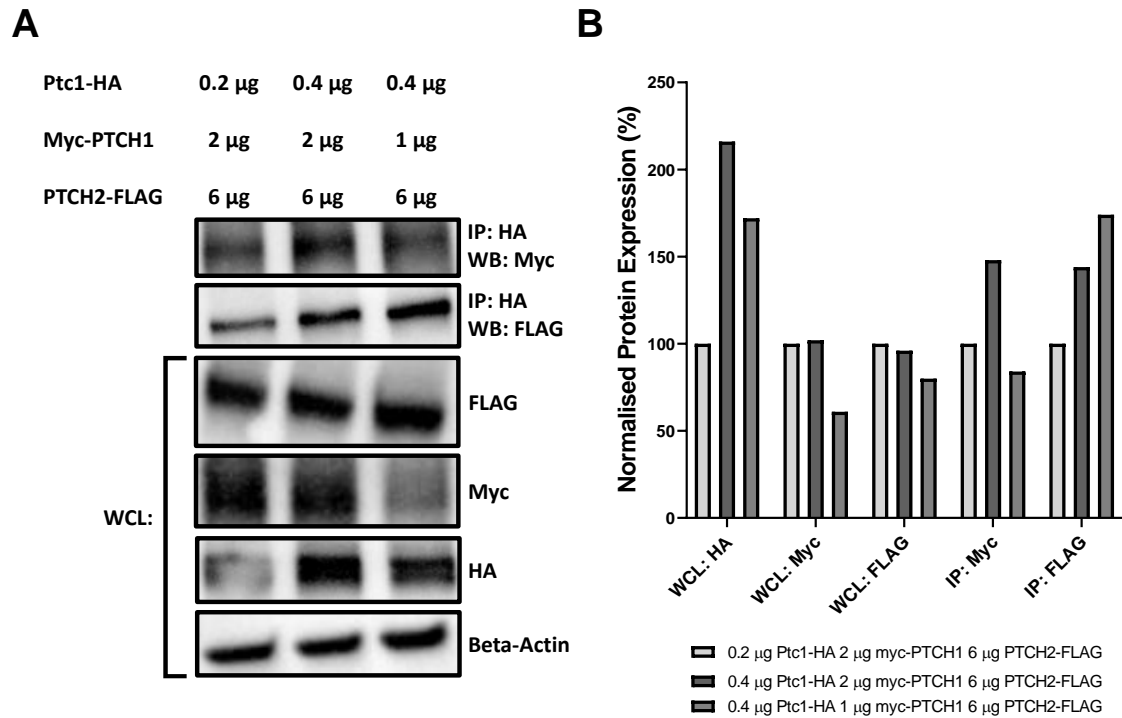


Figure 4.6 Excess over-expression of PTCH2 minimally impaired Patched 1 homo-interactions in HEK293 cells.

Competition-based Co-IP in HEK293 cells transiently co-transfected with Ptc1-HA, myc-PTCH1 and PTCH2-FLAG at the indicated concentrations. Total transfected DNA concentrations were kept consistent by addition of pcDNA 3.1⁺ where required. **(A)** Immunoprecipitation of myc-PTCH1 and PTCH2-FLAG with anti-HA antibody increased in a Ptc1-HA concentration dependent manner (lane 1 vs 2). A 50% reduction of transfected myc-PTCH1 (lane 3 vs 2) resulted in reduced myc-PTCH1 and increased PTCH2-FLAG immunoprecipitation with anti-HA antibody. **(B)** Densitometry analysis of Co-IP data. Conditions were normalised to Beta-actin and subsequently normalised within their own group to lane 1.

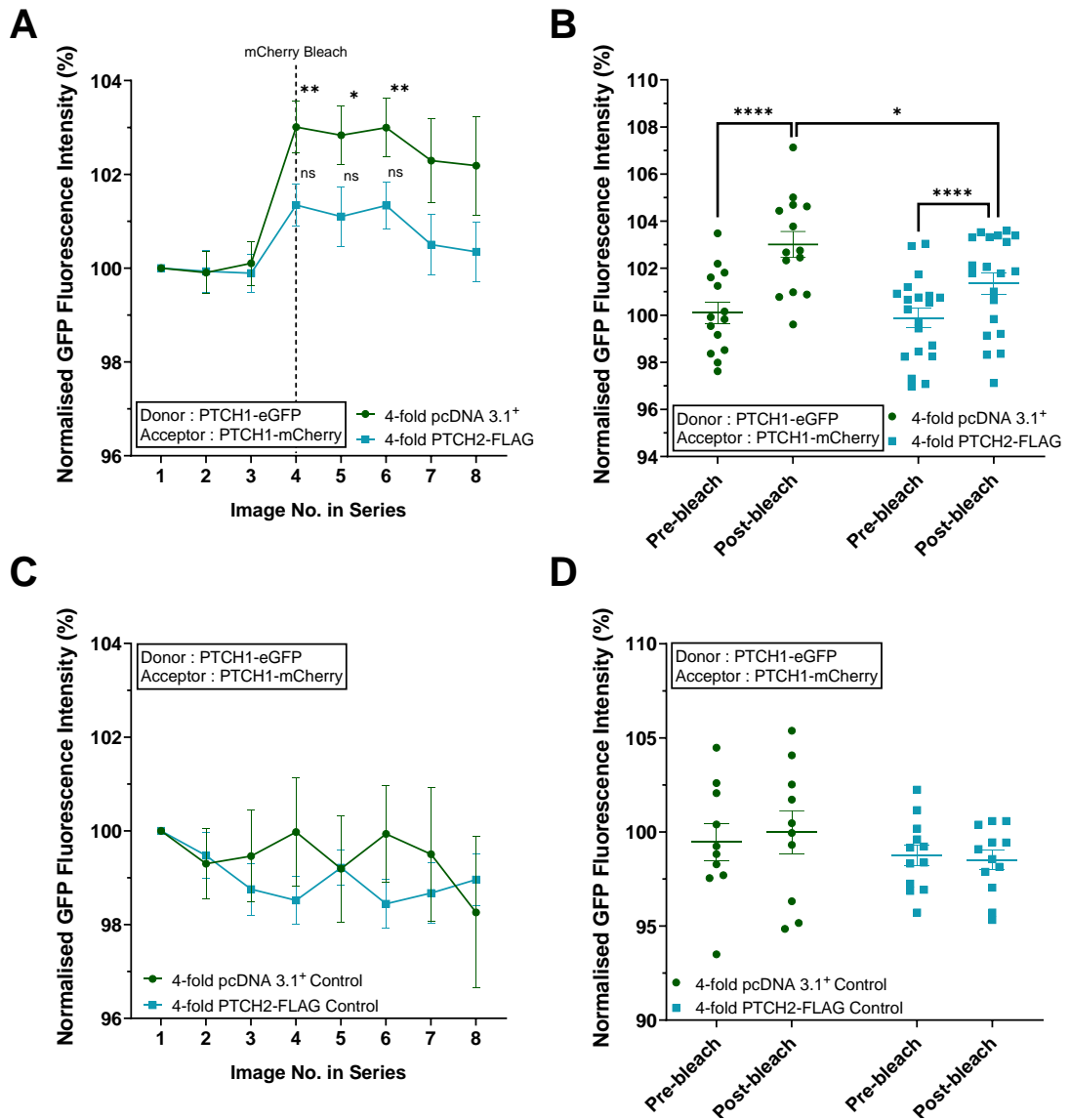


Figure 4.7 Competition-Based FRET assay confirmed an excess of PTCH2-FLAG reduced the frequency of PTCH1 homodimers.

(A) Co-transfection of 4-fold excess of PTCH2-FLAG significantly reduced PTCH1-eGFP:PTCH1-mCherry interactions in HEK293 cells, compared to co-transfection with 4-fold pcDNA 3.1⁺. Data points represent the average +/- SEM of 14 pcDNA 3.1⁺ and 20 PCTH2-FLAG bleached ROIs. Dashed line indicates start of mCherry photo-bleaching (100% 564 nm and 614 nm). **(B)** Separated scatter graph of pre and post bleach images show significant increase in GFP intensity post bleach for 4-fold pcDNA 3.1⁺ and PTCH2-FLAG. **(C&D)** Control no bleach ROIs of conditions in (A&B). There was no significant increase in normalised GFP or difference in rate of fluorophore photo-decay.

4.3.3 In the absence of Patched 1, Patched 2 displays low level activity, which is responsive to N-Shh.

The functional importance of Patched 2, in the context of canonical Patched 1 activities, remains largely unknown. As previously stated, this is a consequence of the highly dominant function of Patched 1, masking both overlapping and potentially divergent roles of Patched 2. The majority of studies affording any functional importance to Patched 2 were conducted within a Patched 1 depleted environment. The evidence that Patched 2 homodimers exist *in vitro*, and display close conformational similarities to that of Patched 1 homodimers, led to the question, do they also share functional characteristics?

Existing evidence that Patched 1 and 2 show similar affinities for their shared ligand, Sonic Hedgehog, suggests that their functional discrepancies arise at another section of the canonical pathway. A strong existing hypothesis is that Patched 2 might be competent in sequestering N-Shh, but infers low sub-stoichiometric inhibition on Smo when unbound by ligand. This could be due to a reduced ability to shuttle cholesterol, or a similar sterol derivative, when compared to Patched 1. Therefore, it was paramount to assess whether Patched 2 homodimers conferred any degree of inhibition on canonical Hh signalling, independent of Patched 1.

Gli luciferase assays, of transiently transfected *Ptc1*^{-/-} MEFs, were implemented to first confirm whether PTCH2 displayed any basal activity, independent of Patched 1. Transfection of Ptc1-HA or PTCH2-FLAG resulted in ~80% or ~20% reduction in Gli respectively (**Figure 4.8A**). Active Gli2 can directly drive the

Chapter 4: Patched homo- and heterodimer interactions display close resemblance, but differing canonical functionality, due to influences of the cytoplasmic domains

expression of Gli1 in a Smo dependent manner. The additional co-transfection of Gli2, alongside Ptc1-HA, PTCH2-FLAG or pcDNA 3.1⁺ further confirmed PTCH2 can significantly reduce Smo driven activation of Gli in cells devoid of Patched 1 **(Figure 4.8B)**.

To further support these findings that PTCH2 is capable of low level activity, additional Gli-luciferase assays were conducted in *Ptc1*^{-/-} MEFs, with and without treatment with KAAD-cyclopamine. KAAD-cyclopamine is a potent inhibitor of Smo, able to inhibit constitutive canonical activity, arising from a loss of Patched 1 function. Results indicated once more, that PTCH2-FLAG inhibited canonical signalling, independently to Patched 1 **(Figure 4.9)**. The addition of 5 µM KAAD-Cyclopamine to cells transfected with PTCH2-FLAG vs pcDNA 3.1⁺ resulted in a greater decrease in Gli. This is indicative of additional inhibition generated by PTCH2, not present in pcDNA 3.1⁺ conditions. Cells transfected with Ptc1-HA displayed the lowest level of Gli and this was unchanged by the addition of 5 µM KAAD-cyclopamine, suggesting maximal inhibition was achieved by Ptc1-HA alone.

To establish whether the inhibitory effects seen with Patched 1 and 2 were achieved through the same cellular mechanism, Hedgehog ligand was utilised. If like Patched 1, Patched 2 inhibits Smo in a sub-stoichiometric manner within the cilium, and can sequester ligand, then N-Shh would reduce inhibition of Gli. Therefore, Gli-luciferase assays were undertaken with the co-transfection of Ptc1-HA or PTCH2-FLAG with N-Shh or pcDNA 3.1⁺ negative control.

The results indicate that both Patched 1 and 2 were responsive to N-Shh, as shown by a reduction in Gli inhibition in co-transfected conditions **(Figure 4.10)**.

Chapter 4: Patched homo- and heterodimer interactions display close resemblance, but differing canonical functionality, due to influences of the cytoplasmic domains

The additional co-transfection of N-Shh to Ptc1-HA and PTCH2-FLAG conditions still showed greater inhibition than pcDNA 3.1⁺ control. The co-transfection of N-Shh and pcDNA 3.1⁺ increased Gli above the basal level seen in pcDNA 3.1⁺ control. This suggests maximal pathway activation is not achieved in the *Ptc1*^{-/-} MEFs, despite a loss of Patched 1. This further supports an activity of PTCH2, as these still retain a low level endogenous PTCH2 expression. It might be the activity of this PTCH2 that is overcome by the addition of N-Shh to pcDNA 3.1⁺ controls.

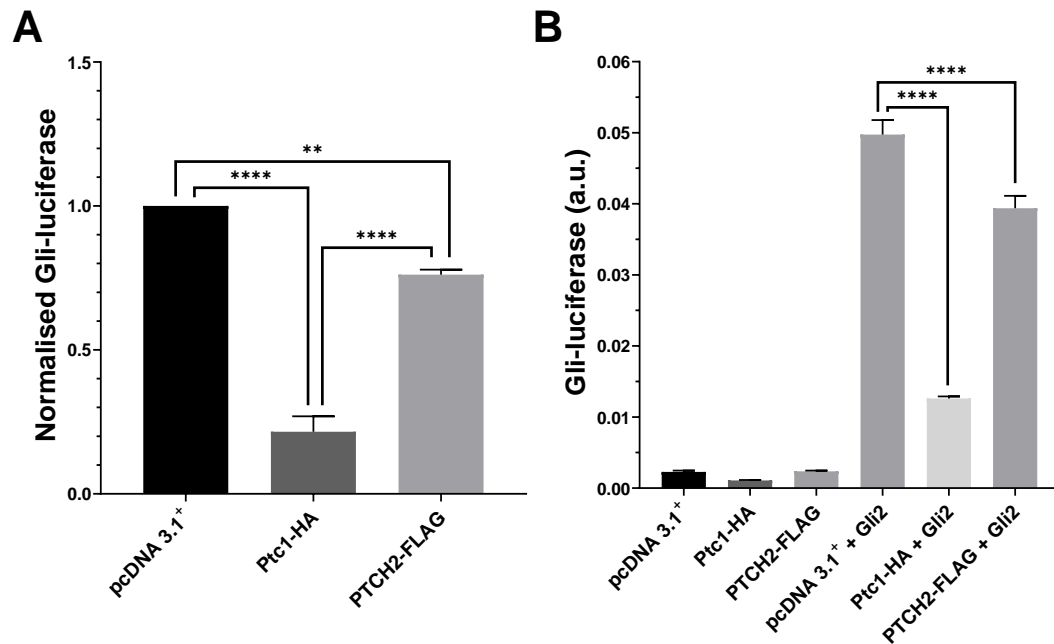


Figure 4.8 Patched 2 displays low level inhibition of the canonical Hh pathway, independent of Patched 1.

Gli-luciferase of transiently transfected *Ptc1*^{-/-} MEFs, with quadruplicate technical repeats per condition. **(A)** Normalised averages from 3 independent experiments, showing maximal inhibition by Ptc1-HA and lesser, but significant inhibition by PTCH2-FLAG. **(B)** Cells transiently co-transfected with pcDNA 3.1⁺, Ptc1-HA or PTCH2-FLAG +/- Gli2. Graph is a single representative experiment, performed in quadruplicate. Both Ptc1-HA and PTCH2-FLAG significantly reduced Gli in conditions co-transfected with Gli2.

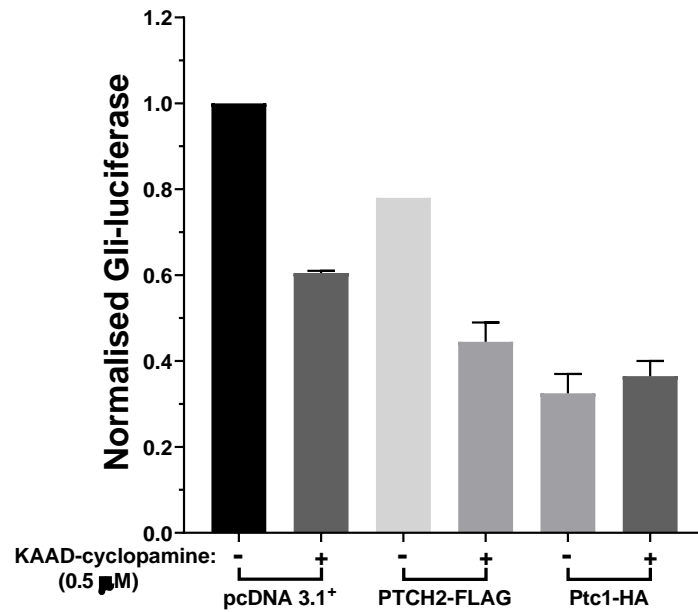


Figure 4.9 Treatment with KAAD-Cycloamine confirmed maximal inhibition achieved by Patched 1, but not PTCH2 alone.

Graph represents the average +/- SEM of 2 independent quadruplicate Gli-luciferase assays. Transiently transfected *Ptc1*^{-/-} MEFs were treated with 5 μM KAAD-Cycloamine or vehicle control.

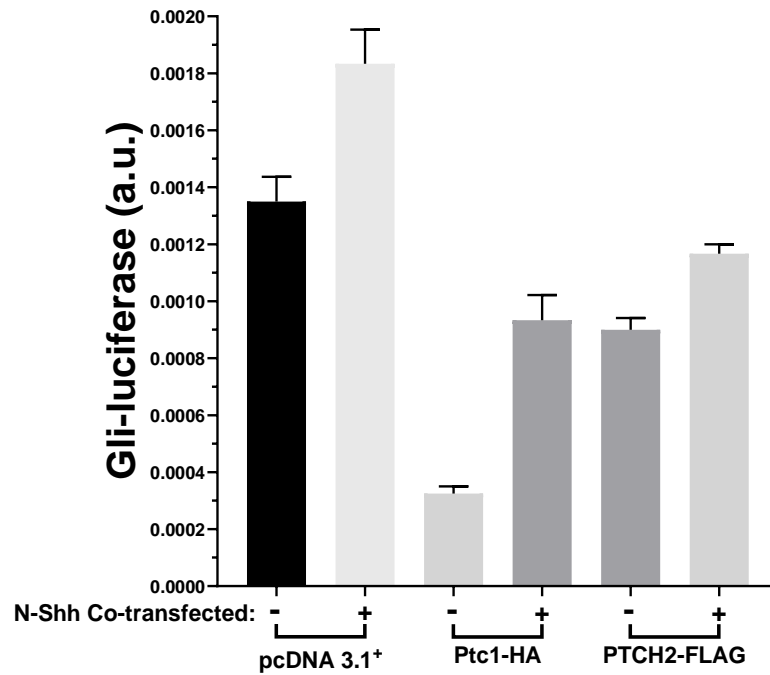


Figure 4.10 PTCH2 activity is responsive to N-Shh.

Graph shows the average \pm SEM of a representative Gli-luciferase, performed with quadruplicate technical repeats. *Ptc1*^{-/-} MEFs were co-transfected with pcDNA 3.1⁺, Ptc1-HA or PTCH2-FLAG with/without N-Shh.

4.3.4 Replication of a PTCH1 inactivating mutation in PTCH2 failed to impair activity.

The implementation of activity impeding mutations, as a method of understanding protein function, is one of the most established and successful approaches in molecular biology. Recent publications have converged on the concept that Patched 1 functions to inhibit Smo through the transportation of cholesterol. A PTCH1 mutant of particular interest, PTCH1-V111F, L114F, W115A, was reported to disrupt the integrity of a cholesterol channel, resulting in significantly diminished canonical function (Zhang et al., 2018).

To better understand the canonical activity state of Patched 2, in context of a cholesterol transportation function, the PTCH1-V111F, L114F, W115A mutations were semi-replicated in PTCH2. The resultant mutant, PTCH2-L82F, L85F, W86A, differed in the substitution of one residue, L82F, which is V111F in PTCH1. The presence of a leucine in PTCH2, instead of a valine, is unlikely to confer a substantial structural difference to that of PTCH1, as the two amino acids only differ by the addition of one methylene group.

Alignment of Ptc1 (PDB ID: 6MG8) and the secondary structure of PTCH2 (UniProtKB: Q9Y6C5) threaded to the template structure of PTCH1 (PDB ID: 6MG8) showed these three residues sit adjacent to a channel within the protein core (**Figure 4.11**). This channel has been found to contain a cholesterol-like density in non-ligand bound Patched 1 (Zhang et al., 2018). Conversely, in ligand bound PTCH1, the N-terminal palmitate of SHH has been shown to occupy this channel in one of the PTCH1 monomers (Qian et al., 2019).

Chapter 4: Patched homo- and heterodimer interactions display close resemblance, but differing canonical functionality, due to influences of the cytoplasmic domains

The two corresponding mutants, PTCH2-L82F, L85F, W86A and PTCH1-V111F, L114F, W115A were generated in tandem by QuikChange XL II mutagenesis. In total, four plasmids; PTCH2-LLW-FLAG, PTCH2-LLW-mCherry, PTCH1-VLW-eGFP and PTCH1-VLW-mCherry, were created and validated by Sanger sequencing.

In order to rule out any possible impairment to localisation, protein maturity and oligomerisation capabilities, arising from the mutations, both PTCH1-VLW and PTCH2-LLW were analysed by the FRET-based assay previously described. In brief, PTCH1-VLW-mCherry was co-transfected with either PTCH1-eGFP or PTCH1-VLW-eGFP and assessed for direct interactions, against PTCH1-eGFP and PTCH1-mCherry homodimers. All 3 combinations of PTCH1 co-transfections resulted in a significant increase in normalised GFP fluorescence intensity, post mCherry photo-bleaching (**Figure 4.12A**). Separate scatter graphs of the individual ROIs (post-bleach image/pre-bleach image) confirmed a comparable increase in GFP intensity in all conditions (**Figure 4.12B**). This confirms that the mutation of V111F,L114F,W115A does not impair PTCH1 protein expression or co-localisation and interaction with full length PTCH1, or itself.

Analysis of HEK293 cells, co-transfected with either PTCH2-eGFP and PTCH2-mCherry, or PTCH2-eGFP and PTCH2-LLW-mCherry, confirmed a significant increase in normalised GFP fluorescence intensity post mCherry photo-bleaching (**Figure 4.13**). This confirmed the mutation of L82F, L85F, W86A did not impair PTCH2 protein expression or co-localisation and interaction with full-length PTCH2.

Chapter 4: Patched homo- and heterodimer interactions display close resemblance, but differing canonical functionality, due to influences of the cytoplasmic domains

The activity state of the two Patched mutants was assessed by Gli-luciferase assay, as previously described. Consistent with the findings of Zhang et al., (2018), the mutation of PTCH1 residues V111F,L114F,W115A impaired PTCH1 activity in *Ptc1*^{-/-} MEFs (**Figure 4.14A**). PTCH1-VLW-eGFP displayed ~15% inhibition of Gli, compared to ~80% by Ptc1-HA.

However, mutation of PTCH2 residues L82F,L85F,W86A did not result in a significant decrease in activity, compared to PTCH2 (**Figure 4.14B**). Consistent with previous results, PTCH2-FLAG showed a significant inhibition of Gli (~20%), compared to pcDNA 3.1⁺. Although PTCH2-LLW activity was not significantly reduced, the SEM was notably larger than that of the corresponding pcDNA 3.1⁺ and PTCH2-FLAG conditions.

One important feature of these luciferase assays to note, is that although PTCH1-VLW-eGFP had severely reduced activity, it still retained some limited function (~15%). At maximal activity, PTCH2 displays ~20% inhibition of Gli, providing a narrow range of function to assess the impact of the mutation, PTCH2-LLW. As a consequence, the sensitivity range of the Gli-luciferase might not afford the required quantitative accuracy, to significantly distinguish these two PTCH2 plasmids. Further repeats of this experiment could reduce the SEM and potentially reveal a significant difference in activity to PTCH2.

To further establish an activity of Patched 2, independent of Patched 1, a stable *Ptc2* KO was attempted in *Ptc1*^{-/-} MEFs. For this work, CRISPR/Cas9 was favoured over siRNA and TALENs techniques, that have previously shown low, variable success rates in the KO of Patched 2 (Veenstra et al., 2018). To this end, specific single guide RNAs targeting the second exon in *Ptc2* were selected using

Chapter 4: Patched homo- and heterodimer interactions display close resemblance, but differing canonical functionality, due to influences of the cytoplasmic domains

Benchling (Biology Software) (2020). These sgRNA primers were sub-cloned into a lentiCRISPR Lko vector, with successful integration confirmed by Sanger sequencing.

Ptc1^{-/-} MEFs were subsequently transfected and single colonies isolated by puromycin selection. After the expansion of isolated single colonies, two clones of interest were investigated further. One clone, 'Ptc2 CRISPR KO Clone 1 *Ptc1*^{-/-} MEFs' referred to as 'Ptc2-KO1' from here, showed promise of successful Ptc2 KO. Total DNA was isolated and processed for validation by Sanger sequencing, but priming was non-specific. Unfortunately, at the time of this submission, further DNA isolation and Sanger sequencing has not been completed.

Despite this, Gli-luciferase assays already conducted with Ptc2-KO1, found an increase in sensitivity to transfected PTCH2 vs *Ptc1*^{-/-} MEFs (**Figure 4.15**). Each cell group was normalised to their corresponding pcDNA 3.1⁺ control, so that changes in Gli between the groups were relative. Transfection of PTCH2-FLAG achieved ~23% inhibition of Gli in *Ptc1*^{-/-} MEFs, compared to ~68% in Ptc2-KO1 cells. Meanwhile, Ptc1-HA transfection produced a similar level of inhibition in *Ptc1*^{-/-} MEFs (~83%) and Ptc2-KO1 (~81%). These findings strongly suggest a significant change in Ptc2-KO1 cells, which is specific to their responsiveness to PTCH2 and not Ptc1. The apparent increased activity of transfected PTCH2 in these cells might result from higher basal Gli activity, through the loss of endogenous Ptc2, from the CRISPR KO.

Chapter 4: Patched homo- and heterodimer interactions display close resemblance, but differing canonical functionality, due to influences of the cytoplasmic domains

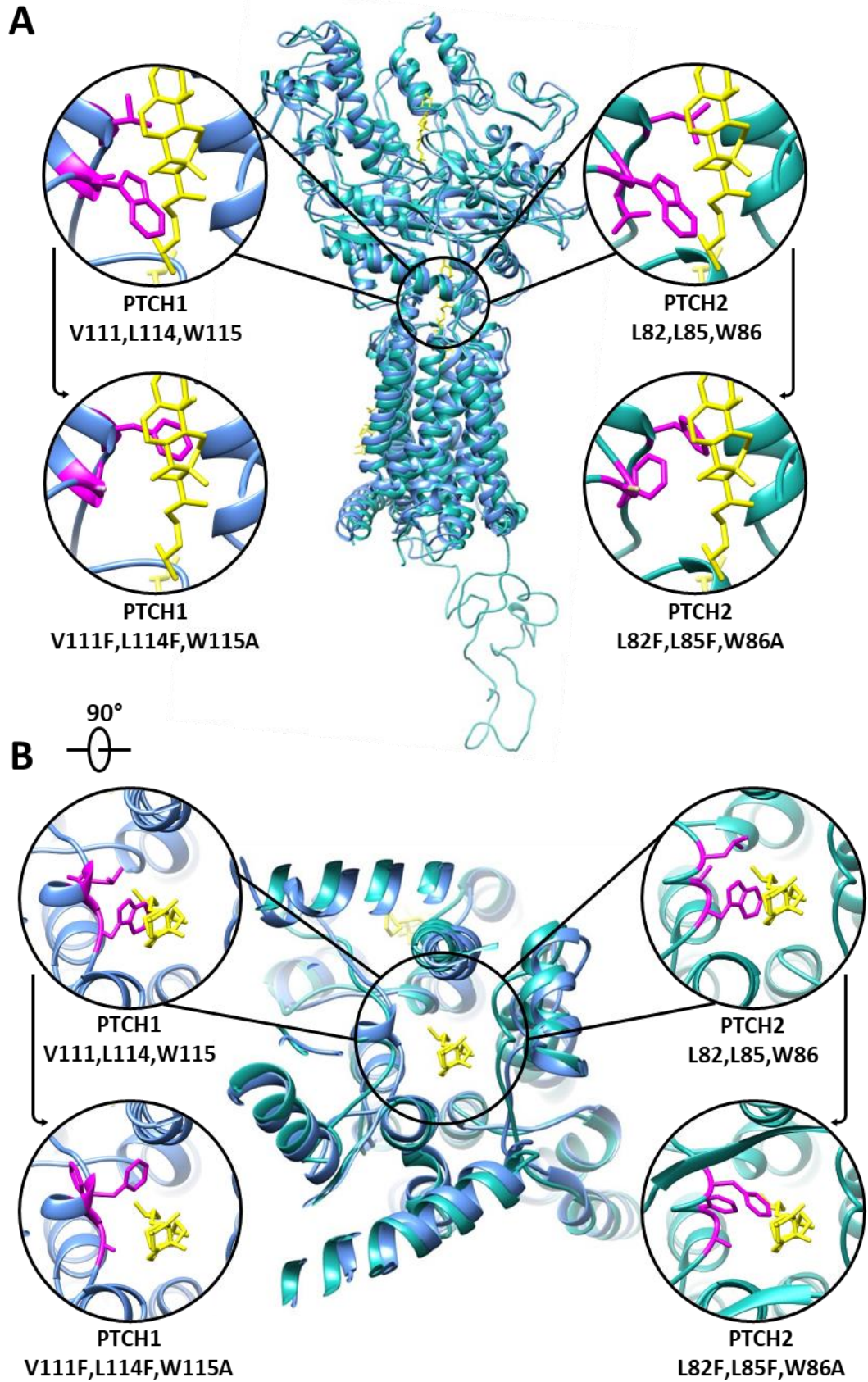


Figure 4.11 Structural alignment of Ptc1 (PDB ID:) and the secondary sequence of PTCH2, threaded to PTCH1 (PBD ID:) Indicating the predicted location and side chain alterations of residues identified to impair canonical function.

Front **(A)** and top down **(B)** structural comparison of Ptc1 (PDB ID: 6MG8) shown in blue, aligned with the protein sequence of PTCH2 (UniProtKB: Q9Y6C5), threaded to the structural template of Ptc1 (PDB ID: 6MG8) shown in turquoise. The putative sterol channel is indicated by a black ring, with expanded views displaying the mutational targeted Ptc1 or PTCH2 residues, in magenta, on the left and right respectively. Cholesterol-like densities are displayed in yellow. The top expansion windows display original residues and their side chains, whilst the windows beneath display the predicted mutational alterations to side-chains. Structural analysis and alterations were performed in Chimera (Pettersen et al., 2004).

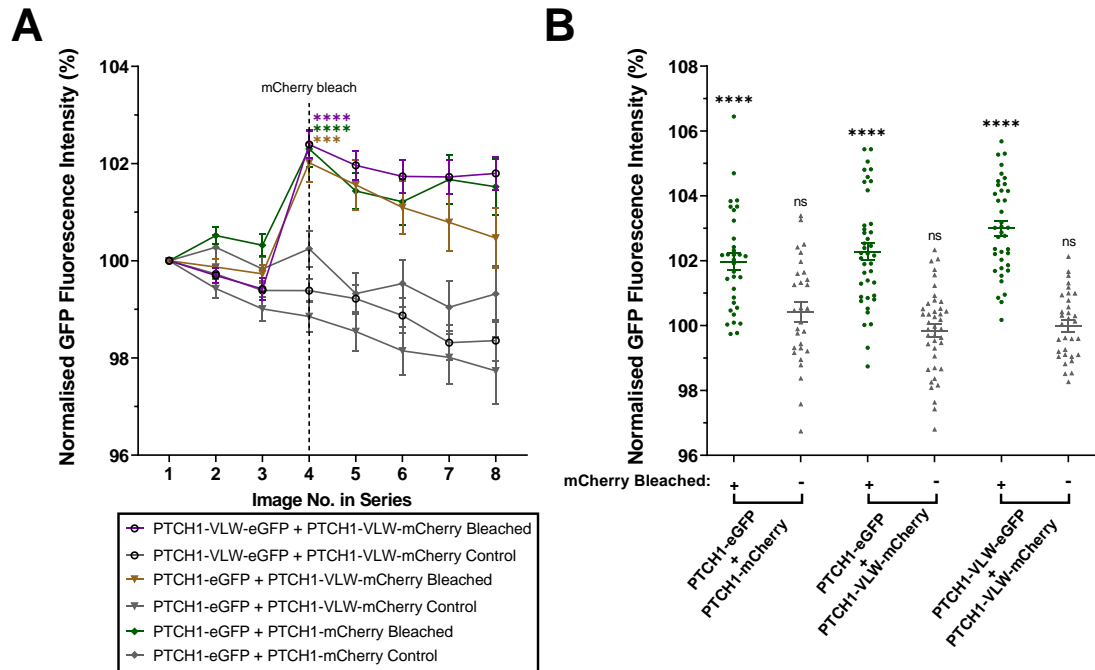


Figure 4.12 PTCH1-VLW forms homo-interactions with itself and with full length PTCH1 in HEK293 cells, despite a reported lack of activity.

(A) Normalised GFP fluorescence intensity values of PTCH1-eGFP and PTCH1-VLW-eGFP reveal a significant increase after photo-bleaching of PTCH1-mCherry or PTCH1-VLW-mCherry. Graph shows average +/- SEM of 30-41 individual ROIs. No significant differences in fluorophore photo-decay rate was seen between the various PTCH1 monomer combinations. **(B)** Separated scatter graph of pre and post bleach images show significant increase in GFP intensity in all post bleach conditions, but not unbleached controls.

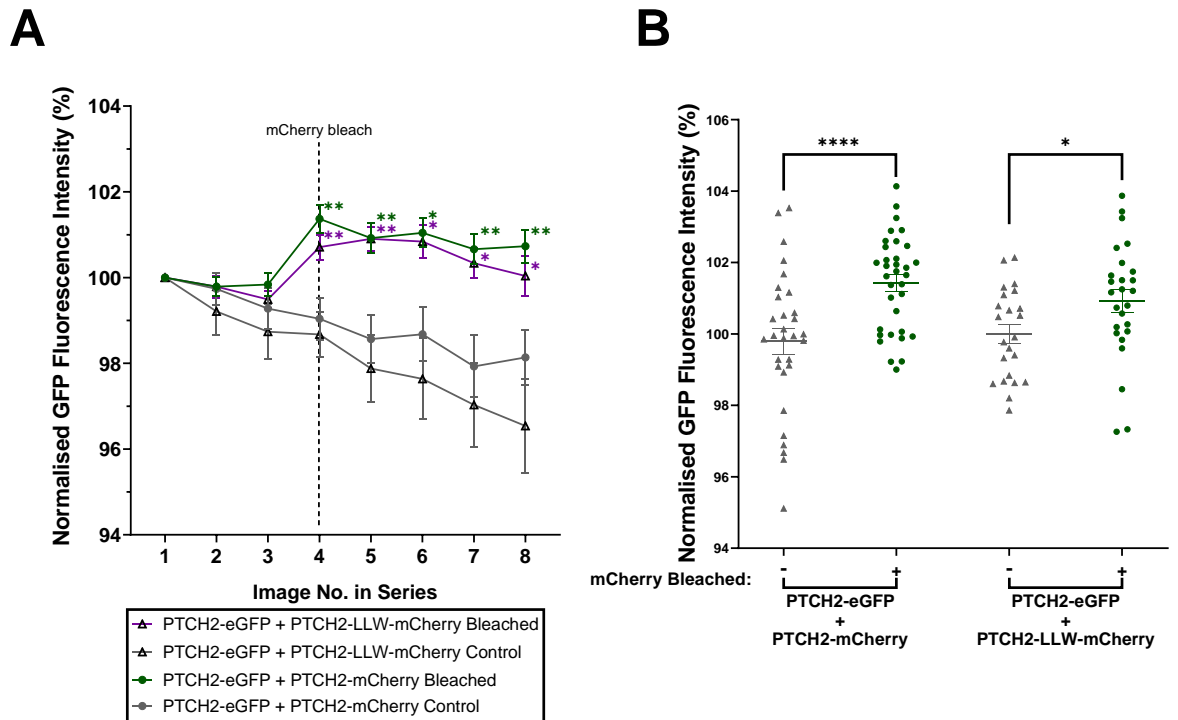


Figure 4.13 PTCH2-LLW, forms homo-interactions with full length PTCH2 in HEK293 cells.

(A) Normalised GFP fluorescence intensity values of PTCH2-eGFP reveal a significant change after the photo-bleaching of PTCH2-mCherry or PTCH2-LLW-mCherry. Graph shows average \pm SEM of 22-32 individual ROIs. No significant differences in fluorophore photo-decay rate was seen between the two Patched monomer combinations. **(B)** Separated scatter graph showing the change in GFP fluorescent intensity for individual ROIs of post-bleach/pre-bleach (image 4/image 3). A significant increase in GFP fluorescent intensity in bleached samples compared to unbleached controls.

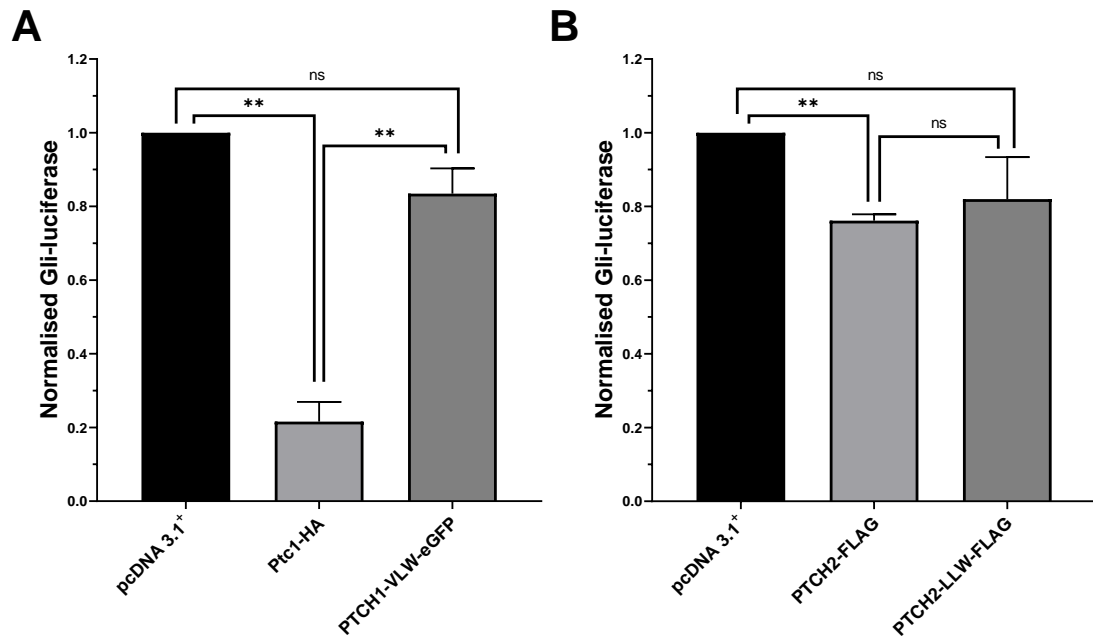


Figure 4.14 PTCH1-VLW has significantly reduced activity, whilst PTCH2-LLW shows no significant difference in activity.

Gli-luciferase assays performed in *Ptc1*^{-/-} MEFs. Graphs display the average +/- SEM of 3 individual experiments, each performed with quadruplicate technical repeats. **(A)** Transfection with Ptc1-HA displayed strong inhibition of Gli, whilst transfection with PTCH1-VLW-eGFP showed no significant inhibition. **(B)** No significant difference in inhibition was detected between PTCH2-FLAG and PTCH2-LLW-FLAG.

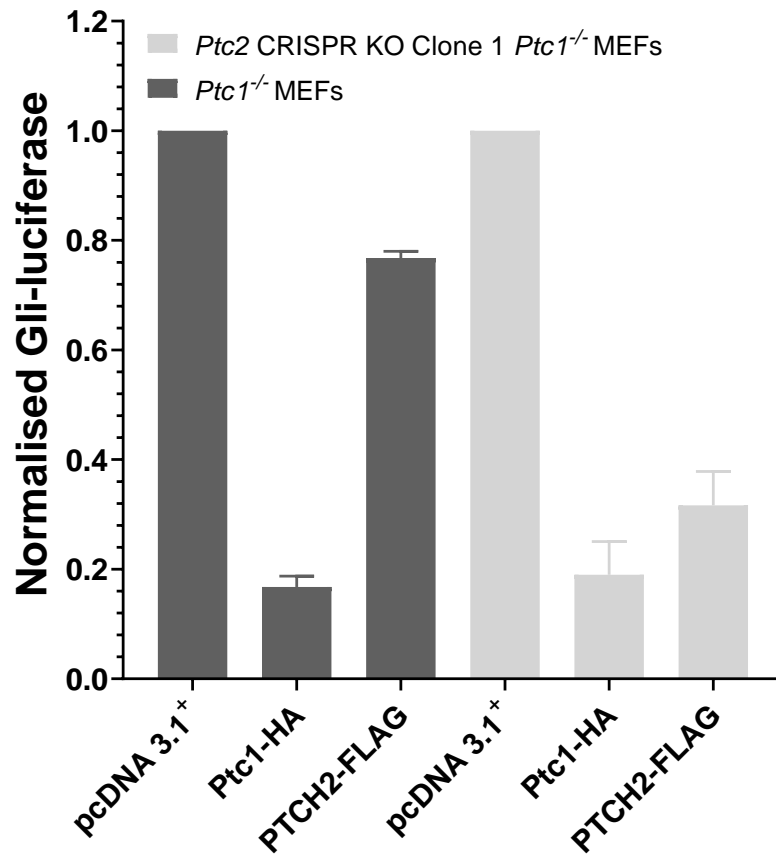


Figure 4.15 *Ptc1*^{-/-} MEFs Selected for *Ptc2* CRISPR KO displayed higher sensitivity to transfected PTCH2.

Gli-luciferase assay performed in *Ptc1*^{-/-} MEFs and *Ptc2* CRISPR KO Clone 1 *Ptc1*^{-/-} MEFs. Graphs display the average +/- SEM of 3 individual experiments, each performed with quadruplicate technical repeats. Each cell group has been normalised to their own pcDNA 3.1⁺ negative control. At the time of submission of this work, confirmation of a successful *Ptc2* KO by Sanger sequencing remained unverified.

4.3.5 Replication of a PTCH1 Gorlin Syndrome related mutation in

PTCH2 simulated a cancerous phenotype, only in the absence of Ptc1.

Due to the limited success in inhibiting Patched 2, through the replication of the impaired PTCH1-VLW mutant, a second, more clinically relevant mutation, PTCH1-D513A, was replicated in PTCH2. A functional impact pertaining to this mutation was first demonstrated in the corresponding aspartic acid of Mouse Ptc1 D499 (Taipale et al., 2002). The 'GxxxDD' motif residing within TM 4 is a highly conserved feature, also seen in trimeric RND proteases and is essential for Patched function. A study of the germline of NBCCS patients identified PTCH1 D513Y within a TM 4 cluster of substitution mutations (Wicking et al., 1997). Recent publications indicate the interaction of D513 with E1095, of TM 10, to maintain a hydrophobic cavity, via the formation of a salt bridge (Kowatsch et al., 2019; Zhang et al., 2020). Mutation of D513 results in a Patched 1 that has reduced canonical activity, but still binds N-Shh.

The corresponding aspartic acid in PTCH2 was identified as D469, by sequence alignment with PTCH1. The predicted structural location of PTCH2-D469 was compared to that of Ptc1-D499 by structural comparison. As of yet, no structure exists for PTCH2, so a model was generated using the online and template depository, Swiss-Model. Briefly, the secondary structure of PTCH2 was threaded through a known structural template of Ptc1 (PDB ID: 6MG8). The resulting structure was then aligned to Ptc1 (PDB ID: 6GM8). As expected, PTCH2 residues D469, E1031 and T1069 displayed a similar location and orientation to that of the known Ptc1 triad, D499, E1081 and T1119 (**Figure 4.16**).

Chapter 4: Patched homo- and heterodimer interactions display close resemblance, but differing canonical functionality, due to influences of the cytoplasmic domains

Therefore, mutation of PTCH2 D469 was a strong candidate to further establish structural similarity to Patched 1. If the triad of interaction partners was a pivotal feature for PTCH2 function, a substitution to alanine would be a logical choice. Alanine cannot form side chain hydrogen bonds and is unlikely to physically disrupt the helices. Hence the suggested hydrogen bond between D499 and E1081 in Ptc1 would be lost in D469A, if it is also natively present in PTCH2.

PTCH2-D469A-FLAG was generated by QuikChange XL II mutagenesis with successful cloning confirmed by Sanger sequencing and western blot. Initial immunofluorescence imaging, in transiently transfected HEK293 cells, showed a potential altered protein localisation profile for PTCH2-D469A-FLAG (**Figure 4.17**). A difference in localisation was also noted for PTCH2-LLW-FLAG, which as previously discussed, yielded no significant difference, mechanistically to PTCH2-FLAG. Observational differences in fixed cell immunofluorescence are not always a strong predictor of functional relevancy.

To determine the activity state of PTCH2-D469A-FLAG, Gli-luciferase assays were conducted in *Ptc1*^{-/-} MEFs. In agreement with results from (**Figure 4.14**), transfection of either PTCH2-FLAG or PTCH2-LLW-FLAG produced a reduction in Gli, compared to pcDNA 3.1⁺ control (**Figure 4.18**). However, transfected PTCH2-D469A-FLAG showed no activity, with Gli levels higher than that to the pcDNA 3.1⁺ control (**Figure 4.18**). Interestingly, firefly luciferase and *Renilla* luciferase values for conditions transfected with PTCH2-D469A-FLAG were significantly higher, at ~2-fold that of the pcDNA 3.1⁺ control. This increase was consistently observed in Gli-luciferase assays of PTCH2-D469A-FLAG to varying degrees of magnitude. This increase did appear to be concentration associated,

Chapter 4: Patched homo- and heterodimer interactions display close resemblance, but differing canonical functionality, due to influences of the cytoplasmic domains

as reductions in transfected DNA yielded small fold increases compared to pcDNA 3.1⁺ controls (data not shown). Taking this finding into consideration alongside the altered localisation by immunofluorescence, PTCH2-D469A-FLAG appears to inflict an increase in cell division and/or cell survival. Moreover, this effect appears to be distinct from the canonical function of PTCH2, as PTCH2-D469A-FLAG showed no activity in Gli-luciferase assays.

Transfection of PTCH2-D469A-FLAG consistently showed increased Gli levels, compared to pcDNA 3.1⁺ controls. It is possible that these observations were a result of PTCH2-D469A-FLAG interactions with endogenous PTCH2, impairing its function. As shown in a previous Gli-luciferase, N-Shh co-transfection with pcDNA 3.1⁺ increased Gli above the basal level in pcDNA 3.1⁺ controls (**Figure 4.10**). This was suggestive of endogenous Ptc2 activity being inhibited by N-Shh, through its binding.

To further establish that PTCH2-D469A-FLAG was inactive, Gli-luciferase with/without KAAD-cyclopamine (5 μ M) treatment were performed. As seen previously, PTCH2-D469A-FLAG displayed no activity alone (**Figure 4.19**). Treatment with KAAD-cyclopamine (5 μ M) in PTCH2-D469A-FLAG transfected cells resulted in a smaller reduction in Gli, compared to conditions of Ptc1-HA or PTCH2-FLAG + KAAD-cyclopamine. It is possible that the reduced effect of KAAD-cyclopamine in PTCH2-D469A-FLAG transfected cells stems from the pro-survival effect observed. In this assay, values for PTCH2-D469A-FLAG were ~7.5-fold (-KAAD-cyclopamine) and ~5.8-fold (+KAAD-cyclopamine) greater than pcDNA 3.1⁺. In comparison, PTCH2-FLAG values were 0.86-fold (-KAAD-cyclopamine) and 1.2-fold (+KAAD-cyclopamine) compared to pcDNA 3.1⁺.

Chapter 4: Patched homo- and heterodimer interactions display close resemblance, but differing canonical functionality, due to influences of the cytoplasmic domains

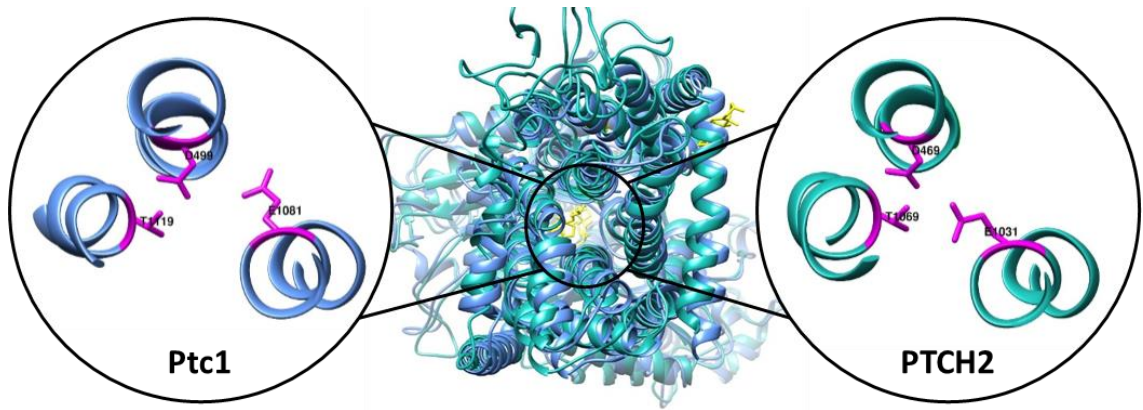


Figure 4.16 Structural comparison of Ptc1-D499 and PTCH2-D469 and their predicted interaction partners.

Comparison of the predicted position of PTCH2-D469 to that of Ptc1-D499. The protein structures are depicted from a bottom-top viewpoint. Ptc1 (PDB ID: 6MG8) is shown in blue. PTCH2, shown in green, represents the secondary structure, threaded into the template structure of Ptc1 (PDB ID: 6MG8). Protein threading was performed in the online and template depository, Swiss-Model (Waterhouse et al., 2018). The Aspartic acid in question and two known interaction partners are shown with side chains in magenta.

Chapter 4: Patched homo- and heterodimer interactions display close resemblance, but differing canonical functionality, due to influences of the cytoplasmic domains

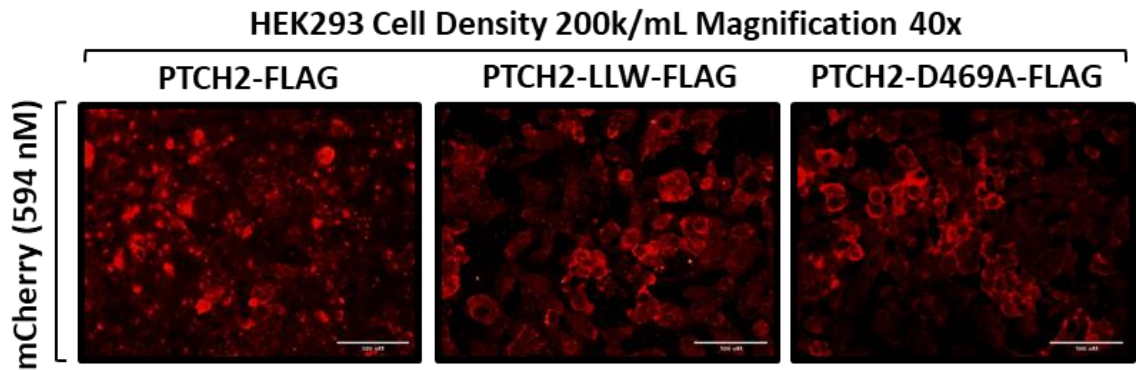


Figure 4.17 Immunofluorescence revealed altered localisation for PTCH2-D469A in HEK293 cells.

HEK293 cells were transiently transfected and fixed in 4% paraformaldehyde ~24 h post transfection. PTCH2 protein expression was imaged with anti-FLAG antibody (Proteintech) and secondary Goat anti-Mouse AlexaFluor 594 antibody (Thermofisher). Cells were imaged at 40 x magnification on an EVOS fluorescent light microscope, using the Texas red (594 nm) filter block. Scale bar, 100 μ M.

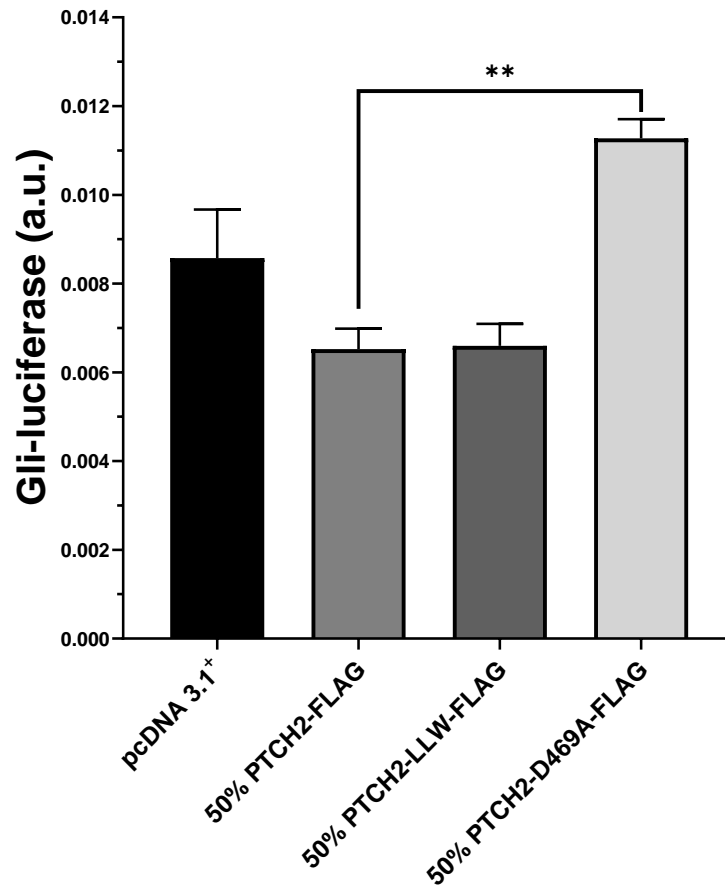


Figure 4.18 PTCH2-D469A showed significantly impaired activity.

Gli-luciferase in *Ptc1*^{-/-} MEFs with mean +/- SEM of quadruplicate technical repeats. PTCH2-D469A-FLAG displayed a significant reduction in the inhibition of Gli, compared to PTCH2-FLAG and PTCH2-LLW-FLAG.

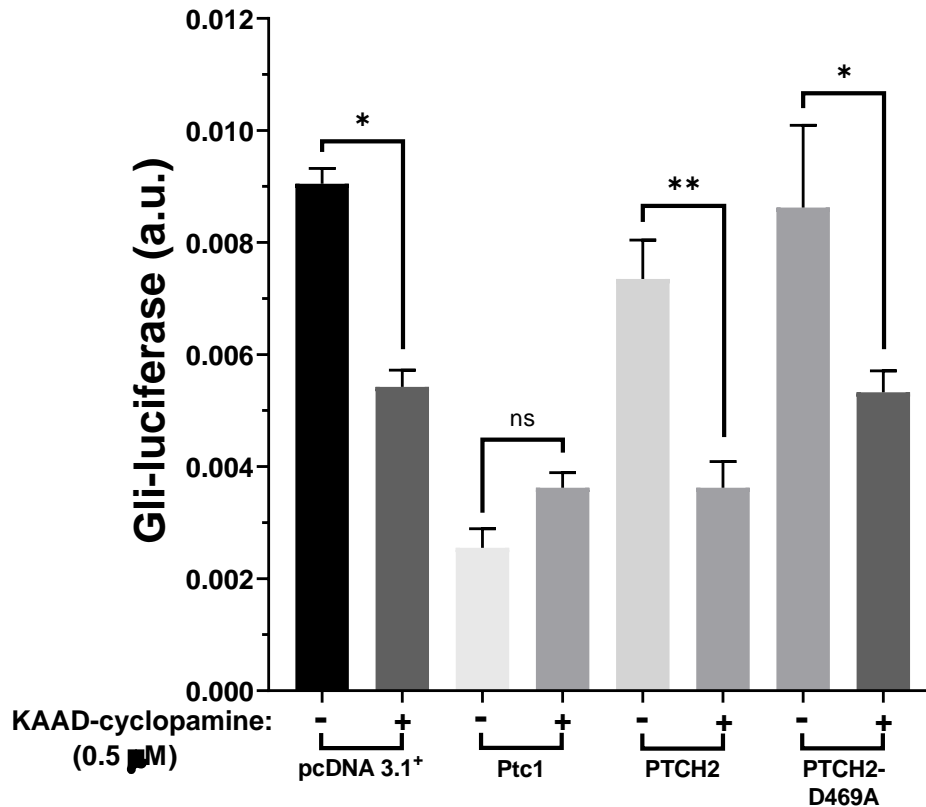


Figure 4.19 KAAD-cyclopamine treatment is less effective in cells transfected with PTCH2-D469A, compared to Ptc1 or PTCH2.

Gli-luciferase in *Ptc1*^{-/-} MEFs with mean +/- SEM of quadruplicate technical repeats. Cells were treated with KAAD-cyclopamine (0.5 μM) or vehicle control. PTCH2-D469A-FLAG + KAAD-cyclopamine achieved an inhibition similar to pcDNA 3.1+ + KAAD-cyclopamine. Whilst Ptc1-HA + KAAD-cyclopamine and PTCH2-FLAG + KAAD-cyclopamine achieved a greater inhibition of Gli.

4.3.6 Patched hetero-interactions confer synergistic canonical activity, in a Patched 1 activity-dependent manner.

To determine whether heterodimers of Patched were functionally relevant, canonically, various ratios of the two plasmids Ptc1-HA and PTCH2-FLAG were co-transfected in *Ptc1*^{-/-} MEFs and subjected to Gli-luciferase assays. As previously described, *Ptc1*^{-/-} MEFs were utilised to ensure the effects measured from transfected conditions were uninfluenced by endogenous Ptc1. To establish their basal activities, Patched 1 and 2 were transfected alone at 100% and 50% (supplemented with 50% pcDNA 3.1⁺). These conditions were compared with the co-transfection of Ptc1-HA and PTCH2-FLAG (50%/50%), to identify any changes in canonical activity.

Consistent with previous Gli-luciferase, 100% Ptc1-HA showed strong activity, whilst 100% PTCH2 showed reduced, but still significant activity (**Figure 4.20**). Both the conditions, 50% Ptc1-HA and 50% PTCH2-FLAG displayed significantly reduced activity compared to their respective 100% conditions. Interestingly, the co-transfection of Ptc1-HA and PTCH2-FLAG (50%/50%) achieved a strong inhibition of Gli that was not significantly different to 100% Ptc1-HA (**Figure 4.20**).

This finding suggests a synergistic interaction between PTCH2 and Ptc1, where the overall level of activity together, was greater than the sum of the individual activities. Indeed, transfection of 50% Ptc1-HA and PTCH2-FLAG alone achieved ~45% and ~12% inhibition respectively. Meanwhile, co-transfection of Ptc1-HA and PTCH2-FLAG (50%/50%) achieved the same average percentage Gli inhibition as 100% Ptc1-HA (~76%). There are several possible explanations for

Chapter 4: Patched homo- and heterodimer interactions display close resemblance, but differing canonical functionality, due to influences of the cytoplasmic domains

this finding; Patched 2 might require the presence of Patched 1 for maximal activation; the formation of heterodimers might dilute the pool of Patched 1 homodimers, and/or; Patched heterodimers may exhibit reduced turnover or increased ciliary retention.

To determine whether the increased activity observed for co-transfected conditions was driven by a specific Patched monomer within the heterodimer, mutant proteins were assessed. The PTCH1-VLW-eGFP and PTCH2-LLW-FLAG plasmids, previously discussed in Results (4.3.4), were assessed for an ability of either Patched 1 or 2 to drive increased activity when co-transfected. Co-transfection of a canonically functional Ptc1-HA, with either PTCH2-FLAG or PTCH2-LLW-FLAG resulted in an increased activity (**Figure 4.21A**). Whereas, co-transfection of the canonically impaired PTCH1-VLW-eGFP, with either PTCH2-FLAG or PTCH2-LLW-FLAG, failed to achieve any detectable increase in activity (**Figure 4.21B**).

These results strongly suggests that the synergistic interaction of Patched heterodimers is limited by the activity state of the Patched 1 monomer involved. Not only was PTCH2 unable to assist the canonically impaired PTCH1-VLW-eGFP, overall activity was potentially worse in co-transfected conditions (**Figure 4.21B**). This could imply that mutations that impair Patched 1 have secondary impact on Patched 2 activity. If so, this mechanism has almost certainly been overlooked during developmental experiments of Patched 1 KO's.

To this end, the contributions of Patched 2 in development might have been attributed solely to Patched 1, because a complete loss or severe functional impairment to Patched 1 prevents these events from occurring. Conversely,

Chapter 4: Patched homo- and heterodimer interactions display close resemblance, but differing canonical functionality, due to influences of the cytoplasmic domains

perturbed Patched 2 function is likely masked by a functional Patched 1. This notion is supported by the finding that PTCH2-D469A-FLAG, could also achieve increased Gli inhibition when co-transfected with Ptc1-HA (50%/50%) (**Figure 4.22**). PTCH2-D469A-FLAG was already confirmed to be non-functional and to promote pro-survival and cell division (**Figure 4.18**). Not only was the degree activity in PTCH2-D469A-FLAG + Ptc1-HA (50%/50%) similar to 100% Ptc1-HA, it was also comparable to PTCH2-FLAG and PTCH2-LLW-FLAG + Ptc1-HA (50%:50%) conditions. This further supports the idea that the activity state of Patched 1 and not Patched 2, is essential to the synergistic effect observed.

Even more strikingly, firefly luciferase and *Renilla* luciferase values of PTCH2-D469A-FLAG + Ptc1-HA co-transfections were grossly normal (~0.96-fold). This finding was also replicated in co-transfection of PTCH2-D469A-FLAG and PTCH1-VLW-eGFP, the impaired Patched 1 mutant.

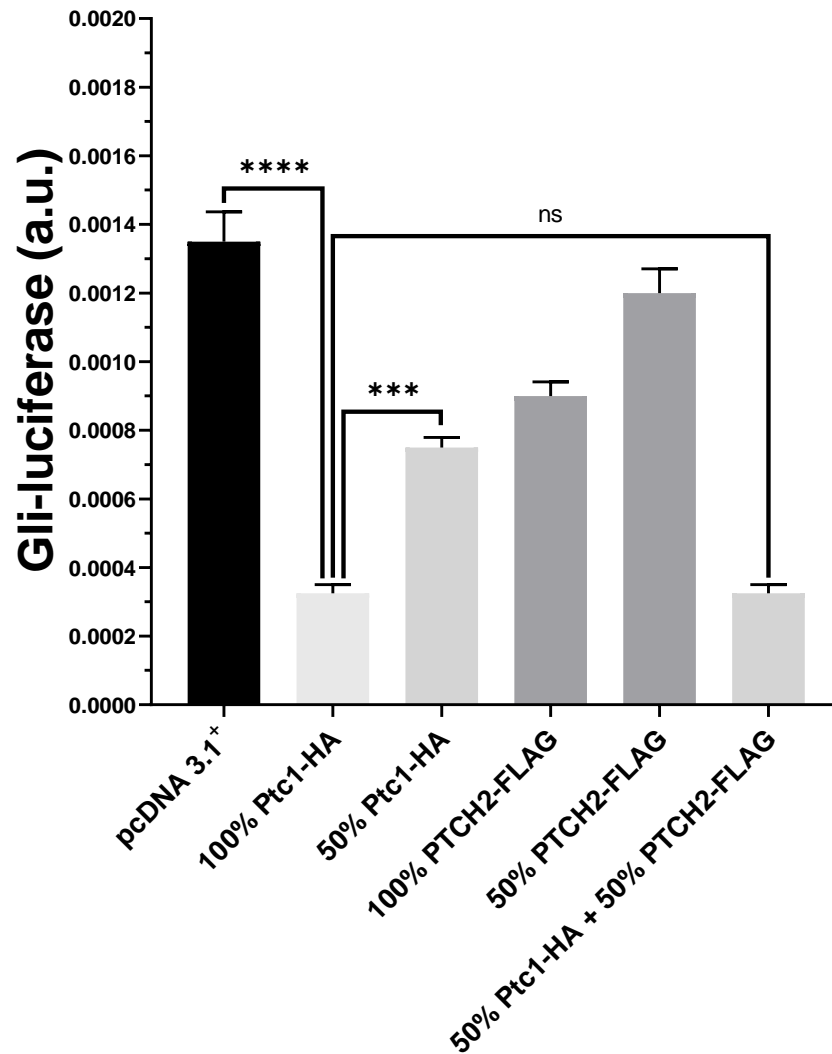


Figure 4.20 Patched heterodimer interactions conferred additional Gli inhibition activity.

Graph shows the mean \pm SEM of a representative Gli-luciferase in *Ptc1*^{-/-} MEFs, performed with quadruplicate technical repeats. Cells were transiently transfected with Ptc1-HA and PTCH2-FLAG individually, at 100% and 50%, and co-transfected at 50% each. Inhibition achieved by 50% Ptc1-HA + 50% PTCH2-FLAG was equal to that of 100% Ptc1-HA.

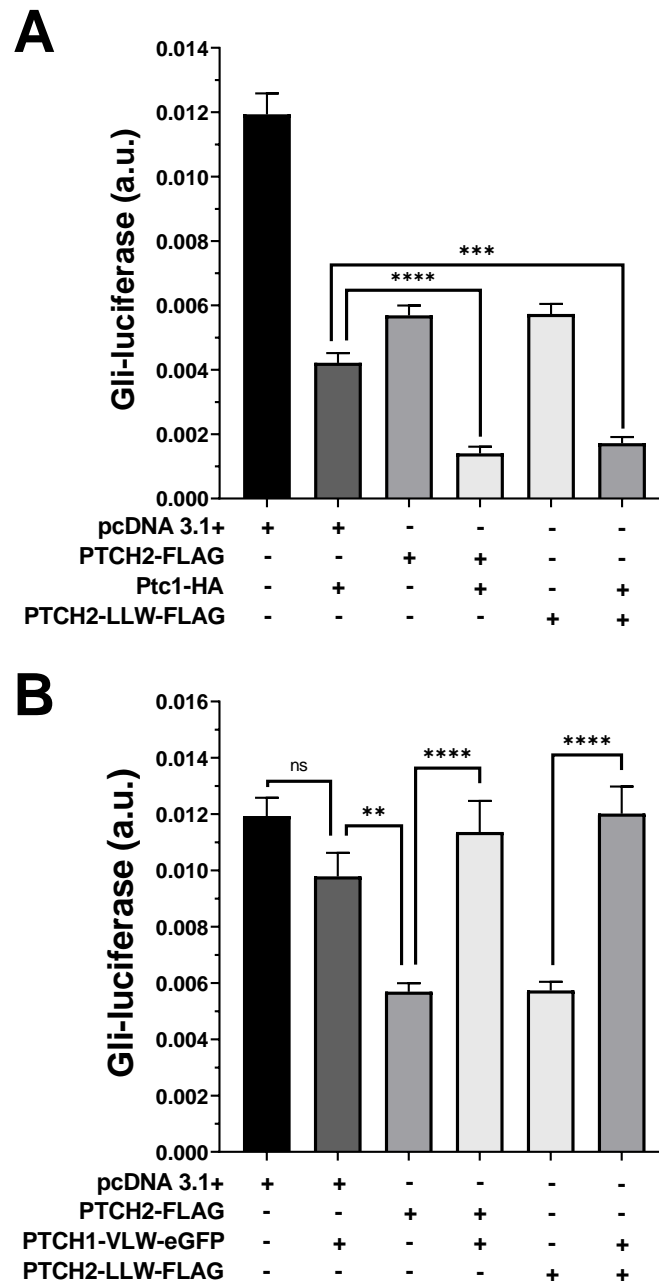


Figure 4.21 Patched heterodimer activity is dependent on the activity-state of the Patched 1 monomer involved.

Graph shows the mean +/- SEM of a single representative Gli-luciferase in *Ptc1*^{-/-} MEFs, performed with 7 technical repeats. **(A)** Co-transfection of Ptc1-HA and PTCH2-FLAG or PTCH2-LLW-FLAG (50:50) achieved strong inhibition of Gli compared to Ptc1-HA + pcDNA 3.1⁺ (50:50). **(B)** Co-transfection of PTCH2-FLAG or PTCH2-LLW-FLAG with PTCH1-VLW-eGFP (50:50) failed to achieve Gli inhibition. Transfection of PTCH2-FLAG or PTCH2-LLW-FLAG with pcDNA 3.1⁺ (50:50) showed significant inhibition of Gli.

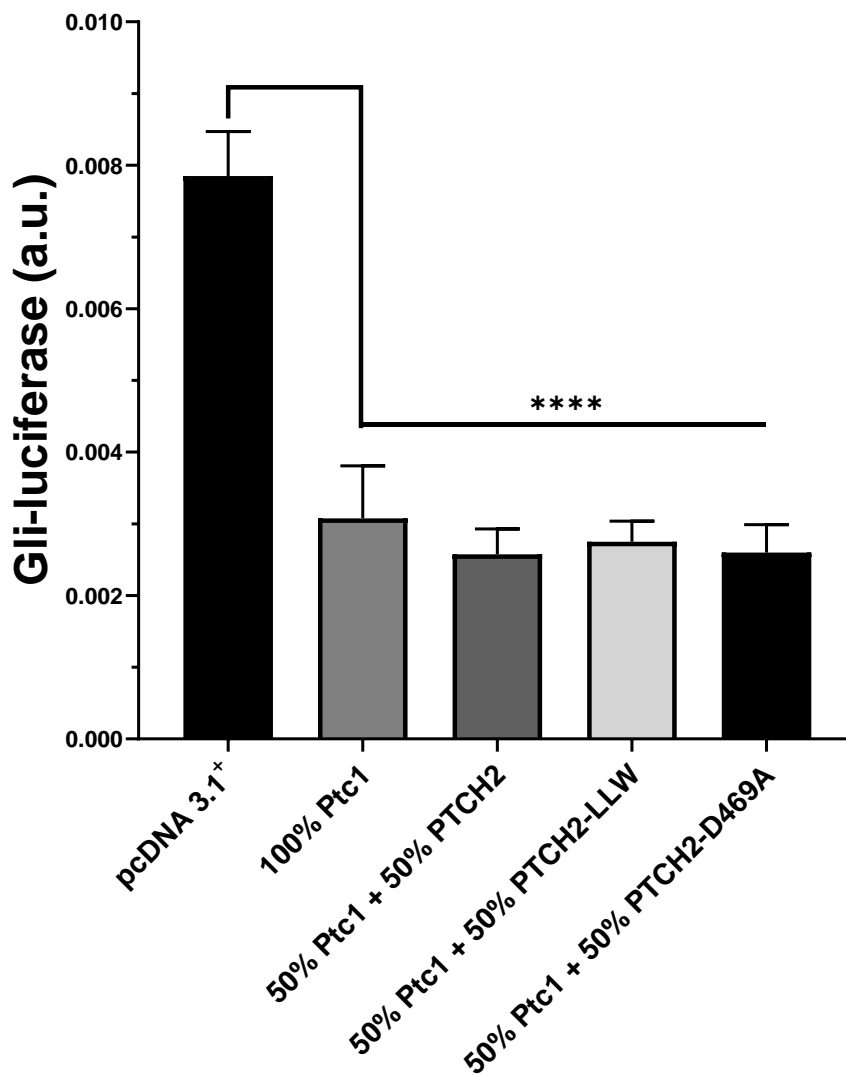


Figure 4.22 Co-transfection of a functionally impaired PTCH2-D469A with Ptc1-HA still produces an additional inhibitory effect on Gli.

Graph shows the mean +/- SEM of a single representative Gli-luciferase in *Ptc1*^{-/-} MEFs, performed with quadruplicate technical repeats. Co-transfection of PTCH2-FLAG, PTCH2-LLW-FLAG or PTCH2-D469A-FLAG with Ptc1-HA (50:50) displayed a significant inhibition of Gli, compared to pcDNA 3.1⁺ control. Inhibition of Gli in all three co-transfections of Patched 1 and 2 plasmids was comparable to 100% Ptc1-HA alone.

4.3.7 The middle cytoplasmic loop and CTD are not essential for

Patched heterodimer interactions

The intrinsically disordered nature of the cytoplasmic domains, shared by both PTCH1 and PTCH2, made them an interesting focus for investigating the divergent functions of these close homologs. As previously discussed in Chapter 3, work by Fleet et al., (2016) showed a redundancy of the SSD and transmembrane domains of Patched, suggesting their functionality was dictated by the flanking cytoplasmic and extracellular domains. It was therefore paramount to build a clearer picture of the Patched heterodimer and the possible functional and structural influence of each proteins' cytoplasmic domains.

As previously demonstrated in chapter 3 (**Results 3.3.4**), the middle loop and the CTD of Patched 1 are not essential to the formation of homodimers. In order to ascertain whether this feature is shared by Patched 1 and 2 heterodimers, Co-IPs were conducted with cytoplasmic domain mutants of each protein. This required the generation of three PTCH2 cytoplasmic domain mutants; PTCH2- Δ ML-FLAG, PTCH2- Δ C-FLAG and PTCH2- Δ ML Δ C-FLAG. Please refer to the PTCH2 hierarchical tree, for a visualisation of the plasmid mutations and their lineage (**Figure 2.1**).

The two single domain deletion mutants were derived from PTCH2-FLAG, using Q5 SDM (NEB) to remove the desired domains. The double domain deletion mutant, PTCH2- Δ ML Δ C-FLAG was subsequently created from the PTCH2- Δ C-FLAG plasmid, with the same primers used to create PTCH2- Δ ML-FLAG. Sanger sequencing confirmed successful mutagenesis. Interestingly, a similar expression profile was seen in the PTCH2 domain mutants, compared to their

Chapter 4: Patched homo- and heterodimer interactions display close resemblance, but differing canonical functionality, due to influences of the cytoplasmic domains

equivalent Ptc1 counterparts. A severe reduction in protein stability was observed for PTCH2- Δ MML-FLAG, but this disruption was mitigated in the subsequent PTCH2- Δ MML- Δ C-FLAG construct. PTCH2- Δ C-FLAG also displayed reduced expression in a similar manner to Ptc1- Δ C-HA. Immunofluorescence of fixed HEK293 cells, transiently transfected with PTCH2, PTCH2- Δ C and PTCH2- Δ MML Δ C revealed comparable protein localisation (**Figure 4.23**).

Initial Co-IP experiments confirmed direct hetero-interactions between PTCH2-FLAG and full length Ptc1-HA, Ptc1- Δ C-HA, Ptc1- Δ MML- Δ C-HA and CTD-HA (**Figure 4.24**). This finding was in agreement with Patched 1 homodimer Co-IP results seen in Chapter 3 (**Figure 3.5**). This indicates that neither the middle loop nor the CTD are essential for Patched heterodimer interactions, but that the CTD does at least associate independently.

The specific expression profiles of full length Ptc1-HA and the domain mutants were also consistent, displaying a reduced stability of Ptc1- Δ C-HA compared to Ptc1-HA. The double mutant, Ptc1- Δ MML- Δ C-HA, also displayed a lower expression level than Ptc1-HA, but increased expression compared to its clonal parent, Ptc1- Δ C-HA (**Figure 4.24**). Moreover, the expression level of PTCH2-FLAG was severely reduced in all co-transfections with a form Ptc1, except the CTD-HA.

This is not only indicative of association, but might also suggest that the two proteins are mutually degraded. The increased reduction of PTCH2-FLAG in the presence of Ptc1-HA compared to with pcDNA 3.1⁺ could be a consequence of a higher turn-over, directed by the additional 'PPXY' motif in the CTD of Patched 1. Co-transfection with the soluble form of patched 1 CTD (CTD-HA) does not reflect

Chapter 4: Patched homo- and heterodimer interactions display close resemblance, but differing canonical functionality, due to influences of the cytoplasmic domains

this reduction in PTCH2-FLAG, however, this form of CTD does not localise to the plasma-membrane.

Co-IPs of Ptc1-HA or Ptc1- Δ ML Δ C-HA with PTCH2-FLAG, PTCH2- Δ C-FLAG or PTCH2- Δ ML Δ C-FLAG confirmed that the middle loop and the CTD of PTCH2 are not strictly required for patched heterodimer interactions either (**Figure 4.25**). The result also indicated that heterodimer interactions do not require either of the two interacting proteins to have the cytoplasmic domains. Ptc1- Δ ML Δ C-HA was found to interact with PTCH2- Δ ML Δ C-FLAG, albeit at much reduced levels (**Figure 4.25**). The reduction in interaction on IP blots appears to be more likely a consequence of reduced protein stability and not a reduced interaction. The apparent lack of requirement of the CTD for Patched 1 homo-interactions and Patched hetero-interactions was also observed with PTCH2 homodimers, via Co-IP of PTCH2-HA and PTCH2- Δ C-FLAG (**Figure 4.26**).

Chapter 4: Patched homo- and heterodimer interactions display close resemblance, but differing canonical functionality, due to influences of the cytoplasmic domains

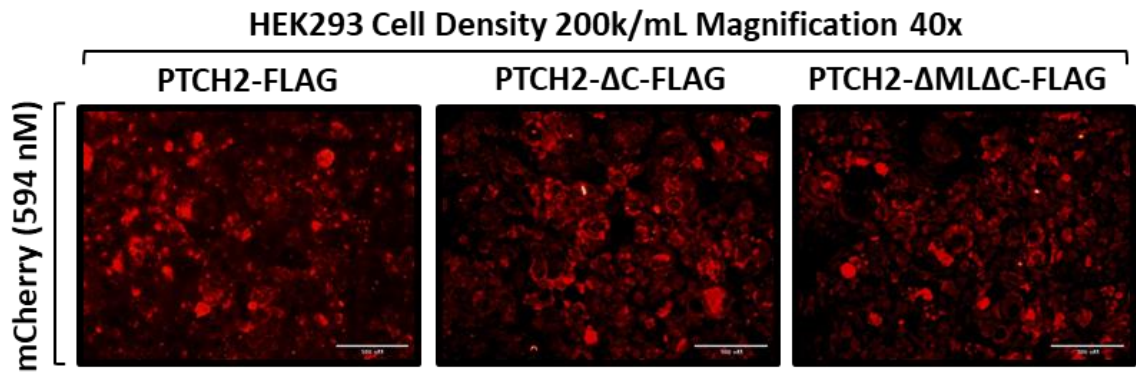


Figure 4.23 Immunofluorescence of PTCH2 and the cytoplasmic domain mutants, PTCH2- Δ C and PTCH2- Δ ML Δ C.

HEK293 cells were transiently transfected and fixed in 4% paraformaldehyde ~24 h post transfection. No obvious change in localisation was seen in cytoplasmic domain mutants of PTCH2. PTCH2 protein expression was imaged with anti-FLAG antibody (Proteintech) and secondary Goat anti-Mouse AlexaFluor 594 antibody (Thermofisher). Cells were imaged at 40 x magnification on an EVOS fluorescent light microscope, using the Texas red (594 nm) filter block. Scale bar, 100 μ M.

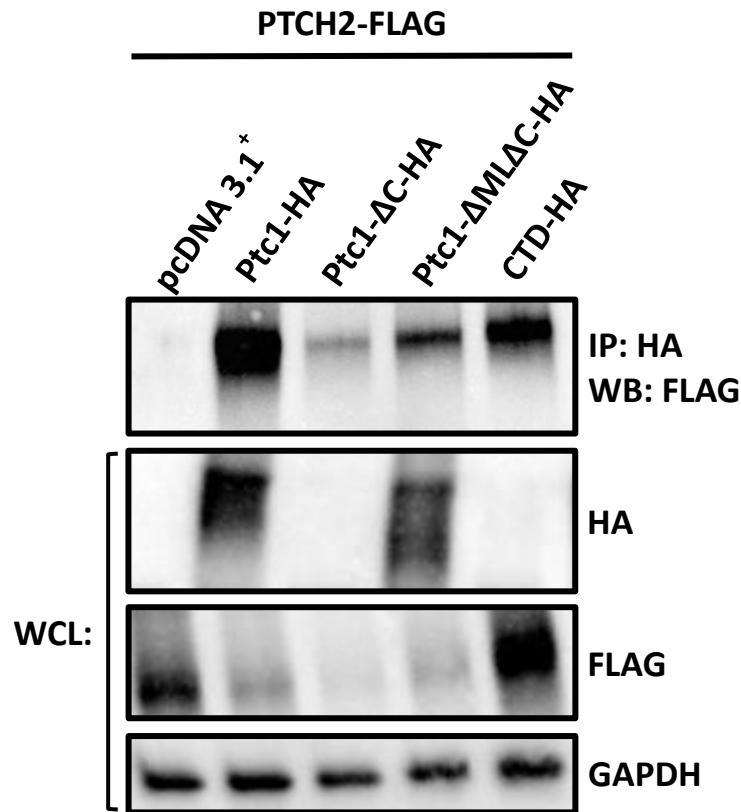


Figure 4.24 The hetero-interaction of Ptc1 and PTCH2 does not require the middle loop or CTD of Ptc1, despite the CTD being able to interact with PTCH2 independently.

HEK293 cells transiently co-transfected with PTCH2-FLAG and each indicated HA plasmid construct or pcDNA 3.1⁺ as a negative control. All forms of Ptc1 successfully immunoprecipitated PTCH2-FLAG with anti-HA antibody (4 μg, Proteintech), as seen by the bands of ~130 kDa in IP: HA, WB: FLAG. Full length Ptc1-HA demonstrated the strongest interaction with PTCH2-FLAG. WCL: Anti-GAPDH displayed relatively similar total levels of protein. Expression of PTCH2-FLAG was impaired by co-expression with all Ptc1-HA constructs, except CTD-HA, which showed an increase compared to pcDNA 3.1⁺. Ptc1-ΔC-HA expression was undetectable in the WCL anti-HA blot.

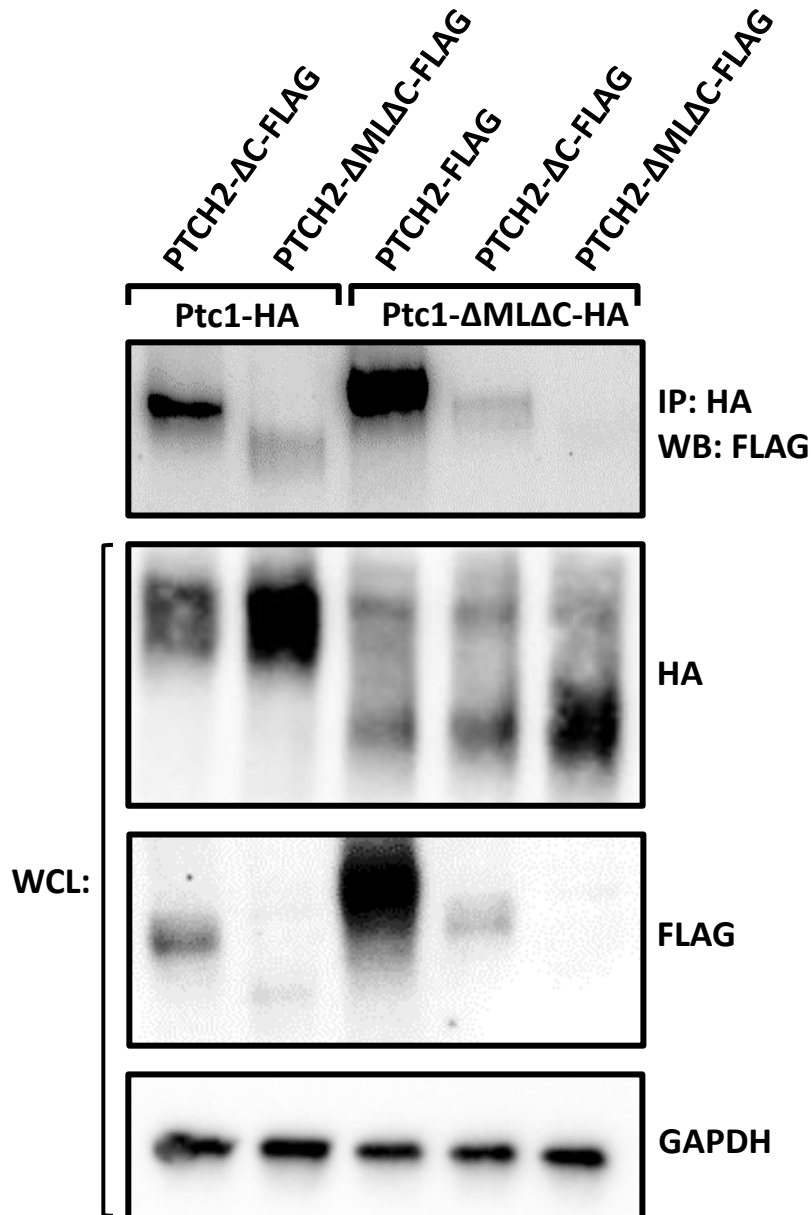


Figure 4.25 Deletion of cytoplasmic domains potentially impaired but did not prevent Patched hetero-interactions in HEK293 cells.

Co-IP with anti-HA antibody, blotting with anti-FLAG. All plasmid combinations displayed positive hetero-interactions. Interaction between Ptc1-ΔMLΔC-HA and PTCH2-ΔMLΔC-FLAG were the most reduced. Reductions in immunoprecipitated protein seen in the IP blot were largely reflective of an overall reduced Patched 1 and/or 2 construct expression, shown in the corresponding WCL blots.

Chapter 4: Patched homo- and heterodimer interactions display close resemblance, but differing canonical functionality, due to influences of the cytoplasmic domains

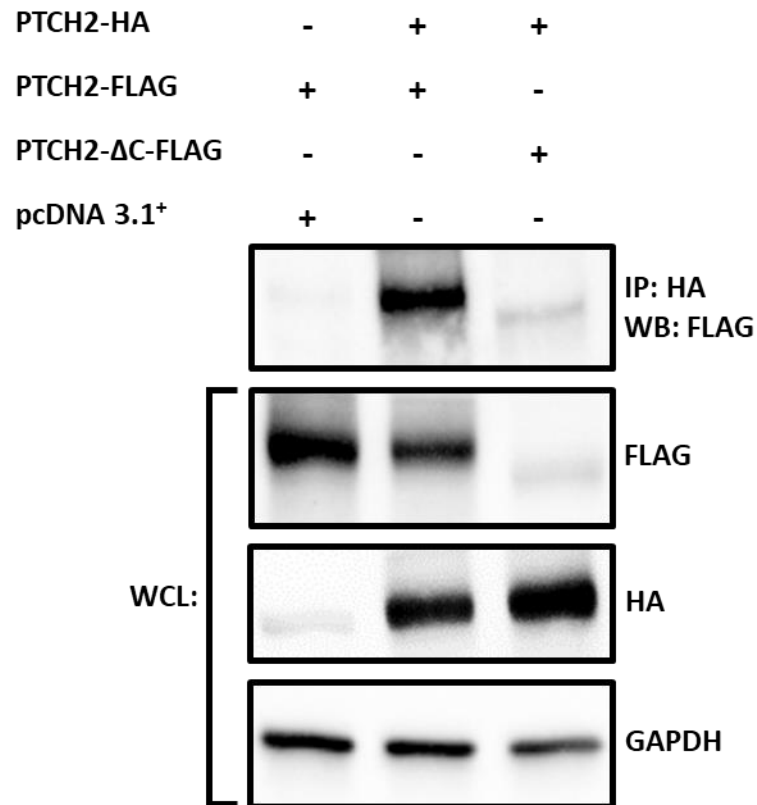


Figure 4.26 Removal of the CTD of PTCH2 does not prevent homodimer interactions with full length PTCH2.

Co-IP of PTCH2-FLAG or PTCH2-ΔC-FLAG by full length PTCH2-HA, using anti-HA antibody, blotting for anti-FLAG antibody. PTCH2 homo-interactions were not abrogated by the removal of the CTD. The reduction of PTCH2-ΔC-FLAG in IP blot was directly related to the reduced expression of the construct, as seen in the WCL.

4.3.8 Effect of Patched cytoplasmic domain mutants on Patched 2

homodimer and Patched 1 and 2 heterodimer canonical

activity.

It was now evident that Patched homo- and heterodimers do not require the two cytoplasmic domains for physical interaction. However, how these domain mutants might effect PTCH2 activity was unknown. It is already established that Ptc1 domain mutants, lacking the middle loop alone or in combination with a deletion of the CTD displayed some level of impairment to activity (**Figure 3.18A**). Meanwhile, despite reduced expression Ptc1- Δ C showed good activity (**Figure 3.18B**). To establish if the activity states of PTCH2- Δ C and PTCH2- Δ ML Δ C reflected the same pattern as Ptc1 mutants, Gli-luciferase assays were performed.

Similar to Ptc1 results, PTCH2- Δ C-FLAG displayed a similar activity to that of PTCH2-FLAG, despite having a much reduced expression via western blot (**Figure 4.27A**). PTCH2- Δ ML Δ C-FLAG also appeared to have similar activity to PTCH2-FLAG (**Figure 4.27B**). These results could be indicative of increased activity through the removal of the CTD, perhaps by alleviating a tempering effect it imposes on PTCH2 activity.

Next, the synergistic interaction previously seen for co-transfections of Ptc1-HA and PTCH2-FLAG were investigated in the context of PTCH2- Δ C-FLAG and PTCH2- Δ ML Δ C-FLAG. Co-transfection of Ptc1-HA and PTCH2- Δ C-FLAG (50%/50%) was found to have increased activity, but to a slightly lower extent than previously seen with PTCH2-FLAG (**Figure 4.28A**). This slightly reduced

Chapter 4: Patched homo- and heterodimer interactions display close resemblance, but differing canonical functionality, due to influences of the cytoplasmic domains

synergy is suspected to be a consequence of the reduced expression of PTCH2- Δ C-FLAG, which likely results in fewer heterodimer interactions. PTCH2- Δ ML Δ C-FLAG also produced an increased Gli inhibition when co-transfected with Ptc1-HA (50%/50%), compared to 100% Ptc1-HA alone (**Figure 4.28B**).

The co-transfection of PTCH2- Δ C-FLAG with PTCH1-VLW-eGFP was also investigated, to confirm whether the same Patched 1 activity-state limitations applied to this protein combination. Consistent with this theory, no apparent inhibition of Gli was observed in PTCH2- Δ C-FLAG + PTCH1-VLW-eGFP (50%/50%) co-transfections, indicating that the lack of activity of Patched 1 was sufficient to prevent activity of Patched 2 (**Figure 4.29**).

To further investigate any possible influence of the cytoplasmic domains on the apparent Patched synergistic activity, Ptc1 domain mutants were co-transfected with PTCH2. Intriguingly, the construct PTCH1-9:18ML-eGFP, which lacks the majority of the middle loop, but retains the CTD, appeared unaffected by the co-transfection of PTCH2-FLAG (**Figure 4.30**). In contrast, both forms of the double cytoplasmic mutant, Ptc1- Δ ML- Δ C-HA and PTCH1-9:18ML-11CTD-eGFP and the CTD mutant, Ptc1- Δ C-HA, showed increased activity when co-transfected with PTCH2-FLAG (**Figure 4.30**). An obvious difference between PTCH1-9:18ML and the other three mutants, which displayed increased activity, is the retention of the CTD in the absence of the middle loop. For reasons still unclear, the subsequent removal of the CTD from middle loop mutants of Patched 1 and 2 improved protein expression.

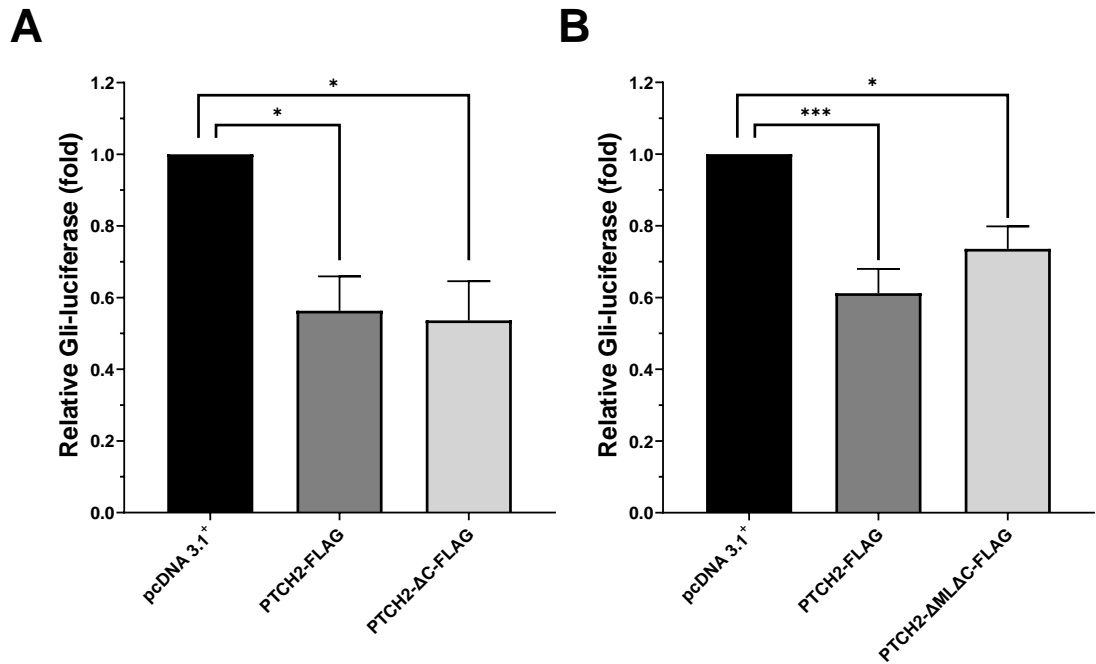


Figure 4.27 Removal of the CTD alone or in combination with the middle loop did not impair PTCH2 activity.

(A) PTCH2-FLAG and PTCH2-ΔC-FLAG displayed a similar inhibition of Gli in *Ptc1*^{-/-} MEFs. Graph represents the mean +/- SEM of 3 individual Gli-luciferase experiments, performed with quadruplicate technical repeats. **(B)** PTCH2-FLAG and PTCH2-ΔMLΔC-FLAG activity was not significantly different, although PTCH2-FLAG showed greater difference to pcDNA 3.1⁺ than PTCH2-ΔMLΔC-FLAG. Graph represents the mean +/- SEM of 5 individual Gli-luciferase experiments in *Ptc1*^{-/-} MEFs, performed with duplicate (3) and quadruplicate (2) technical repeats.

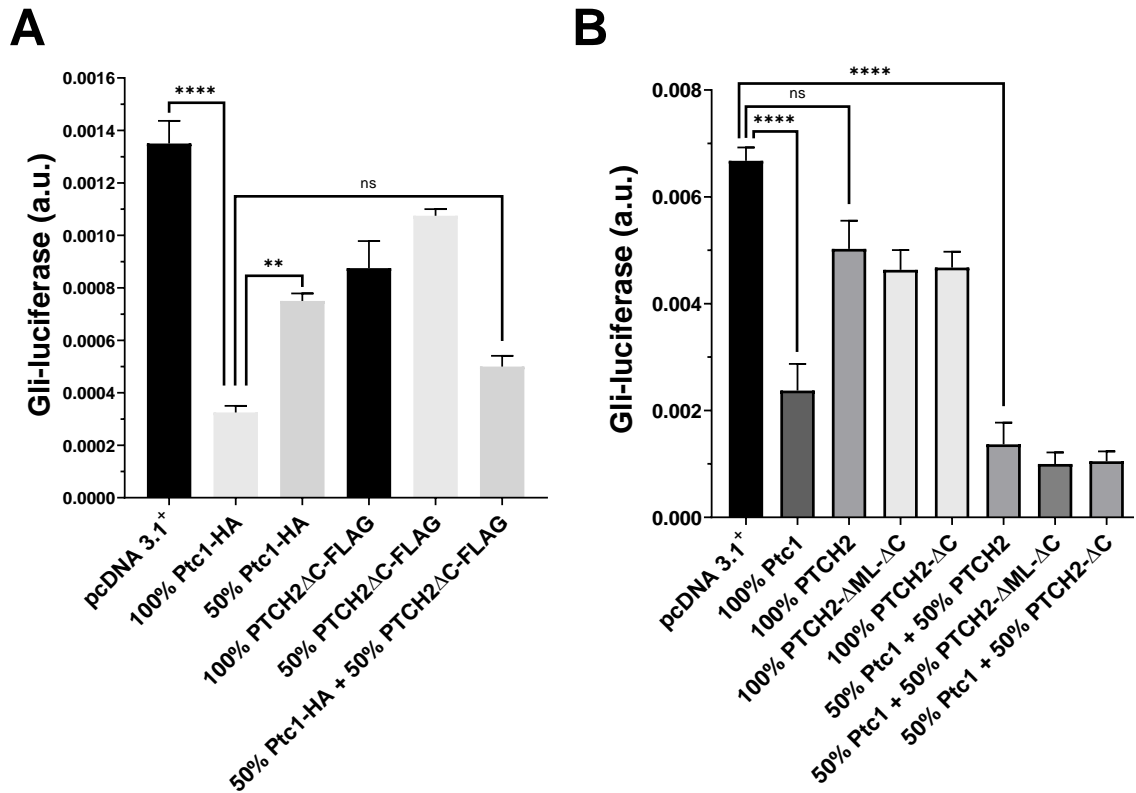


Figure 4.28 Removal of the cytoplasmic domains of PTCH2 does not diminish increased heterodimer activity.

(A) Co-transfection of Ptc1-HA + PTCH2- Δ C-FLAG (50%/50%) displayed comparable activity to that of Ptc1-HA alone (100%). Transfection of Ptc1-HA alone (50%) was significantly less active than Ptc1-HA alone (100%) and Ptc1-HA + PTCH2- Δ C-FLAG (50%/50%). Graph shows the mean \pm SEM of a single representative Gli-luciferase experiment, performed in *Ptc1*^{-/-} MEFs, with quadruplicate technical repeats. **(B)** Co-transfection of Ptc1-HA and either PTCH2-FLAG, PTCH2- Δ C-FLAG or PTCH2- Δ ML Δ C-FLAG (50%/50%) displayed increased activity to that of Ptc1-HA alone (100%). Graph shows the mean \pm SEM of a single representative Gli-luciferase experiment, performed in *Ptc1*^{-/-} MEFs, with quadruplicate technical repeats.

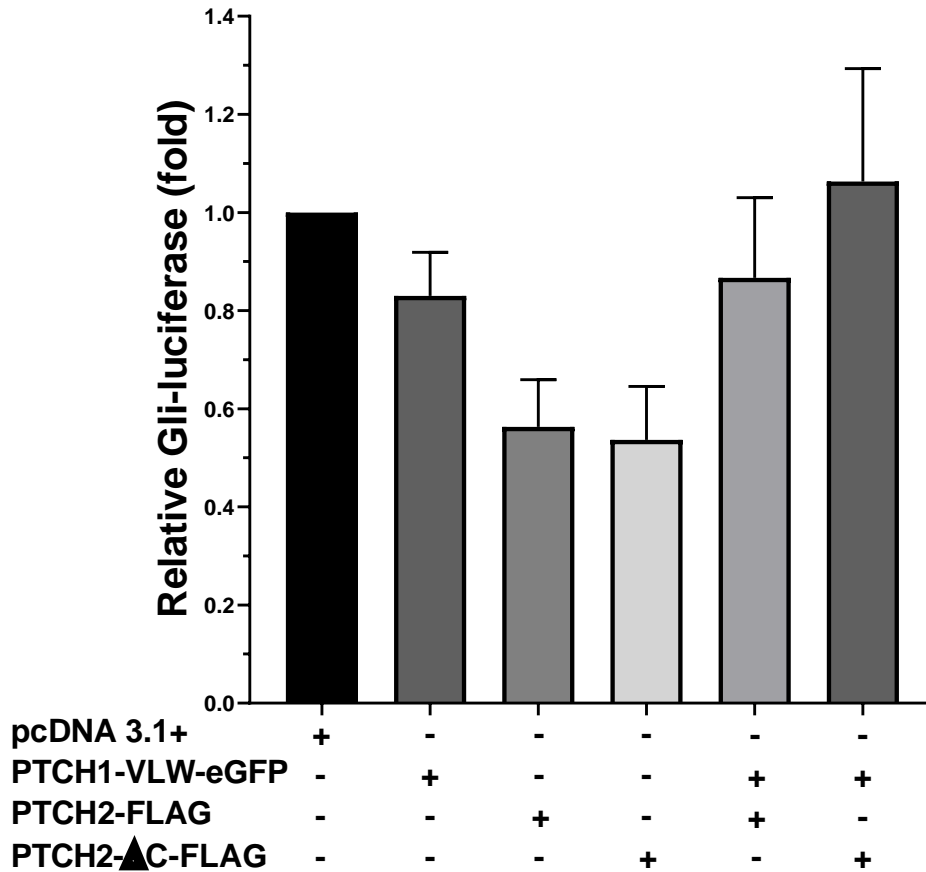


Figure 4.29 PTCH2-ΔC activity is impaired by co-transfection with inactive PTCH1-VLW.

Graph represents the mean +/- SEM of 3 individual Gli-luciferase experiments in *Ptc1*^{-/-} MEFs, performed with duplicate (2) or quadruplicate (1) technical repeats. PTCH2-FLAG and PTCH2-ΔC-FLAG had similar activity when transfected alone. Co-transfection of PTCH2-FLAG or PTCH2-ΔC-FLAG with PTCH1-VLW-eGFP diminished this activity.

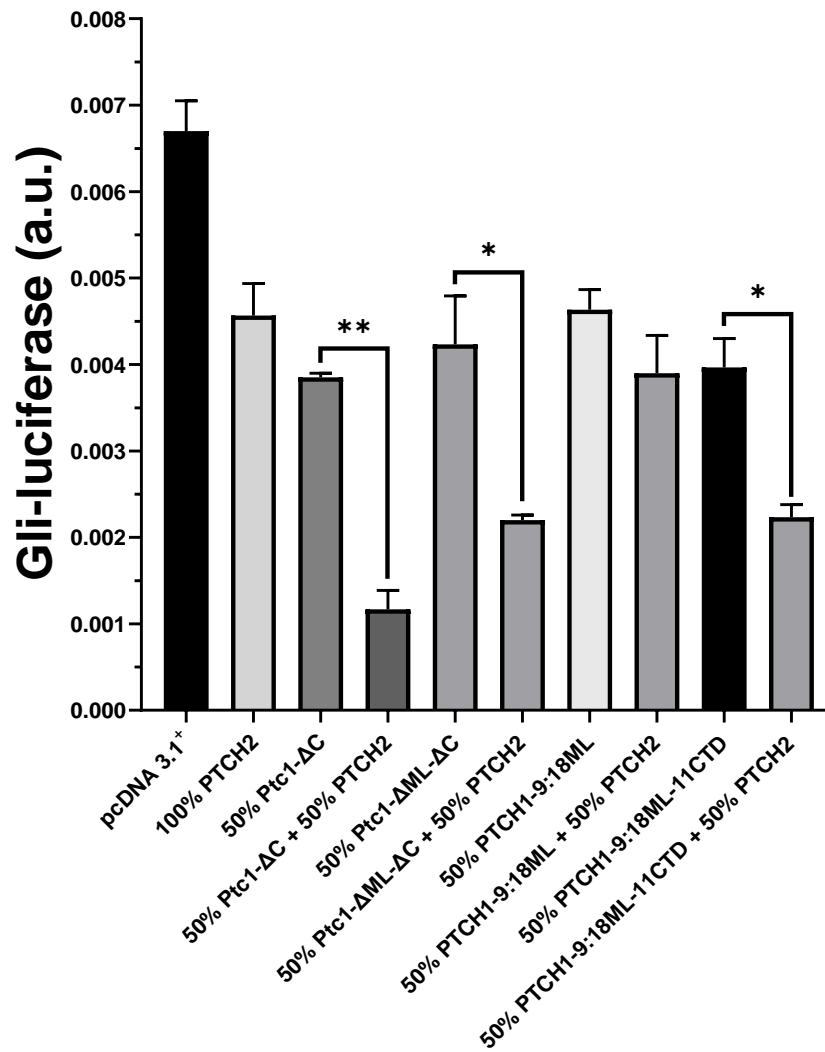


Figure 4.30 Hetero-interactions involving PTCH1-9:18ML display no increase in activity.

Graph represents the mean +/- SEM of a single representative Gli-luciferase experiment in *Ptc1*^{-/-} MEFs, performed with triplicate technical repeats. Activity was significantly increased for Ptc1-ΔC-HA, Ptc1-ΔMLΔC-HA and PTCH1-9:18ML-11CTD-eGFP, when co-transfected with PTCH2-FLAG (50%/50%). No increase in activity was seen for PTCH1-9:18ML-eGFP when co-transfected with PTCH2-FLAG (50%/50%).

4.3.9 Substitution of the CTD of PTCH1 with that of PTCH2 results in a non-functional chimeric protein.

The data presented previously are suggestive of a relationship between the CTD and the functional activity of Patched 1 and 2. Furthermore, this relationship also appears to be influenced by the middle cytoplasmic loop. The association between the CTDs of monomers forming homodimers occurs below the transmembrane domains, in a densely crowded environment. Therefore, it is probable that several points of intramolecular and even intermolecular interaction, occur between the CTDs and the middle cytoplasmic loops.

Removal of the middle loop was found to impair the function of PTCH1 (**Figure 3.18**), perhaps by a loss of stability to the entrance of the cholesterol channel, or by a loss of influence on the CTDs, which would normally retain a conformation for effective cholesterol access and transportation. The additional removal of the CTD in Δ ML mutant PTCH1 exacerbated its canonical inactivity.

Meanwhile, removal of the CTD from full-length PTCH1 appears to possibly have a positive impact on function. Gli inhibition by Ptc1- Δ C-HA appears comparable to that of Ptc1-HA, despite a reduced expression. In agreement, despite having a reduced expression, PTCH2- Δ C-FLAG displayed comparable levels of canonical activity to PTCH2-FLAG. This could suggest that the CTD might impede access to the SSD. The CTD is a region of high variability between Patched 1 and 2, so these differences might in part explain their different degrees of activity. Of particular note, are the first 23 residues of the CTD in Patched 1 that are not present within Patched 2. If an interaction between the middle

Chapter 4: Patched homo- and heterodimer interactions display close resemblance, but differing canonical functionality, due to influences of the cytoplasmic domains

cytoplasmic loop and the CTD are permissible to effective activity, perhaps the reduced length of Patched 2s CTD prevents this interaction occurring.

With mounting experimental evidence that the cytoplasmic domains of Patched impact activity, a Patched 1: Patched 2 domain substitution strategy was implemented. To expose the fundamental functional differences between Patched 1 and 2 the CTD of PTCH1 was replaced by that of PTCH2. The generation of PTCH1CTD2-eGFP was achieved through a two-step cloning process. First, the CTD of PTCH2 was incorporated into PTCH1-eGFP, through In-Fusion cloning. Next the CTD of Patched 1 was removed from this PTCH1-eGFP product, by Q5 SDM (NEB), to leave the CTD of PTCH2 in frame with PTCH1 and the eGFP tag. Successful cloning was confirmed by Sanger sequencing and western blot (**Figure 4.31A**).

The newly generated PTCH1CTD2-eGFP expressed at a comparable level to that of PTCH1-eGFP and PTCH2-eGFP (**Figure 4.31A**). Furthermore, the approximate mass of PTCH1CTD2-eGFP matched that predicted. Expression and localisation of PTCH1CTD2-eGFP was also analysed by immunofluorescence (**Figure 4.31B**). In agreement with the western blot data, PTCH1CTD2-eGFP displayed a similar profile to its parental plasmid, PTCH1-eGFP. To determine whether substitution of the CTD affected localisation, co-localisation with full length PTCH1 was assessed. PTCH1CTD2-eGFP co-localised well with PTCH1-mCherry in HEK293 cells. Furthermore, this localisation was indistinguishable from that of PTCH1-eGFP with PTCH1-mCherry (**Figure 4.32**).

Chapter 4: Patched homo- and heterodimer interactions display close resemblance, but differing canonical functionality, due to influences of the cytoplasmic domains

Next, Co-IP of PTCH1CTD2-eGFP with Ptc1-HA and PTCH2-FLAG confirmed a direct interaction in transiently transfected HEK293 cells (**Figure 4.33**). Subsequent FRET-based experiments further solidified this finding, with detection of a direct interaction between PTCH1CTD2-eGFP and both PTCH1-mCherry and PTCH2-mCherry, in live HEK293 cells (**Figure 4.34**). This experiment also confirmed a connection between CTD length the magnitude of FRET. Average normalised GFP fluorescence intensity, post mCherry bleach, from highest to lowest correlated with combined CTD length of the interaction monomers.

Finally, the activity-state of PTCH1CTD2-eGFP was tested by Gli-luciferase in *Ptc1^{-/-}* MEFs. Surprisingly, PTCH1CTD2-eGFP displayed a complete lack of activity (**Figure 4.35**). This lack of activity is unlikely to be a consequence of reduced ciliary localisation, as previous localisation imaging was similar to PTCH1-eGFP, which achieved strong inhibition of Gli here (**Figure 4.35**). Furthermore, co-transfection of PTCH1-eGFP and PTCH1CTD2-eGFP (50%/50%) failed to achieved synergistic activity above that of PTCH1-eGFP and pcDNA 3.1⁺ (50%50%) (**Figure 4.35**). A direct interaction between these proteins was already confirmed. If PTCH1CTD2-eGFP experienced ciliary localisation issues, this would be apparent in the co-transfected condition. Either PTCH1-eGFP ciliary localisation would have decreased, or PTCH1CTD2-eGFP ciliary localisation would have increased, neither of which are evidenced in the data.

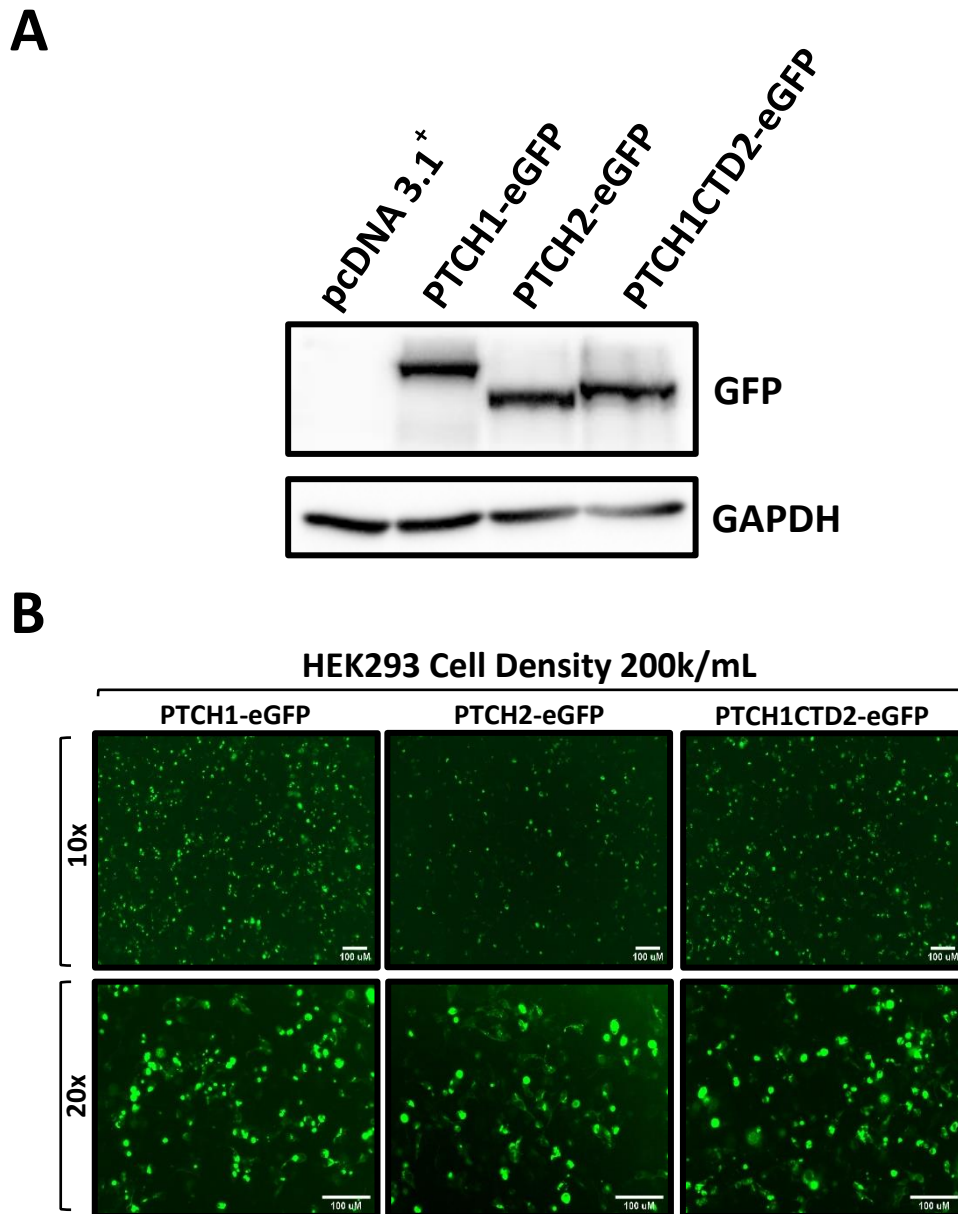


Figure 4.31 PTCH1CTD2 displayed comparable expression and localisation to that of PTCH1 and PTCH2.

(A) Western blot of PTCH1, PTCH2 and PTCH1CTD2 with anti-GFP (Proteintech). Bands observed on the blot were of the expected masses of each protein. Anti-GAPDH confirmed total protein expression of the three constructs was similar. **(B)** Immunofluorescence performed on transiently transfected HEK293 cells. Live cells were imaged with an EVOS fluorescent light microscope at 488 nm (FITC) to excite the C-terminal GFP fluorophores. PTCH1CTD2 displayed comparable fluorescence to its parental plasmid, PTCH1-eGFP. Scale bar, 100 μ M.

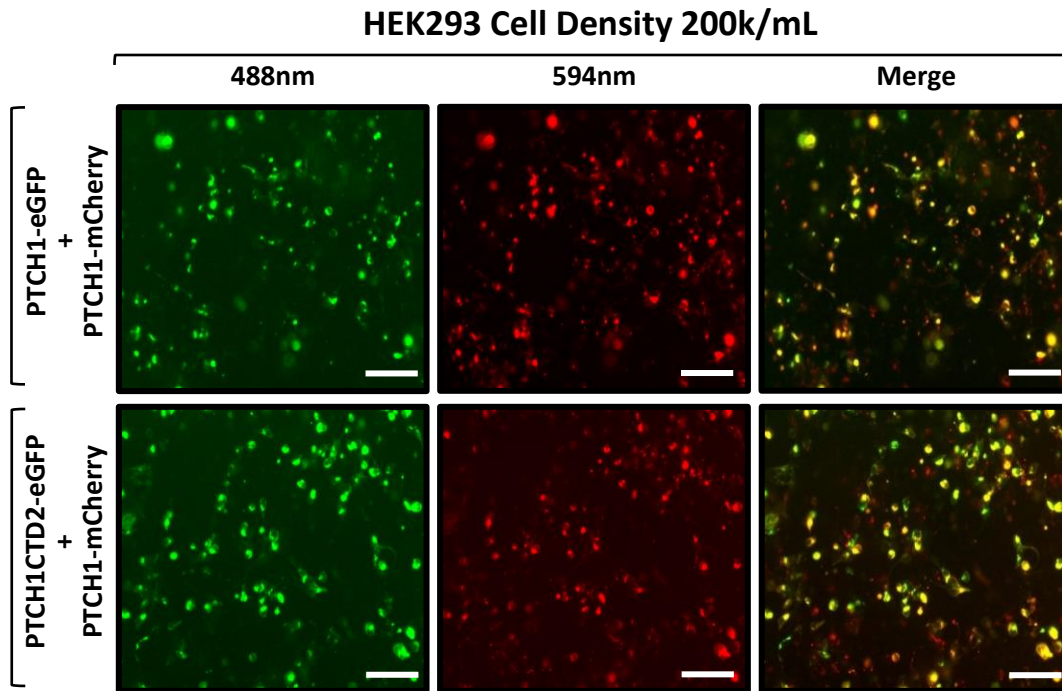


Figure 4.32 PTCH1CTD2 co-localised with PTCH1 in HEK293 cells.

Immunofluorescence of HEK293 cells, transiently co-transfected with PTCH1-mCherry and either PTCH1-eGFP (top row) or PTCH1CTD2-eGFP (bottom row). Expression of all plasmids was confirmed and co-localisation visualised by overlay of GFP (488 nm) and mCherry (594 nm) images. Scale bar, 100 μ M.

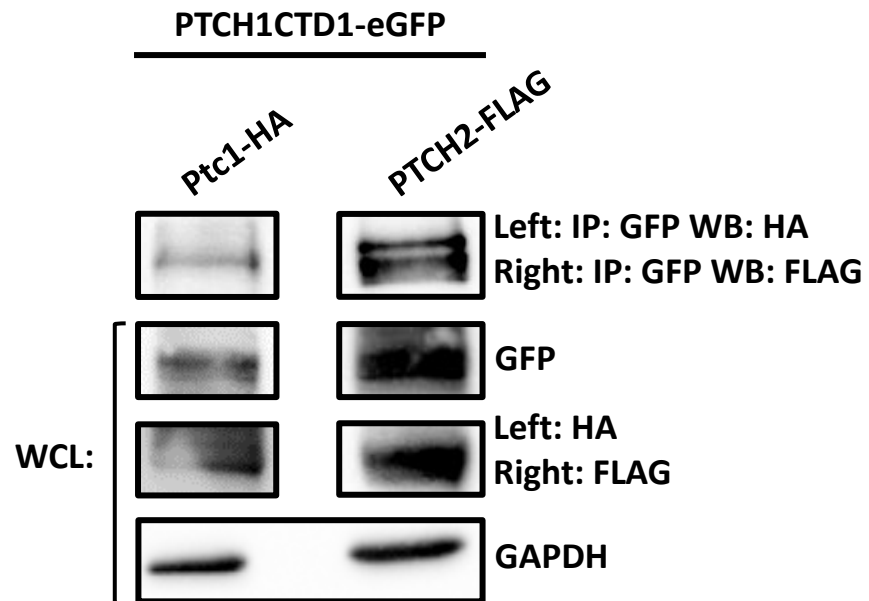


Figure 4.33 PTCH1CTD2 directly interacts with Patched 1 and Patched 2 in HEK293 cells.

Co-IP performed in transiently co-transfected HEK293 cells. PTCH1CTD2-eGFP successfully precipitated both Ptc1-HA and PTCH2-FLAG with anti-GFP antibody (Proteintech). Original images were cropped to remove lanes of un-related conditions.

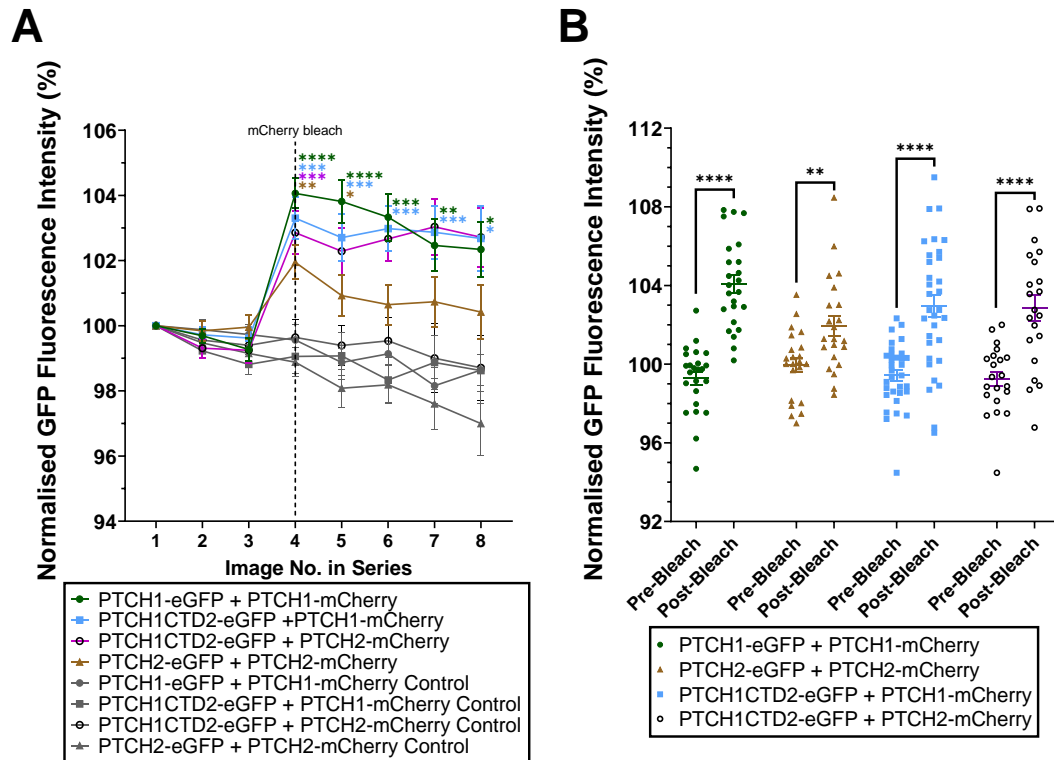


Figure 4.34 PTCH1CTD2 forms heterodimer interactions with both PTCH1 and PTCH2, displaying a CTD-length dependent effect on FRET.

HEK293 cells were transiently co-transfected with different FRET combinations of C-terminally fluorescently labelled Patched as indicated. FRET was determined between proteins by photo-bleaching of the mCherry tagged Patched monomer and detection of an increase in intensity of the GFP tagged Patched monomer. **(A)** Normalised GFP fluorescence intensity values revealed a significant increase in GFP after the photo-bleaching of Patched mCherry monomers, confirming interaction in all combinations. In control (unbleached ROIs), no significant change seen for normalised GFP intensity or in the rate of fluorophore photo-decay. Graph depicts average \pm SEM of 18-33 ROIs for each condition. **(B)** Separated Scatter graph of pre and post bleach images show significant increase in GFP intensity post bleach for all combinations, but with less significance for PTCH2 homodimer interactions.

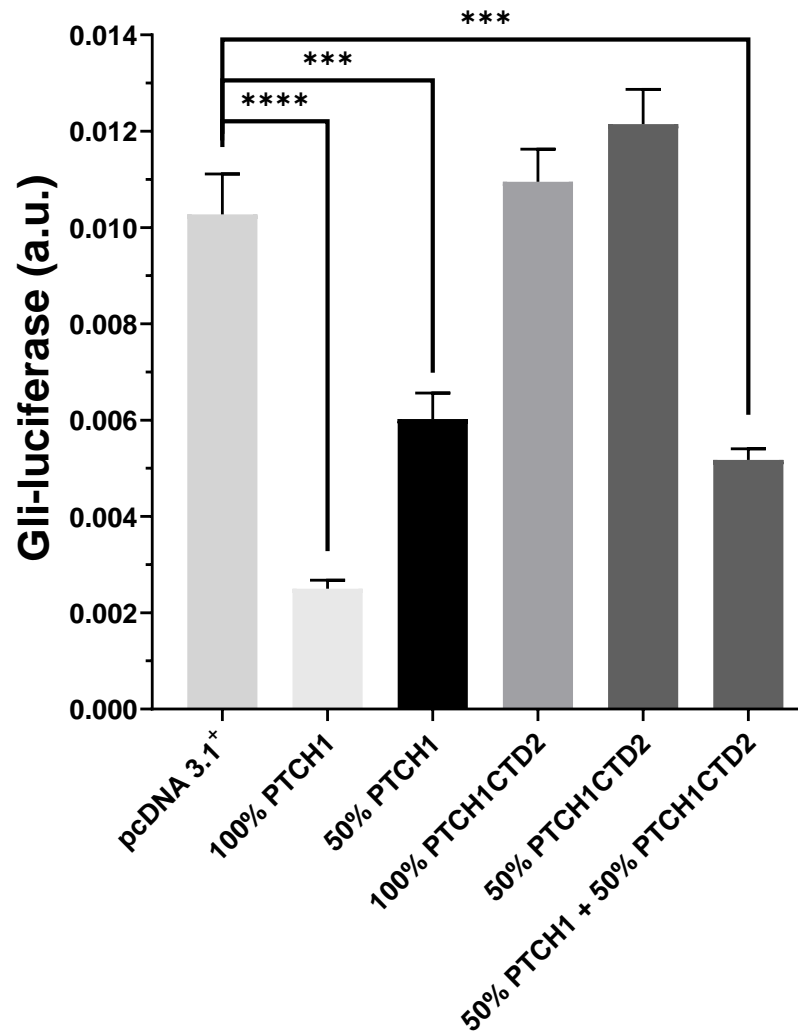


Figure 4.35 PTCH1CTD2 displayed no activity in *Ptc1*^{-/-} MEFs.

Transfection of 100% and 50% of PTCH1-eGFP showed significant activity. Transfection of PTCH1CTD2-eGFP showed no detectable activity. Co-transfection of PTCH1-eGFP and PTCH1CTD2-eGFP (50%/50%) produced activity equivalent to 50% PTCH1-eGFP alone. Graph shows a single representative Gli-luciferase conducted in *Ptc1*^{-/-} MEFs, with quadruplicate technical repeats. Error bars represent the mean +/- SEM.

4.4 Discussion

Often overshadowed by the potency of PTCH1, the cooperative role of PTCH2 in canonical Hh signalling has been troublesome to elucidate. While PTCH1 is clearly the superior relative, PTCH2 is finally receiving recognition for contributions previously overlooked. There is growing evidence that alongside the Hh pathway components, PTCH1 and SUFU, PTCH2 mutations also contribute to the development of NBCCS, albeit with less potent phenotypes (Fujii et al., 2013). Furthermore, mutations in *Ptch2* can exacerbate heterozygous mutations of *Ptch1* (Alfaro et al., 2014; Zhulyn et al., 2015).

The data presented here strongly indicates a structural and functional relationship between PTCH1 and PTCH2. Moreover, this relationship almost certainly resembles that of the PTCH1 homodimer. It is now apparent that Patched 1 and 2 heterodimers, as well as their individual homodimers exist *in vitro*. Cell based assays provide evidence of striking similarities between the three dimer combinations. Patched 1 and 2 display direct competition for binding and the formation of their homodimers does not require the cytoplasmic domains. Moreover, the core SSD of Patched 2 also appears to be important for its activity, and is impaired by mutations recapitulated from existing Patched 1 disease causing mutations.

A potential functional relevance of Patched heterodimers has been shown, whereby increased inhibitory activity is observed in cells co-transfected for Patched 1 and 2, compared to individual Patched 1 or Patched 2 of equal DNA concentration. These data also successfully show that this increased activity

Chapter 4: Patched homo- and heterodimer interactions display close resemblance, but differing canonical functionality, due to influences of the cytoplasmic domains

output of the hetero-interaction is ultimately determined by the activity state of the Patched 1 monomer. Recapitulation of existing PTCH1 mutations in PTCH2 also impaired the activity of the PTCH2 homodimer. The mutation, PTCH2-D469A, mimicked the Gorlin syndrome mutation of PTCH1-D513 and impaired PTCH2 activity. Despite this inactivity, co-transfection of PTCH2-D469A with Ptc1 produced increased activity, above that of Ptc1 alone, and equal to that of PTCH2 with Ptc1.

This was further supported by the finding that co-transfection of various active PTCH2 constructs, with an impaired PTCH1-VLW construct, failed to produce any significant activity. In fact, it appeared that the low level activity witnessed in transfections of PTCH2 alone, were lost, when combined with PTCH1-VLW. This is a strong indication that the synergistic interactions between Patched 1 and 2 can also have the opposite effect, when mutations impact Patched 1. Ciliary localisation of PTCH1 and PTCH1-VLW are believed to be comparable, so differences in activity, when combined with PTCH2, likely stem from the effect of the VLW mutation on activity.

There are several potential explanations for the increased activity seen for Patched heterodimers, when compared to that of homodimers functioning alone. In the first model, PTCH2 operates primarily as a 'sink' for Hh ligand, although it possesses only a small basal activity against Smo, it efficiently sequesters Hh ligand (**Figure 4.37**). PTCH2 achieves a measurable level of Gli inhibition, despite its poor activity, because it has a greater half-life than Patched 1, afforded by its shorter CTD. PTCH2 lacks the Lysine present in PTCH1 at position '1426' which is a target of ubiquitination by the E3 ubiquitin ligase ITCH.

Chapter 4: Patched homo- and heterodimer interactions display close resemblance, but differing canonical functionality, due to influences of the cytoplasmic domains

Through this model, the mere existence of heterodimers serves a dual purpose. Firstly, in the absence of ligand, the stability of Patched 1 monomers is increased, through their association with Patched 2. This effect stems from the differing half-lives of the two Patched proteins. PTCH2 might confer an increased stability to its PTCH1 partner, leading to longer retention within the cilium and thereby increased activity over time (Figure 4.36).

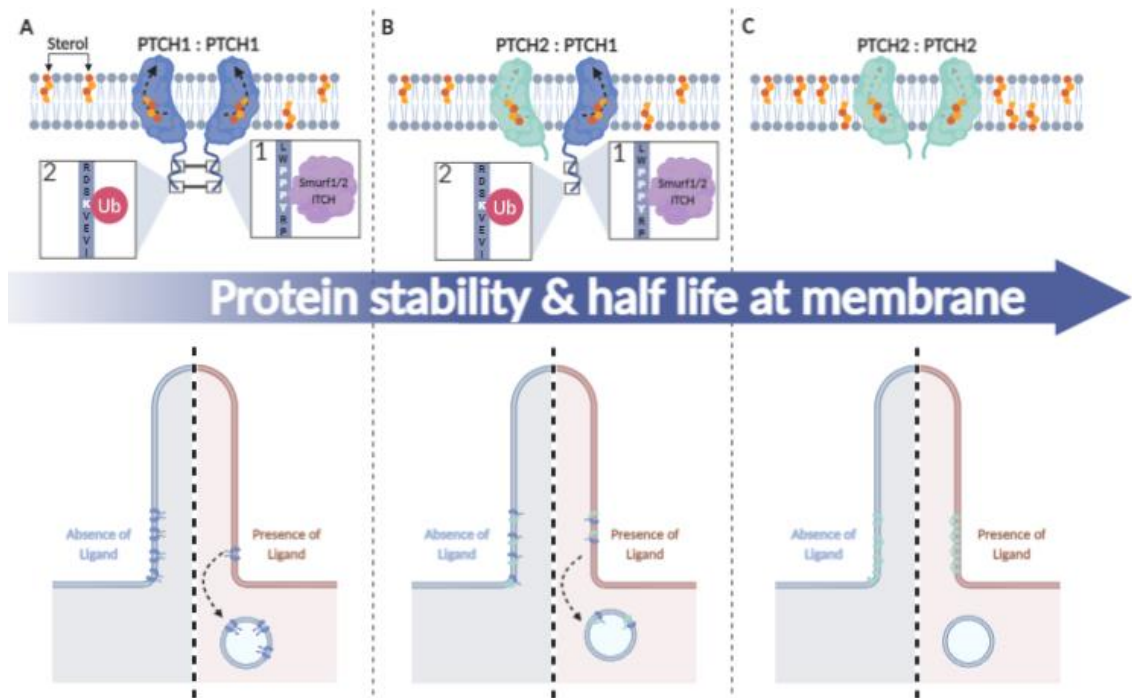


Figure 4.36 Hypothetical differences in protein stability and turnover of Patched homo and heterodimers

This schematic shows the potential differences in stability and turnover of the Patched homo and heterodimers. Protein stability and half-life at the membrane increases from left to right. **(A)** A PTCH1 homodimer possesses two sets of the ubiquitin protein-ligase target motif, PPXY, in the CTDs. Subsequent to the binding of ITCH, ubiquitination of K1413 leads to protein degradation in late endosomes. **(B)** A PTCH1-PTCH2 heterodimer possesses one CTD PPXY motif in the PTCH1. This leads to reduced PTCH1 and slightly increased PTCH2 degradation. **(C)** A PTCH2 homodimer possesses no CTD PPXY motifs, resulting in much increased half-life, through reduced turnover.

Chapter 4: Patched homo- and heterodimer interactions display close resemblance, but differing canonical functionality, due to influences of the cytoplasmic domains

This model agrees with the findings that interactions between PTCH2 and inactive PTCH1-VLW-eGFP, cannot produce an increased activity. Here, despite PTCH2 increasing the retention of PTCH1-VLW within the cilium, it remains inactive and achieves no increased impact of Gli. Moreover, the finding that impaired forms of PTCH2 still illicit an increased activity when paired with an active PTCH1, correlates with the effect being driven by a means separate to the SSD and Smo. Further in agreement, co-transfections of Patched 1 and 2 result in a slight reduction in PTCH2 by western blot, suggesting that hetero-interactions might also increase the degradation of PTCH2 by means of the 'PPXY' present in the CTD of the Patched 1 monomer.

The second potential impact of heterodimers effects ligand stimulation, where the pool of available Patched dimers is increased. Here, the presence of heterodimers effectively dilutes the concentration of Patched 1 homodimers, reducing the number of ShhN:PTCH1 (1:2 ratio) interactions (**Figure 4.37**). A recent structure of N-Shh engaging a PTCH1 homodimer in a 1:2 monomer ratio supports this notion (Qi, Schmiede, Coutavas and Li, 2018). For every heterodimer present and bound by N-Shh, a 'spare' Patched 1 monomer that would have been inactivated, remains functional. Whilst this model relies on a sub-maximal level of N-Shh, it suggests a mechanism by which the expression of PTCH2 might provide an increased level of subtlety in cellular responses to morphogen signals during development.

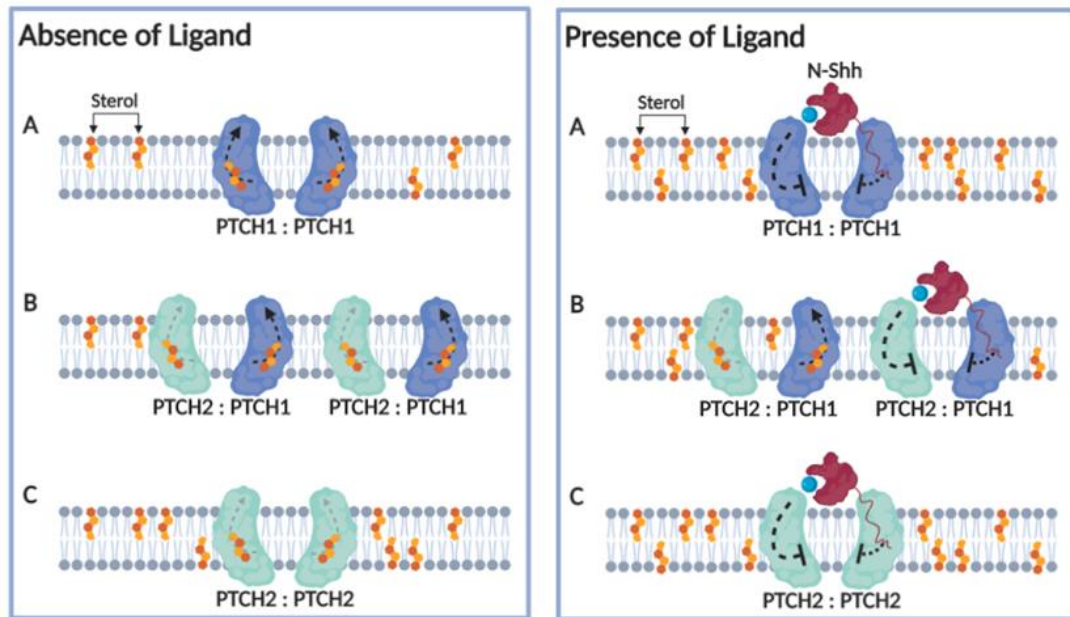


Figure 4.37 Hypothetical impact of the newly discovered Heterodimeric Patched

Schematic detailing the potential mechanistic impact of heterodimeric interactions of Patched in the absence (left) and presence (right) of ligand. **In the absence of ligand: (A)** PTCH1 achieves strong inhibition of the pathway, through the mobilisation of cholesterol. **(B)** PTCH heterodimers also achieve strong pathway inhibition. **(C)** PTCH2 achieves a lower level of pathway inhibition. **In the presence of ligand: (A)** PTCH1 is engaged by ligand in a 2:1 ratio, resulting in loss of activity and consequently, the accumulation of available cholesterol. **(B)** PTCH heterodimers increase the pool of dimers available for sequestering by ligand, resulting in a higher ratio of free, unbound PTCH1 to continue mobilising cholesterol. **(C)** PTCH2 engages ligand in a 2:1 ratio, causing a loss of activity, but the effects on available cholesterol are minimal as PTCH2 mobilises the sterol poorly.

There is also some evidence that effective inhibition of PTCH1 by Shh requires both the Ca^{2+} dependent and palmitoyl moiety interaction interfaces to be engaged. Mutations effecting the Ca^{2+} binding site only were deemed to bind Patched 1, presumably through the palmitoyl moiety, but failed to effectively activate signalling (Izzi et al., 2011).

Chapter 4: Patched homo- and heterodimer interactions display close resemblance, but differing canonical functionality, due to influences of the cytoplasmic domains

While we know Patched 2 binds N-Shh with comparable affinity to Patched 1, we do not know definitively if this is mediated through both N-Shh interaction interfaces (Carpenter et al., 1998). It seems highly likely Patched 2 homodimers will engage N-Shh in a similar manner to Patched 1, but this should be determined experimentally. During this PhD I commenced work towards this goal, through the production of a PTCH2 expression construct, using the baculovirus-infected cell method described for PTCHD1 (**Material and Methods 2.19**) (data not shown). Small scale detergent screens for purification were conducted (data not shown) and hopefully this work can be taken forward at some point in the future.

It has also been proposed that the co-receptors, Gas1, Cdo and Boc are essential for maximal Patched 1:N-Shh binding, but conversely compete with Patched 1 for the Ca²⁺ binding site (Izzi et al., 2011). This presents a far more complex picture, where heterodimeric, homodimeric and monomeric, co-receptor associated forms of Patched all potentially bind Hh ligand with differing functional consequences.

Despite displaying co-expression in several tissues, Patched 1 and 2 do show distinct regions of exclusive expression. It is here that we might expect a larger involvement of the co-receptors. In fact, Ptch2/Gas1 and Ptch1/Boc combinations were recently described to differentially regulate Hh signalling in primordial germ cell migration (Kim et al., 2020). Here, Ptch1 expression was exclusively limited to the somatic cells and Ptch2 expression to the primordial germ cells, negating any possibility of Patched hetero-dimer interactions. An interesting question that arises, is whether the frequency of Patched, co-receptor associations is lower in

Chapter 4: Patched homo- and heterodimer interactions display close resemblance, but differing canonical functionality, due to influences of the cytoplasmic domains

tissues expressing both Patched homologs. Are there endogenous, higher level structures, like the tetrameric PTCH1, that involve the co-receptors, or are these interactions exclusive to monomeric Patched?

Investigation of the influence of the cytoplasmic domains of Patched 1 and 2 on homo and hetero-interactions revealed further commonality. Of particular note was removal of the CTD of Patched 2, which mimicked the characteristics previously described for Ptc1- Δ C in Chapter 3 (**Figure 3.15**). Contrary to an anticipated increase in protein expression, a reduced expression was witnessed for both truncated Patched. However, this reduction was not reflected in the activity level achieved by these proteins, suggesting greater activity and/or increased stability of mature protein compared to full length Patched. Again, this might be a result of the loss of the PPXY motif in the CTD of Patched 1 reducing degradation (Chen et al., 2014).

Although the data presented here strongly supports an activity of the CTD truncated Ptc1 and PTCH2 proteins at the primary cilia, findings of Kim et al., (2015) might dispute this. They reported that Ptch1 with a truncation beyond 1180 displayed impaired ciliary localisation. However, both Fleet (2016) and I report the ciliary localisation and activity of equivalent Ptch1 proteins, with CTD truncations larger than 1180. There are two feasible reasons for this: Ptch1 proteins lacking the majority of the CTD do not experience impaired ciliary localisation, or they do experience localisation impediment, but this is circumnavigated by oligomerisation with endogenous, or exogenously co-expressed un-impaired patched proteins. Experiments performed by Kim et al., (2015) used *Ptc1*^{-/-} MEFs which were also said to lack endogenous Ptch2, while

Chapter 4: Patched homo- and heterodimer interactions display close resemblance, but differing canonical functionality, due to influences of the cytoplasmic domains

the *Ptc1*^{-/-} MEFs in this work and in Fleet (2016) retained endogenous Ptch2. In fact, if hetero-interactions with endogenous Ptch2 are responsible for the ciliary localisation of the CTD mutants of Ptc1 and PTCH2, it further supports my findings of oligomerisation.

Again, findings that both PTCH2 domain mutants could achieve synergistic activity with Ptc1, supports the model of increased Patched 1 activity through increased protein stability and ciliary retention. Co-transfections of PTCH2 with Patched 1 domain mutants lacking either both the cytoplasmic middle loop and/or the CTD also achieved synergistic activity. However, PTCH1-9:18ML appeared to be an exception, which demands further investigation.

A critical finding, in regards to the influences of the CTDs on protein function, comes from the PTCH1CTD2 construct, in which the CTD of PTCH1 was substituted with that of PTCH2. Here, a protein with apparent equivalent expression and a conserved ability to oligomerise, has severely impaired activity. This finding generates several new avenues of investigation. How does a Patched 1 with its CTD removed retain or even have increased activity, whilst substitution for the CTD of PTCH2 abrogates activity? The most logical explanation, is that the CTD of Patched influences the accessibility of the sterol cavity, in a limiting manner.

It was always an intention to generate the corresponding CTD substitution to PTCH1CTD2: PTCH2CTD1. Attempted cloning of PTCH2CTD1 was performed in tandem to PTCH1CTD2, however Sanger sequencing found no positive plasmids. Due to the limited experimental time due to COVID-19, only PTCH1CTD2 was taken forward as positive colonies had been identified. An

Chapter 4: Patched homo- and heterodimer interactions display close resemblance, but differing canonical functionality, due to influences of the cytoplasmic domains

independent group recently reported the generation of a Ptch2 hybrid protein, containing the CTD of Ptch1 (Fleet and Hamel, 2019). Although they concluded that the hybrid was inactive, there are some immediate caveats to this finding. The protein, P2-N+P2-C^{P1-CT} was created as two separate halves, which are reported to non-covalently reconstitute after co-transfection. Despite this claim, there is an obvious reduction in the activity of another hybrid protein, P2-N+P2C, compared to its full length equivalent, Ptch2. The only difference between P2N+P2C and Ptch2 is that the former is two protein halves that reconstituted after transfection. Therefore, this throws doubt over the reported lack of activity of the P2-N+P2-C^{P1-CT}.

The generation of PTCH2CTD1 is a clear priority, to then assess the activity state by Gli-luciferase assay. I hypothesise that PTCH2CTD1 will display increased activity above that seen for PTCH2, due to an association between the middle cytoplasmic loop and the now 'longer' CTD. I believe that an association between the middle loop and the CTD is integral to the activity of Patched. Within this interaction, the CTD is dependent upon the middle loop. The findings that removal of the CTD alone did not impede activity, but removal of the middle loop alone did, suggest a dependency. Such an interaction should be determined by Co-IP of isolated middle loop and CTD domains. Furthermore, the established FRET-based assays could be adapted to assess whether the middle loop exerts either an intramolecular and intermolecular regulatory effect on the CTD. Differences could also be determined between Patched homo- and heterodimers through these experiments.

Chapter 5

Expression, purification and structural analysis of PTCHD1

Chapter 5

Expression, purification and structural analysis of PTCHD1

5.1 Introduction

In silico analysis of PTCHD1 predicts a 12-transmembrane protein of 888 residues; containing an SSD, which encompasses TMs 2-6 and two regions of interest in the CTD: a lysine/glutamic acid rich region and PDZ-binding domain (Noor et al., 2010; Ung et al., 2018). As such, PTCHD1 is highly related to PTCH1 and 2, as well as NPC1. Both PTCH1 and NPC1 have important developmental roles, and mutations within these proteins directly, or in their signalling pathways, have clinical manifestations. Mutations of Shh are a strong cause of autosomal-dominant holoprosencephaly, whilst Niemann-Pick-disease is a neurodegenerative lysosomal lipid-storage disorder. A commonality between PTCH1 and NPC1 is their functional involvement with cholesterol and their integral role in brain development and function. Interestingly, PTCHD1 also appears to have a neuronal function. PTCHD1 is widely expressed in the developing and adult mouse brain, particularly enriched in the cerebellar granule neurons, thalamic reticular nucleus and hippocampal granule cells (Tora et al., 2017). Moreover, hemizygotic loss of PTCHD1 has been reported to produce neurodevelopmental disorders.

Since its initial identification in a male, with a 160 kB deletion within Xp22.11, the PTCHD1 locus has been implicated in several case studies, as a strong candidate in the susceptibility of autism spectrum disorder (ASD). Characterisation of the phenotypes associated with 23 individuals, identified to

carry a PTCHD1 copy number variation (CNV), found a wide degree of variability. There was, however, a consensus for ASD or ASD-like behavioural traits (40%) and two consistent, but subtle dysmorphic features: orofacial hypotonia and mild motor incoordination (Chaudhry et al., 2015).

Neurodevelopmental disorders such as ASD and Intellectual disability (ID) display significant genetic heterogeneity underlying their aetiology. ASD is predominantly known to affect males; in the USA, a 4:1 ratio of males to females have been diagnosed with ASD or ID. This sex-biased characteristic is shared by several other neuropsychiatric diseases and led to the early establishment of a class of 'X-linked' disorders. The X-linked recessive inheritance model best explains both; the high frequency of neuropsychiatric phenotypes in males and; the strikingly high heritability observed amongst siblings. A major issue with the current understanding of the X-linked disorders arises from the finding that CNVs often encompass several genes, masking which genes truly contribute to the observed phenotypic outcome. To this end, many X-linked gene candidates have been identified to have potentially pathological CNVs by whole-genome sequencing or microarray.

Although PTCHD1 mutations are more prevalent than many other ASD risk genes, they still only contribute ~1% of all cases. This low overall frequency, coupled with the large genetic heterogeneity of ASD, produces a significant limitation to clinical identification of relevant PTCHD1 mutations. *In vitro* molecular investigation and structural elucidation of PTCHD1, could provide knowledge of the mechanism through which described PTCHD1 mutations contribute to neurodevelopmental disorders.

Unfortunately, PTCHD1 remains poorly understood, with only a handful of publications expanding upon its possible molecular functions. However, of particular note is a screen in which the coding regions of 900 ASD and 208 ID probands were sequenced, identifying 7 unique PTCHD1 missense variants (ASD: 6 ID: 2) (Noor et al., 2010). A further two PTCHD1 missense mutants were found by Torrico et al., (2015), in one healthy and one ID patient. These putative mutations mapped to the extracellular loops, the 4th transmembrane domain and the cytoplasmic loops (**Figure 5.1A**). These domains are known to harbour several disease-causing mutations in PTCH1. However, alignment of PTCHD1 to PTCH1 and PTCH2 sequences, reveals a relatively low degree of conservation of these native residues as well as their mutational variants (**Figure 5.1B**).

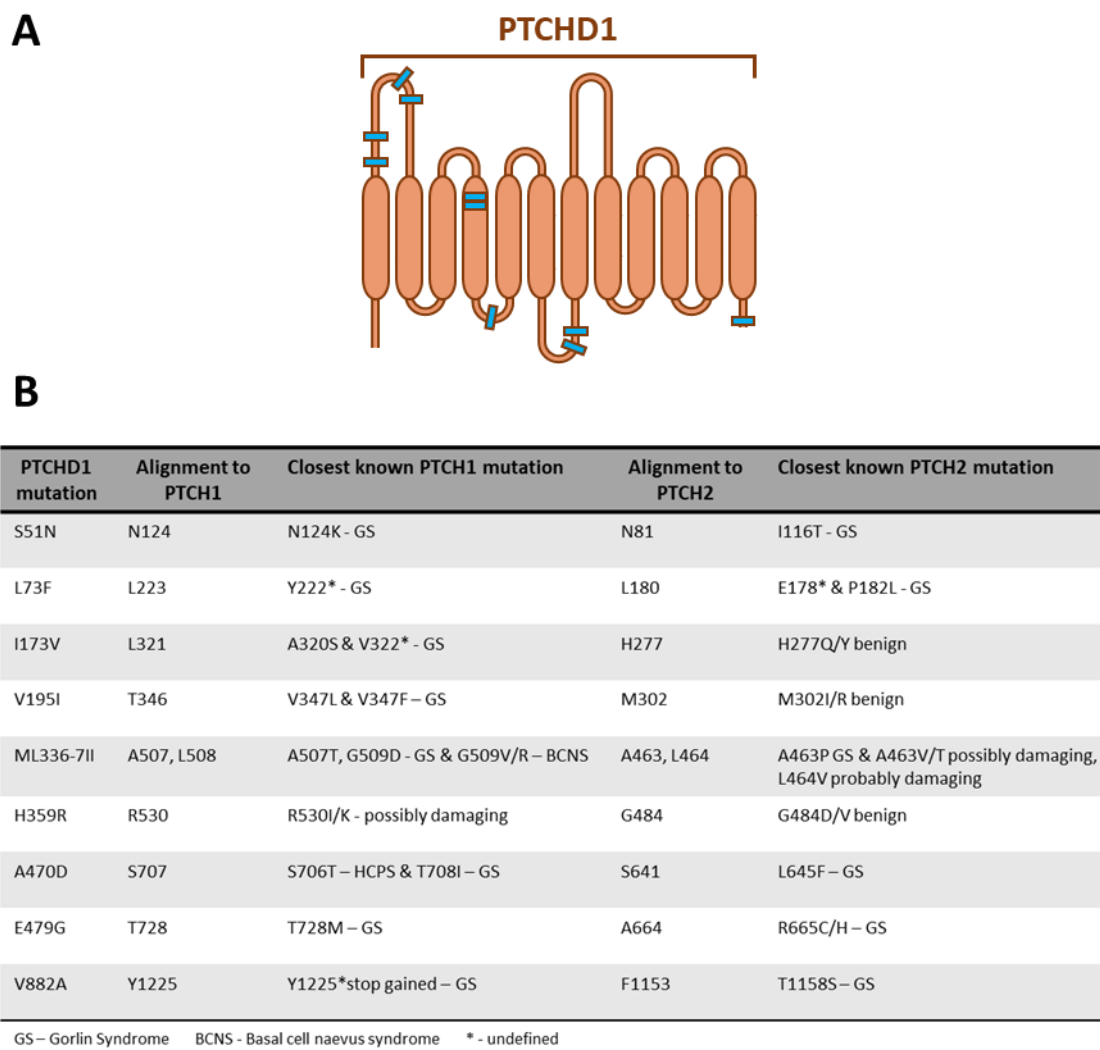


Figure 5.1 Alignment of PTCHD1 mutations to Patched 1 and 2 sequences.

(A) Schematic of PTCHD1 secondary structure, detailing the approximate location of identified mutations as blue bars (Noor et al., 2010; Torrico et al., 2015). (B) Table of PTCHD1 mutations, and their closest PTCH1 and PTCH2 loss-of-function mutations predicted from secondary structure alignment.

Of note, is the PTCHD1 1st ECL mutation, S51N, which aligns to N124 and N81 of the 1st ECL of PTCH1 and PTCH2, respectively. In PTCH1, the immediate neighbouring residue to N124 is V125, one of the three residues mutated in the inactive PTCH1-VLW. This region of PTCH1 is believed to maintain a hydrophobic conduit, essential for cholesterol transport (Zhang et al., 2018). Results shown in Chapter 4 (**Results 4.3.4**) confirmed this mutation impaired

PTCH1 activity, but was not recapitulated in PTCH2. Another PTCHD1 mutation, ML336-7II, aligns to a mutational 'hot spot' within the 4th transmembrane domain and SSD of PTCH1 and PTCH2. The identification of the mutation ML336-7II supports the already anticipated functional importance of the SSD in PTCHD1. However, this by no means confirms any similarities in molecular cargo, or transport mechanism of PTCHD1 and the other Patched proteins.

There is conflicting evidence establishing and dismissing a function of PTCHD1 in the Hedgehog pathway, a role primarily perceived due to the shared protein architecture and the presence of an SSD within PTCHD1. In one study, PTCHD1 was compared to PTCH1 in a Gli-luciferase assay of Smo-transfected C3H10T1/2 cells. Although the authors concluded that PTCHD1 can reduce Gli-reporter activity, it was much less potent than PTCH1 (11.6% vs 73.6%). In fact, 15x more PTCHD1 cDNA was transfected, compared to PTCH1, suggesting any effect observed should be strongly scrutinised (Chung et al., 2014). In parallel to the study of Chung et al., (2014), two independent groups have investigated the activity of PTCHD1 with Gli-luciferase assays with differing results (Noor et al., 2010; Ung et al., 2018). Noor et al., (2010) also utilised C3H10T1/2 cells, stimulating the pathway with the Smo agonist purmorphamine, and observed a reduction in Gli reporter activity by transfection of PTCH1, PTCH2 and PTCHD1. Rather unexpectedly, they reported that an equal, blanket level of inhibition was achieved for all proteins. Meanwhile, Ung et al., (2018) used *Ptc1*^{-/-} MEFs and found PTCHD1 had no activity compared to PTCH1. It is important to note that such discrepancies might have arisen from the use of different cell lines and modes of pathway stimulation. The C3H10T1/2 cells express endogenous PTCH1, whilst *Ptc1*^{-/-} MEFs do not. A possible explanation for PTCHD1 activity

in C3H10T1/2 cells comes from the findings in Chapter 4 (**Results 4.3**), that PTCH1 heterodimers produce synergistic activity. Perhaps the same is true for PTCHD1, when expressed in a cell line positive for PTCH1.

Alongside this co-operative interaction, other findings in Chapter 4 were indicative of more divergent activities of PTCH1 and PTCH2. Prominent differences were observed for the cytoplasmic domains. Typically, the intrinsically disordered cytoplasmic domains of the Patched family of proteins have been underutilised in research focused on canonical Hh signalling. However, there is emerging experimental evidence, presented in Chapter 4 (**Results 4.3**) and by others, of a functional influence, dictated by the cytoplasmic domains (Fleet et al., 2016). Therefore, it seems logical that the cytoplasmic domains of PTCHD1 could confer a highly divergent role to that of PTCH1 and PTCH2.

Whilst not definitive, PTCHD1 KO mice studies suggest that it is not essential for canonical Hh signalling. Loss of PTCHD1 in cerebellum granule cell precursor cells had no significant impact on Hh-responsive proliferation (Tora et al., 2017). Alignment of the CTDs of PTCHD1 and PTCH1 or PTCH2 shows their dissimilarities in sequence and length (**Figure 5.2**). A genetic study of a recent mass evolutionary expansion of Patched genes in *C. elegans*, concluded that later evolutionary proteins contained fewer exons and shorter C-terminal regions (Zhong et al., 2014). In line with a more distant evolutionary connection to the two Patched homologs, the CTD of PTCHD1 is much shorter and contains two unique features: a lysine-rich region and a PDZ-binding motif (**Figure 5.2**).

PTCHD1-CTD	1	-----
PTCH1-CTD	1	SFFGYPYEVSPANGLNRLPTPSPEPPPSVVRFAMPPGHTHSGSDSSDSEYSSQTTVSGLS
PTCHD1-CTD	1	-----TFLPP
PTCH1-CTD	61	EELRHYEAAQQGAGGPAHQVI VEATENPVFAHSTVVHPESRHHP PSNPRQQPHLDSGSLPP
PTCHD1-CTD	6	SKKKRKEKKNP-----
PTCH1-CTD	121	GRQGGQPRRDEPPREGLWPPP YRPRRDAFEISTEGHSGPSNRARWGPRGARSHNPRNPAST
PTCHD1-CTD	17	-----
PTCH1-CTD	181	AMGSSVPGYCQPITTTV TASASVTVAVHPPVPGPGRNPRGGLCPGYPETDHGLFEDPHVP
PTCHD1-CTD	17	-----ENRETEECVEMVDIDSTRVVDQITTV
PTCH1-CTD	241	FHVCERERDSKVEVIELQDVECEERPRGSSN-----
PTCHD1	1	TFLPPSKKKRKEKKNPENR-----EETE--CVEMVDIDSTRVVDQITTV-----
PTCH2-CTD	1	--GPPPEVIQMYKESPEILSPPAPQGGGLRWGASSSLPQS FARVTTSMTVAIHPPPLPGA
PTCHD1		-----
PTCH2-CTD	59	YIHPAPDEPPWSPAATSSGNLSSRGPGPATG

Figure 5.2 Alignment of the C-terminal domain of PTCHD1 to PTCH1 and PTCH2

Alignment of the C-terminal cytoplasmic protein coding region of PTCHD1 to PTCH1 (top) and PTCH2 (bottom). Sequences were obtained from UniProt for PTCHD1: Q96NR3, PTCH1: Q13635 and PTCH2: Q9Y6C5. The lysine-rich region of PTCHD1 is indicated by the blue boxes. The putative PDZ motif is shown within the red boxes.

The PDZ-binding motif, identified at the most distal end of the CTD of PTCHD1, is a strong functional candidate to investigate. Classically, PDZ domains are known to anchor receptor proteins in the plasma membrane. As is the case of PTCHD1, the PDZ binding motif is commonly at the extreme C-termini. PDZ domains often form part of a larger protein scaffold, mediating the formation of multi-protein complexes for specific regulation of localisation. A PDZ-dependent interaction between PTCHD1 and two synaptic proteins, PSD95 and SAP102, was discovered in GST pull downs from total brain extracts (Ung et al., 2018). However, the extent of relevance of these interactions should be carefully considered. PSD95 and SAP102 were found to have distinct localisations within

dendritic spines of the hippocampus, via super resolution light microscopy (Zheng et al., 2011). Furthermore, differential expression of each protein has been observed at different stages of development. Redundancy in their functions has also been demonstrated, within developing glutamatergic synapses, where a 'hand off' appears to occur from SAP102 to PSD95 in the trafficking of AMPA and NDMA receptors after synaptogenesis (Elias et al., 2008).

Affinity purifications from whole brain extracts, using PTCHD1 or PTCHD1- Δ PDZ, identified three components of the retromer complex that interacted exclusively with the PTCHD1 PDZ motif (Tora et al., 2017). The retromer complex is known to be essential to the rapid delivery of signal receptors to local regions in the dendrite branches, such as the post synaptic density. Biochemical analysis revealed PTCHD1 interacts with postsynaptic trafficking proteins, and a large number of ribosomal proteins for undetermined reason (Tora et al., 2017).

Concurrently, the lysine-rich region in the CTD of PTCHD1 suggests a potential link to biomolecular condensation. Lysine/RNA-interactions have been shown to regulate formation of membraneless organelles, such as P-bodies, or RNA and stress granules (Ukmar-Godec et al., 2019). Tau protein, which is highly enriched in lysine, undergoes coacervation with RNA and binds stress granules. These associations can be mitigated through the acetylation of Tau lysines. The dynamics of membraneless structures allow distinct regulation of biochemical reactions and might serve as another delivery method of signalling proteins within neurons. What is currently clear, is that PTCHD1 contains two features associated with the cellular mechanism of membrane receptor trafficking and localisation to the postsynaptic density. Furthermore, a loss of PTCHD1 is

reported in cases of ASD and ID. Finally, PTCHD1 contains an SSD, which is integral to the function of its closest protein relatives.

5.2 Aims and Hypothesis

The possibility that PTCHD1 functions through the mobilisation of cholesterol, in a similar manner to PTCH1, makes it an interesting homolog to investigate structurally. There is very little known functionally about PTCHD1 and no structural work performed, as of yet. Significant information will be gained through the elucidation of the structure of PTCHD1. I hypothesise that the overall architecture of the protein will closely resemble that of PTCH1 and NPC1 and that PTCHD1 will also possess cholesterol binding pockets.

The work performed in this chapter will be presented in a chronological manner as the following aims:

- i. Optimisation of the production and subsequent purification of PTCHD1 from baculovirus infected insect cells;
- ii. Utilisation of negative stain electron microscopy to generate initial structural prediction models of PTCHD1;
- iii. Investigate protein functionality, using both purified PTCHD1 and cell-based expression assays.

5.3 Results

5.3.1 Cloning and Production of PTCHD1 Baculovirus Infected Cells

For the purposes of expression, a pFastBac vector expression system was used to produce baculovirus-infected *Sf9* insect cells (BIICs). PTCHD1 is a membrane protein of low level expression and thus required a system capable of both high yield and moderate glycosylation. Therefore, an insect expression system was preferred over an *E. coli* one, because high expression yields were still achievable, with a moderate level of glycosylation. Mammalian expression systems would have been more favourable, for high level glycosylation, but protein yields would have been severely sacrificed.

Wild-type PTCHD1 cDNA was PCR-amplified from pOPINN-PTCHD1, using primers containing the restriction sites AvrII and SbfI. Subsequent restriction digest of the PCR product and the recipient vector, pFastBac-CVGH, followed by ligation, were used for sub-cloning. The vector pFastBac-CVGH was selected because the final product introduced a C-terminal HRV cleavage site, GFP and an 8xHis tag in frame with PTCHD1 cDNA. Successful cloning was confirmed by Sanger sequencing.

For a detailed explanation of the protocols, please see **(2.18 Generation of Baculovirus)** and **(2.17 Production of Baculovirus Infected Cells (BIICs))**. Briefly, pFastBac-PTCHD1-CVGH was transformed into two *E. coli* strains, DH10Bac (Invitrogen) and Multibac EmBacY (Geneva Biotech), to determine an optimal expression strain. A blue/white screen was performed on selective agar plates to identify positive colonies, which were then expanded and the bacmid

DNA purified for subsequent transfection of *Sf9* cells. The supernatant of transfected *Sf9* cells (V0) was harvested, whilst the cells were kept for confirmation of infection. V0 supernatant was then used to amplify the baculovirus in fresh *Sf9* cells. The supernatant (V1) was collected 24 h after proliferation arrest (PA + 24 h) for subsequent titer testing. Infected *Sf9* cell cultures which doubled once before PA were selected for use as 'BIICs' and stored in LN₂.

5.3.2 Expression and Membrane Preparations

Sf9 cells, at a density of 1×10^6 cells/mL, were infected with PTCHD1 BIICs and PA confirmed after ~24h. Cells were harvested at PA + 48 h by centrifugation, with pellets either flash frozen and stored at -80°C or membranes prepared immediately. Expression of the PTCHD1 construct was confirmed visually, during cell harvesting, by UV light exposure on a small sample (**Figure 5.3**). Membranes were prepared by cell lysis, via sonication, and subsequent membrane fractionation by centrifugation. Successful PTCHD1 expression and membrane fractionation was confirmed by SDS-PAGE, initially visualised for GFP using blue light, then by Coomassie blue stain (**Figure 5.3**).

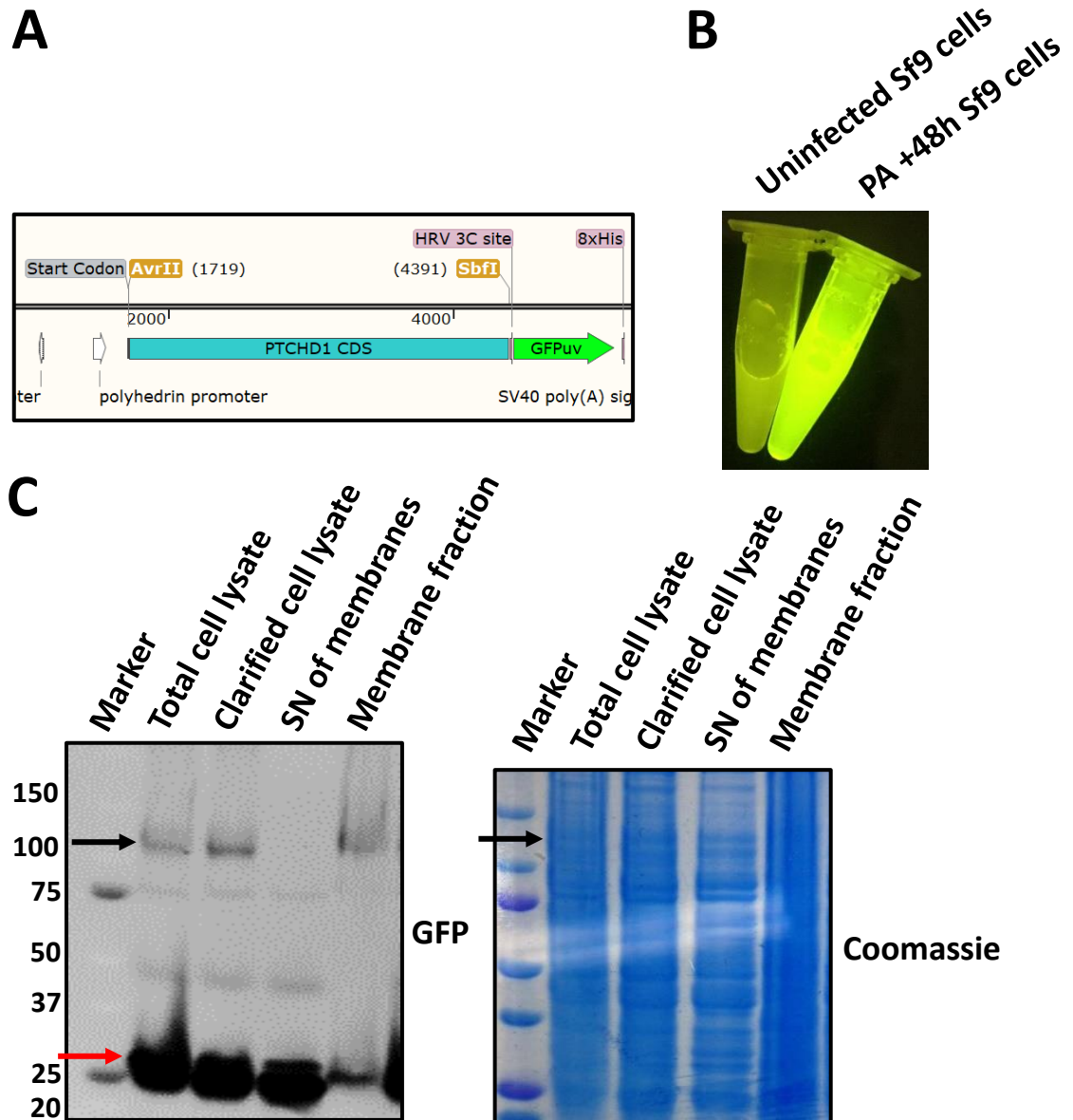


Figure 5.3 Expression and membrane fractionation of PTCHD1 from Sf9 BIIcs.

(A) Section of pFastBac-PTCHD1-CVGH plasmid map showing layout of coding sequence, with C-terminal HRV site, GFP and 8xHis tag. **(B)** Expression of PTCHD1 indirectly confirmed by UV visualisation of the native YFP within the Multibac EmBacY plasmid. Infected cells at PA + 48h were compared to uninfected cells. **(C) Left:** SDS-PAGE imaged under blue light to visualise the C-terminal GFP of PTCHD1 at ~100 kDa, indicated by a black arrow. Free, native YFP of the Multibac EmBacY plasmid was visible at ~25 kDa, indicated by a red arrow. **Right:** Subsequent Coomassie stain of SDS-PAGE for total protein. The approximate location of PTCHD1 is indicated by a black arrow.

5.3.3 Small Scale Detergent Screening

PTCHD1, like PTCH1 and NPC1, contains a SSD, strongly associated with cholesterol. Structures of both PTCH1 and NPC1 have revealed sterol like densities within cavities of the SSD. In some cases, these densities were believed to be cholesterol analogs, such as cholesteryl hemisuccinate (CHS), which were included in the detergent solubilisation process. It seems likely that the sterol analogs conferred a stabilising effect during purification. The similarities of PTCHD1, particularly the SSD, suggests it will also benefit from the stabilising interactions of a sterol analogue, during purification.

On this basis and others, glyco-diosgenin (GDN) was pre-selected as a desired detergent target for PTCHD1 purification. As a synthetic drop-in substitute for digitonin, with several reported advantageous adaptations, GDN was an exciting prospect to investigate. A growing list of membrane protein structures have been published using GDN as the detergent in recent years. In particular, the coupling of GDN with Cryo-EM indicated promising application.

GDN has a steroid-based hydrophobic group attached to a di-maltose head group. This combination has been described as optimal, in achieving good solubilisation, whilst maintaining protein stability (Breibeck and Rompel, 2019). The use of GDN was shown to provide formidable stability to isolated proteins over a 20-day period (Chae et al., 2012). Therefore, GDN could be used for both solubilisation and maintenance of PTCHD1 proteins throughout the purification. This could effectively reduce the amount of physical manipulations, such as

detergent buffer exchange, or supplementation with cholesterol analogs, required during purification.

Moreover, issues of toxicity and concentration variability, associated with digitonin are mitigated with GDN. Initial attempts to solubilise PTCH1 with digitonin, resulted in a temperature-dependent precipitation of the detergent, both in the absence and presence of protein (data not shown). This resulted in a variable, unknown concentration of digitonin in the subsequent purification steps. Recently, GDN (1%) was shown to effectively extract dimeric ATP synthase from yeast mitochondrial membranes (Guo et al., 2017). Previously, this had been achieved through n-Dodecyl β -D-maltoside (DDM) solubilisation with centrifugation in a digitonin, glycerol gradient with anion exchange (Hahn et al., 2016).

Finally, the critical micelle concentration (CMC) of GDN (0.018 mM) is similar to Lauryl Maltose Neopentyl Glycol (LMNG) (0.01 mM) and smaller than digitonin (0.5 mM) and DDM (0.17 mM). A lower CMC is advantageous in reducing empty micelle background interference, during electron microscopy. Misidentification of empty micelles is a pitfall of many membrane protein structural studies. Often, distinguishing between an empty micelle and a micelle containing the transmembrane core with a small protruding extracellular domain can be challenging.

Initial small-scale detergent screens were used to compare the ability of GDN and more conventionally-used detergents, to solubilise and excise PTCHD1 from the membrane fraction. The detergents LMNG, DDM and digitonin served as reference points, used at manufacturer-recommended concentrations, in a

standard buffer of 1x PBS, 200 mM NaCl, 10% glycerol. Both LMNG and DDM were supplemented with CHS, to mimic the presence of cholesterol. Supplementation with CHS was determined not to be required for digitonin or GDN, due to their steroid-based hydrophobic groups.

Solubilisation of 2 g of flash-frozen membranes with each detergent solution for 2 h at 4°C, produced large differences in the percentage of PTCHD1 recovered (**Figure 5.4**). Densitometric analysis of the GFP SDS-PAGE gel revealed DDM + CHS as the most successful detergent, solubilising ~73% of total PTCHD1 (**Figure 5.4B**). LMNG + CHS came in second with ~65%, followed by digitonin at ~41%, and, finally, GDN with ~27% (**Figure 5.4B**).

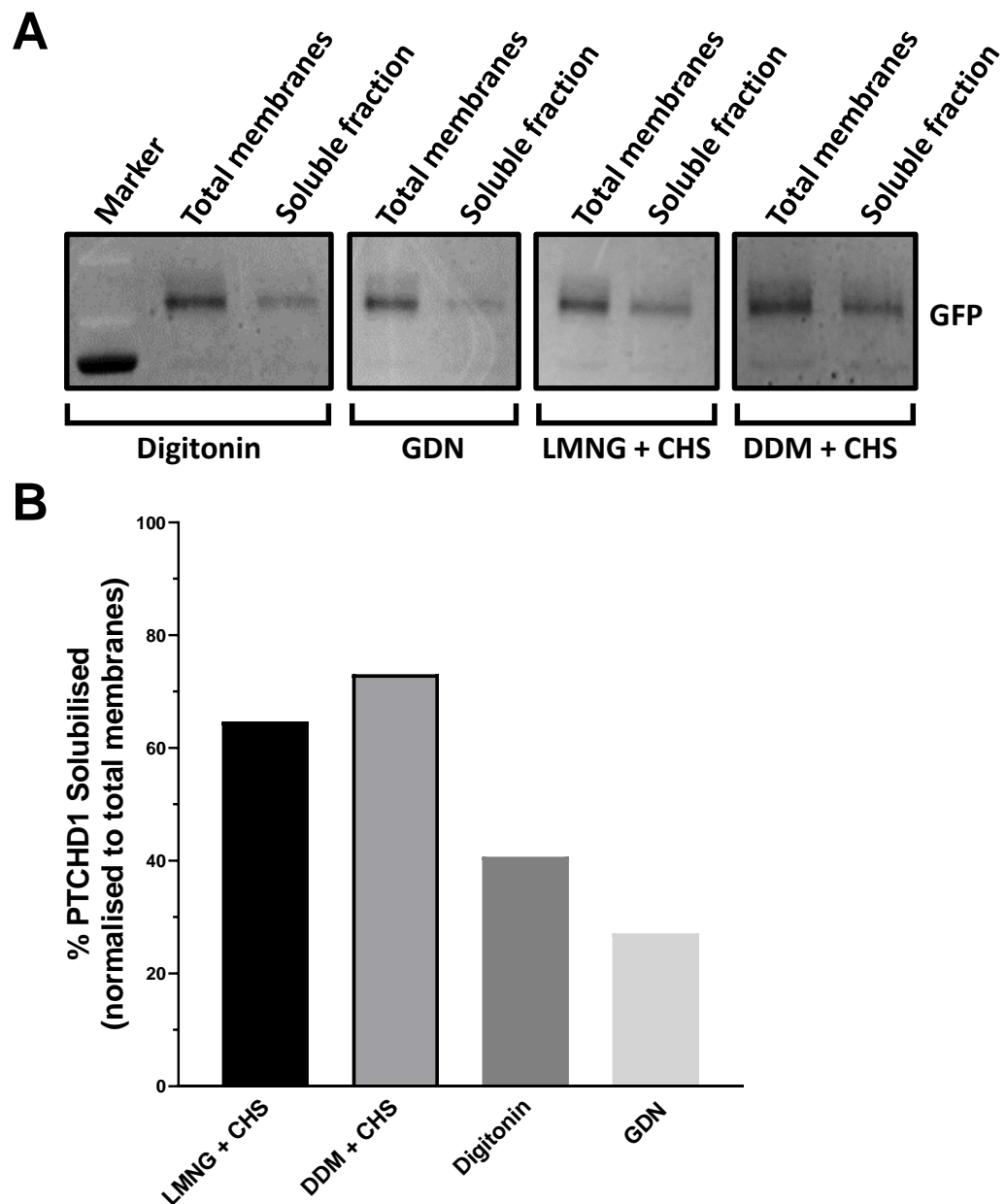


Figure 5.4 Small scale membrane solubilisation detergent screen.

(A) SDS-PAGE gels showing solubilisation screen of four detergents; 1.25% LMNG + 0.125% CHS, 1.25% DDM + 0.125% CHS, 0.2% digitonin and 0.2% GDN. Two grams of membranes prepared from PTCHD1-baculovirus infected *SF9* cells were used for each detergent. The C-terminal GFP of PTCHD1-CVGH was visualised by blue light on a G:Box (SynGene). **(B)** Densitometric analysis of detergent screen SDS-PAGE gels, performed in FIJI. The soluble fraction of each detergent condition was normalised to its corresponding total membrane fraction.

5.3.4 SEC-MALS and mass spectrometry analysis identified a monodispersed peak of PTCHD1 in GDN purification

Due to its strong performance in initial solubilisation screening, LMNG + CHS was selected for further purifications and subsequent analysis. Despite DDM + CHS being the top performer, LMNG was favoured because of its lower CMC (0.001%/0.01mM) to micelle size (92 kDa) ratio. Experimental evidence also suggests that LMNG shows superior thermo-stabilisation, maintenance of solubility, and prevention of purified protein aggregation (Chae et al., 2010). While GDN performed 'poorly' in the initial solubilisation screen of PTCHD1, its use within the lab was considerably less established, than that of the other detergents. As such, the initial conditions and concentrations used were highly likely to be sub-optimal. With optimisation in mind, GDN was also taken forward for further study.

Both detergents, LMNG + CHS (1.25%, 0.125%) and GDN (0.2%), were used in larger purifications from ~13 g of flash-frozen membranes. Spin-concentrated PTCHD1 elution fractions for both LMNG + CHS and GDN were subjected to SEC-MALS analysis, with contrasting results. Despite a poor proportion of PTCHD1 solubilisation, GDN produced a clear elution band for PTCHD1 at ~100 kDa on SDS-PAGE (**Figure 5.5A**). Moreover, the SEC-MALS trace from the purification in GDN displayed a monodispersed peak at ~7 min. Even after a round of flash freezing and storage at -80°C, the thawed protein elution produced

an unaltered SEC-MALS trace, suggesting good quality protein, stabilised well by the GDN micelle complexes. **(Figure 5.5B-C)**.

On the other hand, SEC-MALS analysis of the LMNG + CHS purification produced a lower quality trace, with several shoulders and peaks after the initial peak at ~7 min **(Figure 5.5C)**. Alignment of the two detergent purification SEC-MALS traces indicated that the initial peak at ~7 min was likely to be the protein of interest, PTCHD1 **(Figure 5.5C)**. However, the identity of the purified product still required confirmation. To ascertain whether the peak and predominant product of GDN purifications was PTCHD1, elution fractions were subjected to mass spectrometry protein identification and coverage identification. In brief, ~13 g of flash-frozen membranes were solubilised with 0.2% GDN, with the elution fraction in 0.004% GDN. Visualisation of the purification fractions by SDS-PAGE and blue light imaging (GFP) confirmed successful purification of a protein of the approximate mass of PTCHD1 **(Figure 5.6B)**.

A second SDS-PAGE gel was then run with four lanes of the elution fraction (15 μ L/well) and stained with BioSafe G250 (BIO-RAD) Coomassie. The Coomassie gel was then processed internally by the mass spectrometry facility staff, who performed gel extraction and protein digest. A panel of four digestion agents, trypsin, chymotrypsin, asp-N and trypsin with lys-c was used. This is common practice in initial mass spectrometry experiments to ensure sufficient coverage is achieved for protein ID. The various proteases have different cleavage sites specificity, and thus, can produce peptides of differing length and/or location. Mass spectrometry confirmed PTCHD1 as the most abundant protein in the elution fraction. An overall coverage of 66% was achieved by the combination of

the four proteases (**Figure 5.6A**). As expected, the regions of lowest coverage were the transmembrane domains.

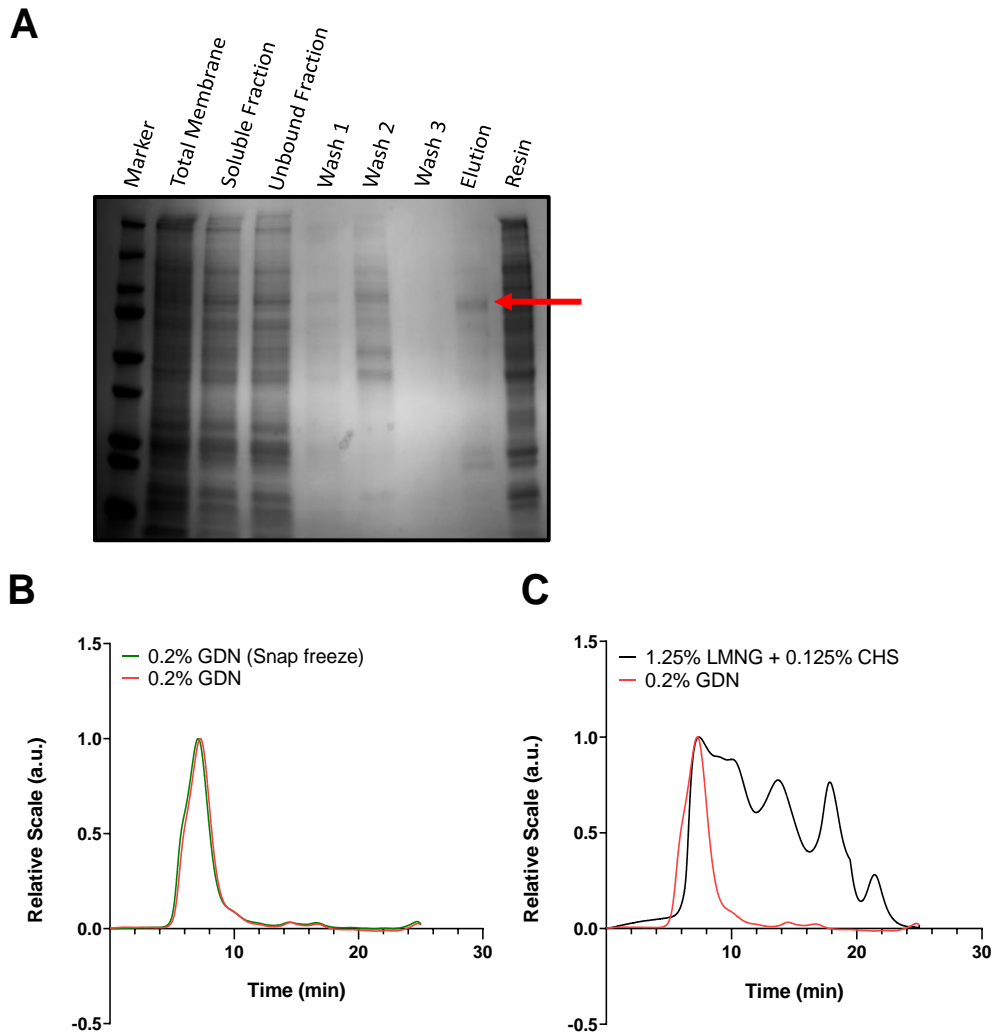


Figure 5.5 SEC-MALS analysis of determined GDN superior to LMNG + CHS for purification of a protein corresponding to the mass of PTCHD1.

(A) SDS-PAGE of 13 g PTCHD1 *Sf9* membranes 0.2%-0.004% GDN purification. Elution fraction showed predominant band at approximate mass of PTCHD1, indicated by a red arrow. **(B)** SEC-MALS analysis of 35 μ L GDN elution fraction, either loaded immediately after purification (red) or after snap freezing and storage at -80°C overnight (green). **(C)** SEC-MALS analysis of 35 μ L LMNG + CHS (1.25%, 0.125%) elution fraction, loaded directly from purification (black), overlay of GDN (0.2%-0.004%) purification (red), indicated a corresponding peak at ~ 7 min.

A



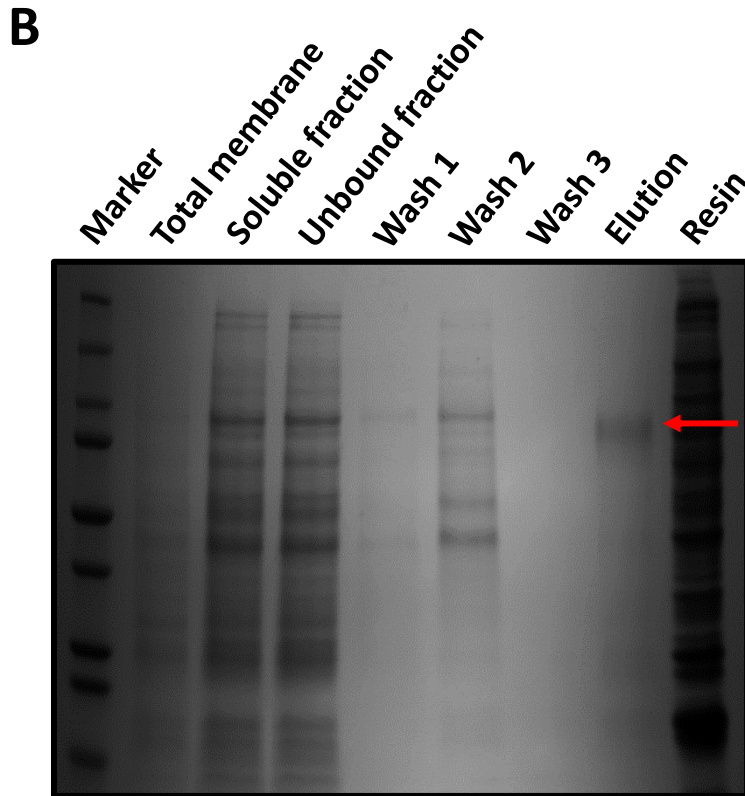


Figure 5.6 Mass Spectrometry confirmed the identity of the purified protein as PTCHD1.

(A) Mass spectrometry analysis of GDN purification elution fractions, digested with trypsin, chymotrypsin, asp-N and trypsin with lys-c, identified PTCHD1 as the primary protein present. An overall combined peptide coverage of 66% was achieved. Blue lines indicate individual peptides detected. **(B)** Coomassie staining of the GDN purification of ~13 g of extracted *Sf9* membranes. Elution fraction concentration, indicated by a red arrow, was estimated to be 379 ng/ μ L in 130 μ L by nanodrop 8000 measurement.

5.3.5 Optimisation for Large Scale Purification of PTCHD1 with GDN.

Although a good quality, homogenous sample of PTCHD1 could be obtained using GDN, further optimisation steps were required, in anticipation of high-resolution cryo-EM. Typically, ~3 μL of purified protein, at a concentration between 1.5-5.0 μg , is applied to grids for cryo-EM. This poses a challenge, especially to membrane proteins, where there is a fine line between achieving maximal concentration, whilst avoiding aggregation. Furthermore, intrinsic protein dynamics within a given protein purification are unique, and by means largely undetermined, even highly similar proteins 'behave' differently in the same conditions.

Although a routine method can be followed for optimisation, the process is largely trial and error based. In order to best optimise the purification of PTCHD1 in GDN, experiments were performed to the original protocol, with a single variable altered independently. This ensured any effects observed were a result of that specific alteration, with the aim to maximise each step of the process independently, to then generate a final optimised protocol.

With the knowledge that purified PTCHD1 appeared stable when flash-frozen and thawed, an increase in solubilisation time was believed unlikely to adversely impact protein quality. Increasing solubilisation time from 2 h to overnight (~18 h) resulted in ~13% more solubilised PTCHD1 protein from the total membrane sample (**Figure 5.7**). Densitometric analysis was used to estimate that 2 h and overnight solubilisations resulted in ~17% and ~30% of total PTCHD1 in the soluble fraction respectively. This increase in solubilisation time translated to a 1.8-fold increase in solubilised PTCHD1 yield.

To further increase PTCHD1 solubilisation, the concentration of GDN used during this step was assessed. Concentrations as high as 2% have been reported in the isolation of homogenous TatBC complex (Wojnowska et al., 2018). TatBC is estimated to be ~440 kDa, which is much larger than the monomer of PTCHD1 at ~100 kDa. However, it was possible that PTCHD1, like PTCH1, could form higher oligomeric structures within the cell. Increasing the concentration of GDN during solubilisation was approached cautiously. If not properly removed, during on column buffer exchange, or in the subsequent concentration 'cut off' step, high concentrations of GDN could pose an issue to downstream applications. GDN has a very low CMC, so empty GDN micelles were a high possibility.

Increasing the concentration of GDN from 0.2% to 0.4% during a 2 h solubilisation, resulted in a 1.29-fold increase in solubilised PTCHD1 (**Figure 5.8**). This increase was reflected in the bound fraction, suggesting that the additional protein solubilised was efficiently extracted and likely mature membrane localised PTCHD1. Up to ~70% of total protein still remained un-solubilised, indicating further increases of GDN could extract more PTCHD1.

Another step identified to be yield limiting, was the immobilisation of PTCHD1 on the HisPur™ Cobalt resin. Quantification and SDS-PAGE analysis of the unbound run-through and subsequent washes, confirmed a large protein loss from the resin (data not shown). HisPur™ Cobalt resin has a binding capacity well in excess of the concentration of PTCHD1 required for cryo-EM. However, it was suspected that an increase of total resin volume could increase recovery of PTCHD1. To this end, the effect of doubling the resin volume from 2% to 4% of the total volume of solubilised fraction loaded was analysed. A sample of 0.8%

GDN solubilisation and a control condition of 1% DDM + 0.1% CHS were assessed alongside the two resin conditions. DDM + CHS originally outperformed GDN considerably, so it was a good positive control to determine improvements of GDN against. It is however important to note that the previous solubilisation was performed in a PBS buffer and since then, this had been switched to a HEPES buffer. Densitometry analysis estimated that the solubilisation of PTCHD1 increased 1.3-fold with 0.8% GDN vs 0.2% GDN (**Figure 5.9B**). Moreover, doubling the resin volume or solubilisation with 0.8% GDN produced a 2.4-fold and a 4-fold increase in eluted PTCHD1 respectively (**Figure 5.9D**).

Many other optimisation steps and alternative methods were conducted but with negative or neutral impact on purification yield. These include, but are not limited to: use of PBS and Tris-based buffers, detergent exchange from DDM + CHS or digitonin into GDN, use of amphipol A8-35, use of different concentrator apparatus or membrane type, altering pH to 6.26 and 8.18, using high salt HEPES buffer, and attempting resin-based cation exchange.

After extensive optimisation efforts, the alterations that showed independent success in improving PTCHD1 yield were combined in a final protocol. A purification was performed on 13.5 g of Sf9 membranes with 0.8% GDN, overnight (18 h). This was followed by immobilisation on a HisPur™ Cobalt resin (7.5% the volume of soluble fraction loaded) and elution in 0.004% GDN, subsequently spin concentrated (MW cut-off 100 kDa). SDS-PAGE of the purification displayed a strong band for PTCHD1 (~100 kDa) in the elution fraction. Estimation of the concentration of PTCHD1 in the spin concentrated elution fraction was 336.7 ng/μL in 250 μL (**Figure 5.10**). This is a 1.71-fold

increase on the total quantity of PTCHD1 purified using the original protocol in the mass spectrometry purification.

Densitometry analysis of the GFP SDS-PAGE estimated ~70% solubilisation of PTCHD1 from total membranes. Furthermore, based upon the unbound fraction, ~55% of this solubilised PTCHD1 was bound to the HisPur™ Cobalt resin (**Figure 5.10B**).

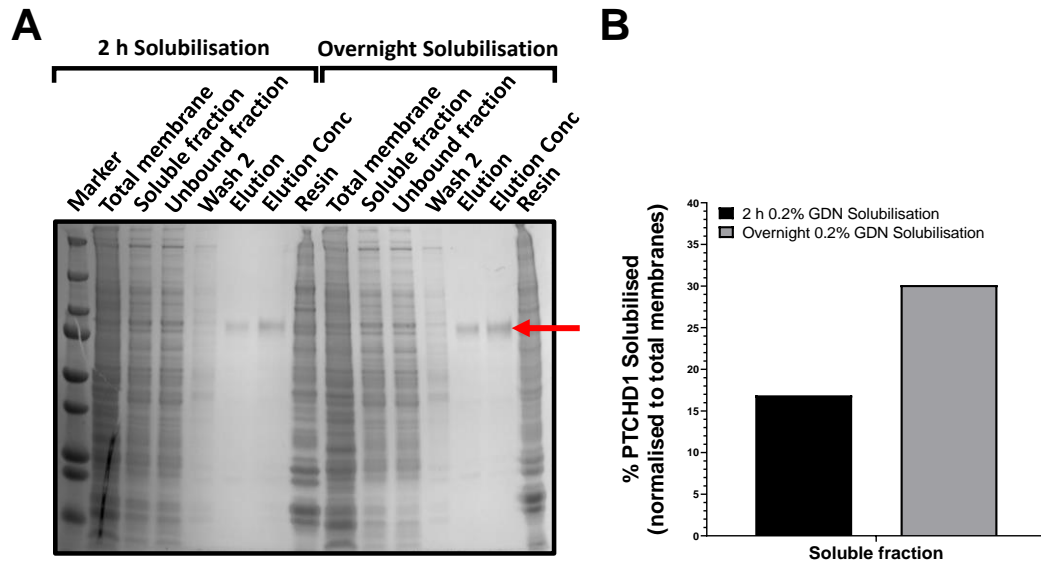


Figure 5.7 A longer solubilisation time resulted in increased PTCHD1 in the soluble fraction.

(A) Coomassie of SDS-PAGE of two 13.5 g membrane purifications, solubilised in 0.2% GDN for either 2 h (left) or overnight (right). PTCHD1 is indicated by a red arrow. **(B)** Densitometry analysis performed in FIJI. The SDS-PAGE soluble fraction bands for 2 h and overnight samples were normalised to their corresponding total membrane band, to estimate the percentage yield of solubilised PTCHD1.

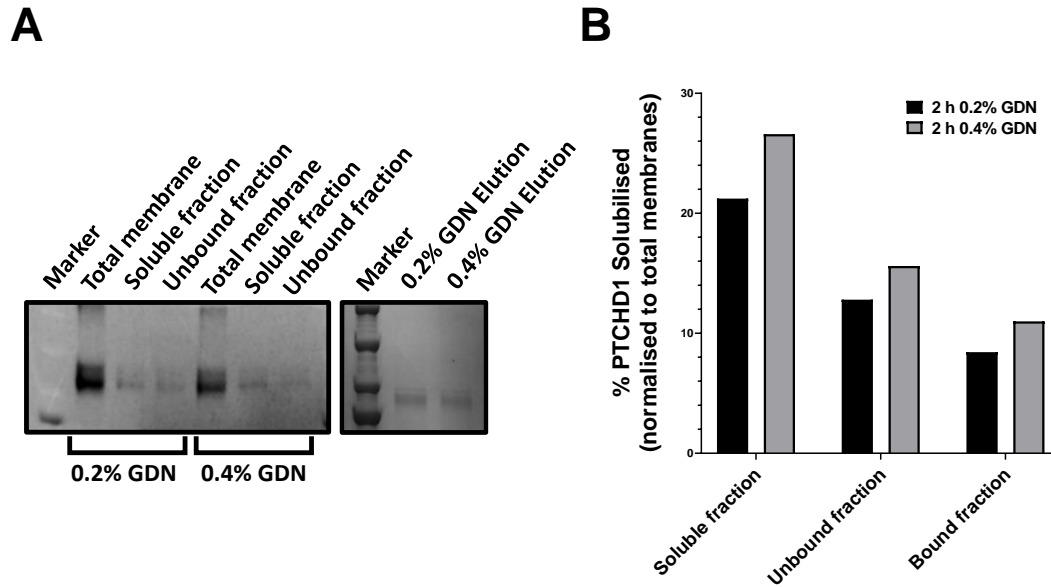


Figure 5.8 Increasing the concentration of GDN during solubilisation increased protein solubilisation.

(A) SDS-PAGE of two purifications of 5 g membranes, solubilised in 0.2% GDN (left) or 0.4% GDN (right). **(B)** Densitometry analysis performed in FIJI. SDS-PAGE bands for 0.2% and 0.4% GDN purifications were normalised to their corresponding total membrane band to estimate the percentage yields of PTCHD1.

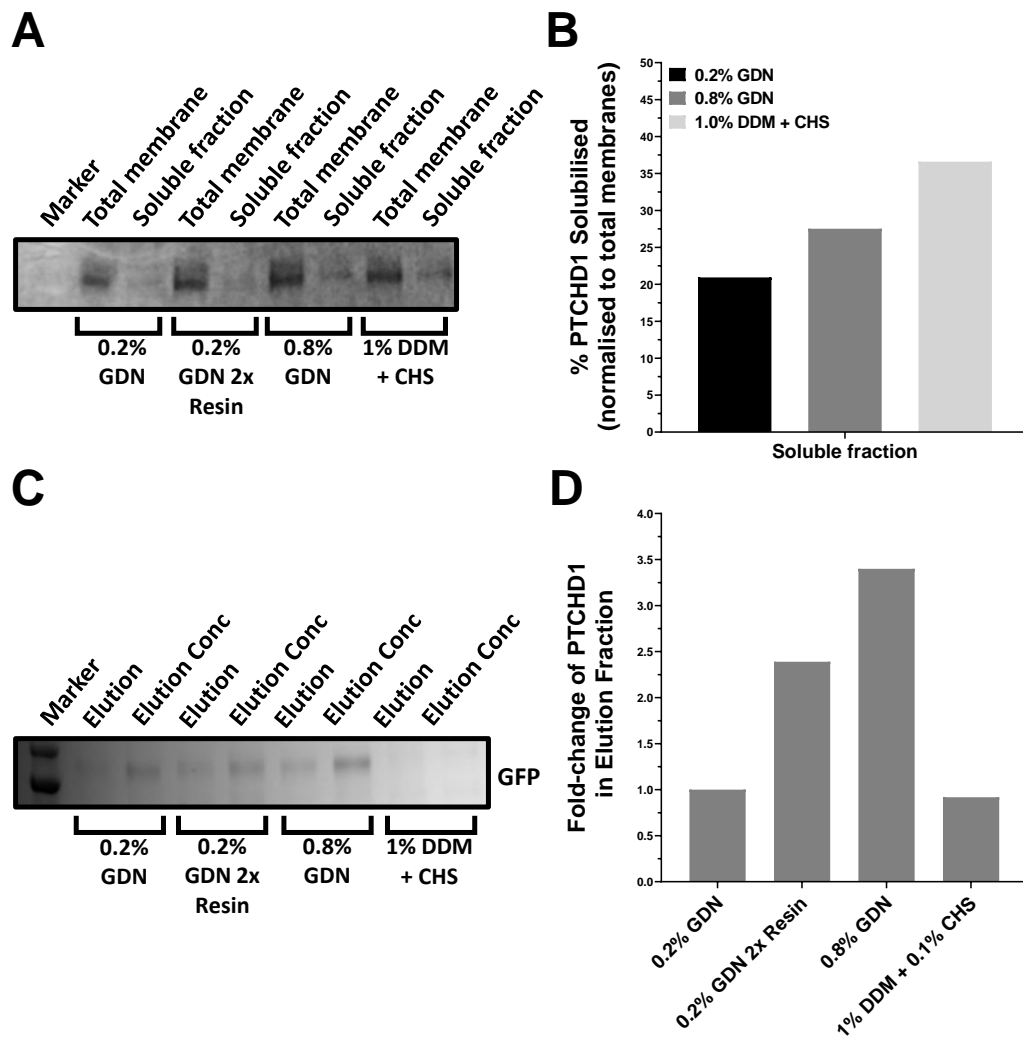


Figure 5.9 Increasing GDN concentration or HisPur™ Cobalt resin volume increased PTCHD1 concentration in elution fractions.

(A) GFP SDS-PAGE of total and solubilised fractions from 4 x 5 g membranes solubilised in 0.2% GDN, 0.2% GDN + 2x resin, 0.8% GDN or 1% DDM + 0.1% CHS for 2 h. **(B)** Densitometry analysis of the GFP SDS-PAGE shown in (A) confirmed increased solubilisation by 0.8% GDN vs 0.2% GDN. Analysis was performed in FIJI. SDS-PAGE bands for soluble fractions were normalised to their corresponding total membrane band, to estimate the percentage yield of PTCHD1 solubilised. **(C)** GFP SDS-PAGE of elution and spin column concentrated elution fractions from same samples described in (A). **(D)** Densitometry analysis of the GFP SDS-PAGE shown in (C) confirmed that increasing either resin volume or GDN concentration increased relative PTCHD1 elution concentration. Analysis was performed in FIJI. SDS-PAGE bands for all elution fractions were normalised against the elution band of 0.2% GDN.

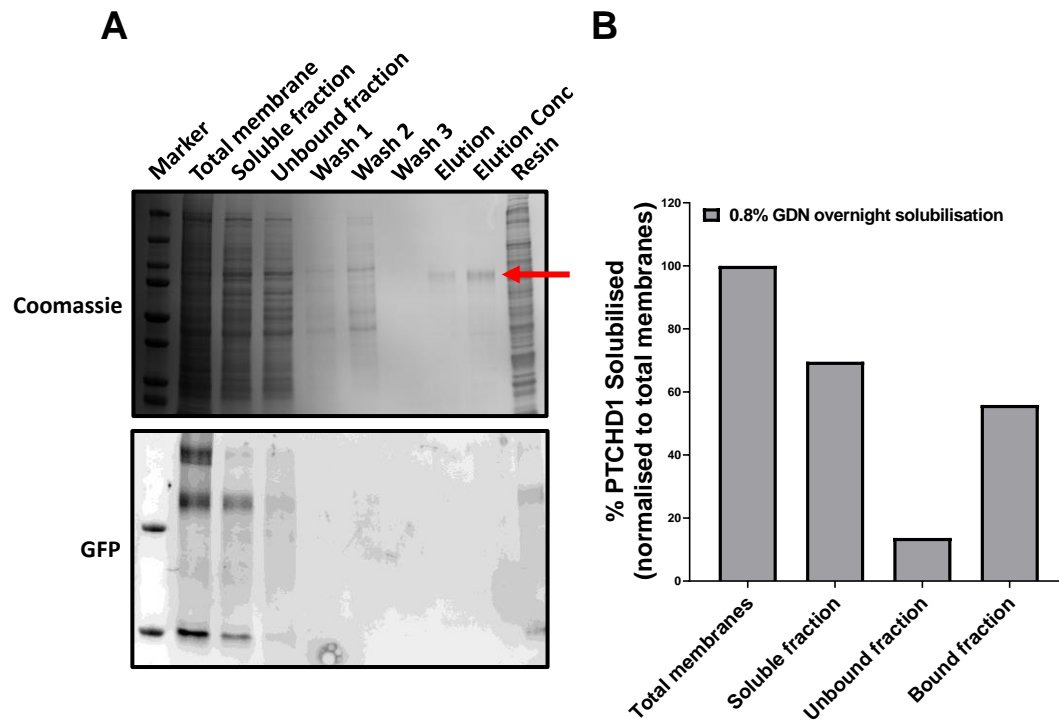


Figure 5.10 Final optimised GDN purification of PTCHD1.

(A) Coomassie and GFP imaging of SDS-PAGE of 0.8% GDN overnight purification of PTCHD1 from 13.5 g membranes harvested from Sf9, PA +48 h PTCHD1-CGHV BIICs infected cells. PTCHD1 in the elution concentration is indicated by a red arrow. Nanodrop measurement estimated a concentration of 336.7 ng/ μ L in \sim 250 μ L total volume. **(B)** Densitometry analysis performed in FIJI. GFP SDS-PAGE purification fractions were normalised to total membrane to estimate the percentage yield of PTCHD1.

5.3.6 Structural analysis of PTCHD1 by negative stain.

Initial structural elucidation experiments, via negative stain, were conducted during optimisation steps. This was primarily intended for brief grid screening, to confirm that improvements to the purification process were reflected in the EM micrographs. While negative stain achieves a much lower resolution than cryo-EM, there are clear advantages, and to obtain a good negative stain is a 'checkpoint' before progressing to cryo-EM.

For a detailed description of the preparation of negative stain grids, please see **(2.26 EM Grid Glow Discharge)** and **(2.27 Electron Microscopy Negative Staining)**. Briefly, purified concentrated PTCHD1 fractions were routinely serially diluted, 1:2, 1:5, 1:10, 1:20 and mounted on glow-discharged copper carbon coated grids. Staining was performed with a 2% uranyl acetate solution, before air drying and storage/imaging. Initial screening was performed using an FEI Technai G2-spirit (screen down: 26.5 kx, screen up 30 kx, pixel size 0.37 nm).

A promising 1:5 dilution protein sample of PTCHD1 (solubilised in 0.8% GDN, overnight and immobilised on 7.5% column volume resin) was selected for a full data acquisition. The carbon grid was examined using an FEI Tecnai F20, 200 KeV, FEG electron source with FEI CETA (CMOS CCD) camera **(Figure 5.11A)**. Screen down and screen up nominal magnifications used for imaging were 25.5 kx and 29 kx respectively, with a pixel size of 0.351nm (EM facility). A total of 41 micrographs were captured and imported into RELION 3 for image processing. For a comprehensive walkthrough of the micrograph processing steps, please see **(Table 2.4 Summary of RELION 3.0 work flow for EM micrograph processing)**.

A total of 4,729 particles, from 38 CTF corrected micrographs, were manually picked. These particles were then used to generate a series of 2D classes, which were subsequently filtered and re-classified once more (**Figure 5.11B**). A 3D model was then generated with a selection of the 2D classes, totalling ~1,100 particles (**Figure 5.11C**).

As the model lacked any discernible features, an EM density map of PTCH1 (EMD ID: 7963) was superimposed for comparison (**Figure 5.11D**). This immediately confirmed that the approximate size and shape of the PTCHD1 model was acceptable. The micelle encapsulating the transmembrane domains of PTCH1 fit well inside the 'head' region of the PTCHD1 model, whilst the protruding ECD's were also largely inside the mesh of the model. However, a section of the ECD's of PTCH1 map clearly protruded from the PTCHD1 model. Upon inspection of the refinement model of this density map (PDB ID: 6DMB), this section corresponded to a large region of ECD2 residues (~K830-G980). The ECD2 of PTCHD1 is approximately 100 residues shorter than that of PTCH1, so it is feasible that a large region of this domains density is absent in the PTCHD1 model.

To gain better clarity, another PTCH1 structure (EMD ID: 8955, PDB ID: 6E1H) was superimposed with the PTCHD1 model (**Figure 5.12**). Here a 2:1 PTCH1:Shh-N complex aligned relatively well, with a single PTCH1 monomer within the PTCHD1 model mesh and the other outside. In particular, a region of the ECD1 lying horizontal to the transmembrane domains sat within a protrusion of the PTCHD1 model. Below this sat Shh-N, completely outside of the PTCHD1 model, as was expected.

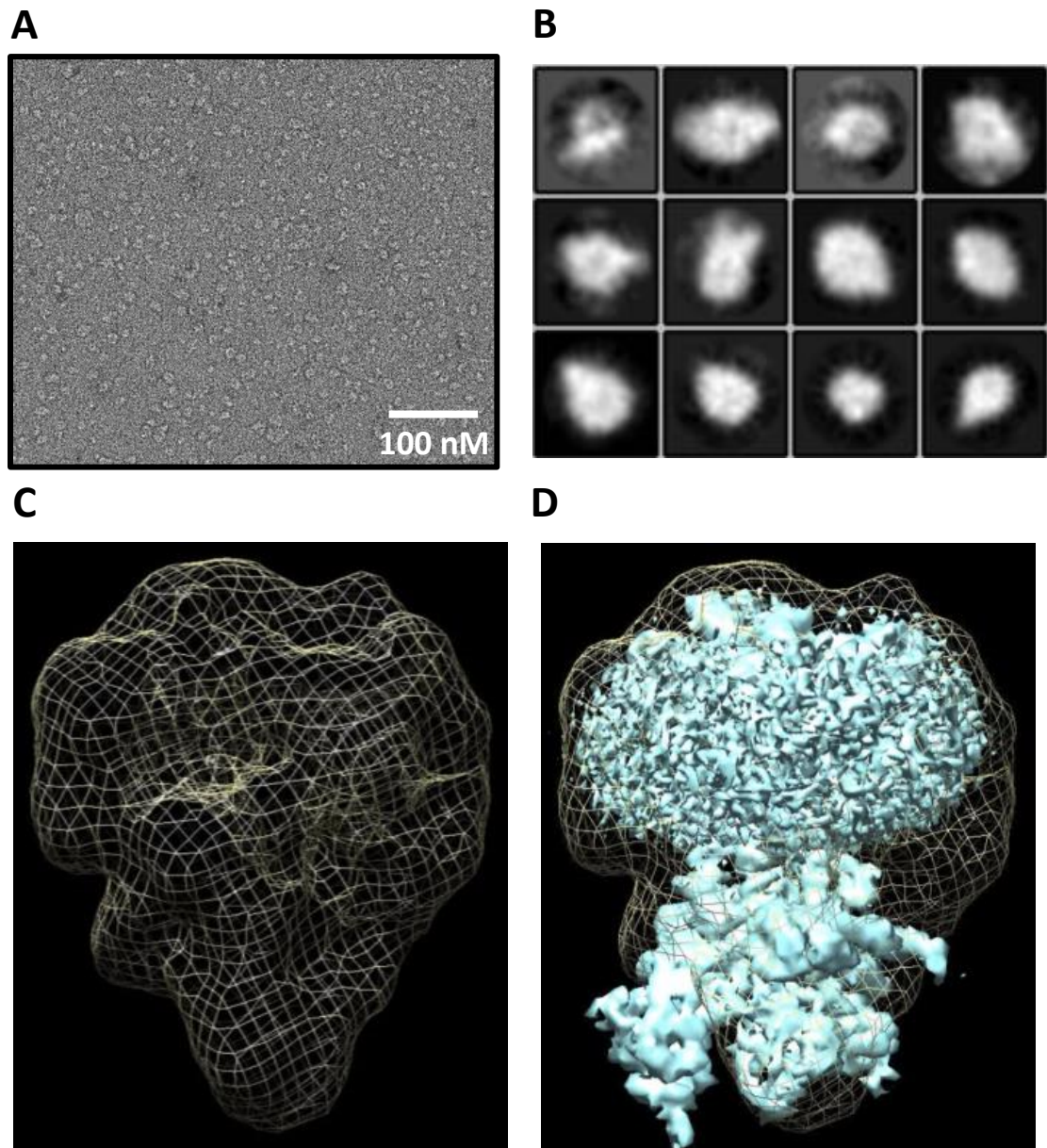


Figure 5.11 Negative stain and 3D model of PTCHD1.

(A) Representative chromatograph of PTCHD1 in 0.004% GDN 1/5 dilution obtained on the FEI Tecnai F20. **(B)** 2D classes generated on RELION 3 from the manual picking of ~4,729 particles. **(C)** A 3D model generated after a second round of 2D refinement (~1,100 particles from selected classes). **(D)** Mapping of the electron density of PTCH1 (EMD ID: 7963) displayed in turquoise onto the 3D model of PTCHD1.

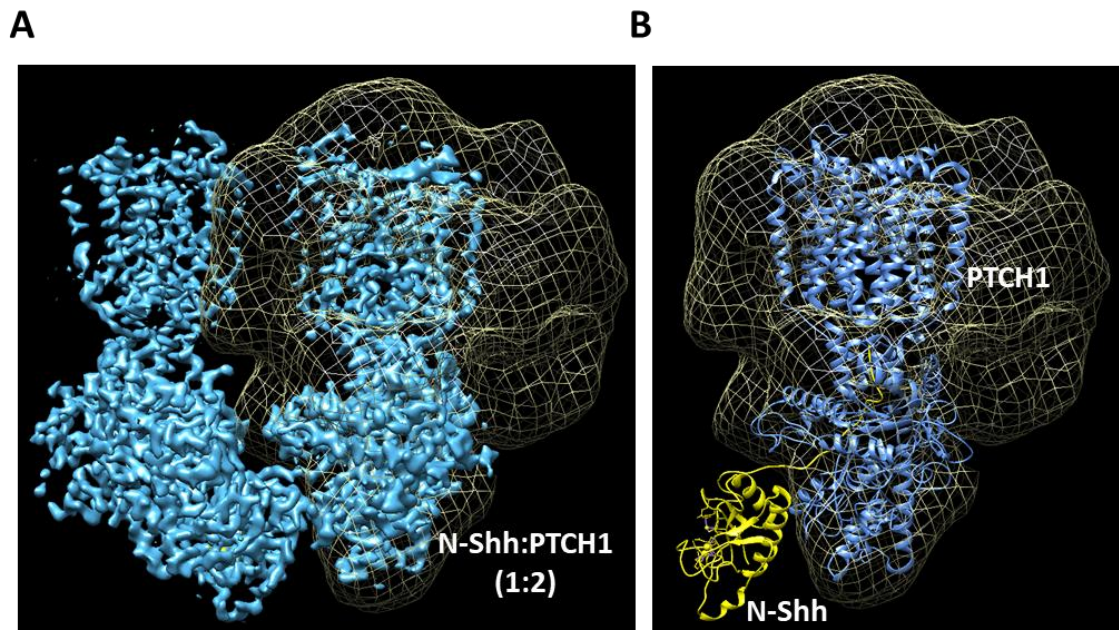


Figure 5.12 Alignment of 2:1 PTCH1:Shh-N complex EM density map to 3D PTCHD1 model.

(A) 3D alignment of the electron density map of the 2:1 PTCH1:Shh-N complex (EMD ID: 8955), (blue) to the 3D model of PTCHD1 generated in RELION 3 (yellow mesh). A single monomer of PTCH1 is within the 3D map of PTCHD1.

(B) 3D alignment of the corresponding ribbon structure of the 2:1 PTCH1:Shh-N complex (PDB ID: 6E1H) to the 3D model of PTCHD1. The second PTCH1 monomer that binds Shh-N in a calcium dependent manner has been removed. PTCH1 (blue), Shh-N (yellow) and PTCHD1 model (yellow mesh). The Shh-N density sits adjacent to the PTCHD1 model as expected.

5.3.7 Progress toward Cryo-EM investigation of PTCHD1.

With a significantly optimised purification protocol, and the potential indication of particles of the approximate dimension of a PTCHD1 monomer, two initial cryo-EM screens were conducted. The first screen indicated several limitations; high background, potentially from the glycerol within the buffer; the grid mesh size was too large, and the protein concentration was quite low (data not shown). Therefore, a purification of PTCHD1 from 15 g of *Sf9* membranes was performed with 0.8%-0.004% GDN. Three specific adjustments were made to address the issues of the previous screen; the 5% glycerol was removed from all buffers during the purification, a spin column concentrator with a lower MWCO (30 kDa) was used during elution fraction concentration, and a grid with mesh size 400 was used. Nanodrop analysis estimated a final concentrated elution fraction of **675 ng/ μ L**. Samples were immediately prepared for negative stain and cryo-EM.

For a detailed description of the vitrification process, please see **(2.28 Vitrification of purified protein)**. Briefly, Quantifoil 1.2 μ m dia (1.3 μ m) 400 Mesh Copper grids were purchased from the EM facility (University of Leeds). Glow-discharged grids were loaded with 3 μ L of purified protein automatically blotted and vitrified, using a Vitrobot MK IV set to 4°C, 100% humidity. Vitrified protein grids were transferred from the liquid ethane for storage in LN₂ until later use. For the purposes of the screen, duplicate grids of neat and 1:2 dilution of PTCHD1 were used.

Grids were clipped and loaded into the FEI Titan Krios 1 by the EM facility team. Screening of the neat PTCHD1 sample was assisted by a member of the EM facility. Although ice thickness, coverage and overall quality was good, particles

were visibly scarce. The background interference was improved in comparison to the first screen with 5% glycerol in the buffer. Imaging towards the periphery of the grid holes revealed some identifiable particles. It was suspected that the particles might be displaying an affinity for the grid surface and as a result much of the protein was lost from the ice.

Future optimisation of the grids and glow-discharge process were planned, but not executed due to COVID-19 disruptions. It was hoped that trial use of gold coated grids, graphene oxide coated grids and glow-discharge with amylamine vapour might provide a suitable surface to optimise PTCHD1 particle distribution.

5.3.8 PTCHD1 binds cholesterol, but displays no function as a Hh pathway negative regulator.

In recent years, strong evidence that both NPC1 and PTCH1 transport cholesterol as their molecular cargo has been presented. Moreover, the data presented in Chapter 4 now indicates PTCH2 also likely shares a functional relationship with cholesterol. To establish whether this functional association is present in PTCHD1, a cholesterol click-reaction assay was performed on purified PTCHD1 protein elution fractions.

In brief, purified PTCHD1 was cross-linked with a PhotoClick cholesterol probe by UV excitation at 365 nm. After, 5-TARMA-Azide was utilised to label cross-linked cholesterol by a 'click-reaction' with the available alkyne group. Finally, the protein sample was subjected to SDS-PAGE and imaged at the excitation wavelength of 5-TAMRA-Azide, 546 nm (**Figure 5.13A**).

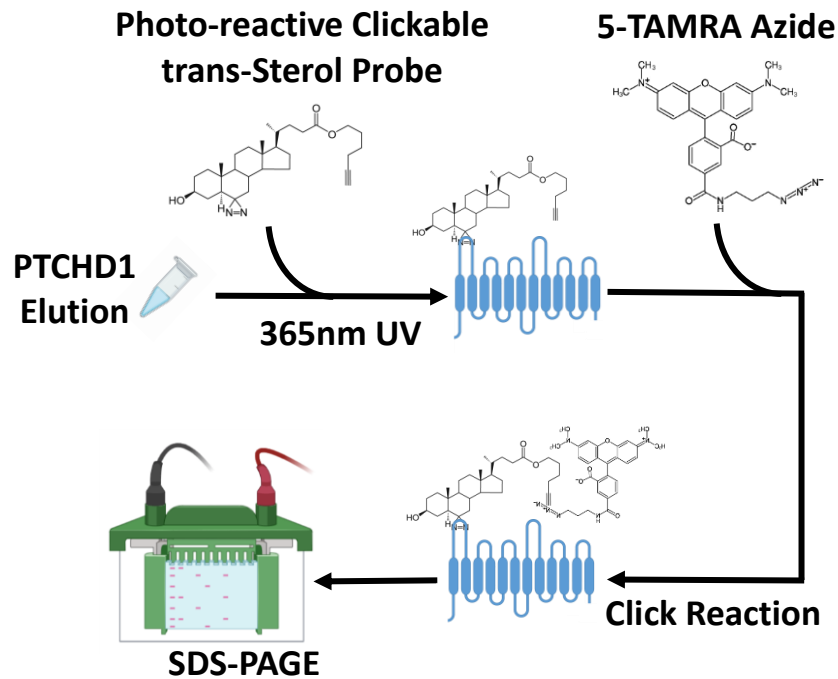
A positive interaction of PTCHD1 with cholesterol was confirmed by the Click-reaction assay (**Figure 5.13B**). A 'no probe' control ensured 5-TAMRA-Azide did not bind non-specifically to PTCHD1, or the GDN micelle. Further controls of 'no UV radiation', 'no click-reaction' and 'no protein', confirmed the specificity of the interaction of the cholesterol probe with PTCHD1. Whilst this result suggests that PTCHD1 is capable of binding cholesterol, it does not determine whether cholesterol is a true functionally relevant endogenous sterol cargo.

Cholesterol has been implicated as the sterol utilised by PTCH1, in its modulation of Smo, to regulate canonical Hh signalling. Early work on PTCHD1 suggested a functional role in canonical Hh signalling, which has since been contradicted by

others. To ascertain whether PTCHD1 can inhibit Smo, a *Ptc1*^{-/-} MEFs Gli-luciferase assay was conducted. Cells transiently transfected with Ptc1-HA displayed robust inhibition of Gli-luciferase activity, whilst no reduction was seen for PTCHD1 (**Figure 5.14**). This indicates that PTCHD1 is incapable of performing a functional role in Hh signalling, at least not in the absence PTCH1. In direct agreement, ligand tracer experiments with PTCHD1 transfected cells failed to detect any specific binding of labelled N-Shh, compared to control cells (data produced by Dr Maren Thomsen, not shown).

The evidence thus far confirms that PTCHD1 can bind cholesterol, but is not sufficient to bind Hh ligand or recover inhibition of the Hh signalling pathway in a cell line devoid of Ptc1, suggesting it is not functionally equivalent to PTCH1. A sensible hypothesis to explain how PTCHD1, a 'probable' cholesterol transporter does not impact Hh signalling is; that it does not localise to the primary cilium, or that it operates more similarly to NPC1, transporting cholesterol in the opposite direction to PTCH1.

A



B

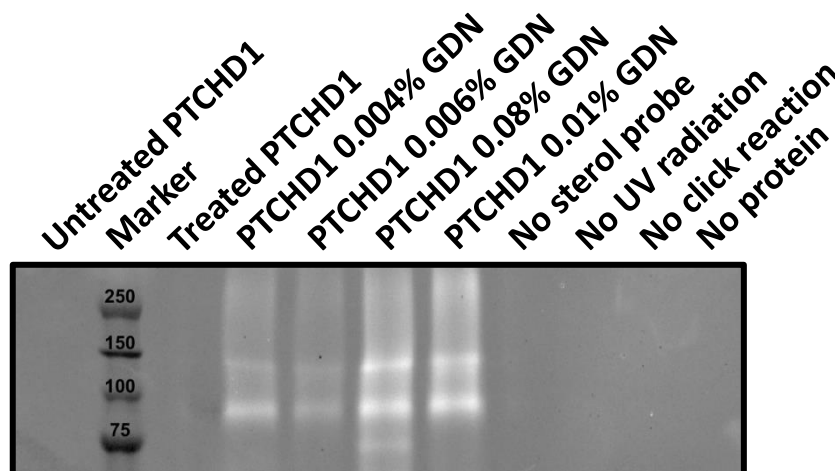


Figure 5.13 PTCHD1 was found to bind cholesterol through Click-reaction assay.

(A) Schematic of the Click-reaction assay. **(B)** SDS-PAGE imaging of 5-TAMRA-Azide (Ex/Em 546/579 nm). PTCHD1 solubilised in batch, in 0.2% GDN, then eluted in different concentrations of GDN (0.004%-0.01%). Elution fractions then subjected to treatments indicated in schematic of Click-reaction.

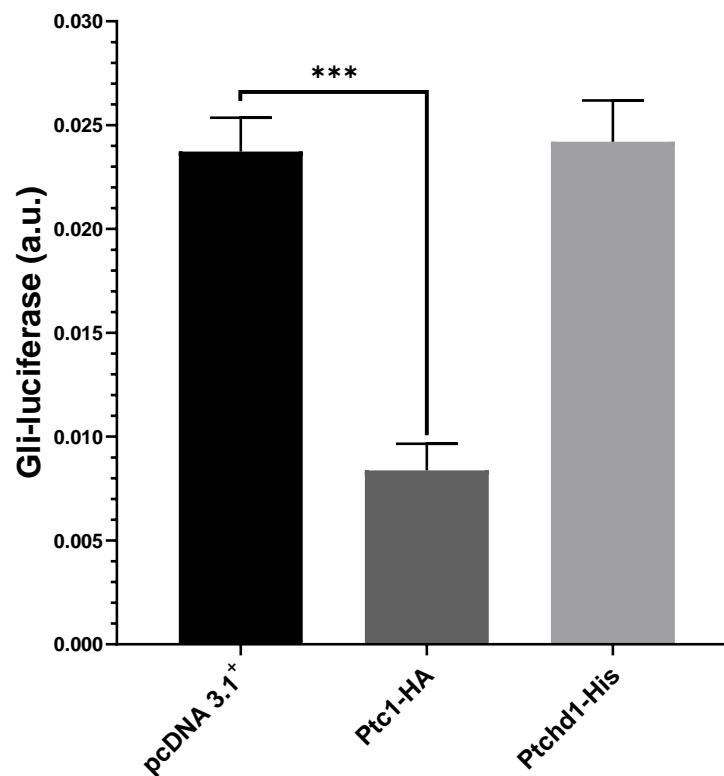


Figure 5.14 PTCHD1 displays no apparent function in canonical Hh signalling.

Gli-luciferase assay of transiently co-transfected *Ptc1*^{-/-} MEFs. Error bars represent mean \pm SEM of a representative experiment performed with quadruplicate conditions. Transfection of Ptc1-HA achieved ~65% inhibition of Gli-luciferase activity, whereas transfection of PTCHD1 showed no inhibition below that of pcDNA 3.1⁺ (negative control).

5.3.9 Immunoprecipitation and mass spectrometry analysis revealed an interaction between PTCHD1 and neuronal ribonucleoprotein granule associated proteins.

In order to investigate the suggested role of PTCHD1 in the Hh signalling pathway further, but to also discover potential unique functions, an immunoprecipitation-based mass spectrometry analysis was performed in HEK293 cells. Other, more suitable cell lines were originally considered for such work, but expression tests ruled these out. SH-SY5Y neuronal-like cells were assessed against HEK293 for transfection and expression of both PTCHD1 and a mutant lacking the first extracellular loop, PTCHD1- Δ Loop-eGFP (**Figure 5.15**).

SH-SY5Y are often used to study neuronal function, but can require differentiation for lineage specific protein expression. SH-SY5Y cells were found to transfect efficiently with a control GFPmax plasmid, but showed no expression of PTCHD1-CHGV or PTCHD1- Δ Loop-eGFP (**Figure 5.15A**). HEK293 cells displayed detectable, albeit low expression of PTCHD1 plasmids, compared to PTCH1-eGFP (**Figure 5.15B**).

The immunoprecipitation mass spectrometry analysis of PTCHD1 interacting proteins followed the standard method of Co-IP, with some adjustments. PTCHD1-CHGV over-expressed in HEK293 cells and precipitated using an anti-His antibody covalently bound to dynabeads. In tandem, a condition using PTCH2-FLAG was run, precipitating using anti-FLAG antibody covalently bound to dynabeads. The lysates eluted from the dynabeads were then subjected to in-house digestion and mass spectrometry at the MS Facility (University of Leeds).

The PTCH2 co-immunoprecipitated proteins served as a 'control' intended to aid in the identification of both Hh related binding partners and non-specific interactions.

Mass spectrometry analysis identified peptides for PTCHD1 and PTCH2 within their respective lysates, confirming successful transfection, expression and pulldown. Protein filtering using the program Peaks selected for peptides with a -10lgP score above a set threshold for quality and confidence purposes. Proteins ID'd with a minimum of 3 unique peptides, above this value were deemed highly likely to be present within the lysate sample. From the PTCHD1 lysate, a total of ~95 unique proteins were found. This protein pool was then subjected to a second round of filtering, against the protein hits of the PTCH2 mass spectrometry analysis. Within the remaining pool of 'PTCHD1-specific interactors' were several interesting and logical associations (**Table 5.1**).

Two of the proteins identified, DYRK1A and NUF2, have histidine stretches within their coding sequences. As a His-tag antibody was used for the IP, there is a potential that these proteins associated directly with the antibody and not via PTCHD1. However, NUF2P was also identified in an independent GST pull down mass spectrometry, performed with PTCHD1 peptide sequences (Tora et al., 2017). Whilst DYRK1A was not identified in that study, its close binding partner, DCAF7 was. STRING analysis of all the identified PTCHD1 interaction partners showed only evidential connections between DCAF7 and DYRK1A (**Figure 5.16**). This suggests it is unlikely that DYRK1A is responsible for the presence of any of the other proteins identified. Moreover, of the 12 other 'key' proteins identified, 11

were also found in the GST PTCHD1 peptide mass spectrometry analysis (**Table 5.1**) (Tora et al., 2017).

Of the GO processes identified, SRP-dependent co-translational protein targeting to membrane (26/92), translational initiation (28/142) and ubiquitin ligase inhibitor activity (3/6) were enriched. A large number of Histones were also observed, with key GO processes, C3HC4-type RING finger domain binding (3/6) and the nucleosome core (23/50). Many of these molecules and the 'key' proteins identified are associated with ribonucleoprotein granules (RNPs).

RNPs are a pathological hallmark of many neurodegenerative diseases, but they also play a pivotal function in healthy cells. RNPs have been found to regulate post-transcriptional expression, stabilise and delay RNA translation, and control protein localisation. Such structures are essential to the ability of neuronal cells, such as dendrites, to enact rapid responses to stimuli at the distal synaptic regions. RNPs can effectively deliver RNA and protein cargo to the synaptic site for later translation. This effectively circumnavigates the delay that would be associated if protein and RNA was processed within the cell body and then transported.

Along with RNPs, a number of similar structures exist in cells, primarily P-bodies and stress granules (SGs). P-bodies show a close relationship with multiple granule structures, with shared regulatory proteins, like Ataxin-2. Exchange of proteins between these two structures has even been demonstrated. Stress granules, as the name suggests, form in the response to cellular stress, be that oxidative, heat, infection or otherwise related. A key difference between SGs and RNPs is that they do not contain stress-induced proteins such as HSP70.

Ataxin-2-like was an interesting association, due to its known involvement in the regulation of stress granule and P-body formation (Kaehler et al., 2012). This effect is mediated through an association with RasGAP-associated endoribonuclease, G3BP, another key protein identified from the mass spectrometry. Ataxin-2-like also contains a PAM2 binding motif, which engages with another protein hit, poly(A)binding protein, PABP. Furthermore, Ataxin-2-like was shown to interact with DDX6 within RNA granules, regulating global mRNA translation and stability (Nonhoff et al., 2007).

DDX3X and DYRK1A have previously been identified along with 67 other genes in a screen of 2,308 individuals with ASD or ASD affected children. DDX3X is highly expressed in the post-synaptic density of the mouse neocortex and is required for neuron generation (Lennox et al., 2020). Missense mutations in DDX3X have been shown to induce ectopic RNPs in neuronal progenitors with impaired translation. DDX3X was recently attributed to being responsible for 1-3% of previously unexplained cases of intellectual disability. The presence of DDX3X and the cohort of RNP components in this mass spectrometry analysis is suggestive of independent convergence of ASD related genes in a common structure. This could provide further explanation of the multifactorial aetiology of ASD, where regulatory dysfunction of RNPs would impact many proteins.

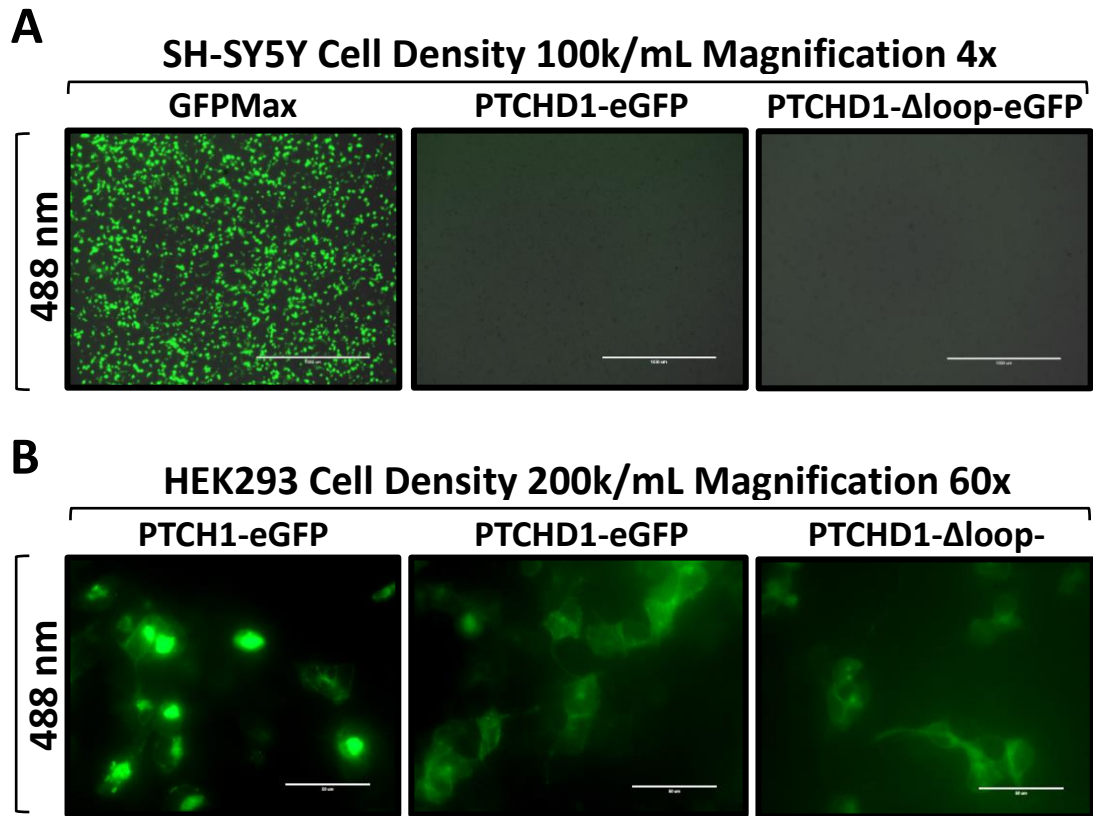


Figure 5.15 Immunofluorescence of PTCHD1 in SH-SY5Y and HEK293 cells.

(A) SH-SY5Y cells transiently transfected with PTCHD1-eGFP, PTCHD1- Δ Loop-eGFP or GFPMax (transfection efficiency control). Imaging at 4 x magnification revealed no discernible GFP expression of PTCHD1 proteins. **(B)** HEK293 cells transiently transfected with PTCHD1-eGFP, PTCHD1- Δ Loop-eGFP or PTCH1-eGFP. Imaging at 60x magnification revealed expression of all three GFP labelled proteins. Immunofluorescence was conducted on an EVOS fluorescent light microscope, on live cells, seeded in 12-well cell culture plates, 24 h post Lipofectamine 2000 transfection.

Protein Name	No. unique peptides	Validated by GST PTCHD1 MS of Tora et al.,(2017)	Reported function
ATXN2L	39	✓ CF	Regulation of stress granule and P-body formation
PABP1	23	✓ MF	Binds the poly(A) tail of mRNA, regulates processes of mRNA metabolism such as pre-mRNA splicing and mRNA stability
HSPA8	12	✓ MF	Functions as ATPase in disassembly of clathrin-coated vesicles in transport of membrane components across cell ¹ . GO Code: regulation of post-synapse organization
DCAF7	10	✓ MF	Associates with DIAPH1 and controls GLI1 transcriptional activity. Binds DYRK1A through its CTD. Inhibits DYRK1A dependent Gli activation and nuclear retention ²
DYRK1A	16	✗	Phosphorylates Gli1 to promote nuclear localisation and transcriptional activity ³ . GO Codes: tau protein binding, transcription coactivator activity, nervous system development
DDX3X	6	✓ CF	ATPase/helicase activity. Independent requirement for efficient stress granule assembly via interaction with EIF4E. Positive regulation of Wnt signalling via stimulation of CSNK1E-mediated DVL2 phosphorylation ⁴
UBB	4	✓ CF	Involved in protein synthesis and degradation. Highly expressed in Gonadotropin-releasing hormone neurons ⁵
CSRP1	4	✓ CF	Potential role in neuronal development. Cysteine-rich domain is highly conserved in steroid receptors
G3BP2	4	✓ CF	Scaffold protein with essential role in cytoplasmic stress granule formation
ATAD3A*	8	✓ MF	Required for enhanced channelling of cholesterol for hormone-dependent steroidogenesis
UBP34	4	✗	Ubiquitin hydrolase that removes conjugated ubiquitin from AXIN1 and AXIN2, regulating Wnt signalling pathway downstream of the beta-catenin destruction complex
DDX6	4	✓ CF	Essential for the formation of P-bodies and ribonucleoprotein granules. GO Codes: negative regulation of neuron differentiation, negative regulation of translation, P-body and stress granule assembly, cadherin binding
NUFP2	25	✓ CF	RNA binding protein found in stress granules

Unless otherwise indicated, reported functions were derived from UniProtKB entries and GO Codes. CF: Cytosolic fraction, MF: Membrane fraction. * Also identified as an interaction partner in PTCH2-FLAG IP Mass Spectrometry 1 (Rothnie et al., 2011), 2 (Morita et al., 2006), 3(Skurat and Dietrich, 2004), 4(Snijders Blok et al., 2015), 5 (Burger et al., 2018)

Table 5.1 Key proteins identified in PTCHD1 Immunoprecipitates by mass spectrometry.

A total of 13 proteins of interest were identified from PTCHD1 IP-based mass spectrometry analysis. The table depicts the protein ID, the number of unique peptides that were identified by mass spectrometry, whether the protein was also present in the mass spectrometry of Tora et al., (2017) (cytosolic –CF- or membrane fraction -MF-) and a brief description of the proteins known function(s).

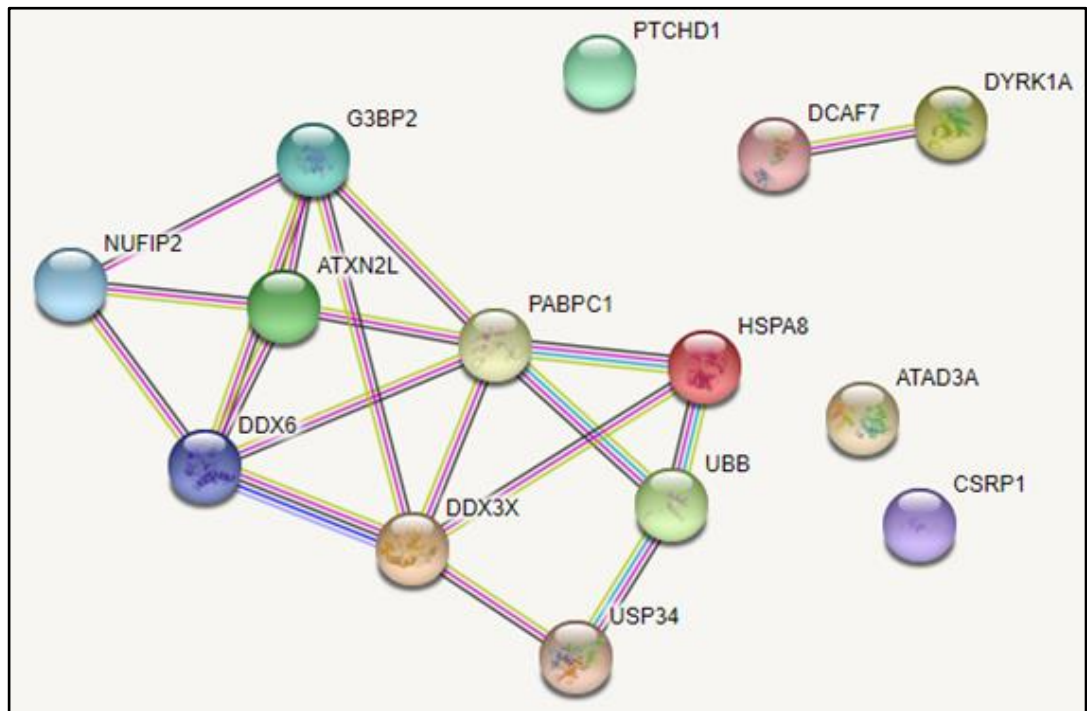


Figure 5.16 STRING analysis of PTCHD1 and mass spectrometry interaction partners.

The 13 proteins identified as interesting potential interaction partners, from the PTCHD1 IP-based mass spectrometry analysis, were input into STRING (Szklarczyk et al., 2019). Evidence-based connections are depicted as strings, between protein 'nodes'.

5.4 Discussion

The initial objective of this work was to obtain and characterise a structure of PTCHD1 by cryo-EM. Although this is not yet a reality, several large steps towards this goal have been achieved. Persevering with GDN over other more commonly used detergents, led to good reward after several optimisation steps. The main theoretical reasons for favouring GDN translated effectively in practice. The hydrophobic steroid-based group appeared to stabilise PTCHD1 well, as shown by the robust SEC-MALS result, post freeze-thaw.

It is of interest that the tetrameric complex of PTCH1 in a 4:2 stoichiometric ratio with ShhN_n was recently presented in GDN (Gong et al., 2018). In line with the SEC-MALS data for LMNG vs GND presented here, they too found the issue of high sample heterogeneity, until they screened additional detergents and selected GDN. Moreover, purifications of PTCH1 in DDM without CHS were found to abrogate binding to ShhN, whilst digitonin purifications appeared unaffected (Gong et al., 2018). This provides further confidence that my approach and detergent choice were correct for PTCHD1.

The negative stain model, generated from ~1,100 particles, was approximately the dimension expected for a protein micelle the size of PTCHD1. Furthermore, superimposition of PTCH1 structures provided some confidence in the data. Whether PTCHD1 progresses to a full data-set in cryo-EM or not, a larger negative stain data-set could almost certainly provide a low resolution structure. With the recent increase in the wealth of PTCH1 structural publications, there is certainly sufficient material to draw from, during the future optimisation of PTCHD1 for cryo-EM.

The link between PTCHD1 and the Hh signalling pathway originates from two key observations. In the developing mouse brain both PTCHD1 and PTCH1 display broad expression, particularly enriched within the cerebellum. *In silico* analysis of PTCHD1 predicted a 12-pass transmembrane protein containing two extracellular domains, two cytoplasmic domains and an SSD characteristic of Patched. Although these were valid reasons to propose a potential involvement in the Hh signalling pathway in the nervous system, evidence is now beginning to allude to a distinct function.

In agreement with others, PTCHD1 was incapable of replacing PTCH1 in Gli-luciferase assays in *Ptc1^{-/-}* cells. In addition, through a ligand tracer experiment with PTCHD1-expressing cells, no binding of unmodified N-Shh was observed (Dr Maren Thomsen, data not shown). The two ECDs of PTCH1, known to engage the Hh ligands, are significantly larger than that of PTCHD1. Recently, the structure of monomeric PTCH1, in complex with ShhN, revealed a Ca²⁺-dependent interaction interface, involving two regions of ECD1 and ECD2 (Gong et al., 2018). Alignment of the secondary sequences of the ECDs of PTCHD1 and PTCH1 suggests that these specific regions are not conserved (**Figure 5.17B**). Moreover, *in silico* generation of a model of PTCHD1, threaded to the structure of monomeric PTCH1 (PDB ID: 6DMY), failed to map residues to these regions (**Figure 5.17A&C**).

It is still possible that other acidic residues of the PTCHD1 ECDs contribute to an interaction interface with the Lysine/Arginine pseudo-active site groove of ShhN. However, this would infer a considerable difference in the endogenous conformation of these domains, due to their reduced lengths compared to

PTCH1. PTCH1 is known to form higher oligomer states and another recent structure depicts tetrameric PTCH1 in a stoichiometric 2:4 ratio with Shh (Qian et al., 2019). Here a second interaction interface, involving the palmitoyl moiety of Shh and the SSD cavity of PTCH1, provides a possible mechanism for lack of PTCHD1:Shh binding, as our recombinant ShhN is not acylated. Although this is plausible, the majority of Hh pathway proteins shown to engage Hh: PTCH1, GAS1, CDO, BOC, DISP1, HHAT and HSPGs, do so via the Ca²⁺ binding site.

While PTCH1 can interact with Shh through the palmitoyl moiety, the functional relevance of this interaction, when isolated from tandem Ca²⁺ engagement, is unclear. Izzi et al., (2011) described a Shh E90A mutant capable of binding PTCH1, but not the co-receptors, which warranted no activity against PTCH1-mediated repression of Smo. It is important to note that upper helical domains of the ECDs of PTCH1 are also absent in NPC1. NPC1 is incapable of binding Shh, despite it also containing an SSD of strong homology to PTCH1. In fact, secondary sequence alignments show the SSD of NPC1 has higher homology to PTCH1 than PTCHD1 (32.53% vs 22.7%). Direct substitution of the SSD of PTCH1 for that of NPC1 produced a non-functional hybrid protein (Fleet and Hamel, 2019). This suggests that the SSD of NPC1, even in the micro-environment of the PTCH1 protein domains, is insufficient to inhibit Hh signalling. It would therefore be logical to presume the SSD of PTCHD1 could also fail to function in the context of Hh signalling. Finally, the IP mass spectrometry data identified several 'interacting' proteins that warrant further investigation. First, direct interaction should be determined with PTCHD1 by co-IP or in situ proximity-ligation assays. Establishment of a neuronal-like cell culture, more relevant to PTCHD1 should be a priority for future cell-based assays.

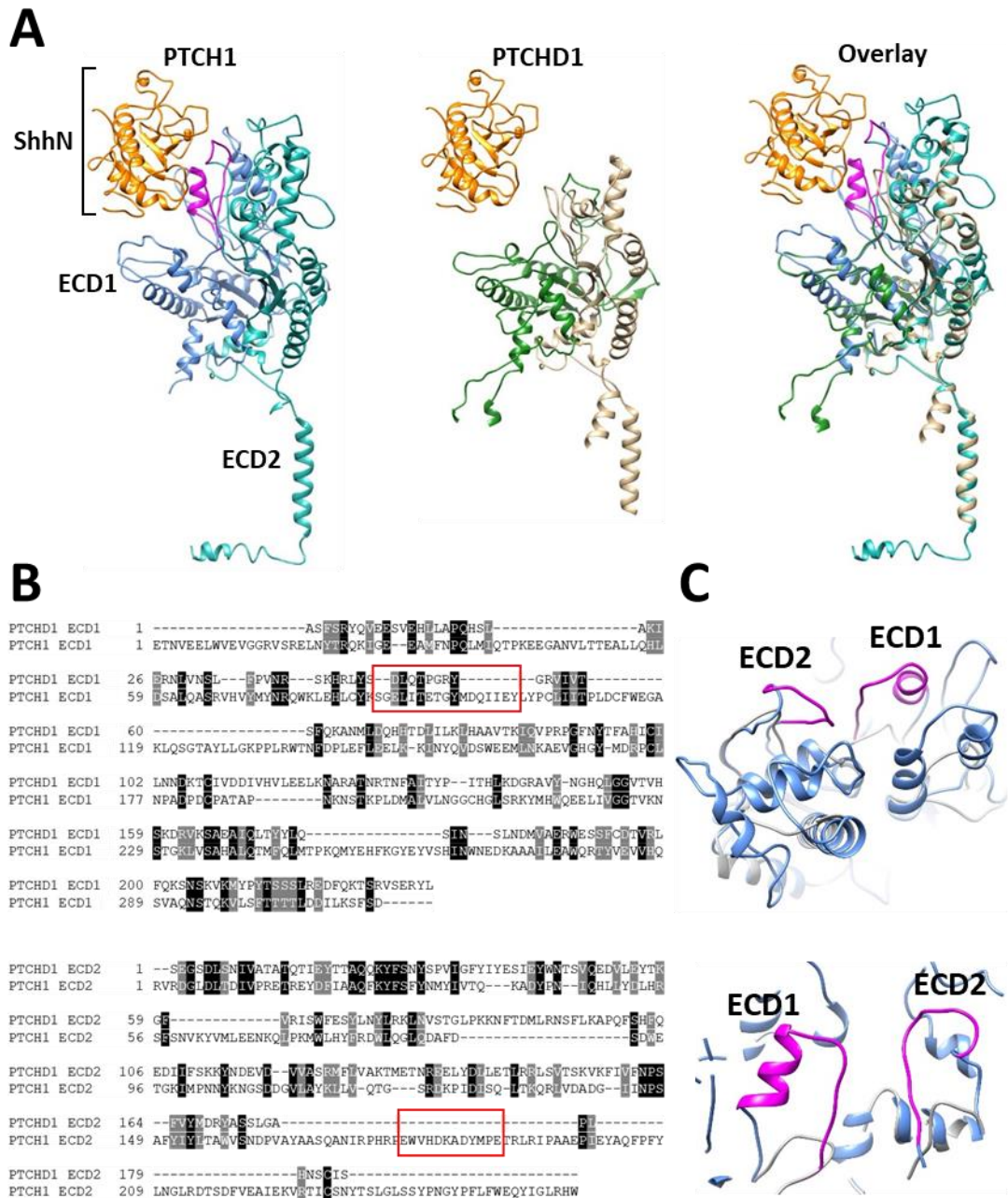


Figure 5.17 ShhN:PTCH1 ECD interface is not conserved in PTCHD1

(A) The secondary sequence of PTCHD1, threaded to ShhN:PTCH1 (PDB ID: 6dmy). Left: PTCH1, showing ECD1 (blue) and ECD2 (green), in complex with ShhN (orange). ECD residues shown to form the interaction interface are depicted in magenta. Middle: PTCHD1 sequence threaded to PTCH1 structure. ECD1 and ECD2 shown in green and grey, respectively. Right: overlay of PTCH1 and PTCHD1 ECDs. (B) Sequence alignment of the ECDs of PTCHD1 and PTCH1. Red boxes indicate PTCH1 residues of the ShhN:PTCH1 interaction interface. (C) Expanded view of the structural alignment of PTCH1, in blue, and PTCHD1 in grey. ShhN:PTCH1 interaction interface residues shown in magenta.

Chapter 6

General Discussion

Chapter 6

General Discussion

PTCH1 is the established negative regulator of the Hh signalling pathway, capable of non-stoichiometric inhibition of Smo, through a cholesterol-dependent transport mechanism. Fundamental to this activity is the SSD, a highly conserved feature in proteins that mobilise sterol molecules. Structural determination of PTCH1 has revealed higher oligomeric states of functional importance (Qi, Schmiede, Coutavas and Li, 2018). PTCH1 shares homology with bacterial RND efflux pump proteins whose oligomerisation is essential to their function (Takatsuka and Nikaido, 2006). Mutation of conserved residues in PTCH1, that are essential to proton translocation activities in RND proteins, impair PTCH1 activity (Taipale et al., 2002).

However, questions still remain regarding: the mechanism by which PTCH1 moves cholesterol; what is the functional relevance of PTCH1 oligomerisation; and do the cytoplasmic domains of PTCH1, which are not structurally determined, have any influence over the canonical inhibition of Smo?

In [Chapter 3](#), the predicted existence, of a now structurally determined sterol cavity in Ptch1, was strongly indicated by mutations selected from homology modelling against a structure of NPC1. The mechanism of PTCH1-dependent inhibition of Smo was investigated, to determine if the function was similar to the bacterial RND proteins, which utilise H⁺ ions to transport molecular cargos. The results were unclear, in line with the findings of others proposing Na⁺ as an alternative ion (Myers et al., 2017). Analysis of the influences of the cytoplasmic domains upon oligomerisation and canonical Hh signalling yielded several

interesting insights: i) an apparent expression dependency of the CTD upon the middle loop ii) the retention of oligomeric interactions despite the removal of the two cytoplasmic domains iii) the impaired ability of domain mutants to function to inhibit Gli-reporter activity. These data are important as they are contradictory to the established view, that removal of both cytoplasmic domains poses no impact upon the canonical function of PTCH1.

Although it is largely established that PTCH1 inhibits Smo through a cholesterol-dependent mechanism, it remains unknown whether this function is shared by other Patched family proteins. Chapter 4 determined several strong connections between the structure and function of PTCH1 and PTCH2. PTCH2 was shown to form homo-interactions, which displayed a small, but significant canonical function in the absence of Ptc1. Furthermore, corresponding mutations produced similar behaviour in both Patched 1 and 2 proteins. Given these similarities and the evidence of functional PTCH1 dimers (Qi, Schmiede, Coutavas and Li, 2018), it was a focus to determine if Patched hetero-interactions of functional relevance existed.

Indeed, not only was the existence of Patched hetero-interactions discovered, the interactions were determined to be competitive with their homo-interaction counterparts. Importantly, these hetero-interactions displayed synergistic canonical activity. Furthermore, this synergistic activity was determined to be dictated by the activity-state of the Ptc1 in the heterodimer. This led to the hypothesis that the synergistic activity of hetero-interactions involves possible increases in protein stability or ciliary retention, dictated by PTCH2. These findings of co-operative function, are even more compelling when considered in

the context of tissues, that display co-expression of Patched 1 and 2, such as the skin.

The question of why PTCH2 is not equivalent to PTCH1 was also moderately addressed. Removal of the cytoplasmic loops of PTCH2 produced a similar picture to that seen for Ptc1, where the CTD displayed a dependency upon the middle loop. Substitution of the CTD of PTCH1 for that of PTCH2 produced a protein of comparable expression and localisation. However, whilst it retained the ability to oligomerise, it had no detectable canonical activity. This was strongly suggestive that the presence of the CTD of PTCH2, in the context of PTCH1, inhibited its activity.

Chapter 5 focused on the more distally related Patched family member, PTCHD1. I optimised the purification of PTCHD1 from *SF9* BIIICs, and generated a low-resolution model by negative stain EM. Using click-chemistry, it was determined that Purified PTCHD1 bound cholesterol. However, through cell based assays, PTCHD1 was determined to be insufficient to inhibit Smo activity in *Ptch1*^{-/-} MEFs, and was unable to bind Shh as a ligand. Proteomic analysis, by way of immunoprecipitation mass spectrometry, revealed associations with stress granule and RNP granule proteins. This supports existing evidence that PTCHD1 has a biological function in neurons, distinct from the Hh pathway, perhaps more similar to the relationship shared by NPC1.

Together, these results provide novel insights into the activities of three Patched family members, revealing shared and divergent biochemical functions.

Bibliography

- Aanstad, P., Santos, N., Corbit, K.C., Scherz, P.J., Trinh, L.A., Salvenmoser, W., Huisken, J., Reiter, J.F. and Stainier, D.Y.R. 2009. The Extracellular Domain of Smoothed Regulates Ciliary Localization and Is Required for High-Level Hh Signaling. *Current Biology*. **19**(12), pp.1034–1039.
- Adolphe, C., Junker, J.P., Lyubimova, A., van Oudenaarden, A. and Wainwright, B. 2016. Patched Receptors Sense, Interpret, and Establish an Epidermal Hedgehog Signaling Gradient. *Journal of Investigative Dermatology*.
- Alfaro, A.C., Roberts, B., Kwong, L., Bijlsma, M.F. and Roelink, H. 2014. Ptch2 mediates the Shh response in Ptch1^{-/-} cells. *Development (Cambridge)*. **141**(17), pp.3331–3339.
- Allen, B.L., Song, J.Y., Izzi, L., Althaus, I.W., Kang, J.S., Charron, F., Krauss, R.S. and McMahon, A.P. 2011. Overlapping roles and collective requirement for the coreceptors GAS1, CDO, and BOC in SHH pathway function. *Developmental Cell*. **20**(6), pp.775–787.
- Allen, B.L., Tenzen, T. and McMahon, A.P. 2007. The Hedgehog-binding proteins Gas1 and Cdo cooperate to positively regulate Shh signaling during mouse development. *Genes and Development*. **21**(10), pp.1244–1257.
- Amaral, L., Martins, A., Spengler, G. and Molnar, J. 2014. Efflux pumps of Gram-negative bacteria: What they do, how they do it, with what and how to deal with them. *Frontiers in Pharmacology*. **4 JAN**.
- Anderson, R.G.W. 1972. The three-dimensional structure of the basal body from the rhesus monkey oviduct. *Journal of Cell Biology*. **54**(2), pp.246–265.

Bibliography

- Anes, J., McCusker, M.P., Fanning, S. and Martins, M. 2015. The ins and outs of RND efflux pumps in *Escherichia coli*. *Frontiers in Microbiology*. **6**(JUN), p.587.
- Arendsdorf, A.M., Marada, S. and Ogden, S.K. 2016. Smoothened Regulation: A Tale of Two Signals. *Trends in Pharmacological Sciences*. **37**(1), pp.62–72.
- Bakshi, A., Chaudhary, S.C., Rana, M., Elmets, C.A. and Athar, M. 2017. Basal cell carcinoma pathogenesis and therapy involving hedgehog signaling and beyond. *Molecular Carcinogenesis*. **56**(12), pp.2543–2557.
- Battle, C., Ott, C.M., Burnette, D.T., Lippincott-Schwartz, J. and Schmidt, C.F. 2015. Intracellular and extracellular forces drive primary cilia movement. *Proceedings of the National Academy of Sciences of the United States of America*. **112**(5), pp.1410–1415.
- Belusa, R., Wang, Z.M., Matsubara, T., Sahlgren, B., Dulubova, I., Nairn, A.C., Ruoslahti, E., Greengard, P. and Aperia, A. 1997. Mutation of the protein kinase C phosphorylation site on rat $\alpha 1$ Na⁺,K⁺-ATPase alters regulation of intracellular Na⁺ and pH and influences cell shape and adhesiveness. *Journal of Biological Chemistry*. **272**(32), pp.20179–20184.
- Benchling 2021 Cloud-Based Informatics Platform for Life Sciences R&D | Benchling. *Benchling*. [Online]. [Accessed 21 February 2021]. Available from: <https://www.benchling.com/>.
- Bidet, M., Joubert, O., Lacombe, B., Ciantar, M., Nehmé, R., Mollat, P., Brétilon, L., Faure, H., Bittman, R., Ruat, M. and Mus-Veteau, I. 2011. The hedgehog receptor patched is involved in cholesterol transport L. Johannes, ed. *PLoS ONE*. **6**(9), p.e23834.

Bibliography

- Blassberg, R., Macrae, J.I., Briscoe, J. and Jacob, J. 2016. Reduced cholesterol levels impair Smoothed activation in Smith-Lemli-Opitz syndrome. *Human Molecular Genetics*. **25**(4), pp.693–705.
- Bosanac, I., Maun, H.R., Scales, S.J., Wen, X., Lingel, A., Bazan, J.F., De Sauvage, F.J., Hymowitz, S.G. and Lazarus, R.A. 2009. The structure of SHH in complex with HHIP reveals a recognition role for the Shh pseudo active site in signaling. *Nature Structural and Molecular Biology*. **16**(7), pp.691–697.
- Breibeck, J. and Rompel, A. 2019. Successful amphiphiles as the key to crystallization of membrane proteins: Bridging theory and practice. *Biochimica et Biophysica Acta - General Subjects*. **1863**(2), pp.437–455.
- Broekhuis, J.R., Verhey, K.J., Jansen, Gert, Hildebrandt, F., Benzing, T., Katsanis, N., Sung, C., Leroux, M., Silverman, M., Leroux, M., Doroquez, D., Berciu, C., Anderson, J., Sengupta, P., Nicastro, D et al., 2014. Regulation of Cilium Length and Intraflagellar Transport by the RCK-Kinases ICK and MOK in Renal Epithelial Cells K. Stieger, ed. *PLoS ONE*. **9**(9), p.e108470.
- Buglino, J.A. and Resh, M.D. 2008. Hhat is a palmitoyltransferase with specificity for N-palmitoylation of Sonic Hedgehog. *Journal of Biological Chemistry*. **283**(32), pp.22076–22088.
- Burger, L.L., Vanacker, C., Phumsatitpong, C., Wagenmaker, E.R., Wang, L., Olson, D.P. and Moenter, S.M. 2018. Identification of genes enriched in GnRH neurons by translating ribosome affinity purification and RNAseq in mice. *Endocrinology*. **159**(4), pp.1922–1940.
- Byrne, E.F.X., Sircar, R., Miller, P.S., Hedger, G., Luchetti, G., Nachtergaele, S.,

Bibliography

- Tully, M.D., Mydock-Mcgrane, L., Covey, D.F., Rambo, R.P., Sansom, M.S.P., Newstead, S., Rohatgi, R. and Siebold, C. 2016. Structural basis of Smoothed regulation by its extracellular domains. *Nature*. **535**(7613), pp.517–522.
- Carpenter, D., Stone, D.M., Brush, J., Ryan, A., Armanini, M., Frantz, G., Rosenthal, A. and De Sauvage, F.J. 1998. Characterization of two patched receptors for the vertebrate hedgehog protein family. *Proceedings of the National Academy of Sciences of the United States of America*. **95**(23), pp.13630–13634.
- Chae, P.S., Rasmussen, S.G.F., Rana, R.R., Gotfryd, K., Chandra, R., Goren, M.A., Kruse, A.C., Nurva, S., Loland, C.J., Pierre, Y., Drew, D., Popot, J.L., Picot, D., Fox, B.G., Guan, L et al., 2010. Maltose-neopentyl glycol (MNG) amphiphiles for solubilization, stabilization and crystallization of membrane proteins. *Nature Methods*. **7**(12), pp.1003–1008.
- Chae, P.S., Rasmussen, S.G.F., Rana, R.R., Gotfryd, K., Kruse, A.C., Manglik, A., Cho, K.H., Nurva, S., Gether, U., Guan, L., Loland, C.J., Byrne, B., Kobilka, B.K. and Gellman, S.H. 2012. A new class of amphiphiles bearing rigid hydrophobic groups for solubilization and stabilization of membrane proteins. *Chemistry - A European Journal*. **18**(31), pp.9485–9490.
- Chaudhry, A., Noor, A., Degagne, B., Baker, K., Bok, L.A., Brady, A.F., Chitayat, D., Chung, B.H., Cytrynbaum, C., Dymont, D., Filges, I., Helm, B., Hutchison, H.T., Jeng, L.J.B., Laumonnier, F et al., 2015. Phenotypic spectrum associated with PTCHD1 deletions and truncating mutations includes intellectual disability and autism spectrum disorder. *Clinical Genetics*. **88**(3), pp.224–233.

Bibliography

- Chen, H., Liu, Y. and Li, X. 2020. Structure of human Dispatched-1 provides insights into Hedgehog ligand biogenesis. *Life Science Alliance*. **3**(8).
- Chen, J.K., Taipale, J., Cooper, M.K. and Beachy, P.A. 2002. Inhibition of Hedgehog signaling by direct binding of cyclopamine to Smoothed. *Genes & development*. **16**(21), pp.2743–8.
- Chen, M.H., Li, Y.J., Kawakami, T., Xu, S.M. and Chuang, P.T. 2004. Palmitoylation is required for the production of a soluble multimeric Hedgehog protein complex and long-range signaling in vertebrates. *Genes and Development*. **18**(6), pp.641–659.
- Chen, M.H., Wilson, C.W., Li, Y.J., Law, K.K. Lo, Lu, C.S., Gacayan, R., Zhang, X., Hui, C.C. and Chuang, P.T. 2009. Cilium-independent regulation of Gli protein function by Sufu in Hedgehog signaling is evolutionarily conserved. *Genes and Development*. **23**(16), pp.1910–1928.
- Chen, X., Morales-Alcala, C.C. and Riobo-Del Galdo, N.A. 2018. Autophagic flux is regulated by interaction between the C-terminal domain of PATCHED1 and ATG101. *Molecular Cancer Research*. **16**(5), pp.909–919.
- Chen, X.L., Chinchilla, P., Fombonne, J., Ho, L., Guix, C., Keen, J.H., Mehlen, P. and Riobo, N.A. 2014. Patched-1 proapoptotic activity is downregulated by modification of K1413 by the E3 ubiquitin-protein ligase Itchy homolog. *Molecular and cellular biology*. **34**(20), pp.3855–66.
- Chuang, P.T. and McMahon, A.P. 1999. Vertebrate hedgehog signalling modulated by induction of a hedgehog- binding protein. *Nature*. **397**(6720), pp.617–621.
- Chung, J.H., Larsen, A.R., Chen, E. and Bunz, F. 2014. A PTCH1 homolog

Bibliography

transcriptionally activated by p53 suppresses hedgehog signaling. *Journal of Biological Chemistry*. **289**(47), pp.33020–33031.

Cooper, M.K., Wassif, C.A., Krakowiak, P.A., Taipale, J., Gong, R., Kelley, R.I., Porter, F.D. and Beachy, P.A. 2003. A defective response to Hedgehog signaling in disorders of cholesterol biosynthesis. *Nature Genetics*. **33**(4), pp.508–513.

Corbit, K.C., Aanstad, P., Singla, V., Norman, A.R., Stainier, D.Y.R. and Reiter, J.F. 2005. Vertebrate Smoothed functions at the primary cilium. *Nature*. **437**(7061), pp.1018–1021.

Corcoran, R.B. and Scott, M.P. 2006. Oxysterols stimulate Sonic hedgehog signal transduction and proliferation of medulloblastoma cells. *Proceedings of the National Academy of Sciences of the United States of America*. **103**(22), pp.8408–13.

Dahmane, N., Lee, J., Robins, P., Heller, P. and Ruiz I Altaba, A. 1997. Activation of the transcription factor Gli1 and the sonic hedgehog signalling pathway in skin tumours. *Nature*. **389**(6653), pp.876–881.

Dardis, A., Zampieri, S., Gellera, C., Carrozzo, R., Cattarossi, S., Peruzzo, P., Dariol, R., Sechi, A., Deodato, F., Caccia, C., Verrigni, D., Gasperini, S., Fiumara, A., Fecarotta, S., Carecchio, M et al., 2020. Molecular Genetics of Niemann–Pick Type C Disease in Italy: An Update on 105 Patients and Description of 18 NPC1 Novel Variants. *Journal of Clinical Medicine*. **9**(3), p.679.

Delling, M., DeCaen, P.G., Doerner, J.F., Febvay, S. and Clapham, D.E. 2013. Primary cilia are specialized calcium signalling organelles. *Nature*.

Bibliography

504(7479), pp.311–4.

Denef, N., Neubüser, D., Perez, L. and Cohen, S.M. 2000. Hedgehog induces opposite changes in turnover and subcellular localization of patched and smoothed. *Cell*. **102**(4), pp.521–531.

Desai, P.B., Stuck, M.W., Lv, B. and Pazour, G.J. 2020. Ubiquitin links smoothed to intraflagellar transport to regulate Hedgehog signaling. *Journal of Cell Biology*. **219**(7), pp.1–40.

Deshpande, I., Liang, J., Hedeem, D., Roberts, Kelsey J., Zhang, Y., Ha, B., Latorraca, N.R., Faust, B., Dror, R.O., Beachy, P.A., Myers, B.R. and Manglik, A. 2019. Smoothed stimulation by membrane sterols drives Hedgehog pathway activity. *Nature*. **571**(7764), pp.284–288.

Ding, Q., Fukami, S.I., Meng, X., Nishizaki, Y., Zhang, X., Sasaki, H., Dlugosz, A., Nakafuku, M. and Hui, C.C. 1999. Mouse suppressor of fused is a negative regulator of Sonic hedgehog signaling and alters the subcellular distribution of Gli1. *Current Biology*. **9**(19), pp.1119–1122.

Echelard, Y., Epstein, D.J., St-Jacques, B., Shen, L., Mohler, J., McMahon, J.A. and McMahon, A.P. 1993. Sonic hedgehog, a member of a family of putative signaling molecules, is implicated in the regulation of CNS polarity. *Cell*. **75**(7), pp.1417–1430.

Eguether, T., SanAgustin, J.T., Keady, B.T., Jonassen, J.A., Liang, Y., Francis, R., Tobita, K., Johnson, C.A., Abdelhamed, Z.A., Lo, C.W. and Pazour, G.J. 2014. IFT27 links the bbsome to ift for maintenance of the ciliary signaling compartment. *Developmental Cell*. **31**(3), pp.279–290.

Elias, G.M., Elias, L.A.B., Apostolides, P.F., Kriegstein, A.R. and Nicoll, R.A.

Bibliography

2008. Differential trafficking of AMPA and NMDA receptors by SAP102 and PSD-95 underlies synapse development. *Proceedings of the National Academy of Sciences of the United States of America*. **105**(52), pp.20953–20958.
- Etheridge, L.A., Crawford, T.Q., Zhang, S. and Roelink, H. 2010. Evidence for a role of vertebrate *Disp1* in long-range Shh signaling. *Development*. **137**(1), pp.133–140.
- Ezratty, E.J., Stokes, N., Chai, S., Shah, A.S., Williams, S.E. and Fuchs, E. 2011. A role for the primary cilium in notch signaling and epidermal differentiation during skin development. *Cell*. **145**(7), pp.1129–1141.
- Fleet, A., Lee, J.P.Y., Tamachi, A., Javeed, I. and Hamel, P.A. 2016. Activities of the cytoplasmic domains of patched-1 modulate but are not essential for the regulation of canonical hedgehog signaling. *Journal of Biological Chemistry*. **291**(34), pp.17557–17568.
- Fleet, A.J. and Hamel, P.A. 2019. The protein-specific activities of the transmembrane modules of *Ptch1* and *Ptch2* are determined by their adjacent protein domains. *Journal of Biological Chemistry*. **293**(43), pp.16583–16595.
- Fujii, K., Ohashi, H., Suzuki, M., Hatsuse, H., Shiohama, T., Uchikawa, H. and Miyashita, T. 2013. Frameshift mutation in the *PTCH2* gene can cause nevoid basal cell carcinoma syndrome. *Familial Cancer*. **12**(4), pp.611–614.
- Funabashi, T., Katoh, Y., Okazaki, M., Sugawa, M. and Nakayama, K. 2018. Interaction of heterotrimeric kinesin-II with IFT-B-connecting tetramer is crucial for ciliogenesis. *Journal of Cell Biology*. **217**(8), pp.2867–2876.

Bibliography

- Gallet, A., Ruel, L., Staccini-Lavenant, L. and Thérond, P.P. 2006. Cholesterol modification is necessary for controlled planar long-range activity of Hedgehog in *Drosophila epithelia*. *Development*. **133**(3), pp.407–418.
- Garcia-Gonzalo, F.R., Corbit, K.C., Sirerol-Piquer, M.S., Ramaswami, G., Otto, E.A., Noriega, T.R., Seol, A.D., Robinson, J.F., Bennett, C.L., Josifova, D.J., García-Verdugo, J.M., Katsanis, N., Hildebrandt, F. and Reiter, J.F. 2011. A transition zone complex regulates mammalian ciliogenesis and ciliary membrane composition. *Nature Genetics*. **43**(8), pp.776–784.
- Garcia-Gonzalo, F.R., Phua, S.C., Roberson, E.C., Garcia, G., Abedin, M., Schurmans, S., Inoue, T. and Reiter, J.F. 2015. Phosphoinositides Regulate Ciliary Protein Trafficking to Modulate Hedgehog Signaling. *Developmental Cell*. **34**(4), pp.400–409.
- Goetz, J.A., Singh, S., Suber, L.M., Kull, F.J. and Robbins, D.J. 2006. A highly conserved amino-terminal region of Sonic Hedgehog is required for the formation of its freely diffusible multimeric form. *Journal of Biological Chemistry*. **281**(7), pp.4087–4093.
- Gong, X., Qian, H., Cao, P., Zhao, X., Zhou, Q., Lei, J. and Yan, N. 2018. Structural basis for the recognition of Sonic Hedgehog by human Patched1. *Science*. **361**(6402).
- Gritli-Linde, A., Lewis, P., McMahon, A.P. and Linde, A. 2001. The whereabouts of a morphogen: Direct evidence for short- and graded long-range activity of Hedgehog signaling peptides. *Developmental Biology*. **236**(2), pp.364–386.
- Grover, V.K., Valadez, J.G., Bowman, A.B. and Cooper, M.K. 2011. Lipid modifications of Sonic hedgehog ligand dictate cellular reception and signal

Bibliography

- response J. E. Treisman, ed. *PLoS ONE*. **6**(7), p.e21353.
- Guan, L. and Nakae, T. 2001. Identification of essential charged residues in transmembrane segments of the multidrug transporter MexB of *Pseudomonas aeruginosa*. *Journal of Bacteriology*. **183**(5), pp.1734–1739.
- Guo, H., Bueler, S.A. and Rubinstein, J.L. 2017. Atomic model for the dimeric FO region of mitochondrial ATP synthase. *Science*. **358**(6365), pp.936–940.
- Hahn, A., Parey, K., Bublitz, M., Vonck, J., Kü, W., Mills, D.J., Zickermann, V. and Meier, T. 2016. Structure of a Complete ATP Synthase Dimer Reveals the Molecular Basis of Inner Mitochondrial Membrane Morphology
Accession Numbers 5FL7 Hahn et al Article Structure of a Complete ATP Synthase Dimer Reveals the Molecular Basis of Inner Mitochondrial Membrane Morphology. *Molecular Cell*. **63**, pp.445–456.
- He, M., Agbu, S. and Anderson, K. V. 2016. Microtubule Motors Drive Hedgehog Signaling in Primary Cilia. *Trends in Cell Biology*.
- Hilgendorf, K.I., Johnson, C.T. and Jackson, P.K. 2016. The primary cilium as a cellular receiver: Organizing ciliary GPCR signaling. *Current Opinion in Cell Biology*. **39**, pp.84–92.
- Holtz, A.M., Peterson, K.A., Nishi, Y., Morin, S., Song, J.Y., Charron, F., McMahon, A.P. and Allen, B.L. 2013. Essential role for ligand-dependent feedback antagonism of vertebrate hedgehog signaling by PTCH1, PTCH2 AND HHIP1 during neural patterning. *Development (Cambridge)*. **140**(16), pp.3423–3434.
- Hu, A. and Song, B.L. 2019. The interplay of Patched, Smoothed and cholesterol in Hedgehog signaling. *Current Opinion in Cell Biology*. **61**,

Bibliography

pp.31–38.

Huang, P., Nedelcu, D., Watanabe, M., Jao, C., Kim, Y., Liu, J. and Salic, A. 2016. Cellular Cholesterol Directly Activates Smoothed in Hedgehog Signaling. *Cell*. **166**(5), pp.1176-1187.e14.

Huang, P., Zheng, S., Wierbowski, B.M., Kim, Y., Nedelcu, D., Aravena, L., Liu, J., Kruse, A.C. and Salic, A. 2018. Structural Basis of Smoothed Activation in Hedgehog Signaling. *Cell*. **174**(2), pp.312-324.e16.

Huangfu, D. and Anderson, K. V. 2005. Cilia and Hedgehog responsiveness in the mouse. *Proceedings of the National Academy of Sciences of the United States of America*. **102**(32), pp.11325–11330.

Huangfu, D., Liu, A., Rakeman, A.S., Murcia, N.S., Niswander, L. and Anderson, K. V. 2003. Hedgehog signalling in the mouse requires intraflagellar transport proteins. *Nature*. **426**(6962), pp.83–87.

Hui, C.C., Slusarski, D., Platt, K.A., Holmgren, R. and Joyner, A.L. 1994. Expression of three mouse homologs of the drosophila segment polarity gene cubitus interruptus, Gli, Gli-2, and Gli-3, in ectoderm-and mesoderm-derived tissues suggests multiple roles during postimplantation development. *Developmental Biology*. **162**(2), pp.402–413.

Humke, E.W., Dorn, K. V., Milenkovic, L., Scott, M.P. and Rohatgi, R. 2010. The output of Hedgehog signaling is controlled by the dynamic association between Suppressor of Fused and the Gli proteins. *Genes and Development*. **24**(7), pp.670–682.

Ihrie, R.A., Shah, J.K., Harwell, C.C., Levine, J.H., Guinto, C.D., Lezameta, M., Kriegstein, A.R. and Alvarez-Buylla, A. 2011. Persistent Sonic Hedgehog

Bibliography

- Signaling in Adult Brain Determines Neural Stem Cell Positional Identity. *Neuron*. **71**(2), pp.250–262.
- Inoue, Takanari, Lin, Y.C., Niewiadowski, P., Lin, B., Nakamura, H., Phua, S.C., Jiao, J., Levchenko, A., Inoue, Takafumi and Rohatgi, R. 2013. Chemically inducible diffusion trap at cilia reveals molecular sieve-like barrier. *Nature Chemical Biology*. **9**(7), pp.437–443.
- Ishikawa, H., Thompson, J., Yates, J.R. and Marshall, W.F. 2012. Proteomic analysis of mammalian primary cilia. *Current Biology*. **22**(5), pp.414–419.
- Izzi, L., Lévesque, M., Morin, S., Laniel, D., Wilkes, B.C., Mille, F., Krauss, R.S., McMahon, A.P., Allen, B.L. and Charron, F. 2011. Boc and gas1 each form distinct shh receptor complexes with ptch1 and are required for shh-mediated cell proliferation. *Developmental Cell*. **20**(6), pp.788–801.
- Jacob, J. and Briscoe, J. 2003. Gli proteins and the control of spinal-cord patterning. *EMBO Reports*. **4**(8), pp.761–765.
- Jacoby, M., Cox, J.J., Gayral, S., Hampshire, D.J., Ayub, M., Blockmans, M., Pernot, E., Kisseleva, M. V., Compère, P., Schiffmann, S.N., Gergely, F., Riley, J.H., Pérez-Morga, D., Woods, C.G. and Schurmans, S. 2009. INPP5E mutations cause primary cilium signaling defects, ciliary instability and ciliopathies in human and mouse. *Nature Genetics*. **41**(9), pp.1027–1031.
- Jeong, J. and McMahon, A.P. 2005. Growth and pattern of the mammalian neural tube are governed by partially overlapping feedback activities of the hedgehog antagonists patched 1 and Hhip1. *Development*. **132**(1), pp.143–154.
- Kaehler, C., Isensee, J., Nonhoff, U., Terrey, M., Hucho, T., Lehrach, H. and

Bibliography

- Krobitsch, S. 2012. Ataxin-2-Like Is a Regulator of Stress Granules and Processing Bodies J. Ma, ed. *PLoS ONE*. **7**(11), p.e50134.
- Kawamura, S., Hervold, K., Ramirez-Weber, F.A. and Kornberg, T.B. 2008. Two patched protein subtypes and a conserved domain of group I proteins that regulates turnover. *Journal of Biological Chemistry*. **283**(45), pp.30964–30969.
- Kawasaki, M., Ezura, Y., Hayata, T., Notomi, T., Izu, Y. and Noda, M. 2015. TGF- β Suppresses Ift88 Expression in Chondrocytic ATDC5 Cells. *Journal of Cellular Physiology*. **230**(11), pp.2788–2795.
- Kim, E.H., Nies, D.H., McEvoy, M.M. and Rensing, C. 2011. Switch or funnel: How RND-type transport systems control periplasmic metal homeostasis. *Journal of Bacteriology*. **193**(10), pp.2381–2387.
- Kim, H.S., Nagore, D. and Nikaido, H. 2010. Multidrug efflux pump MdtBC of *Escherichia coli* is active only as a B₂C heterotrimer. *Journal of Bacteriology*. **192**(5), pp.1377–1386.
- Kim, J., Hsia, E.Y.C., Brigui, A., Plessis, A., Beachy, P.A. and Zheng, X. 2015. The role of ciliary trafficking in Hedgehog receptor signaling. *Science Signaling*. **8**(379), p.ra55.
- Kim, Y., Lee, J., Seppala, M., Cobourne, M.T. and Kim, S.H. 2020. Ptch2/Gas1 and Ptch1/Boc differentially regulate Hedgehog signalling in murine primordial germ cell migration. *Nature Communications*. **11**(1), pp.1–16.
- Kinnebrew, M., Iverson, E.J., Patel, B.B., Pusapati, G. V., Kong, J.H., Johnson, K.A., Luchetti, G., Eckert, K.M., McDonald, J.G., Covey, D.F., Siebold, C., Radhakrishnan, A. and Rohatgi, R. 2019. Cholesterol accessibility at the

Bibliography

- ciliary membrane controls hedgehog signaling. *eLife*. **8**.
- Kowatsch, C., Woolley, R.E., Kinnebrew, M., Rohatgi, R. and Siebold, C. 2019. Structures of vertebrate Patched and Smoothed reveal intimate links between cholesterol and Hedgehog signalling. *Current Opinion in Structural Biology*. **57**, pp.204–214.
- Kozlov, A.M., Darriba, D., Flouri, T., Morel, B. and Stamatakis, A. 2019. RAxML-NG: a fast, scalable and user-friendly tool for maximum likelihood phylogenetic inference J. Wren, ed. *Bioinformatics*. **35**(21), pp.4453–4455.
- Larkins, C.E., Aviles, G.D.G., East, M.P., Kahn, R.A. and Caspary, T. 2011. Arl13b regulates ciliogenesis and the dynamic localization of Shh signaling proteins. *Molecular biology of the cell*. **22**(23), pp.4694–703.
- Lee, K.H., Johmura, Y., Yu, L.R., Park, J.E., Gao, Y., Bang, J.K., Zhou, M., Veenstra, T.D., Yeon Kim, B. and Lee, K.S. 2012. Identification of a novel Wnt5a-CK1 ϵ -Dvl2-Plk1-mediated primary cilia disassembly pathway. *EMBO Journal*. **31**(14), pp.3104–3117.
- Lee, Y., Miller, H.L., Russell, H.R., Boyd, K., Curran, T. and McKinnon, P.J. 2006. Patched2 modulates tumorigenesis in Patched1 heterozygous mice. *Cancer Research*. **66**(14), pp.6964–6971.
- Lennox, A.L., Hoye, M.L., Jiang, R., Johnson-Kerner, B.L., Suit, L.A., Venkataramanan, S., Sheehan, C.J., Alsina, F.C., Fregeau, B., Aldinger, K.A., Moey, C., Lobach, I., Afenjar, A., Babovic-Vuksanovic, D., Bézieau, S et al., 2020. Pathogenic DDX3X Mutations Impair RNA Metabolism and Neurogenesis during Fetal Cortical Development. *Neuron*. **106**(3), pp.404-420.e8.

Bibliography

- Li, X., Wang, J., Coutavas, E., Shi, H., Hao, Q. and Blobel, G. 2016. Structure of human Niemann-Pick C1 protein. *Proceedings of the National Academy of Sciences of the United States of America*. **113**(29), pp.8212–7.
- Liem, K.F., He, M., Ocbina, P.J.R. and Anderson, K. V. 2009. Mouse Kif7/Costal2 is a cilia-associated protein that regulates Sonic hedgehog signaling. *Proceedings of the National Academy of Sciences of the United States of America*. **106**(32), pp.13377–13382.
- Lu, X., Liu, S. and Kornberg, T.B. 2006. The C-terminal tail of the Hedgehog receptor Patched regulates both localization and turnover. *Genes and Development*. **20**(18), pp.2539–2551.
- Luchetti, Giovanni, Sircar, Ria, Kong, J.H., Nachtergaele, Sigrid, Sagner, A., Byrne, E.F., Covey, D.F., Siebold, Christian, Rohatgi, Rajat. 2016. Cholesterol activates the G-protein coupled receptor Smoothed to promote Hedgehog signaling. *eLife*. **5**, pp.1055–1056.
- Ma, Y., Erkner, A., Gong, R., Yao, S., Taipale, J., Basler, K. and Beachy, P.A. 2002. Hedgehog-mediated patterning of the mammalian embryo requires transporter-like function of dispatched. *Cell*. **111**(1), pp.63–75.
- Mao, J., Ligon, K.L., Rakhlin, E.Y., Thayer, S.P., Bronson, R.T., Rowitch, D. and McMahon, A.P. 2006. A novel somatic mouse model to survey tumorigenic potential applied to the Hedgehog pathway. *Cancer Research*. **66**(20), pp.10171–10178.
- Marigo, V., Davey, R.A., Zuo, Y., Cunningham, J.M. and Tabin, C.J. 1996. Biochemical evidence that patched is the hedgehog receptor. *Nature*. **384**(6605), pp.176–179.

Bibliography

- Martinelli, D.C. and Fan, C.M. 2007. Gas1 extends the range of Hedgehog action by facilitating its signaling. *Genes and Development*. **21**(10), pp.1231–1243.
- McLellan, J.S., Zheng, X., Hauk, G., Ghirlando, R., Beachy, P.A. and Leahy, D.J. 2008. The mode of Hedgehog binding to Ihog homologues is not conserved across different phyla. *Nature*. **455**(7215), pp.979–983.
- Mikami, A., Tynan, S.H., Hama, T., Luby-Phelps, K., Saito, T., Crandall, J.E., Besharse, J.C. and Valle, R.B. 2002. Molecular structure of cytoplasmic dynein 2 and its distribution in neuronal and ciliated cells. *Journal of Cell Science*. **115**(24), pp.4801–4808.
- Milenkovic, L., Scott, M.P. and Rohatgi, R. 2009. Lateral transport of Smoothened from the plasma membrane to the membrane of the cilium. *Journal of Cell Biology*. **187**(3), pp.365–374.
- Milenkovic, L., Weiss, L.E., Yoon, J., Roth, T.L., Su, Y.R.S., Sahl, S.J., Scott, M.P. and Moerner, W.E. 2015. Single-molecule imaging of Hedgehog pathway protein Smoothened in primary cilia reveals binding events regulated by Patched1. *Proceedings of the National Academy of Sciences of the United States of America*. **112**(27), pp.8320–8325.
- Morita, K., Celso, C. Lo, Spencer-Dene, B., Zouboulis, C.C. and Watt, F.M. 2006. HAN11 binds mDia1 and controls GLI1 transcriptional activity. *Journal of Dermatological Science*. **44**(1), pp.11–20.
- Motoyama, J., Heng, H., Crackower, M.A., Takabatake, T., Takeshima, K., Tsui, L.C. and Hui, C.C. 1998. Overlapping and non-overlapping Ptch2 expression with Shh during mouse embryogenesis. *Mechanisms of Development*. **78**(1–2), pp.81–84.

Bibliography

- Motoyama, J., Takabatake, T., Takeshima, K. and Hui, C.C. 1998. Ptch2, a second mouse Patched gene is co-expressed with Sonic hedgehog. *Nature Genetics*. **18**(2), pp.104–106.
- Murakami, S., Nakashima, R., Yamashita, E. and Yamaguchi, A. 2002. Crystal structure of bacterial multidrug efflux transporter AcrB. *Nature*. **419**(6907), pp.587–593.
- Myers, B.R., Neahring, L., Zhang, Y., Roberts, K.J. and Beachy, P.A. 2017. Rapid, direct activity assays for Smoothed reveal Hedgehog pathway regulation by membrane cholesterol and extracellular sodium. *Proceedings of the National Academy of Sciences of the United States of America*. **114**(52), pp.E11141–E11150.
- Nachtergaele, S., Whalen, D.M., Mydock, L.K., Zhao, Z., Malinauskas, T., Krishnan, K., Ingham, P.W., Covey, D.F., Siebold, C. and Rohatgi, R. 2013. Structure and function of the Smoothed extracellular domain in vertebrate Hedgehog signaling. *eLife*. **2**, p.e01340.
- Nachury, M. V., Loktev, A. V., Zhang, Q., Westlake, C.J., Peränen, J., Merdes, A., Slusarski, D.C., Scheller, R.H., Bazan, J.F., Sheffield, V.C. and Jackson, P.K. 2007. A Core Complex of BBS Proteins Cooperates with the GTPase Rab8 to Promote Ciliary Membrane Biogenesis. *Cell*. **129**(6), pp.1201–1213.
- Nachury, M. V. and Mick, D.U. 2019. Establishing and regulating the composition of cilia for signal transduction. *Nature Reviews Molecular Cell Biology*. **20**(7), pp.389–405.
- Nachury, M. V, Seeley, E.S. and Jin, H. 2010. Trafficking to the ciliary membrane: how to get across the periciliary diffusion barrier? *Annual review of cell and*

Bibliography

developmental biology. **26**, pp.59–87.

Nieuwenhuis, E., Motoyama, J., Barnfield, P.C., Yoshikawa, Y., Zhang, X., Mo, R., Crackower, M.A. and Hui, C. 2006. Mice with a Targeted Mutation of Patched2 Are Viable but Develop Alopecia and Epidermal Hyperplasia. *Molecular and Cellular Biology*. **26**(17), pp.6609–6622.

Niewiadomski, P., Kong, J.H., Ahrends, R., Ma, Y., Humke, E.W., Khan, S., Teruel, M.N., Novitch, B.G. and Rohatgi, R. 2014. Gli protein activity is controlled by multisite phosphorylation in vertebrate hedgehog signaling. *Cell Reports*. **6**(1), pp.168–181.

Nonhoff, U., Ralser, M., Welzel, F., Piccini, I., Balzereit, D., Yaspo, M.L., Lehrach, H. and Krobitsch, S. 2007. Ataxin-2 interacts with the DEAD/H-box RNA helicase DDX6 and interferes with P-bodies and stress granules. *Molecular Biology of the Cell*. **18**(4), pp.1385–1396.

Noor, A., Whibley, A., Marshall, C.R., Gianakopoulos, P.J., Piton, A., Carson, A.R., Orlic-Milacic, M., Lionel, A.C., Sato, D. 2010. Disruption at the PTCHD1 locus on Xp22.11 in autism spectrum disorder and intellectual disability. *Science Translational Medicine*. **2**(49), p.49ra68.

Ohgami, N., Kot, D.C., Thomas, M., Scott, M.P., Chang, C.C.Y. and Chang, T.Y. 2004. Binding between the Niemann-Pick C1 protein and a photoactivatable cholesterol analog requires a functional sterol-sensing domain. *Proceedings of the National Academy of Sciences of the United States of America*. **101**(34), pp.12473–12478.

Ortmann, C., Pickhinke, U., Exner, S., Ohlig, S., Lawrence, R., Jboor, H., Dreier, R. and Grobe, K. 2015. Sonic hedgehog processing and release are

Bibliography

- regulated by glypican heparan sulfate proteoglycans. *Journal of Cell Science*. **128**(12), pp.2374–2385.
- Pathi, S., Pagan-Westphal, S., Baker, D.P., Garber, E.A., Rayhorn, P., Bumcrot, D., Tabin, C.J., Blake Pepinsky, R. and Williams, K.P. 2001. Comparative biological responses to human Sonic, Indian, and Desert hedgehog. *Mechanisms of Development*. **106**(1–2), pp.107–117.
- Pearse, R. V., Vogan, K.J. and Tabin, C.J. 2001. Ptc1 and Ptc2 transcripts provide distinct readouts of Hedgehog signaling activity during chick embryogenesis. *Developmental Biology*. **239**(1), pp.15–29.
- Pedersen, L.B. and Akhmanova, A. 2014. Kif7 keeps cilia tips in shape. *Nature Cell Biology*. **16**(7), pp.623–625.
- Pepinsky, R.B., Zeng, C., Went, D., Rayhorn, P., Baker, D.P., Williams, K.P., Bixler, S.A., Ambrose, C.M., Garber, E.A., Miatkowski, K., Taylor, F.R., Wang, E.A. and Galdes, A. 1998. Identification of a palmitic acid-modified form of human Sonic hedgehog. *Journal of Biological Chemistry*. **273**(22), pp.14037–14045.
- Perrin, E., Fondi, M., Papaleo, M.C., Maida, I., Buroni, S., Pasca, M.R., Riccardi, G. and Fani, R. 2010. Exploring the HME and HAE1 efflux systems in the genus Burkholderia. *BMC Evolutionary Biology*. **10**(1).
- Petrov, K., Wierbowski, B.M., Liu, J. and Salic, A. 2020. Distinct Cation Gradients Power Cholesterol Transport at Different Key Points in the Hedgehog Signaling Pathway. *Developmental Cell*. **55**(3), pp.314-327.e7.
- Pettersen, E.F., Goddard, T.D., Huang, C.C., Couch, G.S., Greenblatt, D.M., Meng, E.C. and Ferrin, T.E. 2004. UCSF Chimera - A visualization system

Bibliography

- for exploratory research and analysis. *Journal of Computational Chemistry*. **25**(13), pp.1605–1612.
- Porter, J.A., von Kessler, D.P., Ekker, S.C., Young, K.E., Lee, J.J., Moses, K. and Beachy, P.A. 1995. The product of hedgehog autoproteolytic cleavage active in local and long-range signalling. *Nature*. **374**(6520), pp.363–366.
- Pos, K.M. 2009. Drug transport mechanism of the AcrB efflux pump. *Biochimica et Biophysica Acta - Proteins and Proteomics*. **1794**(5), pp.782–793.
- Qi, C., Minin, G. Di, Vercellino, I., Wutz, A. and Korkhov, V.M. 2019. Structural basis of sterol recognition by human hedgehog receptor PTCH1. *Science Advances*. **5**(9), p.eaaw6490.
- Qi, X., Schmiede, P., Coutavas, E. and Li, X. 2018a. Two patched molecules engage distinct sites on hedgehog yielding a signaling-competent complex. *Science*. **362**(6410).
- Qi, X., Schmiede, P., Coutavas, E., Wang, J. and Li, X. 2018. Structures of human Patched and its complex with native palmitoylated sonic hedgehog. *Nature*. **560**(7716), pp.128–132.
- Qian, H., Cao, P., Hu, M., Gao, S., Yan, N. and Gong, X. 2019. Inhibition of tetrameric Patched1 by Sonic Hedgehog through an asymmetric paradigm. *Nature Communications*. **10**(1), pp.1–9.
- Radhakrishnan, A., Rohatgi, R. and Siebold, C. 2020. Cholesterol access in cellular membranes controls Hedgehog signaling. *Nature Chemical Biology*. **16**(12), pp.1303–1313.
- Raleigh, D.R., Sever, N., Choksi, P.K., Sigg, M.A., Hines, K.M., Thompson, B.M., Elnatan, D., Jaishankar, P., Bisignano, P., Garcia-Gonzalo, F.R., Krup, A.L.,

Bibliography

- Eberl, M., Byrne, E.F.X., Siebold, C., Wong, S.Y et al., 2018. Cilia-Associated Oxysterols Activate Smoothed. *Molecular Cell*. **72**(2), pp.316-327.e5.
- Ramsbottom, S. and Pownall, M. 2016. Regulation of Hedgehog Signalling Inside and Outside the Cell. *Journal of Developmental Biology*. **4**(3), p.23.
- Rana, R., Carroll, C.E., Lee, H.J., Bao, J., Marada, S., Grace, C.R.R., Guibao, C.D., Ogden, S.K. and Zheng, J.J. 2013. Structural insights into the role of the Smoothed cysteine-rich domain in Hedgehog signalling. *Nature Communications*. **4**, p.2965.
- Riobo, N.A., Saucy, B., DiLizio, C. and Manning, D.R. 2006. Activation of heterotrimeric G proteins by Smoothed. *Proceedings of the National Academy of Sciences of the United States of America*. **103**(33), pp.12607–12612.
- Rix, S., Calmont, A., Scambler, P.J. and Beales, P.L. 2011. An Ift80 mouse model of short rib polydactyly syndromes shows defects in hedgehog signalling without loss or malformation of cilia. *Human Molecular Genetics*. **20**(7), pp.1306–1314.
- Rohatgi, R., Milenkovic, L., Corcoran, Ryan B. and Scott, M.P. 2009. Hedgehog signal transduction by Smoothed: pharmacologic evidence for a 2-step activation process. *Proceedings of the National Academy of Sciences of the United States of America*. **106**(9), pp.3196–201.
- Rohatgi, R., Milenkovic, L. and Scott, M.P. 2007. Patched1 regulates hedgehog signaling at the primary cilium. *Science*. **317**(5836), pp.372–6.
- Rothnie, A., Clarke, A.R., Kuzmic, P., Cameron, A. and Smith, C.J. 2011. A

Bibliography

sequential mechanism for clathrin cage disassembly by 70-kDa heat-shock cognate protein (Hsc70) and auxilin. *Proceedings of the National Academy of Sciences of the United States of America*. **108**(17), pp.6927–6932.

Scheres, S.H.W. 2019. *Single-particle processing in relion-3.1*.

Scott, C. and Ioannou, Y.A. 2004. The NPC1 protein: Structure implies function. *Biochimica et Biophysica Acta - Molecular and Cell Biology of Lipids*. **1685**(1–3), pp.8–13.

Seeley, E.S. and Nachury, M. V. 2010. The perennial organelle: assembly and disassembly of the primary cilium. *Journal of Cell Science*. **123**(4).

Shioi, R., Karaki, F., Yoshioka, H., Noguchi-Yachide, T., Ishikawa, M., Dodo, K., Hashimoto, Y., Sodeoka, M. and Ohgane, K. 2020. Image-based screen capturing misfolding status of Niemann-Pick type C1 identifies potential candidates for chaperone drugs. *PLoS ONE*. **15**(12 December).

Sinha, S. and Chen, J.K. 2006. Purmorphamine activates the Hedgehog pathway by targeting Smoothened. *Nature chemical biology*. **2**(1), pp.29–30.

Skurat, A. V. and Dietrich, A.D. 2004. Phosphorylation of Ser640 in Muscle Glycogen Synthase by DYRK Family Protein Kinases. *Journal of Biological Chemistry*. **279**(4), pp.2490–2498.

Snijders Blok, L., Madsen, E., Juusola, J., Gilissen, C., Baralle, D., Reijnders, M.R.F., Venselaar, H., Helmsmoortel, C., Cho, M.T., Hoischen, A., Vissers, L.E.L.M., Koemans, T.S., Wissink-Lindhout, W., Eichler, E.E., Romano, C et al., 2015. Mutations in DDX3X Are a Common Cause of Unexplained Intellectual Disability with Gender-Specific Effects on Wnt Signaling. *American Journal of Human Genetics*. **97**(2), pp.343–352.

Bibliography

- Spasic, M. and Jacobs, C.R. 2017. Primary cilia: Cell and molecular mechanosensors directing whole tissue function. *Seminars in Cell and Developmental Biology*. **71**, pp.42–52.
- Strope, P.K. 2015. Molecular Evolution of Sterol-Sensing Domain in Eukaryotes. . (January 2009), pp.1–2.
- Strutt, H., Thomas, C., Nakano, Y., Stark, D., Neave, B., Taylor, A.M. and Ingham, P.W. 2001. Mutations in the sterol-sensing domain of patched suggest a role for vesicular trafficking in smoothed regulation. *Current Biology*. **11**(8), pp.608–613.
- Sturleya, S.L., Pattersonb, M.C. and Pentchevc, P. 2009. Unraveling the sterol-trafficking defect in Niemann-Pick C disease. *Proceedings of the National Academy of Sciences of the United States of America*. **106**(7), pp.2093–2094.
- Sun, S., Fisher, R.L., Bowser, S.S., Pentecost, B.T. and Sui, H. 2019. Three-dimensional architecture of epithelial primary cilia. *Proceedings of the National Academy of Sciences of the United States of America*. **116**(19), pp.9370–9379.
- Szklarczyk, D., Gable, A.L., Lyon, D., Junge, A., Wyder, S., Huerta-Cepas, J., Simonovic, M., Doncheva, N.T., Morris, J.H., Bork, P., Jensen, L.J. and Von Mering, C. 2019. STRING v11: Protein-protein association networks with increased coverage, supporting functional discovery in genome-wide experimental datasets. *Nucleic Acids Research*. **47**(D1), pp.D607–D613.
- Taipale, J., Cooper, M.K., Maiti, T. and Beachy, P.A. 2002. Patched acts catalytically to suppress the activity of Smoothed. *Nature*. **418**(6900),

Bibliography

pp.892–7.

- Takabatake, T., Takahashi, T.C., Takabatake, Y., Yamada, K., Ogawa, M. and Takeshima, K. 2000. Distinct expression of two types of *Xenopus* Patched genes during early embryogenesis and hindlimb development. *Mechanisms of Development*. **98**(1–2), pp.99–104.
- Takatsuka, Y. and Nikaido, H. 2006. Threonine-978 in the transmembrane segment of the multidrug efflux pump AcrB of *Escherichia coli* is crucial for drug transport as a probable component of the proton relay network. *Journal of Bacteriology*. **188**(20), pp.7284–7289.
- Taylor, M.D., Liu, L., Raffel, C., Hui, C. chung, Mainprize, T.G., Zhang, X., Agatep, R., Chiappa, S., Gao, L., Lowrance, A., Hao, A., Goldstein, A.M., Stavrou, T., Scherer, S.W et al., 2002. Mutations in *SUFU* predispose to medulloblastoma. *Nature Genetics*. **31**(3), pp.306–310.
- Tenzen, T., Allen, B.L., Cole, F., Kang, J.S., Krauss, R.S. and McMahon, A.P. 2006. The Cell Surface Membrane Proteins Cdo and Boc Are Components and Targets of the Hedgehog Signaling Pathway and Feedback Network in Mice. *Developmental Cell*. **10**(5), pp.647–656.
- Tora, D., Gomez, A.M., Michaud, J.F., Yam, P.T., Charron, F. and Scheiffele, P. 2017. Cellular functions of the autism risk factor *PTCHD1* in mice. *Journal of Neuroscience*. **37**(49), pp.11993–12005.
- Torricco, B., Fernández-Castillo, N., Hervás, A., Milà, M., Salgado, M., Rueda, I., Buitelaar, J.K., Rommelse, N., Oerlemans, A.M., Bralten, J., Freitag, C.M., Reif, A., Battaglia, A., Mazzone, L., Maestrini, E et al., 2015. Contribution of common and rare variants of the *PTCHD1* gene to autism spectrum

Bibliography

- disorders and intellectual disability. *European Journal of Human Genetics*. **23**(12), pp.1694–1701.
- Tickle, C. and Towers, M. 2017. Sonic hedgehog signaling in limb development. *Frontiers in Cell and Developmental Biology*. **5**(FEB), p.14.
- Tukachinsky, H., Kuzmickas, R.P., Jao, C.Y., Liu, J. and Salic, A. 2012. Dispatched and Scube Mediate the Efficient Secretion of the Cholesterol-Modified Hedgehog Ligand. *Cell Reports*. **2**(2), pp.308–320.
- Tukachinsky, H., Lopez, L. V. and Salic, A. 2010. A mechanism for vertebrate Hedgehog signaling: Recruitment to cilia and dissociation of SuFu-Gli protein complexes. *Journal of Cell Biology*. **191**(2), pp.415–428.
- Tukachinsky, H., Petrov, K., Watanabe, M. and Salic, A. 2016. Mechanism of inhibition of the tumor suppressor Patched by Sonic Hedgehog. *Proceedings of the National Academy of Sciences of the United States of America*. **113**(40), pp.E5866–E5875.
- Ukmar-Godec, T., Hutten, S., Grieshop, M.P., Rezaei-Ghaleh, N., Cima-Omori, M.S., Biernat, J., Mandelkow, E., Söding, J., Dormann, D. and Zweckstetter, M. 2019. Lysine/RNA-interactions drive and regulate biomolecular condensation. *Nature Communications*. **10**(1), pp.1–15.
- Ung, D.C., Iacono, G., Méziane, H., Blanchard, E., Papon, M.A., Selten, M., van Rhijn, J.R., Montjean, R., Rucci, J., Martin, S., Fleet, A., Birling, M.C., Marouillat, S., Roepman, R., Selloum, M et al., 2018. Ptchd1 deficiency induces excitatory synaptic and cognitive dysfunctions in mouse. *Molecular Psychiatry*. **23**(5), pp.1356–1367.
- Veenstra, V.L., Dingjan, I., Waasdorp, C., Damhofer, H., van der Wal, A.C., van

Bibliography

- Laarhoven, H.W., Medema, J.P. and Bijlsma, M.F. 2018. Patched-2 functions to limit Patched-1 deficient skin cancer growth. *Cellular Oncology*. **41**(4), pp.427–437.
- Vorobyeva, A.G. and Saunders, A.J. 2018. Amyloid- β interrupts canonical Sonic hedgehog signaling by distorting primary cilia structure. *Cilia*. **7**(1), p.5.
- Wang, Q., Asarnow, D.E., Ding, K., Zhang, Y., Ma, Y., Cheng, Y. and Beachy, P.A. 2020. Dispatched conformational dynamics couples transmembrane Na⁺ flux to release of lipid-modified Hedgehog signal. *bioRxiv*.
- Waterhouse, A., Bertoni, M., Bienert, S., Studer, G., Tauriello, G., Gumienny, R., Heer, F.T., De Beer, T.A.P., Rempfer, C., Bordoli, L., Lepore, R. and Schwede, T. 2018. SWISS-MODEL: Homology modelling of protein structures and complexes. *Nucleic Acids Research*. **46**(W1), pp.W296–W303.
- Wicking, C., Shanley, S., Smyth, I., Gillies, S., Negus, K., Graham, S., Suthers, G., Haites, N., Edwards, M., Wainwright, B. and Chenevix-Trench, G. 1997. *Most Germ-Line Mutations in the Nevoid Basal Cell Carcinoma Syndrome Lead to a Premature Termination of the PATCHED Protein, and No Genotype-Phenotype Correlations Are Evident.*
- Wilson, C.W., Chen, M.H. and Chuang, P.T. 2009. Smoothed adopts multiple active and inactive conformations capable of trafficking to the primary cilium. *PLoS ONE*. **4**(4).
- Wojnowska, M., Gault, J., Yong, S.C., Robinson, C. V. and Berks, B.C. 2018. Precursor-Receptor Interactions in the Twin Arginine Protein Transport Pathway Probed with a New Receptor Complex Preparation. *Biochemistry*.

Bibliography

57(10), pp.1663–1671.

Xiao, X., Tang, J.-J., Peng, C., Li, B.-L., Qiu, W.-W. and Correspondence, B.-L.S.

2017. Cholesterol Modification of Smoothed Is Required for Hedgehog Signaling. *Molecular Cell*. **66**, pp.154–162.

Yue, S., Tang, L.-Y., Tang, Ying, Tang, Yi, Shen, Q.-H., Ding, J., Chen, Y., Zhang,

Z., Yu, T.-T., Zhang, Y.E. and Cheng, S.Y. 2014. Requirement of Smurf-mediated endocytosis of Patched1 in sonic hedgehog signal reception. *eLife*.

3.

Zaphiropoulos, P.G., Undén, A.B., Rahnama, F., Hollingsworth, R.E. and

Toftgård, R. 1999. *PTCH2, a Novel Human Patched Gene, Undergoing Alternative Splicing and Up-regulated in Basal Cell Carcinomas 1*.

Zeng, X., Goetz, J.A., Suber, L.M., Scott, W.J., Schreiner, C.M. and Robbins, D.J.

2001. A freely diffusible form of Sonic hedgehog mediates long-range signalling. *Nature*. **411**(6838), pp.716–720.

Zhang, Y., Bulkley, D.P., Xin, Y., Roberts, K.J., Asarnow, D.E., Sharma, A.,

Myers, B.R., Cho, W., Cheng, Y. and Beachy, P.A. 2018. Structural Basis for Cholesterol Transport-like Activity of the Hedgehog Receptor Patched. *Cell*.

175(5), pp.1352-1364.e14.

Zhang, Y., Lu, W.J., Bulkley, D.P., Liang, J., Ralko, A., Han, S., Roberts, K.J., Li,

A., Cho, W., Cheng, Y., Manglik, A. and Beachy, P.A. 2020. Hedgehog pathway activation through nanobody-mediated conformational blockade of the Patched sterol conduit. *Proceedings of the National Academy of Sciences of the United States of America*. **117**(46), pp.28838–28846.

Zheng, C.-Y., Wang, Y.-X., Kachar, B. and Petralia, R.S. 2011. Differential

Bibliography

localization of SAP102 and PSD-95 is revealed in hippocampal spines using super-resolution light microscopy. *Communicative & integrative biology*. **4**(1), pp.104–5.

Zheng, X., Mann, R.K., Sever, N. and Beachy, P.A. 2010. Genetic and biochemical definition of the Hedgehog receptor. *Genes and Development*. **24**(1), pp.57–71.

Zhong, Y., Gu, L.J., Sun, X.G., Yang, S.H. and Zhang, X.H. 2014. Comprehensive analysis of patched domain-containing genes reveals a unique evolutionary pattern. *Genetics and Molecular Research*. **13**(3), pp.7318–7331.

Zhulyn, O., Nieuwenhuis, E., Liu, Y.C., Angers, S. and Hui, C. chung 2015. Ptch2 shares overlapping functions with Ptch1 in Smo regulation and limb development. *Developmental Biology*. **397**(2), pp.191–202.